Evaluation of HIC Resistance in Two X70 Pipeline Steels Using Ultrasonic Testing

by

Steffen Gawor

A thesis submitted in partial fulfillment of the requirements for the degree of

Master of Science

in

Chemical Engineering

Department of Chemical and Materials Engineering

University of Alberta

Abstract

An evaluation of the resistance of two different X70 pipeline steels to hydrogen-induced cracking in severe (pH 2.7 and 1 atm H_2S) and intermediate (pH 5.5 and 1 atm H_2S) sour service conditions was undertaken. The two steels used in this work, X70-X and X70-B, were selected based on their different calcium to sulfur ratios. X70-X and X70-B possess calcium to sulfur ratios of 2.5 and about 0.5, respectively.

Using the NACE standard TM0284-2016 and solution C, samples were tested at pH levels of 2.7 and 5.5 for test periods of 1 to 64 days. Cracking was then evaluated using ultrasonic techniques. At a pH of 2.7, both steels showed cracking after one day in test solution and reached a crack equilibrium after 4 to 8 days. Samples tested at a pH of 5.5 showed cracking after 32 days for steel X70-B and after 64 days for X70-X. For X70-B, a crack equilibrium seemed to be reached after 32 days. In direct comparison with the low calcium to sulfur ratio in X70-B, X70-X showed an increased resistance to hydrogen-induced cracking.

In this work, an ultrasonic procedure, using the crack to backwall signal ratio (CBR), was developed and is used to quantify the extent of cracking in X70-X and X70-B. CBR maps and histograms give information about the location, extent and distribution of cracks. To compare different steels and conditions, a global crack to backwall ratio (GCBR) is obtained by the numerical calculation of the normalized integral of the local CBR values. The GCBR for X70-X after 16 days in a pH 2.7 solution is about 0.3. For X70-B, under identical solutions, a worse GCBR of about 0.55 was recorded. X70-X generally shows a better resistance to hydrogen-induced cracking than X70-B in test solutions of pH 2.7 and 5.5 and for 1 atmospheric pressure of hydrogen sulfide.

It always seems impossible until it's done.

(Nelson Mandela)

Acknowledgements

First and foremost, I would like to express my deepest appreciation to Dr. Hani Henein and Dr. Jingli Luo for the opportunity to carry out research in the field of corrosion. The ability to work on hydrogen-induced cracking as part of my master's degree helped me find a field of research excites me and brings me joy. I am grateful to have had the ongoing support of Dr. Barry Wiskel, without whom this thesis would not have been the same. I appreciate all his help and would like to thank him for the guidance through this project and all the fruitful discussions. His help during the course of my research has been invaluable.

Many thanks to the members of the AMPL research group. You are the best research group anyone could hope for! Special thanks go to Jonas Valloton. He has always been available for discussions and helped me on several occasions with SEM work for my research. His assistance has been invaluable to me and I would like to express my appreciation for his help.

I would like to thank Laurie Collins for his guidance throughout my project. Without his help, I probably would not have started to work on ultrasonic methods for the evaluation of my results. Laurie has always been available for phone calls and the conference calls shed some light on areas that weren't always clear. I also would like to thank Muhammad Arafin for sharing his comprehensive knowledge with me and for his feedback on my research. During my research, Roxanne Stankievech helped me with the planning of my tests, selection of my steel samples and shared her knowledge in the field of corrosion with me. Her help has been invaluable for me and I would like to thank her for all her help. I also would like to thank Tirdad Nickchi for his support with my project. I appreciate the fast and comprehensive responses to my emails and his cooperation with my long term HIC tests. Without him, my project could have been delayed for months. Special thanks go to Curtis Finch for his assistance with the equipment at EVRAZ, his help with the hydrogen analyzer and for running the tests for me in my absence. If it wouldn't have been for his help, my research could have taken significantly longer.

Of course, I would like to thank my parents, Astrid and Thomas Gawor, as well as my sister, Mareike, and my grandparents, Ruth, Uschi and Fred, who supported me during the entire length of my academic path. Their support has been invaluable to me and I am truly grateful to have such an amazing family. I would like to thank Cody Tischler and Jerome Ang for all the fruitful and interesting conversations we had and for helping me to get my mind off research for a while to recharge my batteries. Of course, the list of people would be incomplete without thanking Kevin Dunker and Matt Ansley. You helped me take my mind off things and always cheered me up.

Thank you all for being such good friends.

I also would like to thank Janice and John Day for always welcoming me to their home and including me in their holidays. My Canadian experience wouldn't be the same without you. Finally, I could not have been able to complete this research without Alyssa Day. You were always there for me when I needed you and always helped me find my motivation to finish my studies. Thank you for being the amazing and caring person you are, my life wouldn't be the same without you.

Last, but not least, I would like to thank EVRAZ NA, TC Energy and NSERC for their support for this project. Without their help, this research would not have been possible.

Contents

List of Tables

List of Figures

Chapter 1

Introduction

Hydrogen-induced cracking was first mentioned in the 1950s and its prevention has since gained significant importance. In 1984, the NACE TM0284 standard was created. This standard allows the replication of conditions leading to hydrogen-induced cracking and is intended to give information about the resistance of a steel to the formation of hydrogen-induced cracks. Over the years, this standard has been extended by additional testing solutions and methodologies. However, limitations of this standard still prevail. The testing time is chosen based on the partial pressure of hydrogen sulfide and does not vary with changes in the pH level. Furthermore, the analysis and classification of the tested samples has only localized significance and is time intensive.

In this work the effect of pH value and partial pressure of H_2S on the cracking behaviour of different microalloyed X70 pipeline steels with different calcium to sulfur ratios will be studied using the latest iteration of the NACE standard. The two steels are tested in a NACE TM0284-2016 solution C under different conditions and testing times. Four objectives can be defined:

1. Determine equivalent testing conditions for low and high pH levels, as well as low and high hydrogen sulfide partial pressures to allow for a conversion between mild and sour service tests.

2. Utilize ultrasonic probes to scan cracks over the entire area of the sample to quantify cracking and create ultrasonic maps showing the location of each crack on a grid.

3. Compare the results of steels with different calcium to sulfur ratios to show the significance of manganese sulfide shape control.

4. Analyze the testing times and conduct ultrasonic and hydrogen measurements to visualize cracking behaviour over time.

The thesis will be organized as follows. In a first chapter, a literature review on hydrogen induced cracking and ultrasonic crack testing will be presented. Following this is the description of materials and experimental methods used in this work. The results will then be presented and discussed. Finally, concluding remarks will be drawn.

Chapter 2

Literature Review

For the purpose of this research, the literature review is divided into six sections. In a first section, the history of hydrogen-induced cracking, natural occurrences of hydrogen sulfide and its applications are discussed. This is followed by a brief literature review of the work done on X grade pipeline steel, a description of the NACE TM0284 standard and the electrochemical principles involved in the process. The physical background of ultrasonic wave types and interfaces, as well as the working principle of ultrasonic probes is described. Afterwards, the effects of alloying elements and inclusions on hydrogen-induced cracking are examined. The mechanisms for hydrogen uptake and common methods for the measurement of hydrogen build-up in steel are explained.

2.1 Hydrogen-Induced Cracking

Corrosion is a phenomenon that affects many aspects of our lives and is categorized into several different types. The topic of this work is hydrogen-induced cracking and as such, this first section of the literature review will provide a comprehensive background about the history of hydrogen-induced cracking, as well as applications and natural occurrences of hydrogen sulfide.

2.1.1 Historical Overview

Over the course of the last 100 years, the demand for technology, energy and mobility has drastically increased. To accommodate these demands, copious amounts of resources are necessary [1]. Two very important resources are natural gases and crude oils. These fossil substances are used for a variety of applications, including transportation and production of electrical and thermal energy. One of the biggest obstacle for mankind is posed by the limitation of accessibility and usability of these resources. To meet the continuously growing demand, the expansion of oil and gas pipelines as well as the discovery of new oil and gas wells is necessary. This endeavour has forced mankind to drill deeper and transport greater amounts of oil and gas, pushing the mechanical properties of pipelines to their limits.

Natural gas and crude oils usually carry by-products, such as hydrogen sulfide. An increased

concentration of these by-products can lead to undesirable side effects which ultimately can lead to pipeline failures. While failures can range from small leaks to ruptures, one frequent problem is hydrogen blistering, accompanied by hydrogen-induced cracking. These phenomena have been linked to an increased sourness of the transported product. This sourness can be a result of an increased hydrogen sulfide concentration, which, if the concentration of hydrogen sulfide reaches a certain threshold, is also referred to as sour service.

As the production of sour gas increased during the 1950s, new challenges, such as sulfur deposition and increased corrosion due to the increased amount of H_2S, needed to be overcome. Hydrogen-induced cracking was first reported by Paredes and Mize [2] in 1954 when they determined the cause of an "unusual" pipeline failure to be the formation hydrogen blisters in steel. In 1972, an undersea pipeline in the Gulf of Persia indicated leaking just a few weeks after it was put in service [3]. One suspected contribution of the failure of this X65 pipeline was the low-temperature rolling process used to manufacture the steel. In 1974, a sour-gas pipeline in Saudi Arabia failed after only a few weeks of operation [4]. The failure affected a length of about 10 km. As a result of these and other pipeline failures and incidents due to hydrogen induced cracking, research has been carried out to reproduce the conditions which lead to hydrogen induced cracking. The first standard test for hydrogen induced cracking was established in 1984 by the National Association of Corrosion Engineers (NACE). This test is referred to as the NACE Standard TM0284. The latest iteration of this test was released in 2016 and contains a new test solution with varying pH level and partial pressure of hydrogen sulfide. This variation of parameters allows the reproduction of specific conditions, as concentrations of hydrogen sulfide and pH levels vary from well to well. [5,6]

2.1.2 General Concept of Hydrogen-Induced Cracking

Wet H_2S conditions can lead to hydrogen blistering, hydrogen-induced cracking, stress-oriented hydrogen-induced cracking and sulfide stress cracking [7–11]. This work focuses on hydrogen-induced cracking, which sometimes is also referred to as step-wise cracking [3]. For any material to be affected by hydrogen-induced cracking, it must be susceptible to cracking. The criteria for susceptibility are the amount of hydrogen available, the microstructure present in the steel, and the tensile stress or restraint level (Fig. 2.1). Hydrogen can be generated during acid -base reactions and hydrogen evolution reactions at the steel surface. In the presence of hydrogen sulfide, hydrogen, in its atomic form, diffuses into the steel and forms molecular hydrogen at trapping sites. Additional information about the mechanisms of hydrogen uptake are presented in dedicated sections of the literature review. Different microstructures, such as inclusions and metallographic phases, can act as crack initiation sites, buffer zones or crack barriers. More information about microstructures are presented in a dedicated section. Tensile stresses can arise from processing of the steel, e.g. cold working, thermal treatments, welding, grinding, etc. [12]. Additionally, tensile stresses can be induced by environmental factors, such as temperature or pressure changes. As such, controlling the tensile stress in pipelines can prove difficult. In order for hydrogen induced cracking to occur, all of these factors must be present. Hydrogen-induced cracking can be described in three steps [13]:

1. **Hydrogen generation:** As a result of the hydrogen evolution reaction, hydrogen is generated at the steel surface. The generated hydrogen remains adsorbed in this first step.

2. **Hydrogen diffusion:** Hydrogen atoms desorb from the steel surface and diffuse into the steel matrix. This phenomenon is possible, due to the poisonous effect of hydrogen sulfide and its ions, which prevent the formation of molecular hydrogen at the steel surface [14].

3. **Hydrogen accumulation:** In the third step, hydrogen atoms inside the steel will diffuse to hydrogen traps. These hydrogen traps can be voids around inclusions or metallographic phases, such as martensite. As the hydrogen atoms get trapped, the internal pressure increases locally, leading to crack initiation upon exceeding the threshold of the matrix.

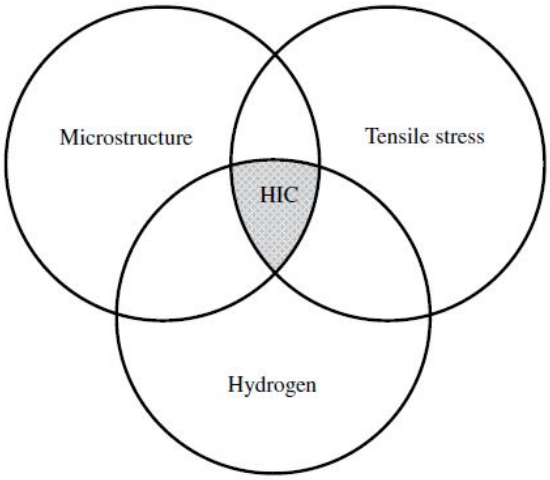

Figure 2.1: Factors influencing susceptibility to hydrogen-induced cracking [15]

2.1.3 Natural Occurrences of Hydrogen Sulfide

Many hydrocarbon reservoirs contain natural H_2S and CO_2 [16]. According to Orr [17], sulfur constitutes about one percent of the dry mass of living organisms. The majority of the amount of sulfur is contributed by cysteine and methionine amino acids. These amounts of sulfur can lead to the generation of H_2S. However, some sour gas fluids have been measured to have an H_2S content of up to 94%. These findings suggest, that a significant portion of H_2S has its origins in sulfate rich minerals. The work of Marriott et al. [16] narrows the production mechanisms of H_2S down to aquathermolysis, microbial sulfate reduction and thermochemical sulfide reduction. More detailed information on these processes and industrial uses of hydrogen sulfide can be found in Appendix A.

2.2 HIC Testing

Over the years, HIC testing has been carried out for a wide variety of steels. The majority of research carried out focused on the effect of inclusions [18–33] and alloying elements [20,23,24,27,30,34–38] on hydrogen-induced cracking. Research was carried out for pipeline steels ranging from X42 to X120. A more detailed summary of the findings, specific to elements of this research is presented in section 2.4. To the knowledge of the author, little work has been done specifically about the correlation between exposure time, pH and partial pressure of hydrogen sulfide for X70 steels.

In the work of Kittel et al. [39], the effect of exposure time for various pH levels is compared for X65 pipeline steel and analyzed using hydrogen permeation testing and ultrasonic crack evaluation of HIC tests. Their work showed that mild sour service conditions generally resulted in the need for longer testing times to reach a state of equilibrium. Figure 2.2 shows the crack to area ratio (CAR) over time for X65 steel under different conditions. It can be seen that a reduced partial pressure of hydrogen sulfide resulted in a lower equilibrium CAR. A direct comparison between 1 atm H_2S and 0.1 atm H_2S shows that hydrogen sulfide is the rate limiting step for HIC cracking, as the maximum extent of hydrogen-induced cracking is lowered with along with the partial pressure of hydrogen sulfide. However, higher pH levels tend to need more time to establish cracks within the steel sample. This can be explained by the reduced hydrogen uptake, due to a limitation in availability of hydrogen. According to earlier work of Kittel et al. [40], the critical threshold of hydrogen inside the steel is between 0.90 ppm and 1.00 ppm H_2. The ultrasonic maps presented in their work show consistent results for samples tested at the same conditions [39].

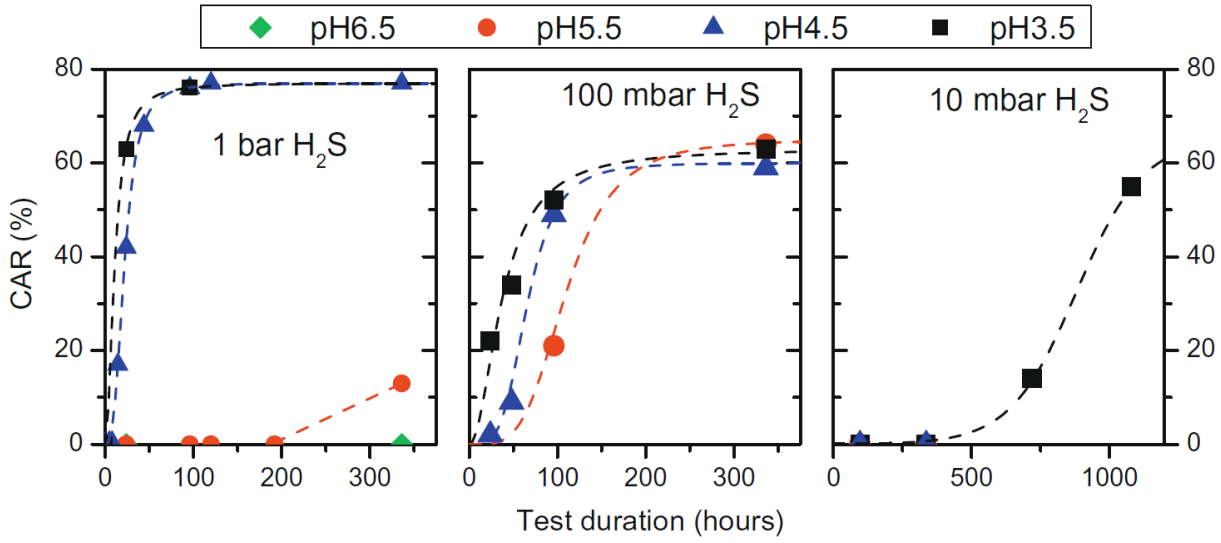

Figure 2.2: HIC test results of X65 pipeline steel, obtained by Kittel et al. [39]

In this work, the latest iteration of the NACE standard TM0284-2016 is used to study the effects of pH, partial pressure of hydrogen sulfide and exposure time on hydrogen-induced cracking

of X70 pipeline steel. The setup and testing procedure, as well as the chemical composition of the test solution will be explained in the following sections.

2.2.1 NACE Standard TM0284-2016

The NACE Standard TM0284 is a test method designed to evaluate the resistance of pipelines and pressure vessels to hydrogen-induced cracking (HIC) due to the absorption of hydrogen released as a result of aqueous sulfide corrosion. A schematic diagram of the experimental setup is shown in Figure 2.3. The gas cylinders are connected to a flow-meter to allow for a controlled gas flow. As a safety measure, the gas is directed into a trap. From the trap, the gas is bubbled into the test vessel from the bottom. Any gas not dissolved into the test solution and dwelling above the test solution will escape the test vessel and is collected in a second trap. Any gas collected in the trap will be neutralized in a scrubber solution containing 10% NaOH.

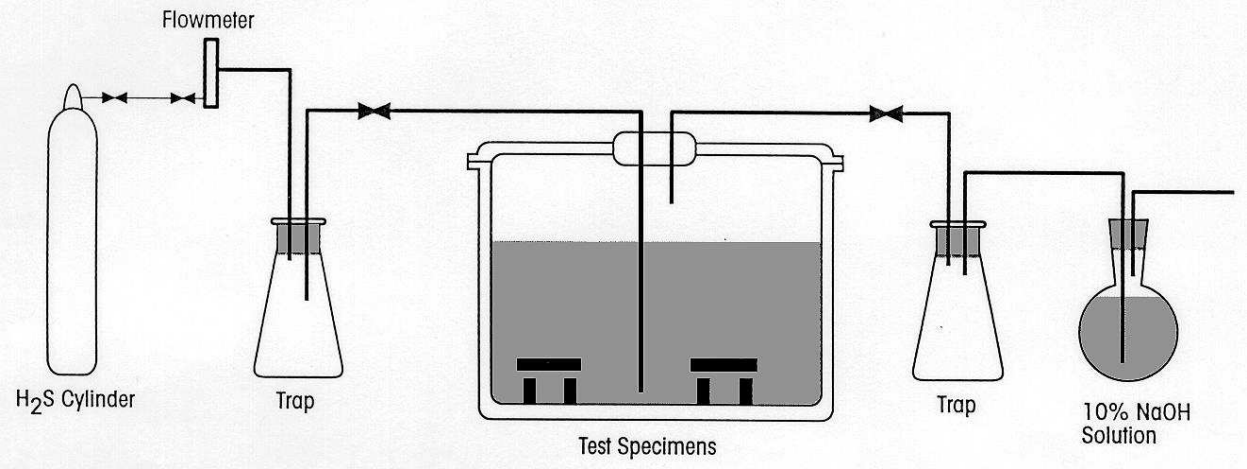

Figure 2.3: Schematic diagram of test setup [6]

The contents of the three test solutions used in the NACE standard TM0284-2016 (A-C) are shown in Table 2.1. All test solutions are to be used at ambient temperature and pressure. Solution A and C are based on deionized or distilled water, test solution C consists only of synthetic seawater saturated with H_2S. The combined gas pressure of CO_2 and H_2S in solution C is the ambient gas pressure of about 1 bar. Hydrochloric acid and sodium hydroxide are used in solution C to adjust the pH to the target pH. The pH must be adjusted to ± 0.2 of the target pH. All chemicals must be of reagent grade.

In this work, a modified solution C* is used for 0.1 atm H_2S is used. The difference between C and C* is the use of nitrogen instead of carbon dioxide. In this work, both solutions are used. However, the majority of experiments are carried out using 0.9 atm nitrogen.

Table 2.1: Composition of different test solutions according to NACE TM0284-2016 [6]

Substance	Solution A	Solution B	Solution C	Solution C*
H_2O [wt.%]	94.5	-	94.6	94.6
Synthetic Seawater [wt.%]	-	100	-	-
CH_3COOH [wt.%]	-	0.5	-	-
CH_3COONa [wt.%]	-	-	0.4	0.4
NaCl [wt.%]	5	-	5	5
H_2S [atm]	1	1	0.1 to 1	0.1 to 1
CO_2 [atm]	-	-	$1 - H_2S$ [atm]	-
N_2 [atm]	-	-	-	$1 - H_2S$ [atm]
HCl [wt.%]	-	-	pH dependent	pH dependent
NaOH [wt.%]	-	-	pH dependent	pH dependent

2.2.2 Electrochemical Stability of Iron Sulfides

According to Taylor [41] and Smith and Miller [42], polymorphous iron sulfides can be formed during hydrogen sulfide corrosion processes. The formation of these polymorphous phases depend on the ambient temperature, the pH level, the exposure time and their electrochemical stability [43]. A list of common polymorphous iron sulfides can be seen in Table 2.2. It can be seen that amorphous iron sulfide, as well as cubic iron sulfide are unstable and will transform into mackinawite, troilite or pyrrhotite, respectively. Research has shown, that under sour service corrosion conditions, mackinawite, cubic ferrous sulfide, troilite, pyrrhotite, as well as greigite and pyrate are formed [44–48]. However, the initial corrosion product is widely considered to be mackinawite [43].

Table 2.2: Polymorphous phases of iron sulfide, adapted from Ning et al. [43]

Name	Chemical Formula	Crystal Structure	Properties
Amorphous	FeS	nano-crystalline	unstable; converts to mackinawite
Mackinawite	FeS	tetragonal (2D layer)	metastable; initial corrosion product
Cubic FeS	FeS	cubic	very unstable; never found naturally; can transform to mackinawite, troilite or pyrrhotite
Troilite	FeS	hexagonal	Stoichiometrix end member of the $Fe_{1-x}S$ group ($x = 0$)
Pyrrhotite	$Fe_{1-x}S$	monoclinic (Fe_7S_8) or	thermodynamically stable; most abundant

Continued on next page

Table 2.2 – Continued from previous page

Name	Chemical Formula	Crystal Structure	Properties
		hexagonal ($Fe_{10}S_{11}$)	iron sulfide in the earth
Smythite	$Fe_{3+x}S_4$	trigonal hexagonal	metastable; related to the $Fe_{1-x}S$ group
Greigite	Fe_3S_2	cubic	metastable Fe^{2+} Fe^{3+} sulfide
Pyrite	FeS_2	cubic	thermodynamically stable; abundant mineral of earth's surface
Marcasite	FeS_2	orthorhombic	metastable

Similar to the correlation between iron and carbon with respect to temperature and composition, iron and water form a complex system with a strong dependency on the pH, temperature and electrochemical potential. These systems can be visualized as Pourbaix diagrams and show stable phase regions as a function of pH level. Figure 2.4 shows the Fe-H_2O system at 25 ° C. Represented as dotted lines are the redox reactions of water. The area in between the two dotted lines represents the stable phase of H_2O, below this area H_2 is stable, above O_2. Horizontal, solid lines indicate pure redox reactions. These lines show an independency of the pH level. Displayed as vertical, solid lines are pure acid-base reactions. These are independent on the electrochemical potential and are only influenced by the pH level. In case of this Pourbaix diagram, one can recognize that iron in its Fe state does not have a stable phase in the H_2O area, instead, phases like Fe^{2+}, Fe^{3+}, Fe_3O_4 and $Fe(OH)_2$ are favourable. It can be seen that Fe^{3+} does not have an electrochemically stable phase for pH levels greater than 2. Similarly, Fe^{2+} is not stable at pH levels greater than about 8. If the electrochemical potential of the water is sufficiently high, i.e. high oxygen concentration is available, iron will form oxidization layers, such as Fe_2O_3 to impede the corrosion reaction [49]. This process is referred to as anodic passivation. Analogously, a low electrochemical potential will favour the mechanism of cathodic protection and form phases such as $Fe(OH)_2$.

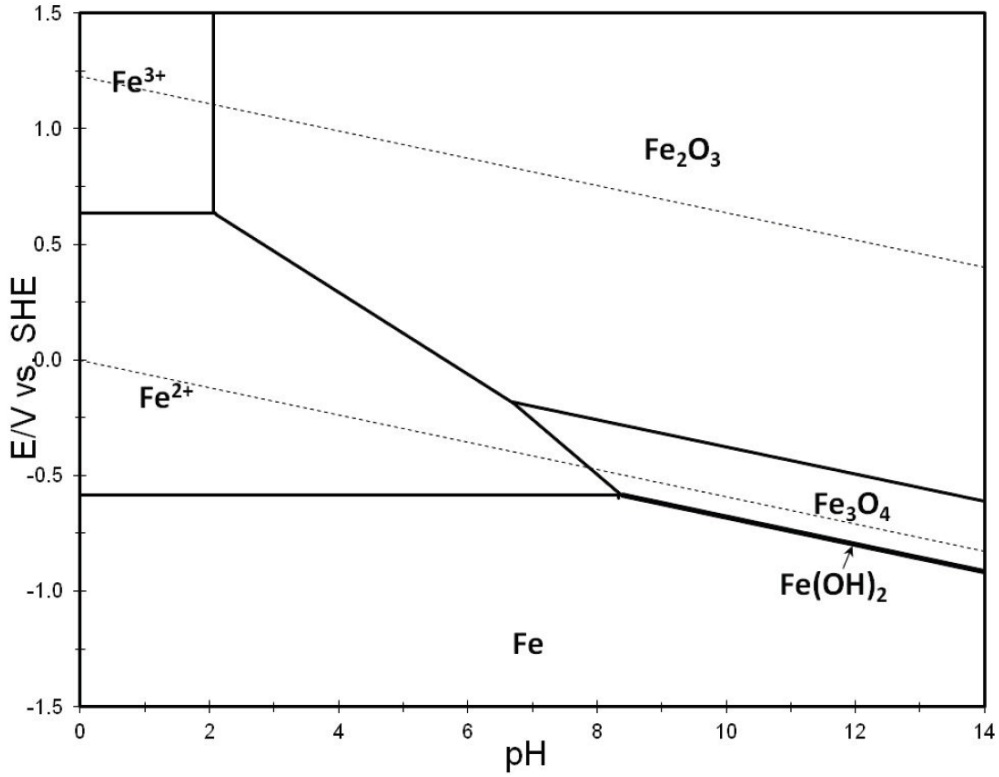

Figure 2.4: Pourbaix diagram for Fe-H_2O system at 25 °C [43]

Introducing partial pressures of hydrogen sulfide ranging from 40 ppm to 8000 ppm [43] to the Pourbaix diagram (Fig.2.5), changes the stability of phases drastically. It can be seen that Fe^{2+} is now only stable until a pH of about 4.3 is reached. The phases Fe_3O_4 and $Fe(OH)_2$ are no longer stable and instead, the formation of FeS in its mackinawite phase are favoured for lower electrochemical potentials. Considering the relatively high pH levels of hydrogen sulfide, the change in stability region allows for the creation of iron sulfides if the pH reaches a local level of about 4.3. Furthermore, the addition of hydrogen sulfide to the system increases the required electrochemical potential for the anodic passivation mechanism and thus increases the likelihood of corrosion.

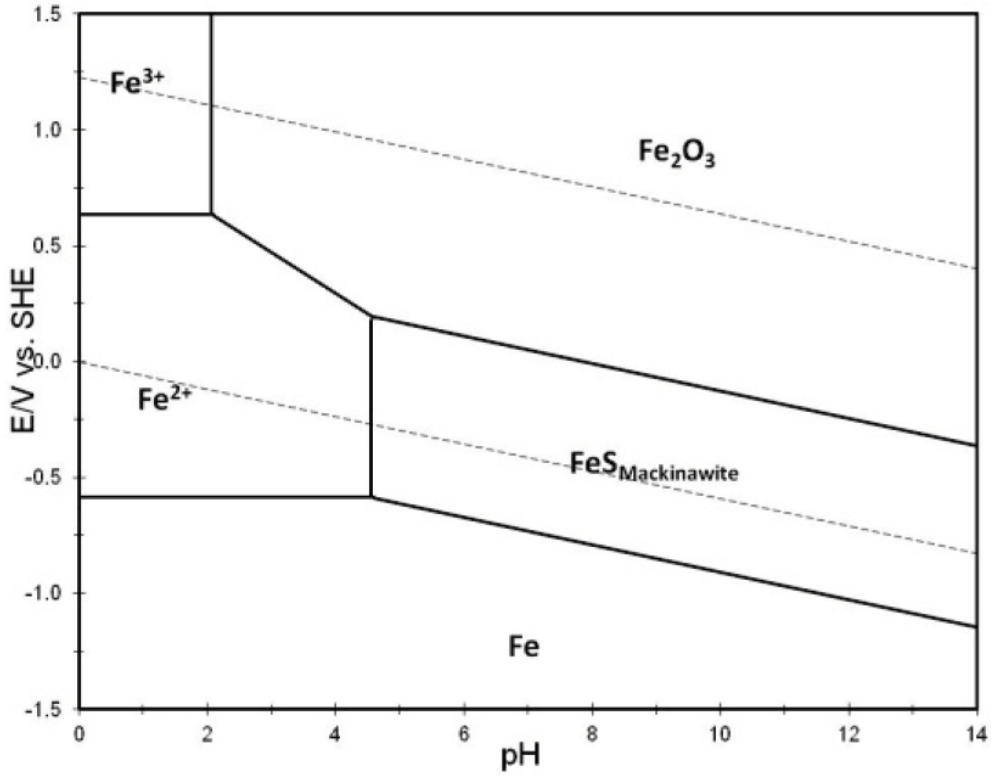

Figure 2.5: Pourbaix diagram for Fe-H_2O-H_2S (mackinawite) system at 25 °C [43]

As mackinawite is a metastable phase, further phase transformations will occur over time. Considering the known phases of iron sulfide in corrosive systems, the Pourbaix diagram can be extended by greigite, pyrrhotite and pyrite (Fig. 2.6). It can be seen that mackinawite no longer forms stable phases. Furthermore, it is noticeable, that both greigite and Fe^{3+} are incapable of forming stable phases over the entire pH range. The overall stability of Fe^{2+} is pushed towards lower electrochemical potentials and anodic passivation is no longer possible, as Fe_2O_3 does not form stable phases in the displayed range. For conditions in the H_2 region, pyrrhotite will be formed at pH levels greater than 4.2. As can be seen, the dominating phase in this system for the liquid region is Pyrite.

Additional Pourbaix diagrams for the Fe-H_2O-H_2S system can be found in the work of Gao et al. [50]. In their work, they created Pourbaix diagrams for 120 °C while considering only mackinawite. Compared to the results at 25 °C, the stability zone of Fe^{3+} is reduced in size in favour for the stability of Fe_2O_3. The stability of mackinawite is slightly reduced at higher pH levels. Gao et al. observed the formation of troilite, pyrrhotite and finally pyrite from mackinawite using TEM techniques.

In the work of Zhao et al. [51], Pourbaix diagrams for Fe-H_2O-Cr,Fe-H_2O-Cl^-, Fe-H_2O-CO_2 and, by superposition, Fe-H_2O-Cr-Cl^--CO_2 can be seen. The diagrams shown in this work are valid for temperatures of 95 °C, 120 °C, 150 °C and 180 °C. For the HP-13Cr steel used in their

work, they identify the passivity regions to be Cr_2O_3 and $Cr(OH)_3$ (s).

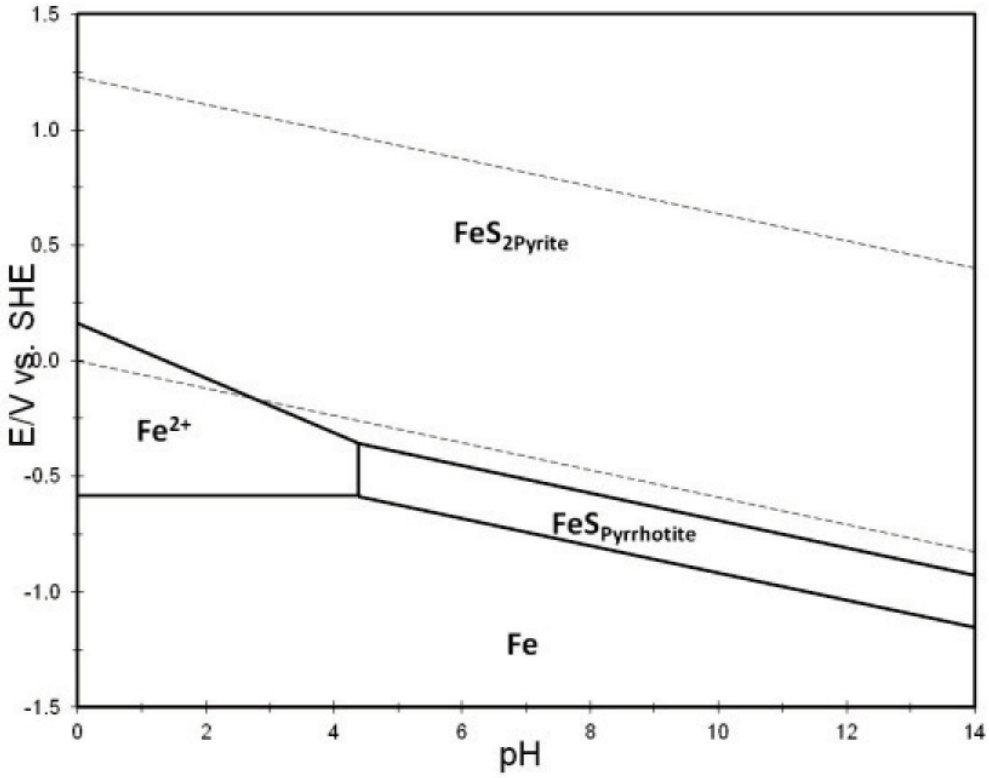

Figure 2.6: Pourbaix diagram for Fe-H_2O-H_2S (mackinawite, greigite, pyrrhotite and pyrite) system at 25 °C [43]

2.2.3 Microbiologically Influenced Corrosion

According to Ravishankar and Zarasvand [52], the presence of microbes (i.e. bacteria [53], fungi [53] and algae [54]) and their resulting biofilms can alter the electrochemical reaction involved in corrosion. Due to the metabolic activity of these microbes, the interface between the biofilm and the metallic surface can, depending on the microorganisms, both accelerate and inhibit corrosion. This active involvement in the corrosion process can occur in form of the formation of differential concentration cells, generation of corrosive substances, alternation of anion ratios or the inactivation of corrosion inhibitors. For hydrogen-induced cracking, the most significant impact is the generation of corrosive substances, such as hydrogen sulfide.

As presented earlier, the generation of hydrogen sulfide is associated with sulfate reducing bacteria. In complex biochemical reactions, sulfide oxidizing bacteria generate sulfuric acid. This sulfuric acid is the converted into hydrogen sulfide in the presence of sulfate reducing bacteria. To prevent this constant generation of hydrogen sulfide in oil and gas pipelines, heterotrophic nitrate-reducing bacteria are introduced to the system [52]. The work of Thauer et al. [55] has shown that the energy gain for nitrate reducing reactions is significantly greater than that of sulfate reducing

reactions. As a result of this, the presence of nitrate-reducing bacteria effectively suppresses the reactions of sulfate reducing bacteria.

Although microbiologically influenced corrosion is often an additional factor for hydrogen-induced cracking, the presence of biofilms has also been linked to the inhibition of corrosion in form of the removal of corrosion agents, the formation of protective layers, the elimination of corrosion-causing bacteria by their corresponding antimicrobial agents, the production of peptide corrosion inhibitors, and the production of iosurfactants [52].

2.3 Ultrasonic Crack Testing

Ultrasonic test methods have many applications. The purpose in this work is to generate maps showing the crack locations over the entire area of the sample. Furthermore, the use of non-destructive ultrasonic measurements over the traditional cutting method allows for a significant decrease in analysis time. In a first section, an overview over different techniques used for the evaluation of hydrogen-induced cracking is presented. This is followed by the theoretical background. First, different types of ultrasonic waves and their differences are presented. Afterwards, an explanation of ultrasonic interfaces. In a last subsection, the principle of flaw detection using ultrasonic probes is described.

2.3.1 Ultrasonic Crack Evaluation of Hydrogen-Induced Cracking

Ultrasonic testing has long been used to evaluate types of hydrogen damage. In 1978, Szilard and Haynes [56] used ultrasonic data to correlate changes in the ultrasonic velocity to hydrogen embrittlement. In their work, they used shear waves to determine the hydrogen embrittlement damage in tensile test samples during strain tests.

A variety of ultrasonic techniques can be used for the determination of hydrogen-induced cracks. The two most common ultrasonic techniques are A- and C-scans. While the A-scan focuses on a single location and detects cracks in one dimension, the C-scan scans cracks along a two dimensional grid [57]. Both of theses techniques have their individual applications. An A-scan can be used to confirm the presence of cracks in a pipeline or to measure the crack growth in a certain location over time. However, for hydrogen-induced cracking, C-scans are more desirable as they can be used to determine the location and size of individual cracks. In 1993, Revie et al. [58] used C-scan traces to analyze the cracking behaviour of various steels exposed to test solutions with pH levels ranging from 1.1 to 5.9. Ultrasonic testing was carried out prior to testing, to check for existing cracks and after charging for 96h. Krüger et al. [59] used spectral analysis techniques for the detection of minute cracks in steel after exposed to a solution containing hydrogen sulfide in compliance to the NACE standard TM0177. In the work of Kittel et al. [39], ultrasonic maps, showing the crack to area ratios (CAR), are generated to compare the cracking behaviour of X65 steels exposed to different test solutions. For the calculation of the CAR ratio, the area affected by cracks was divided by the overall area. The solutions used vary in the pH and hydrogen sulfide

concentration. In 2016, Nardo et al. [60] used phased array ultrasonic methods coupled with post processing techniques to determine the crack formation of carbon steel pressure vessels exposed to hydrogen sulfide environments. Hwang et al. [61] analyzed the formation of cracks in steel samples using C-scans coupled with synthetic aperture focusing techniques.

2.3.2 Wave Types

According to Chemat [62], the frequency range of ultrasound is 16 kHz - 1 GHz. Common types of ultrasonic waves are longitudinal waves, surfaces waves and shear waves. In this work, a longitudinal probe with an operating frequency of 10 MHz is used. The following two subsections describe and compare the properties and differences of both longitudinal and shear waves.

In longitudinal wave, as the name implies, particles travel parallel to the wave direction [63]. A typical example for this type of wave are audible sound waves, such as music coming from a speaker. Figure 2.7 shows a visualization of both longitudinal and shear waves. Commonly, longitudinal waves reach velocities of about 5900 m s^{-1} in steel.

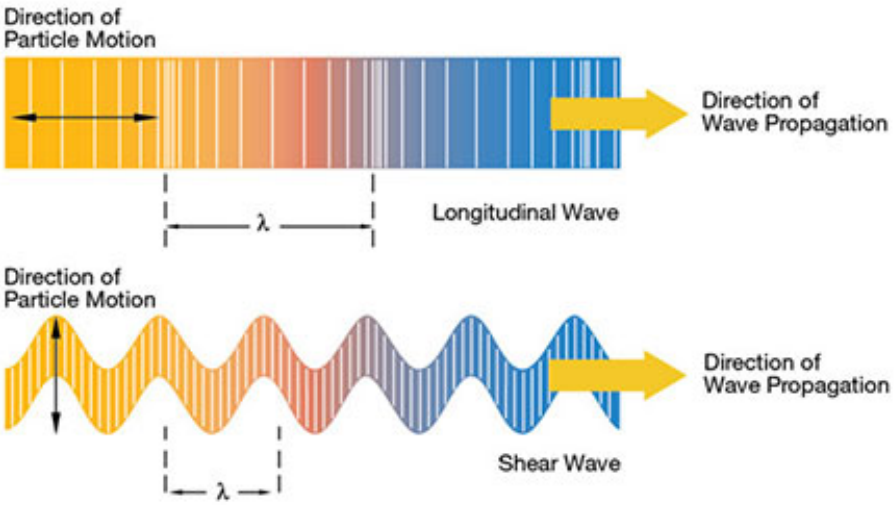

Figure 2.7: Longitudinal and shear wave motions [63]

It is possible for a longitudinal sound wave to convert into a shear wave if the angle between the transducer and the medium is sufficiently large [64]. If the transducer is not perfectly orthogonal to the surface of the medium, the longitudinal wave may be accompanied by a shear wave. This phenomenon is visualized in Figure 2.8.

Other than longitudinal waves, particles in shear waves propagate perpendicular to the wave direction [63]. This behaviour can be seen in Figure 2.7, where the shear wave resembles the movement of a sinus wave. In direct comparison with the longitudinal wave, shear wave of the same frequency exhibit a shorter wavelength (λ) and ultrasonic velocity. A typical shear velocity in steel is 3250 m s^{-1}. Common applications for shear wave are measurements at angles and

curvatures. It should be noted that shear waves can only exist in solid materials, not in gases or liquids. At boundaries, shear waves can convert into longitudinal waves through reflection or refraction.

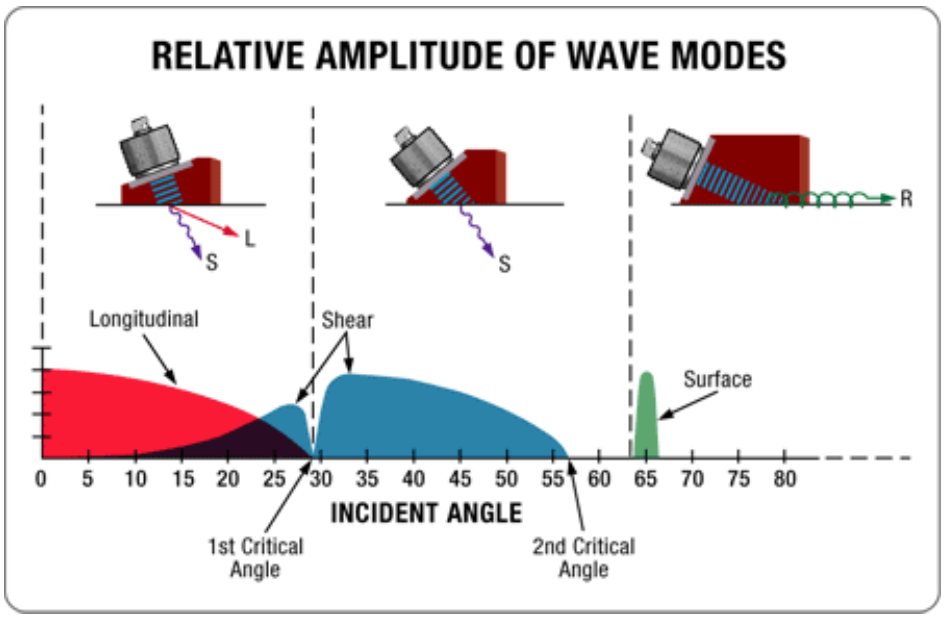

Figure 2.8: Longitudinal and shear wave motions [64]

2.3.3 Interfaces

Interfaces can be described as areas of different physical properties [64]. For ultrasonic measurements, two properties are of immediate relevance; the speed of sound in the material and the angle at which the ultrasonic beams enter the medium. If the speed of sound of the new media is greater than in the previous media, the beam angle of the sound waves will increase based on the principle of refraction [65]:

$$\sin(\theta_1) = \frac{v_1 t}{AB} \qquad \& \qquad \sin(\theta_2) = \frac{v_2 t}{AB} \tag{2.1}$$

In this equation, θ_1 represents the angle at which the sound wave travels through media 1, θ_2 represents the refracted angle of the sound wave in media 2, v_1 represents the velocity in media 1, v_2 represents the velocity in media 2, t represents the time and AB the distance between point A and B. A visualization of this process can be seen in Figure 2.9. Division of these two equations leads to Snell's equation:

$$\frac{\sin(\theta_1)}{\sin(\theta_2)} = \frac{v_1}{v_2} \tag{2.2}$$

Where θ_1 and θ_2 represent the angles at which the wave moves through the medium and v_1 and v_2 are the corresponding velocities of the sound waves in medium 1 and 2.

The change in direction of the wave can be explained using the principle of Huygens. In Figure 2.9, the two wave fronts are visualized in red and blue and move along the two dash-dotted

lines. The horizontal in the center of the graph represents the boundary between medium 1 and 2. Although represented as straight lines, wave fronts can be understood as spherical movements with their greatest intensity localized at the lines visualized in Figure 2.9. Once a wave front hits an obstacle, such as a boundary, this spherical movement bends, or refracts, and a new wave front is created based on the principle of superposition. This process is visualized in Figure 2.10 using the example of light waves reflecting off a mirror.

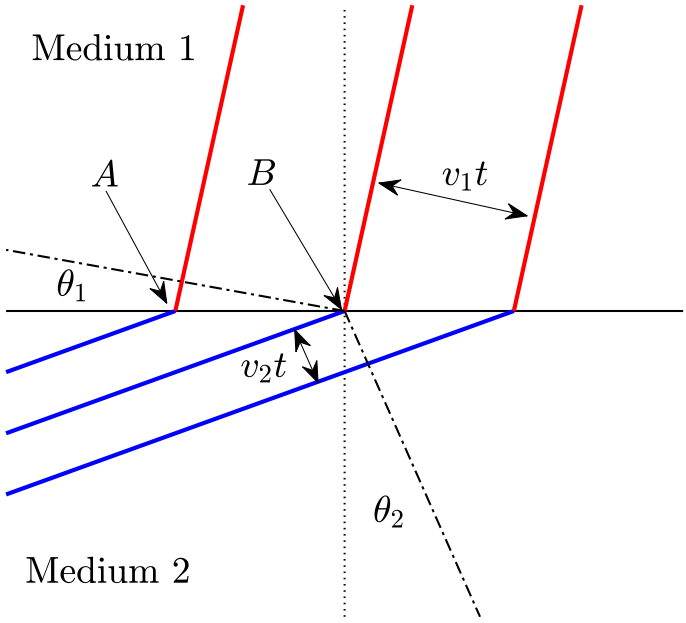

Figure 2.9: Visualization of wave refraction

In case of ultrasonic waves, the majority of the wave energy is refracted as it passes a boundary, if the wave velocity of the new medium is greater than that of the current medium. As can be seen in Equation 2.2, the change in movement angle relative to the boundary of the material depends on the velocity of both mediums. If v_2 is larger than v_1, the resulting angle will be larger as well. As the angle of the new wave is of refractive nature, the wave is bent in the opposite direction as for reflection. If the velocity of the wave is drastically reduced in the new medium, the wave is reflected.

As can be seen in Figure 2.8, the entry angle into the new medium is of importance as well, as a conversion of signal can occur for higher entry angles. While shear waves are stable from entry angles between 30° and about 55°, longitudinal waves start to transform into shear waves at entry angles greater than 5°. If the entry angle is larger than about 60°, the wave is converted into a surface wave and does not penetrate the new medium.

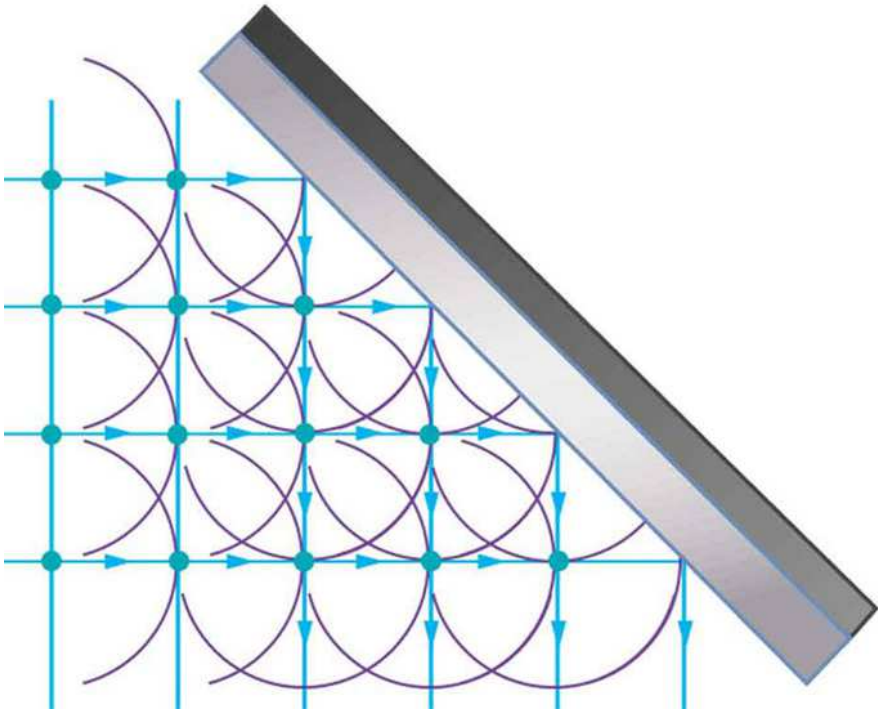

Figure 2.10: Visualization of Huygens principle using light waves reflecting off a mirror [66]

For all waves, conditions can be categorized into two areas, the near field and the far field. In the near field, the outer boundaries of the beam can be assumed parallel to each other. If sound travels through a media over a prolonged distance, the beam angle in the far field, or Fraunhofer zone, will increase due to heat dissipation and the resulting attenuation. This can be seen in the following equation:

$$\alpha = \sin^{-1}\left(\frac{0.514v}{d_p f}\right) \tag{2.3}$$

In this equation, α represents the deviation half angle of the beam compared to a perpendicular beam, v is the speed of sound in the media, d_p is the effective diameter of the ultrasonic probe and f is the operating frequency. The factor of 0.514 is a constant used for the -6 dB boundary of the beam to account for irregular derivations of the beam angle [67, 68]. To define the outer limit of the beam, a factor of 1.22 should be used. The -6 dB boundary of a beam is the point at which the energy of the beam is about a quarter the energy of the core of the beam [69].

The distance between the near and far field can be expressed using the Fraunhofer distance [70]:

$$d_f = \frac{2d_p^2}{\lambda} \tag{2.4}$$

In this equation, d_f is the Fraunhofer distance, d_p is the largest size of the radiator and λ is the

wavelength. The wavelength can be described as a function of velocity and frequency [65]:

$$\lambda = \frac{v}{f} \tag{2.5}$$

where λ is the wavelength, v the velocity of the wave and f the frequency. Using the same variables, these two equations can be combined to:

$$d_f = \frac{2d_p^2 f}{v} \tag{2.6}$$

As can be seen, the Fraunhofer distance is anti proportional to the speed of sound. The greater the speed of sound, the shorter the Fraunhofer distance. As a consequence, materials with a greater speed of sound gain an additional error faster than those with a lower speed of sound.

2.3.4 Flaw Detection

Ultrasonic crack testing is a non-destructive test method to determine flaws in materials, to measure the thickness of a material or to obtain information about the microscopic structure in steels and other metallic alloys. According to Wiskel et al. [71], ultrasonic testing is widely used to access the weld quality in pipeline steel during the manufacturing process, installation and welding of individual pipeline pieces. In their work, they used the ultrasonic velocity to determine the uniformity of the metallographic microstructure of API 5L X70 pipeline steel using longitudinal and shear waves. In their work, Buschow et al. [72], stated that ultrasonic analysis is not equally adequate for all kinds of steel. Those with larger grain sizes can result in a large amount of background noise, which deteriorates the accuracy of the measurement.

Ultrasonic probes operate based on the principle of piezoelectric ceramics or composites [73]. The piezoelectric effect describes the polarization of a crystal as a result of mechanical stress [74]. This polarization results in a conversion from mechanical energy to electrical energy and vise versa. Using the phenomenon it is possible to both emit and detect sonic waves in a single probe by applying an electric signal to the probe and monitoring its change over time. The corresponding function would show a voltage dependency over time and can be used to determine the distance between the probe and the first detected interface. If the thickness of the test sample is known, the time difference between to data peaks can be correlated to:

$$\Delta t = \frac{2d}{v_s} \tag{2.7}$$

where Δt describes the difference in time, d the distance to the interface and v_s the velocity of sound in the test sample. The factor 2 results from the principle of reflection, as the ultrasonic signal is reflected from the interface (d) and is detected by the probe (d). Over time, the signal attenuates as it is dissipated into heat due to imperfections in the material of the test sample [64]. This results in a steady decay of measured peak heights.

2.4 Microstructural Effects on Hydrogen-Induced Cracking

The phenomenon of hydrogen-induced cracking is influenced by a wide variety microstructures and inclusions. In this work, two X70 pipeline steels with different calcium to sulfur ratios are compared with respect to their cracking behaviour over time. A literature review on the known effects of different metallographic inclusions and microstructures is presented in a first subsection. Followed by this is a description of sulfide and oxide shape control, as well as deoxygenation and desulfurization.

2.4.1 Effect of Inclusions and Microstructure on Hydrogen-Induced Cracking

Zhu and Oda stated in their work, that defects in the material, such as vacancies, dislocation, grain boundaries and phase interfaces are the main trap sites for hydrogen in iron [75]. According to Chan and Charles [76], the main diffusive path in a ferrite/pearlite structure was along the ferrite grains or interfaces between ferrite and pearlite. Furthermore, pearlite acts as an effective barrier to hydrogen diffusivity. If the local density of trapped hydrogen reaches a critical value, a crack can be initiated [29]. This critical value depends on the trapping energy of the dislocation [77]. The largest trapping energies can be found in phase interfaces and grain boundaries.

Liu et al. [78] studied the effect of microstructure and inclusions on the susceptibility of HIC of X120 pipeline steel. In their work, they found that steel containing granular bainite and martensite/austenite show more susceptibility to HIC. The susceptibility was also increased by larger amounts, areas and volume fraction of inclusions.

Du et al. [29] presented in their work that hydrogen-induced cracking is primarily initiated at the interface between ferritic and pearlitic bands and nucleates at inclusions. In the steel they studied, an A537 steel, they found the main inclusions for nucleation to be manganese sulfide and aluminum oxide. These results are supported by the findings of Ouhiba [79]. In her work, she studied hydrogen induced cracking and sulfide stress cracking in low alloy casing pipes, such as L80, and found the elongated manganese sulfide inclusions to be the main initiation site for cracking. Furthermore, her work shows that most cracks occur in the enriched centerline segregation zone. Huang et al. [80] carried out experiments using the NACE TM0284 standard on hydrogen induced cracking of welded X100 pipeline steel. In their work, they found the initiation sites for HIC to be globular inclusions enriched in Al, Ca, Si and Mn. The cracks found in their research were primarily transgranular. Due to strict sulfur control, no manganese sulfide was found in their steel. Using SEM and EDS analysis, the majority of inclusions was determined to be globular Al-Ca-Si-O compounds. Additionally, globular Al_2O_3, CaO and SiO_2 inclusions were found. In the work of Xue and Cheng [25], silicon enriched aluminum oxide inclusions are believed to be the main crack initiation sites, due to their hardness, brittleness and incoherence with the metal matrix. In their work, only few manganese sulfide inclusions were found, as a result of sulfur level control. Dong et al. [81] studied hydrogen-induced cracking in X70 steel. In their work, the most significant impact on cracking is believed to be oxide inclusions, rather than titanium or niobium

nitrides. Furthermore, their research concluded that cracks seem to appear at polygonal ferrite grain boundary interfaces. No cracks were observed at acicular ferrite grain boundaries.

Gao et al. [82] compared the hydrogen induced cracking behaviour of different microstructures. In their work, they evaluated the corrosion resistance of granular bainite and lath bainite (GB+LB), granular bainite and acicular ferrite (GB+AF) and quasi-polygonal ferrite (QF) using the NACE standard TM0284. They found granular bainite and acicular ferrite to have the best combination of mechanical properties and resistance to HIC among the phases studied. Quasi-polygonal ferrite inhibits a good resistance to HIC, but has a coarser microstructure than GB+LB and AB+AF. The worst resistance to cracking was found in granular bainite and lath bainite structures. An analysis of their studies showed that larger sizes and volume fractions of lath bainite and martensite/austenite are responsible for poor corrosion resistance.

In their work, Latifi et al. [83] and Beidokhti et al. [84] studied the resistance to hydrogen-induced cracking of X65 and X70 steels, respectively. Their work shows and confirms that acicular ferrite possesses a higher resistance to HIC. It is suggested that acicular ferrite could act as an effective reversible hydrogen trapping site [85]. Being reversible, this trapping site could allow trapped hydrogen to escape before a critical concentration is reached.

Carneiro et al. [86] studied the influence of chemical composition and microstructure of linepipe steel on hydrogen induced cracking. Their work showed best results for a homogeneously quenched and tempered bainite microstructure with little martensite.

2.4.2 Limits to Aluminum and Silicon Content in Steel Deoxidation

One common alloying element for the deoxidation of steel is aluminum [87]. Due to its high affinity for oxygen, aluminum tends to form aluminum oxides in molten steel. This is especially important for the addition of zirconium, niobium and titanium to the steel as the purpose for these elements is to react with the carbon or nitrogen dissolved in the steel. As excessive aluminum decreases the hardness of steel, the amount of aluminum added to the melt is usually controlled to 1.5% or less.

Another element used for the deoxidation is silicon. To achieve a reduction of unwanted oxides, at least 0.1% is added to the melt. However, due to adverse effects on the softness of steels, the amount of silicon added to the melt is usually less than 1% [87, 88].

2.4.3 Shape Control of Sulfides and Desulfurization

The addition of manganese to a steel allows the formation of sulfides. However, due to the high plasticity, manganese sulfide tends to deform into elongated inclusions during the hot rolling process [89]. To some extent, the shape of the inclusions can be modified using cross rolling techniques. However, the most effective way to prevent elongated sulfides is to modify the chemistry of the steel. In their work, Luyckx et al. [89] stated that the properties of a sulfide shaping element should include high melting points and stabilities, as well as not being able to deform as easy as manganese sulfide at hot rolling conditions. In addition to these criteria, the element needs to be relatively inexpensive, available in large quantities and should not be hazardous in its use. Figure

2.11 shows a periodic table of elements containing possible sulfide formers. Luyckx et al. single out calcium, uranium and rare earth elements (abbreviated as R.E.) as potential sulfide formers. Although both zirconium and titanium have the potential of forming stable sulfides, their affinities towards carbon and nitrogen make them an undesirable choice [89].

The use of uranium as an alloying element is attractive from the perspective of its capabilities, however, its radioactive nature and mostly restricted availability make uranium unsuitable for the purpose of sulfide shape control. Rare earth elements, like cerium, are, despite their name, available in large amounts, mostly as minerals or ores. The work of Luyckx has shown that a cerium to sulfur ratio of 1.5 in aluminum-killed steels results in exclusively globular rare earth inclusions instead of elongated manganese sulfide inclusions. Additionally, their work showed a significant increase in toughness in traverse direction without affecting the tensile properties of the steel.

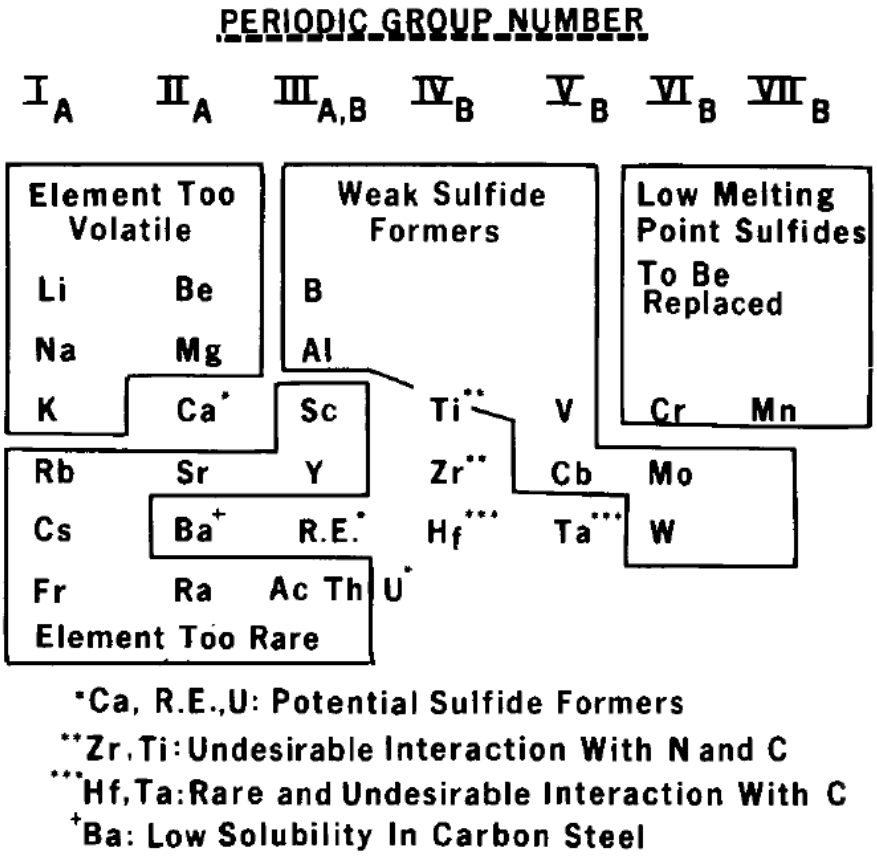

Figure 2.11: Periodic table of elements with potential sulfide shaping elements [89]

Adding calcium to steel will form globular CaS and (Ca, Mn)S [88]. These inclusions posses higher melting points than MnS and readily dissolve in molten steel. This behaviour actively reduces the amount of MnS inclusions in the steel. As stated by Ushijima et al. [90], a Ca/S ratio of greater than 2 is required for completely globular inclusions. Smaller ratios result in incompletely spherical inclusions and become crack initiation sites. According to Wilson [91], inclusions remaining after

the calcium treatment of a steel are only slightly deformed during hot rolling and remain embedded in the steel matrix. Due to the high affinities for both sulfur and oxygen, the desulfurization using calcium needs to be coupled with extensive deoxidization techniques as calcium tends to increase the size of oxides and oxysulfides [92,93]. Furthermore, it is desirable to form liquid oxide inclusions containing about 50% CaO and 50% Al_2O_3 while allowing the formation of CaS and CaS−MnS precipitates [94–96].

In the work of Kaushik et al. [94], steelmaking parameters for sulfide control were established. According to their work, it is necessary to desulfurize steel to very low levels of sulfur, and to ensure specific ratios between sulfur, calcium and oxygen to achieve good shape control of sulfides. The ratios established in their work are a Ca/S ratio of 2.0 and a Ca/O ratio of 1.0.

2.4.4 Alloying Elements Affecting the Resistance to Hydrogen-Induced Cracking

Adding copper to HSLA steels can increase the resistance to hydrogen-induced cracks. For solutions containing synthesized seawater, increasing amounts of copper lower the hydrogen embrittlement and corrosion rates [97]. Yamada et al. [97] found that a copper content of 0.26% maximizes the depression of corrosion and reduces the hydrogen uptake and thus prevents hydrogen crack from occurring. A copper content of 0.30% is associated with the formation of a protective film in solutions containing hydrogen sulfide and for pH levels above 4.5 [97, 98]. This anodic passivation greatly reduces the corrosion and hydrogen uptake and can prevent hydrogen cracking completely. Adding 0.1% molybdenum hinders anodic passivation in solution and is thus increasing the corrosion rate and hydrogen uptake. While required to achieve a desirable hot strength, nickel can decrease the resistance to hydrogen-induced cracking. A concentration of about 0.2% nickel is considered compatible with copper. Amounts greater than 1% increase the sensitivity to sulfide stress cracking by causing anodic dissolution. This phenomenon can be counteracted by adding 0.6% chromium.

Adding boron to HSLA steel increases the weldability and cold resistance, reduces the hardness in the heat-affected zone and allows for a reduction of the weld heat temperature [99,100]. However, the addition of boron to steels containing extremely low carbon contents of 0.01% or lower can have adverse effects on hydrogen-induced cracking by resulting in intergranular failure on shock loading.

According to Ohtani [99], a concentration of 0.005% phosphorous benefits the formation of bainite and martensite structures and provides a high resistance to hydrogen-induced cracking for all manganese levels.

2.5 Hydrogen Uptake

Hydrogen-induced cracking is generally caused by the pressure exerted by hydrogen from within the steel matrix. In this section, the electrochemical reactions causing hydrogen to build up in steel, as well as methods for the measurement of hydrogen build-up within the steel matrix are presented.

2.5.1 Hydrogen Evolution Reaction

According to Popov [101], hydrogen generation occurs at the metallic surface, using it as a catalyst. In a first step, the electroactive species, i.e. the hydronium formed during the acid reactions, is transported to the electrode, i.e. the metallic surface. The second step consists of the discharge reaction of the hydronium, in which the hydronium reacts with free electrons and adsorbs to the metallic surface. Followed by this is the desorption of hydrogen from the metallic surface and the catalytic desorption, also referred to as the electrochemical desorption, emission or hydrogen reformation. Lastly, gaseous, i.e. molecular hydrogen, is formed from the desorbed hydrogen atoms. The overall reaction is as follows [101]:

$$2\,H_3O^+ + 2\,e^- \longrightarrow H_2 + 2\,H_2O \tag{2.8}$$

where e^- are free electrons at the metallic surface. The slowest of the four mechanisms controls the overall reaction and hydrogen overvoltage. According to MacInnes [102], hydrogen overvoltage can be defined a a difference in potential between a reversible hydrogen electrode and an electrode, forming H_2 from H in the same solution. Once equilibrium is reached, the hydrogen overpotential will cease to exist.

Several mechanisms to describe the hydrogen evolution reaction exist [101]. However, common mechanisms to describe the hydrogen evolution reaction are those defined by Volmer, Tafel, Heyrovsky and Horiuti [103–106].

Volmer-Tafel: The Volmer-Tafel mechanism assumes fast recombination but rate-limiting discharge:

$$2\,H_3O^+ + 2\,M + 2\,e^- \longrightarrow 2\,MH_{ads} + 2\,H_2O2\,MH_{ads} \rightleftharpoons H_2 + 2\,M \tag{2.9}$$

Volmer-Heyrovsky: The Volmer-Heyrovsky mechanism assumes slow discharge and fast electrochemical desorption:

$$H_3O^+ + M + e^- \longrightarrow MH_{ads} + H_2OMH_{ads} + H_3O^+ + e^- \rightleftharpoons H_2 + M + H_2O \tag{2.10}$$

Tafel-Horiuti: The Tafel-Horiuti mechanism assumes fast discharge and slow recombination:

$$2\,H_3O^+ + 2\,M + 2\,e^- \longrightarrow 2\,MH_{ads} + 2\,H_2O2\,MH_{ads} \rightleftharpoons H_2 + 2\,M \tag{2.11}$$

Heyrovsky-Horiuti: The Heyrovsky-Horiuti mechanism assumes fast discharge and slow desorption:

$$H_3O^+ + e^- \longrightarrow MH_{ads} + H_2OMH_{ads} + H_3O^+ + e^- \longrightarrow H_2 + M + H_2O \tag{2.12}$$

Hydrogen Sulfide Poisoning: Although not defined as a hydrogen evolution mechanism, the presence of aqueous hydrogen sulfide is associated with an increased hydrogen uptake due to its

poisonous effects [107]. An explanation for this phenomenon is the increase of hydrogen overvoltage in the presence of aqueous hydrogen sulfide as a result of the interference with the desorption of adsorbed hydrogen [108–110].

2.5.2 Measurement of Hydrogen Concentration

As hydrogen build-up inside the steel matrix is responsible for the initiation of cracks within the steel, the measurement of hydrogen concentrations give important information about the quality of a steel. In general, hydrogen can occur as very reversible, reversible and irreversible in the steel matrix [111]. Very reversible hydrogen is defined as hydrogen in interstitial lattice sites and is associated with an activation energy of 7.7 kJ/mol [112]. Very reversible hydrogen is highly mobile and diffuses at room temperature [111].

Reversible hydrogen can occur as a Ti substitutional atom, at grain boundaries, dislocations, some forms of martensite, as well as in phase interfaces, such as ferrite/carbide or ferrite/cementide [111]. The activation energies for reversible hydrogen show a range from 17.2 kJ/mol for grain boundaries [113] to 36.4 kJ/mol for overaged martensite [114]. Research carried out on the measurement of reversible hydrogen indicates a hydrogen release at temperatures below 300°C [111, 113–120].

Irreversible hydrogen is located in microvoids [113,118,119], as well as on inclusions, such as iron oxide or manganese sulfide [118, 119]. The activation energy for hydrogen in microvoids has been found to be 35.2 kJ/mol [113] to 48.3 kJ/mol [118], inclusions show activation energies from 50.6 kJ/mol to 112.1 kJ/mol [119]. Irreversible hydrogen is released at temperatures below 340°C [113, 118, 119] from microvoids and at temperatures of 430°C and greater from inclusions [115, 118, 119]. A table showing the activation energies and release temperatures for selected hydrogen traps is shown in Figure 2.3.

Several methods are available for the measurement of hydrogen. The accepted standard method is the mercury displacement method, as described in ISO 3690:2012 [121], AS/NZS 3752:2006 [122] and AWS A4.3-93 R2006 [123]. A derivation of this method is the much safer Japanese glycerine method [124].

A very widely used standard method is gas chromatography [121–124]. One of the biggest advantages of this method are the response time and the reduction in measuring error, compared to displacement methods. Furthermore, the lack of heavy metals in this method leads to an inherently safer test setup for both environment and operator. While the displacement method is commonly only used to determine hydrogen levels, gas chromatography measurements allow for the detection of other gases, such as nitrogen, as well.

Although it is not part of any standard known to the author, the method of hot extraction can be used for the extraction of diffusible hydrogen with testing times of half an hour or less by heating up the sample to about 400°C [125, 126]. Other test methods worth mentioning are laser ablation methods [127], opto-electronic methods [128] and methods involving polymer electrode-based sensors [129].

In the work of Angus [130], he compared the hydrogen damage in X52, X60, X70 and 100XF steels with respect to their hydrogen accumulation. Using both the mercury displacement method and a LECO RH-404, he determined the hydrogen concentration after charging to be the lowest in the X52 steel and the highest in the 100XF. Applying strain prior to testing increased the amount of diffusible hydrogen measured. Overall, the amount of hydrogen measured was higher in the mercury displacement method than the LECO induction melting analyzer.

Table 2.3: Reversible and Irreversible hydrogen trapping sites and corresponding release temperatures, adapted and modified from Olson et al. [111]

Hydrogen Trap	**Activation Energy [kJ/mol]**	**Peak Temp [°C]**	**Ref.**
Very reversible			
Interstitial lattice site	7.7	-	[112]
Reversible			
Ti substitional atom	26	-	[115]
grain boundaries	17.2	112	[113]
	26	-	[117]
dislocations	-	270	[118]
	24		[116, 120]
	26.8	215	[113]
ferrite/carbide interface	-	115	[118]
ferrite/cementide interface	18	160	[119]
	18.4	-	[114]
	-	123	[113]
ferrite carbide (average)	26.8	-	[114]
tempered martensite	29.7	-	[114]
overaged martensite	36.4	-	[114]
Irreversible			
microvoids	48.3	338	[118]
	35.2	305	[113]
	36.8	330	[119]
iron oxide	50.6	430	[119]
	69.5	530	[119]
MnS	72.3	496	[118]
Al_2O_3	79	580	[131]
Al_2O_3 or SiO_2	86.2	630	[119]
	112.1	750	[119]
TiC	88.2	-	[115]

The measurement of hydrogen can be associated with measuring errors due to the properties and availability of hydrogen atoms and molecules, as well as other environmental influences. One example for this is the lab to lab variation of results obtained using the glycerine displacement method [124]. In this method, a measurement error is caused by the purity of the glycerine, as well as the absorption of other gases. One of the biggest issues with hydrogen concentration measurements, however, is the fast diffusion rate of hydrogen. For accurate measurements in HIC bars, the samples need to be tested immediately after they are taken out of the test solution in order to maintain the diffusible hydrogen content. Furthermore, to prevent any oxidation, the measurement of hydrogen should be carried out in a completely inert atmosphere, especially if testing is done at elevated temperatures.

2.6 Summary

The summary is organized into four sections. First, the phenomenon of hydrogen-induced cracking is summarized. Followed by this is a summary of the fundamentals of ultrasonic crack testing. In a third subsection, the effects of inclusions and microstructures on hydrogen-induced cracking are summed up. Lastly, techniques for the measurement of the hydrogen build-up within the steel matrix are summed up.

2.6.1 Hydrogen-Induced Cracking

Hydrogen sulfide naturally occurs in both natural gas and crude oil as a result of aquathermolysis and sulfate reduction reactions. Although hydrogen sulfide has its applications, like the production of elemental sulfur or the enrichment of deuterium, the poisonous effect of hydrogen sulfide and its ions can prevent the formation of molecular hydrogen during the acid dissociations and reaction at the steel surface. Due to thermodynamic instabilities, atomic hydrogen is forced to diffuse into the steel matrix, where it forms molecular hydrogen at imperfections and defects, such as voids, inclusions or grain boundary interfaces. While atomic hydrogen is able to diffuse easily within the steel, molecular hydrogen can get trapped at imperfections and defects, resulting in a steady hydrogen build-up over time. If this value reaches a certain threshold, the force exerted by the hydrogen onto the steel matrix will initiate a crack, which can then propagate and greatly diminish the properties of the steel.

2.6.2 HIC Testing

The majority of research carried out on hydrogen-induced cracking is focused on the effect of inclusions, microstructures or alloying elements. To fully understand hydrogen-induced cracking, the effects of pH level, H_2S partial pressure and exposure time need to be studied. To the knowledge of the author, little to no coherent work focused on these factors has been done for X70 pipeline steel. Research carried out on X65 steel indicated prolonged equilibrium CAR values for increased pH levels. Furthermore, the partial pressure of hydrogen sulfide effectively acts as a rate limiting

step for the absorption of hydrogen into the steel matrix and therefore requires longer exposure times to exceed the critical pressure of molecular hydrogen within the steel matrix.

Hydrogen-induced cracking is a complex process. Depending on the pH of the test solution, different chemical reactions can occur. Furthermore, the electrochemical stability of iron undergoes changes as the pH increases. For these reasons, tests carried at different pH levels are not necessarily comparable as the steel might be passivated at a certain pH threshold and therefore shows a greater resistance to corrosion. A reduction in partial pressure of hydrogen-sulfide primarily acts as a rate limiting step for the formation of molecular hydrogen within the steel and as such, prolongs the hydrogen uptake. This process can then benefit other reactions to take place.

2.6.3 Ultrasonic Crack Testing

Ultrasonic waves can be classified as longitudinal, shear and surface waves. While longitudinal and shear waves are able to penetrate the surface and travel within a media, surface wave are limited to a surface distribution. As such, ultrasonic crack testing relies exclusively on longitudinal and shear waves. Depending on the angle at which the sound waves enter a new media, longitudinal waves can be partially or completely converted into shear waves, which results, among other consequences, in a drastic reduction of the speed of sound in the media. As sound passes from one medium to another of different physical properties at an angle, refraction occurs based on the principle of Huygens and Snell's law. Because of these reasons, an entry angle of 0° is desirable, if possible.

Waves can be classified into near field and far field zones. As a wave enters the far field zone, or Fraunhofer zone, it will bend into a conical shape, increasing the effective wave front area. The so called Fraunhofer distance can be calculated as a function of speed of sound, frequency and effective diameter of the radiator. Additionally, the energy of a wave travelling back and forth in a medium is slowly dissipated into heat. This attenuates the output signal and causes a reduction in measured signal strength.

A variety of ultrasonic test methods can be used. The most common methods are A- and C-scans. For hydrogen-induced cracking, C-scans are often desirable for their ability to capture ultrasonic maps of entire samples showing the location and lengths of individual cracks. Furthermore, ultrasonic methods can be coupled with several post processing methods to further improve the accuracy.

2.6.4 Microstructural Effects on Hydrogen-Induced Cracking

It has been shown in literature that hard metallographic phases, such as martensite, elongated metallographic phases, such as lath bainite, as well as elongated inclusions, such as manganese sulfite are common initiation and propagation sites for hydrogen-induced cracks. Furthermore, a common initiation site for hydrogen-induced cracking is the centerline region. Due to cooling mechanisms and temperature dependent saturation limits, inclusions, such as manganese sulfide or titanium carbide precipitate in this region and can have detrimental effects on the steel properties. It is widely believed that globular shaped inclusions result in a better resistance to hydrogen-induced

cracking. For this reason, calcium is added to HSLA steel to control the shape of manganese sulfide inclusions by forming calcium sulfides and complex $(Ca, Mn)S$ inclusions. For calcium to sulfur ratios of greater than 2.0, the resulting inclusions are globular and increase the resistance to hydrogen-induced cracking. If the ratio is less than 2.0, or if the steel was not properly deoxygenized prior to adding calcium, however, the resulting inclusions are unstable and not perfectly globular and excessive formation of calcium oxide can occur. It has been suggested that rare earth elements, such as cerium are also suitable for the shape control of manganese sulfides. However, a good oxygen control is required, as these elements also tend to be strong oxide formers. One of the biggest advantages of rare earth elements are their great stabilities and high melting points. In case of cerium, a Ce/S ratio of 1.5 has been shown to cause the formation of exclusively globular inclusions.

2.6.5 Hydrogen Uptake

Several methods for the measurement of hydrogen concentration exist. The most commonly used methods are displacement methods, of either glycerine or mercury, gas chromatography methods or hot extraction coupled with a detector. Depending on the available inclusions and imperfections, hydrogen can be available in diffusible and trapped states. Diffusible hydrogen in commonly located at interstitial sites and, as the name suggests, is readily diffusible at room temperature. Hydrogen located at a trapping site, such as manganese sulfide, requires additional energy in order to diffuse to the surface. This can be achieved by heating a sample above the critical temperature for the corresponding trapping site.

2.6.6 Research Contribution

The literature review shows a variety of research carried out on hydrogen-induced cracking. However, only little research was done on varying pH and testing times involving X grade pipeline steel in combination with ultrasonic crack testing. In this work, the effects of pH and testing time of X70 pipeline steel are evaluated using signal to backwall ratio ultrasonic method. The results are then analyzed using histograms and ultrasonic maps, as well as plots showing the global crack to backwall ratio as a function of testing time.

Chapter 3

Materials and Experimental Methods

In this section, the materials and experimental methods will be described. In a first section, the steels and their chemistries used for the experiments will be presented. This is followed by the definition of the NACE TM0284-2016 standard, as well as the sour service regions defined in NACE MR0175. This section also includes the test setup and procedure used for the experiments carried out as part of this work. Afterwards, the test setup and procedure for the ultrasonic crack evaluation are presented. In a final section, the hydrogen analyzer used for this work is presented and the procedure used to measure hydrogen in the HIC samples is explained.

3.1 Steels and Sample Preparation

For all experiments, X70 steels from three different heat numbers are used. Table 3.1 shows the indicators used to mark the steel samples, their heat numbers, and selected compositions of alloying elements. A full table of steel chemistries can be found in appendix A. The steel Heat X shows a good calcium to sulfur ratio and a lower sulfur content compared to the remaining steels. This steel is expected to show a better resistance to hydrogen-induced cracking. It is indicated with an X to have a good visual distinction to the stamps of the other steels. The steels with the heat number Heat B1 and Heat B2 show a greater sulfur content and a worse calcium to sulfur ratio and are expected to be more prone to cracking due to hydrogen-induced cracking. Furthermore, the steel with heat number Heat B2 shows a higher copper content. Both steels were stamped with the letter B to distinguish them from the steel samples marked with an X.

All steels were taken from line pipe with a thickness of 12.7 mm. The pipelines were welded using the spiral method and the samples were taken from the rolling direction and 180° off the weld. In a first step, 250 mm× 430 mm steel plates were plasma cut from the pipelines. The heat affected zone from the plasma cuts was then removed by cutting about 15 mm off the plates from each side. Each steel plate was then cut into about 25 mm thick strips along the rolling direction of the pipeline using a vertical saw. In a next step, these strips were cut down to pieces with lengths of 105 mm and 125 mm using an abrasive saw. In a final step, the samples were then ground flat and to a length of 100 mm and 120 mm.

Table 3.1: Selection of steel chemistries and heat indicators for steels X70-X and X70-B, provided by EVRAZ NA Regina

Component	**X70-X**	**X70-B**	
[wt.%]	**Heat X**	**Heat B1**	**Heat B2**
S	0.001	0.0057	0.0057
Ca/S	2.5	0.386	0.439
Mn	1.59	1.62	1.59
Cu	0.28	0.27	0.36
Ca	0.0025	0.0022	0.0025
Ce	0.001	0.0021	0.0016

3.2 Hydrogen-Induced Cracking

According to NACE MR0175 [8] and NACE TM0284-2016 [6], hydrogen-induced cracking is strongly influenced by both the pH of the solution and the partial pressure of hydrogen sulfide. The correlation for this dependency can be seen in Figure 3.1. The intensity and severity of sulfide stress cracking can be categorized into mild, intermediate and severe sour service [8]. A visualization of these zones can be seen in Figure 3.1. Conditions with a hydrogen sulfide partial pressure of less than about 0.003 atm are considered as non-sour.

Based on the premise that hydrogen-induced cracking depends on the surrounding conditions, five cases are suggested in this work. First, indicated as red circles in Figure 3.1, two test conditions at a pH of 2.7 are chosen, one at 1 atm hydrogen sulfide and one at a reduced partial pressure of 0.1 atm hydrogen sulfide. Both of these conditions are well located in the severe sour service region, which suggests the occurrence of cracking after a short period of time.

Represented in yellow triangles are the test conditions located in the intermediate sour service region. These tests are carried out at a pH of 5.5 for 1 atm hydrogen sulfide and at a pH of 4.5 for 0.1 atm hydrogen sulfide to follow the trend of the boundary between the severe sour service and the intermediate sour service region.

Lastly, represented as a green square, is the test condition representing the mild sour service region. The parameters for this test is a pH of 6.5 and a partial pressure of 1 atm hydrogen sulfide.

The purpose of this work is to compare these conditions at different testing times and determine correlations between pH levels and hydrogen sulfide partial pressures with respect to the cracking behaviour for X70-X and X70-B.

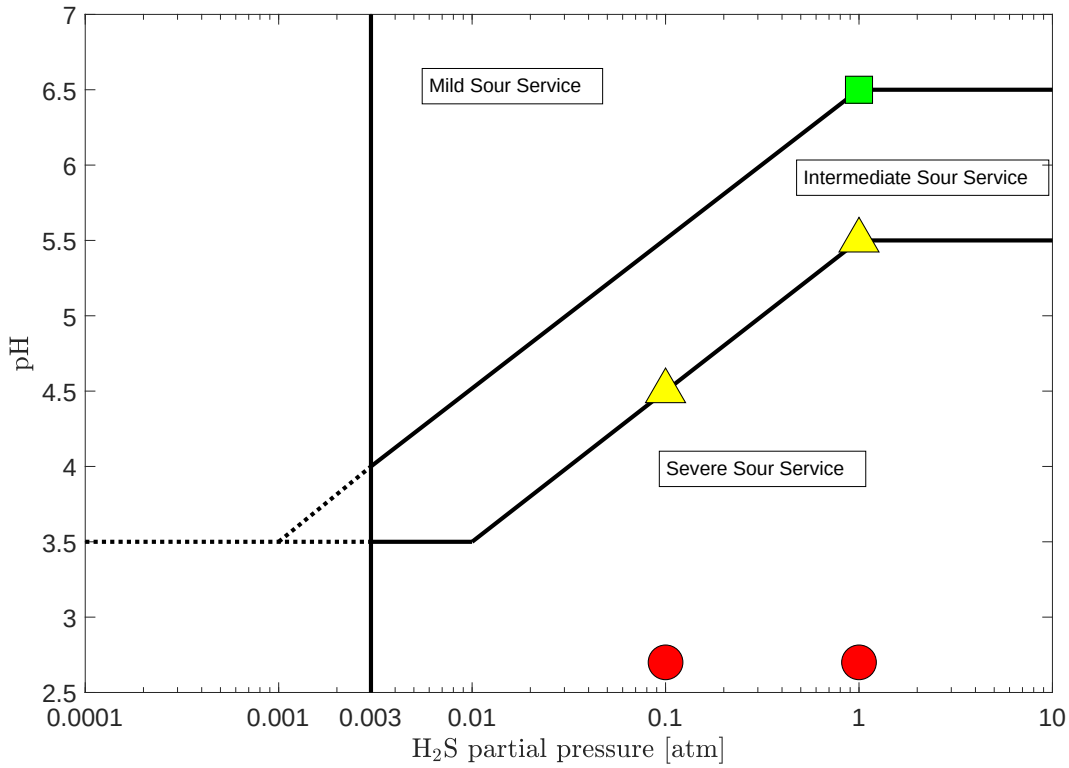

Figure 3.1: Sour service regions and test location, adapted from NACE MR0175 [8]

3.2.1 Test Procedure of NACE TM0284

In a first step, the testing solution is prepared and the initial pH level is measured. For each condition, 8 liters of test solution are prepared and deaerated using a constant nitrogen flow for 24 hours. Prior to testing, all steel samples are degreased and cleaned in an acetone bath and taken out right before submersion in the test solution to minimize the effect of substances adhering to the surface. All samples are fixed between small polymer rods on their small, long side (short-transverse direction) and placed in the test vessel. The top of the vessel is then prepared by applying vacuum grease, closed and filled with the prepared test solution. Further deaeration is being carried out using nitrogen for 1 hour.

After completion of the deaeration process, the solution is saturated with hydrogen sulfide for 1 hour and the saturation pH and concentration of hydrogen sulfide is measured using a pH probe and iodometric titration, respectively. A description of the iodometric titration can be found in appendix A. Upon completion of the saturation process, the hydrogen sulfide flow is reduced to a slow bubbling flow to maintain the hydrogen sulfide concentration over the entire testing time. Once the test is complete, the final pH and hydrogen sulfide concentration are measured and the test vessel is emptied. All samples are thoroughly cleaned to ensure no remaining test solution is

on the surface or in crevices as this could result in post test cracking. In a final step, all samples are labelled and prepared for ultrasonic evaluation.

3.3 Metallographic Analysis

The standard method for the analysis of HIC bars, as defined by the NACE standard TM0284, is to cut the HIC bar perpendicular to the rolling direction every 25 mm. The last of the four resulting sample pieces is discarded and the cut surfaces of the remaining three are polished for microscope analysis. Polishing is done using either an auto-polisher or a manual rotary polisher. A first, but optional step, is to mount the samples into epoxy. After this, the samples can be polished using grinding paper with grid sized ranging from about 320 to 1000. After this, particle emulsions are used to achieve a mirror finish. This is then followed by etching the sample in nitol for a few seconds to increase the visibility of grain boundaries under the microscope. In a last step, the sample is then rinsed off using ethanol and dried.

Using 200x magnification, an optical microscope is used to determine the presence of inclusions in the section of the HIC bar. For analysis purposes, the length and thickness of these cracks is recorded and used to calculate crack to length ratios (CLR), crack to thickness ratios (CTR) and crack sensitivity ratios (CSR). These values can then be put in relation to acceptance criteria.

In this work, only few samples were metallographically analyzed. The purpose of this work is to establish an ultrasonic evaluation method to facilitate the analysis process and allow the analysis of the entire sample, rather than a selection of cut surfaces. This method is described in the following section.

3.4 Ultrasonic Testing

After completion of the HIC test, each sample is scanned using a longitudinal ultrasonic probe. The test setup used in this work is presented in 3.4.1. In section 3.4.2, the testing procedure used for the collection of the ultrasonic data, as well as the evaluation of crack severity is described. Additional information can be found in appendix B.

3.4.1 Test Setup

The test setup of the ultrasonic equipment used in this work can be seen in Figure 3.2. The steel sample is scanned using an ultrasonic probe (V203-RM) and the signal is transferred to the pulse transmitter/receiver board (Socomate USPC7100). There are two inputs on the pulse transmitter/receiver board, however, only one is being used as the other one has been damaged. As can be seen in the schematic, the signal is then passed on to both the trigger amplifier box and the digitizer board (ALGTe1.0). The signal past on to the trigger amplifier is boosted from 1V to 3V and is then transmitted to the digitizer board. From there, the data can be read and saved in the IW Flaw Detector software. The signal gain can be controlled in the USPC7100 software. It

should be noted, that the trigger amplifier box requires two power inputs. The ultrasonic probe used in this work is a longitudinal probe with a diameter of 5 mm.

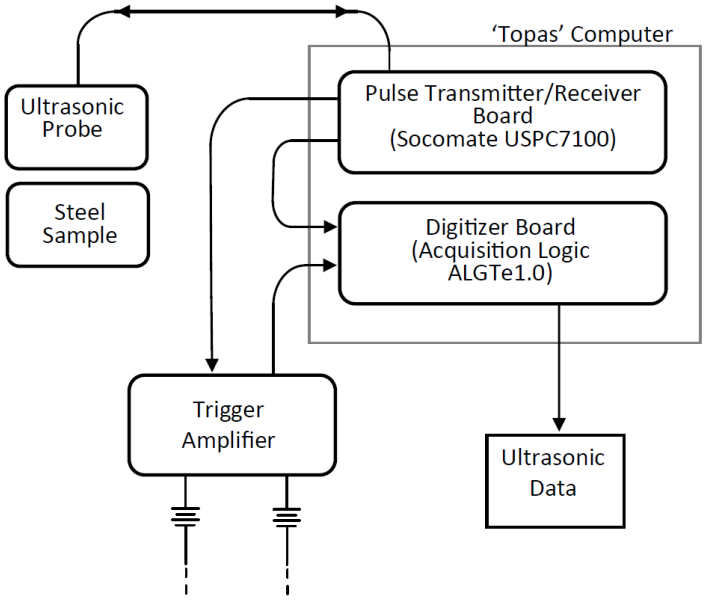

Figure 3.2: Schematic view of ultrasonic test setup, adapted from safety operating procedure (SOP), written by Kartik Vasudev (2018)

3.4.2 Test Procedure and Evaluation of Cracks in HIC Samples

A grid of 5 mm squares is applied to the top surface of the sample (Fig. 3.4). Each test sample is scanned at the same locations. Figure 3.3 shows schematic view of a HIC sample and its dimensions. A total of 80 data sets is collected for each sample. The data acquisition is performed without the use of a delay block, as preliminary testing using an acrylic delay block with a length of about 7 mm did not show the typical attenuation of the signal over time. Furthermore, a significant increase in background noise is noticeable when using the delay block.

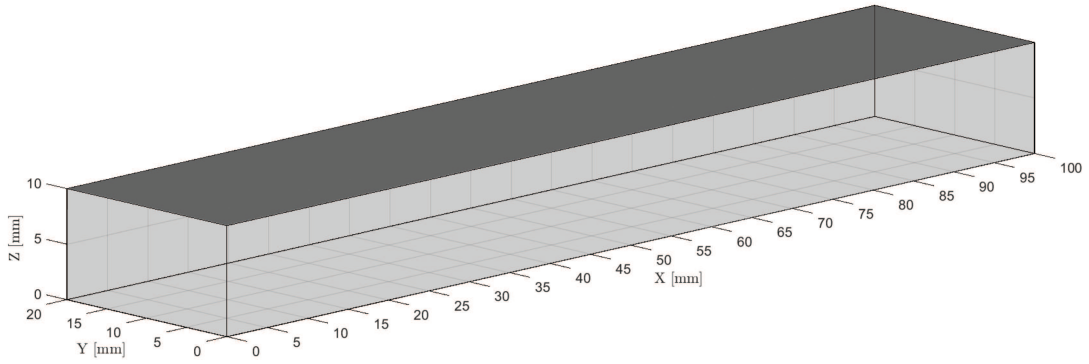

Figure 3.3: Schematic view of test sample and measuring grid. Ultrasonic measurements are taken from the top of the sample (dark grey).

All data sets for each sample are saved as .txt files and labelled with numbers between 01 to 80 to represent the designated location on the sample. The orientation in which data sets are collected is left to right and bottom to top, e.g. the first data set is collected at $X = 0$ and $Y = 0$, the second data set is located at $X = 5$ and $Y = 0$, and so on.

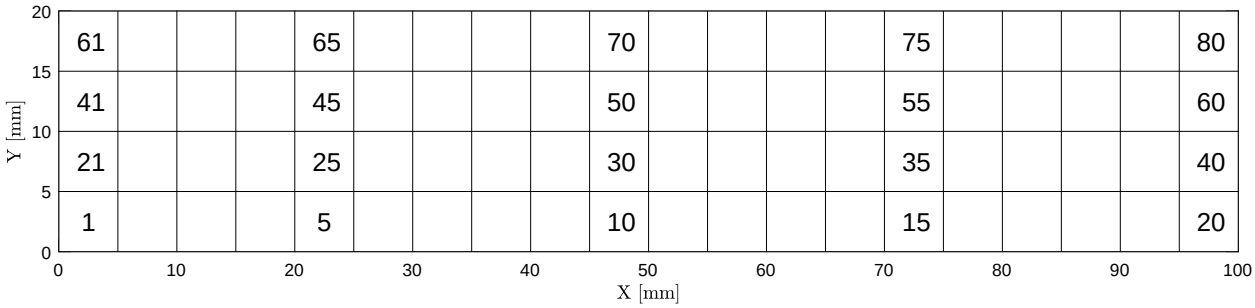

Figure 3.4: Schematic view of measuring grid (X-Y plane) with location numbering

For the analysis, a Matlab script is used to find all peaks associated with the sample, calculate the time difference at which the peaks were measured and plot both a binary and a grey-scale crack map of the steel sample. The binary ultrasonic map indicates areas affected by cracking and is used to calculate the Crack to Area Ratio (CAR). By separating the backwall signal and the crack reflections, it is possible to calculate the ratio between crack and backwall signal. This signal is referred to as Crack to Backwall Ratio (CBR) and is displayed using the grey-scale maps. A histogram showing the distribution of local CBR ratios is generated to visualize the crack growth over time. Further information, including the Matlab code, can be found in appendix B.

3.4.3 Detection of Cracks in Ultrasonic Data

Three general types of ultrasonic signals can be detected. These signals can indicate the lack of a crack in a location, the exclusive detection of cracks in a test location or the partial presence of cracks. The time difference between two ultrasonic peaks represents a reflection of the ultrasonic signal from the probe to the first interface. As the distance is expressed in a unit of time, a conversion to a unit of distance is necessary:

$$d = \frac{\Delta t v_s}{2} \tag{3.1}$$

In this equation, Δt represents the distance between two peak, in seconds, and v_s represents the speed of sound in the steel. Considering the ultrasonic data of a location without the presence of cracks (Fig. 3.5), the distance can be calculated using the first two peaks. To simplify the calculation, a speed of sound of 6000 m/s is chosen in this example. In reality, this value would be closer to 5900 m/s. The time difference between two peaks can be measured to be about 3 μs. This results in a interface to probe distance of 9 cm.

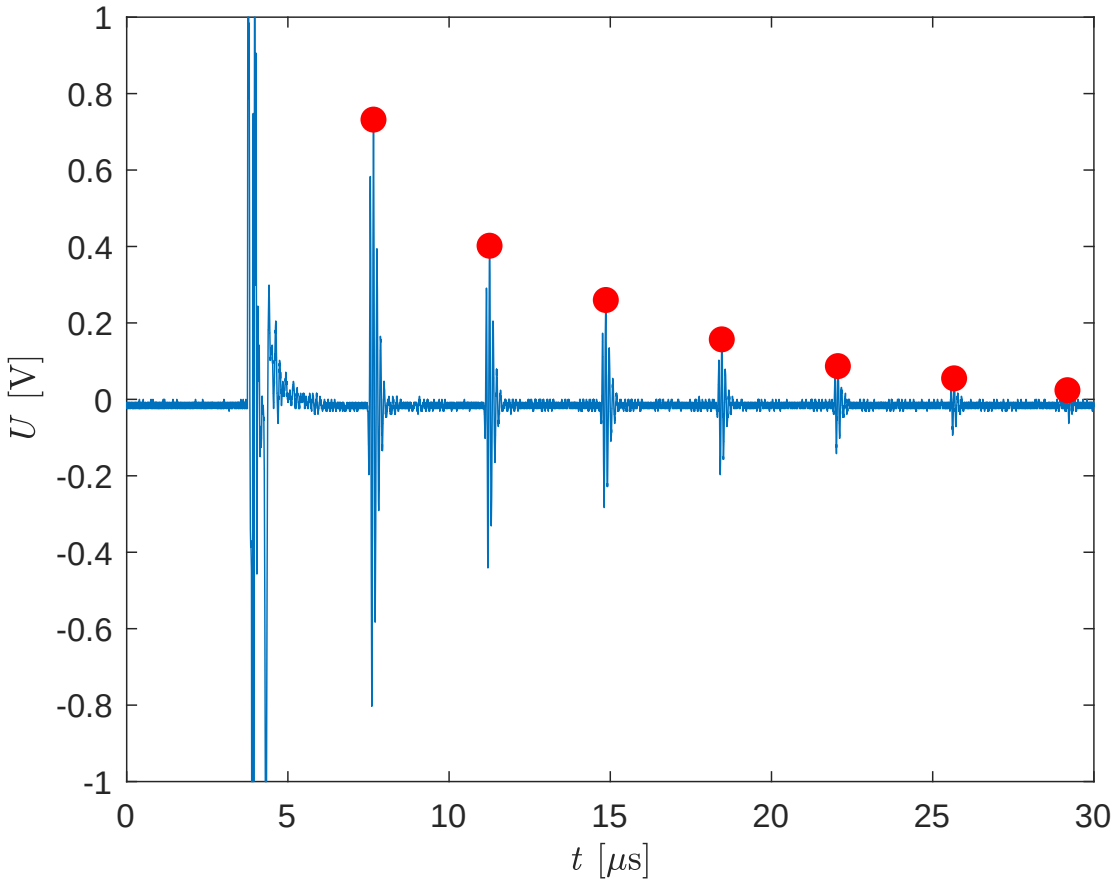

Figure 3.5: Ultrasonic data without presence of a crack.

For an ultrasonic data set taken from a location exposed to a full crack (Fig. 3.6), the time difference between two peaks can be measured to be about 1.5 μs. Using the same equation and assumptions, this results in a interface to probe distance of 4.5 cm and therefore corresponds to a crack in the centreline region.

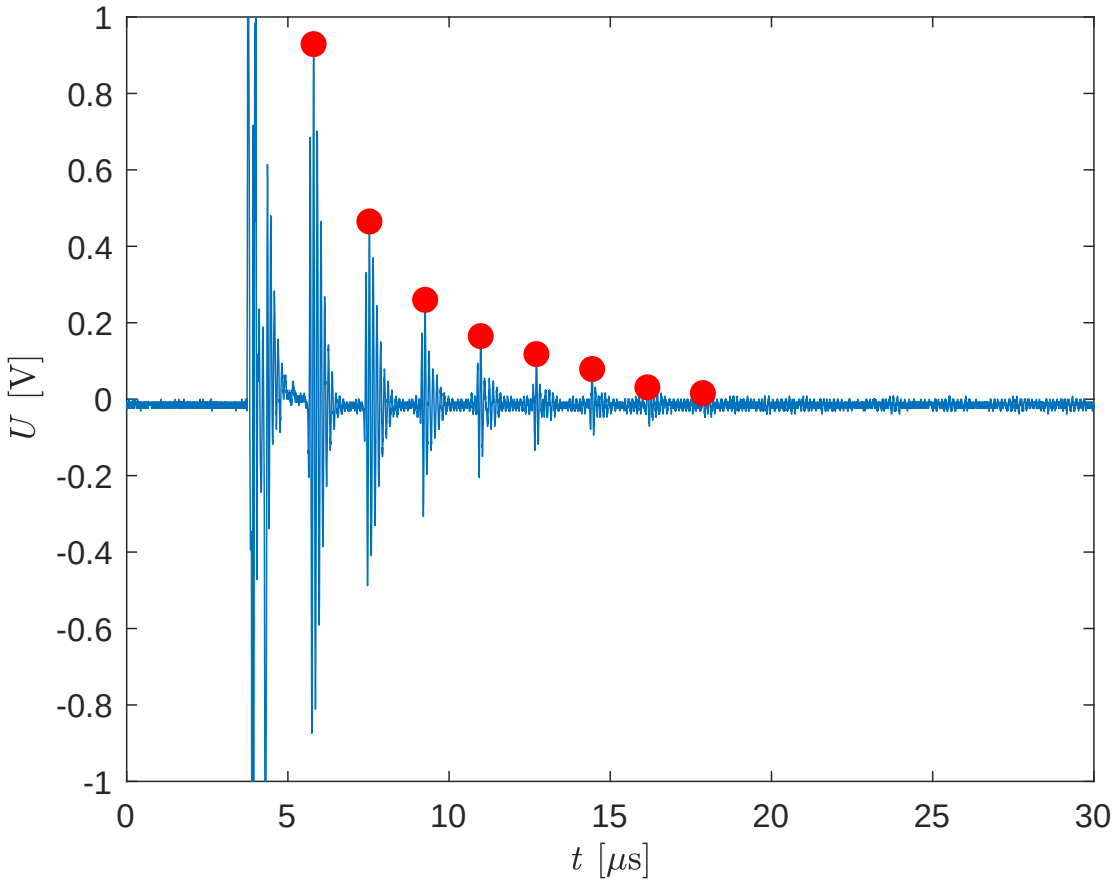

Figure 3.6: Ultrasonic data with presence of a full crack.

Under the assumption that a crack is either exclusively present or not, a global crack to area ratio (CAR) can be calculated:

$$\mathrm{CAR} = \frac{\sum_{i=1}^{n} m_i}{n} \tag{3.2}$$

Where m_i indicates the binary cracking condition in location i and n represents the total number of zones. In this work, 80 test locations are chosen, i.e. $n = 80$. As m_i is binary, a value 0 is assumed if no crack is present and a value of 1 is assumed if a crack was detected. The CAR value therefore expresses the ratio of crack affected zones of the amount of total zones scanned. To localize the findings, CAR maps can be generated. An example of this can be seen in Figure 3.7, where black represents crack and white indicates crack free zones.

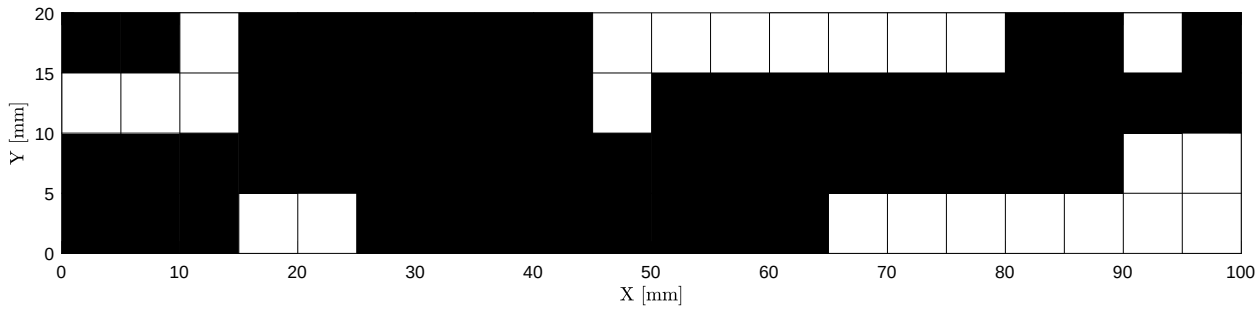

Figure 3.7: CAR map for steel X70-X after 8 days in a test solution of pH 2.7 and 1 atm H_2S.

In some cases, both the back wall of the steel and a crack interface are picked up by the ultrasonic probe. This indicates that a crack is present in the scanning location, but does not cover the entire area. However, for the CAR ratio, this would be considered a full crack, regardless of how small the crack is. Figure 3.8 shows one of those data sets. Although the time difference between two peaks represents a crack, the difference in resulting voltage between three adjacent peaks indicates that more than one interface was detected during the scan. Considering the first three highlighted peaks (1-3), it can be seen that peak two (2) shows a significantly greater intensity than peak one (1) and three (3). This is a result of the detection of backwall and partial cracks.

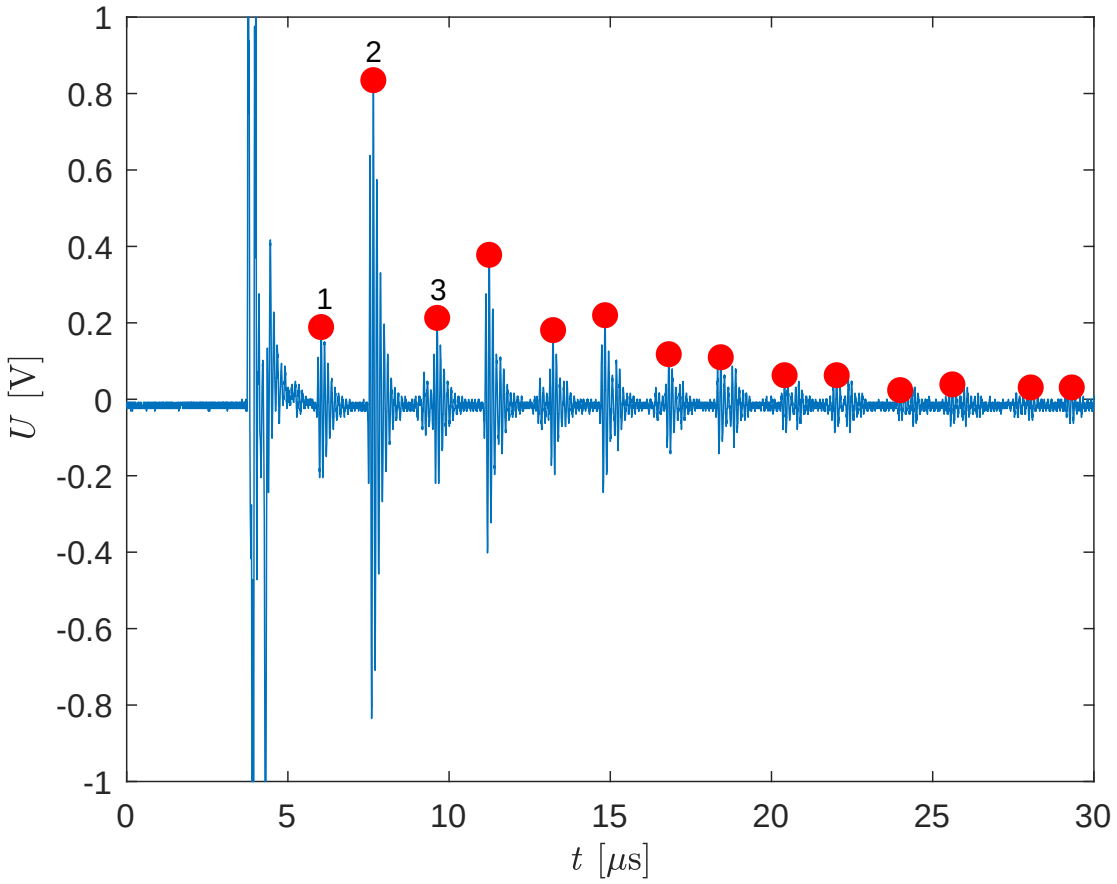

Figure 3.8: Ultrasonic data for partially cracked scanning location.

Assuming that the backwall signal is not affected by the crack signal, the backwall peak intensity can be separated from the crack peak intensity (Fig. 3.9). Using an exponential function of type

$$f(t) = A_0 \exp(A_1 t) \tag{3.3}$$

where A_0 and A_1 are fitting parameters, the data can then be fitted and interpolated. As the function $f(t)$ is defined to go through peak two (2), the first crack peak after the detection of the backwall signal, peak three (3), can then be used to calculate a local crack to backwall ratio (CBR):

$$\text{CBR} = \frac{\chi(t_0)}{f(t_0)} \tag{3.4}$$

Where t_0 represents the detection time of peak three (3), $\chi(t_0)$ represents a crack peak at time t_0 and $f(t_0)$ represents the corresponding, interpolated backwall signal at t_0. The local CBR for the example given in Figure 3.9 can be calculated to be about 0.38.

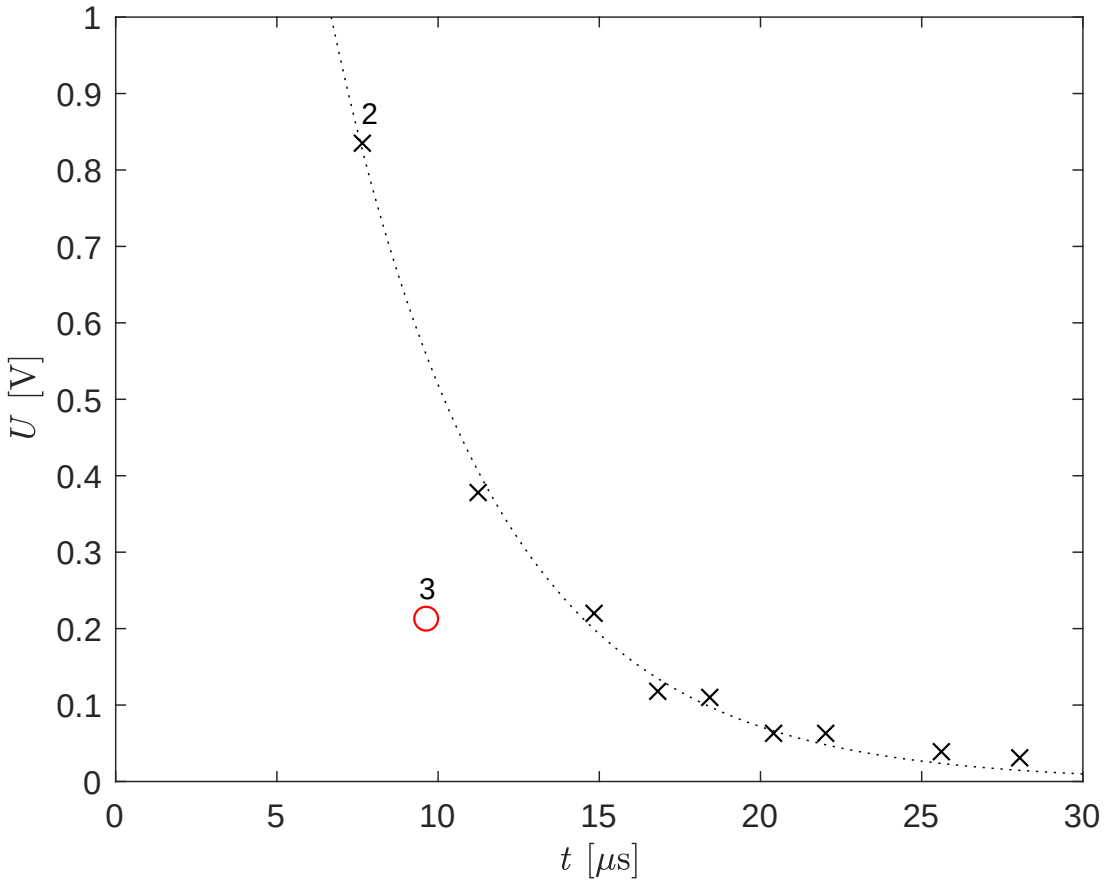

Figure 3.9: Ultrasonic data for partial cracked scanning location.

Analogous to the CAR map, a CBR map can be generated (Fig. 3.10). In this map, the extent of cracking of each location is represented gradually in grey scale. The grey scale is based on 32 different grey tones and visualizes an increase in intensity with increasing darkness of grey tones. Similar to the CAR map, white indicates crack free zones and black marks fully cracked zones. Partial cracks are shown in grey. The greater the CBR, the darker the grey on the map.

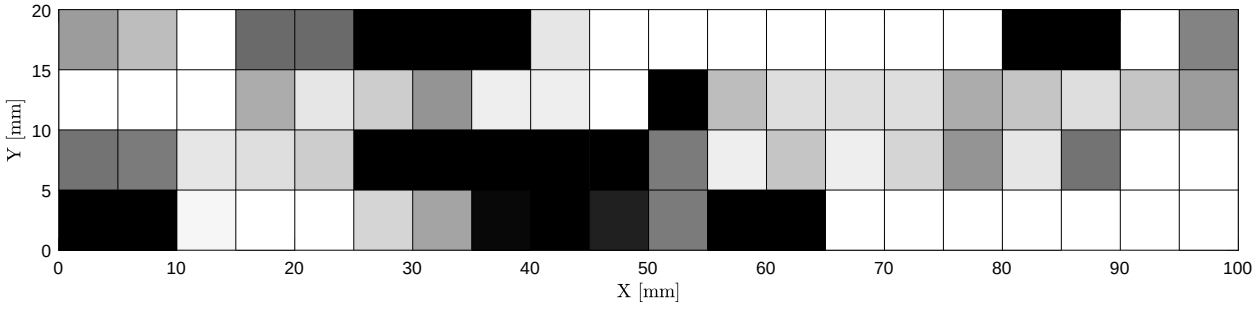

Figure 3.10: CBR map for steel X70-X after 8 days in a test solution of pH 2.7 and 1 atm H_2S.

In addition to ultrasonic maps, histograms showing the distribution of local CBR can be generated (Fig. 3.11). A CBR of zero (0.00) correlates to a zone completely unaffected by cracks. A CBR of one (1.00) indicates full crack coverage in a scanning location. Using these histograms, the crack growth can be visualized. A high number of CBR equal to 1 and relatively low amounts of smaller CBR's would correlate to a high number of crack initiation points. Analogously, a wider spectrum of CBR's greater than zero (0.00) and smaller than one (1.00) could indicate that cracks spread from fewer location.

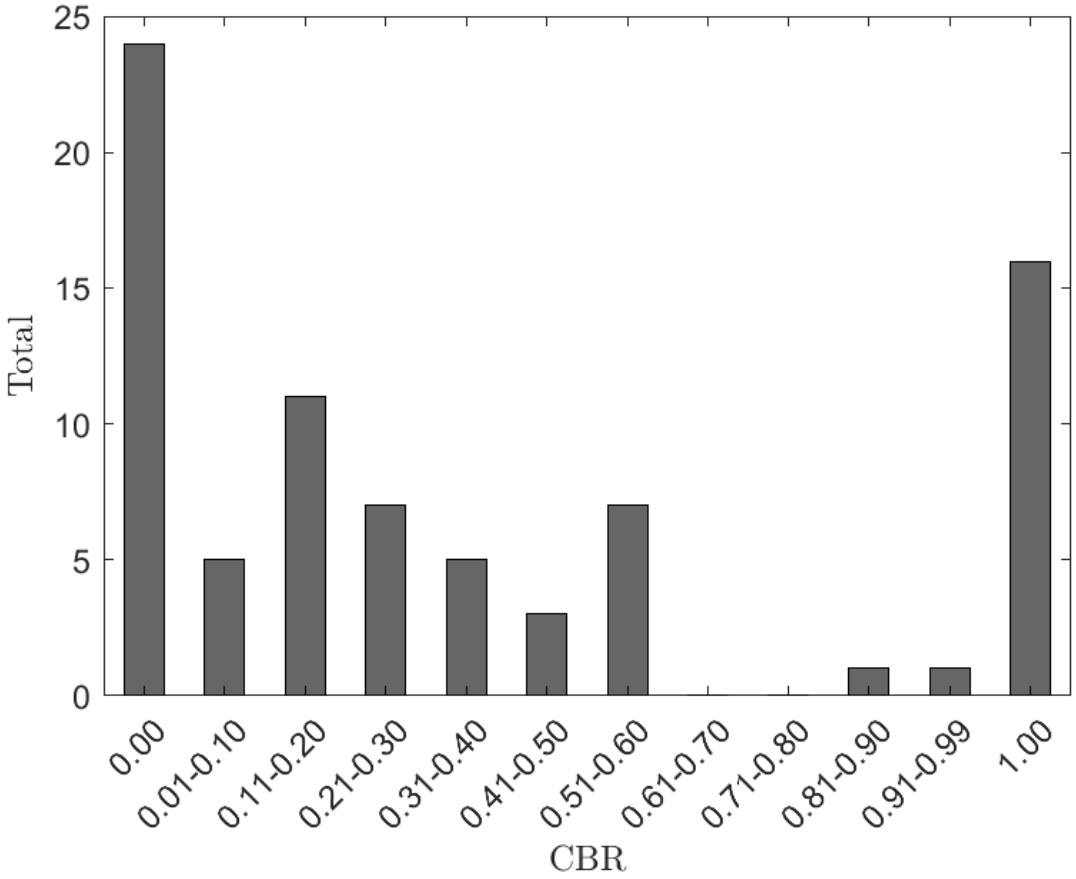

Figure 3.11: Histogram showing the distribution of CBR for steel X70-X tested at a pH of 2.7 using 1 atm H_2S for 8 days.

Modification of equation 3.2 leads to the global crack to backwall ratio, GCBR:

$$\text{GCBR} = \frac{\sum_{i=1}^{n} \text{CBR}_i}{n} \tag{3.5}$$

Where CBR_i represents the local CBR at location i and n is the total number of scanning locations. In this work, all local crack to backwall ratios are referred to as CBR and all global crack to backwall ratios as local GCBR.

3.5 Hydrogen Concentration Measurement

In order to measure the hydrogen build-up in steel, a LECO DH603 Hydrogen Determinator is used. This device is capable of measuring the residual amount of hydrogen in the steel sample by hot extraction and a thermal conductivity detector. Prior to analyzing any samples, the hydrogen analyzer must be calibrated using calibration samples. In the following subsection, the theoretical principle of operation, the calibration and the analysis of samples are explained.

3.5.1 Principle of Operation

The principle of operation is only briefly described in the manual. To extract hydrogen from the sample, hot extraction is used. In case of the LECO D603, the extraction temperature is 1100°C. Once the hydrogen enters the gas flow, it is measured using a thermal conductivity detector and expressed in parts-per-million (ppm). For the ambient gas flow, helium and nitrogen are used.

3.5.2 Calibration of Analyzer

Calibration of the LECO D603 Hydrogen Determinator is done using calibration samples. The samples used for this work have a hydrogen content of 1.00±0.50 ppm and a weight of 5.0000±0.0001 g. In a first step, the exact weight of the sample is measured using a precision scale and entered into the interface of the analyzer. Once the analyzer has reached its operating temperature of 1100°C, a series of blank tests is completed. The purpose of these tests is to clear the tubing of the analyzer from all residual oxygen or hydrogen. All samples are inserted into the analyzer in glass boats. These glass boats are inserted into the analyzer during the start up procedure and taken out after completing the blank tests. To begin a calibration test, the sample ID is entered in the system and the background signal is measured. When indicated by the system, the furnace door is opened, the calibration sample is inserted into the furnace and the measurement of hydrogen is started. Upon completion, the analyzed calibration sample is removed from the furnace and placed in the discard pile. After running another blank test, the procedure is repeated until at least three successful hydrogen curves were measured. The curves are then selected and a calibration is fitted for these curves. It is recommended to repeat this procedure at least every time the analyzer is heated up from room temperature.

3.5.3 Measurement of Residual Hydrogen Content in HIC Samples

The measurement of residual hydrogen in HIC samples is similar to the calibration process. According to the devices instruction manual, the hydrogen analyzer can analyze samples with a weight of up to 5 g.

The first step for the determination of residual hydrogen in HIC samples is sample preparation. In this work, HIC samples with a length of 120 mm were prepared and tested along regular HIC samples. Upon extraction from the test vessels, all samples were cleaned. The 120 mm samples are then stored in liquid nitrogen to reduce the diffusion of hydrogen.

After calibration of the analyzer, small sections of the 120 mm sample are cut using a precision saw and stored in acetone until the samples are ready to be tested. Similar to the calibration of the analyzer, the exact weight of the samples is measured using a precision scale and entered into the system. Prior the weighing the samples, the samples pieces are taken out of the acetone and dried using duster spray. After cleaning and weighing the sample, the analysis process is started. After each sample, a blank test is run to clear the measurement chamber from residual hydrogen and oxygen.

Chapter 4

Results

The results obtained during the course of this work are divided into four sections. In a first subsection, the validation of the obtained data sets is shown. Finally, the data sets for severe, intermediate and mild sour service are presented. This is followed by the results obtained from the ultrasonic crack evaluation. Afterwards, SEM images confirming the presence of manganese sulfide at the crack sites are shown. In a final section, the results obtained from the LECO D603 hydrogen analyzer are presented.

4.1 Validation of Ultrasonic Data

To validate the ultrasonic method used in this work, a tested HIC bar was scanned using a 5 mm longitudinal ultrasonic probe. The corresponding ultrasonic map can be seen in Figure 4.1. In order to compare the ultrasonic data to microscopic images, five slices of the steel sample were cut using a precision saw. The location of these cuts are in vertical direction between 65 and 90 mm. All cuts were taken in the center of the ultrasonic testing location, i.e. 67.5 mm, 72.5 mm, 77.5 mm, 82.5 mm and 87.5 mm. The slices were then mounted in epoxy and roughly polished to show cracks.

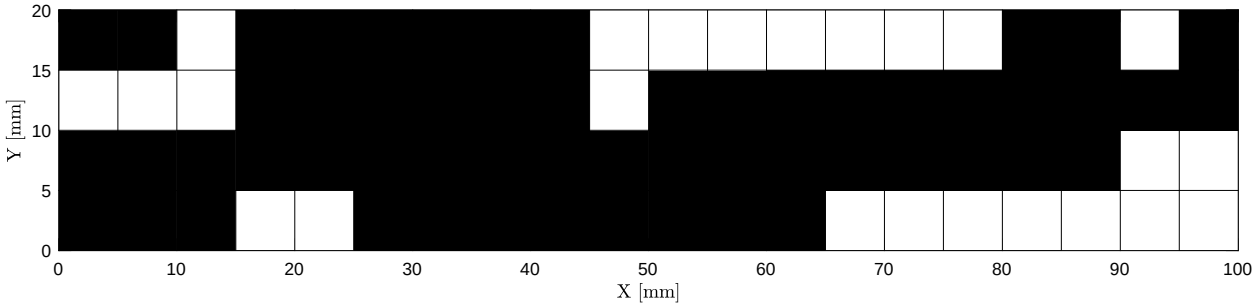

Figure 4.1: Ultrasonic map (CAR) for steel X70-X after 8 days in NACE TM0284-2016 solution C with pH 2.7 at 1 atm H_2S

The cracks detected under the microscope are visualized for each slice in Figure 4.2. Each crack

is represented by a rectangular box and is indicated by a corresponding letter. The diagonally running lines, as well as the darker circles, are remnants from the polishing process and were used to manually align the microscope images.

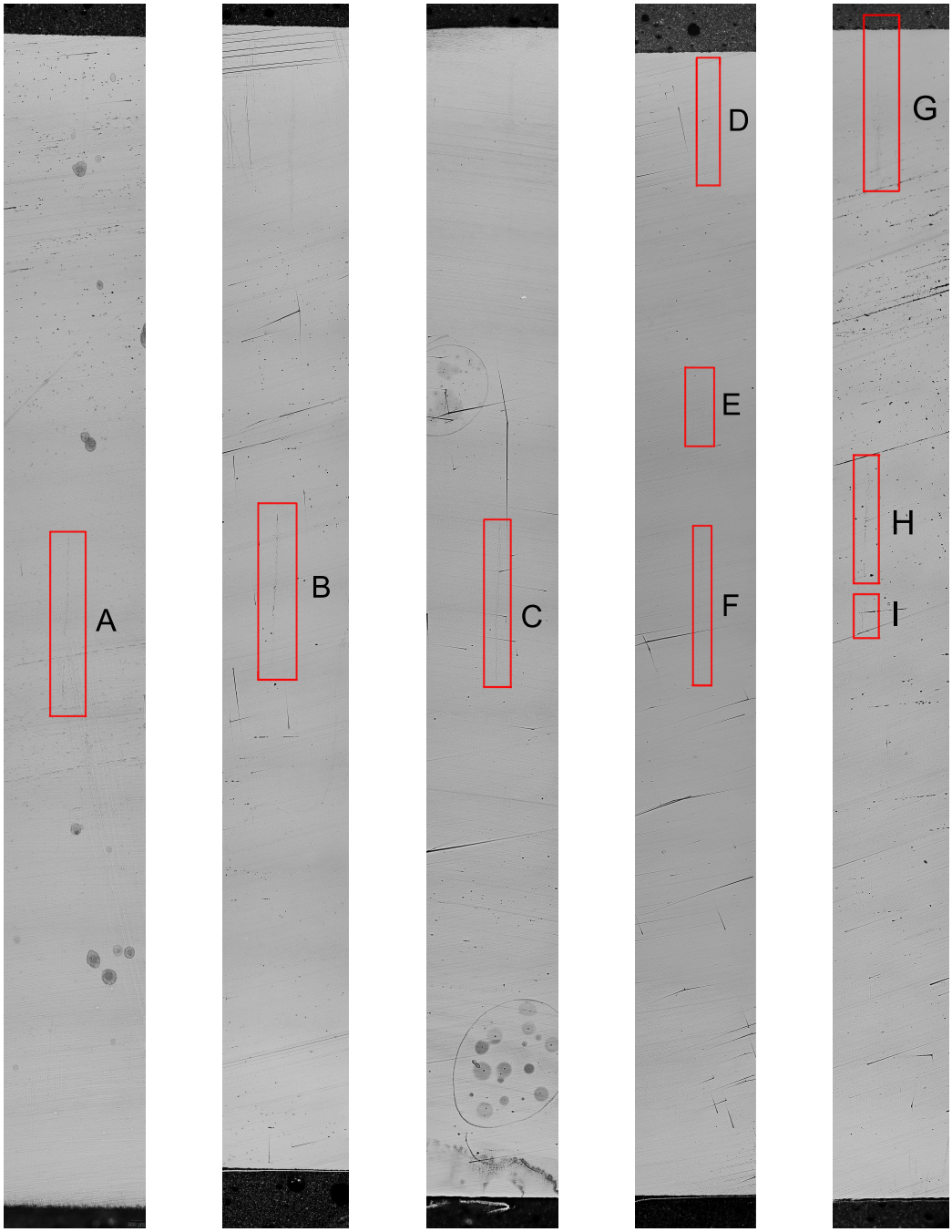

Figure 4.2: Microscope image stacks of slices (a) - (e) from HIC bar tested at pH 2.7 and 1 atm H_2S for 8 days

For each slice, 12 to 16 microscope images were taken along the centerline and manually aligned and stacked to generate coherent microscope maps. All image stacking was done in Adobe Photoshop using masks, manually alignment of each image and the auto-blend function to eliminate differences in contrast. Prior to stacking, the contrast in each image was boosted to increase the visibility of scratches and marks on the steel. This procedure significantly simplified the stacking process.

It can be seen that slices (a)-(c) (Fig. 4.2 (a)-(c)) cracks spread along the two center zones of the corresponding ultrasonic map (Fig. 4.1). In slice (d), three individual cracks (D, E and F) are detected. These cracks are located in the top three regions of the ultrasonic map. A similar behaviour can be observed in slice (e). The cracks G and H were found in the top two regions of the ultrasonic map. The smallest observed crack, crack I, is located on the interface between the two center zones of the ultrasonic map. A microscope image showing crack H and I can be found in Figure 4.3. No cracks were found in areas marked in white on the ultrasonic map. A comparison between the microscope maps for slices (a)-(e) and the corresponding areas of the ultrasonic map indicates a perfect match.

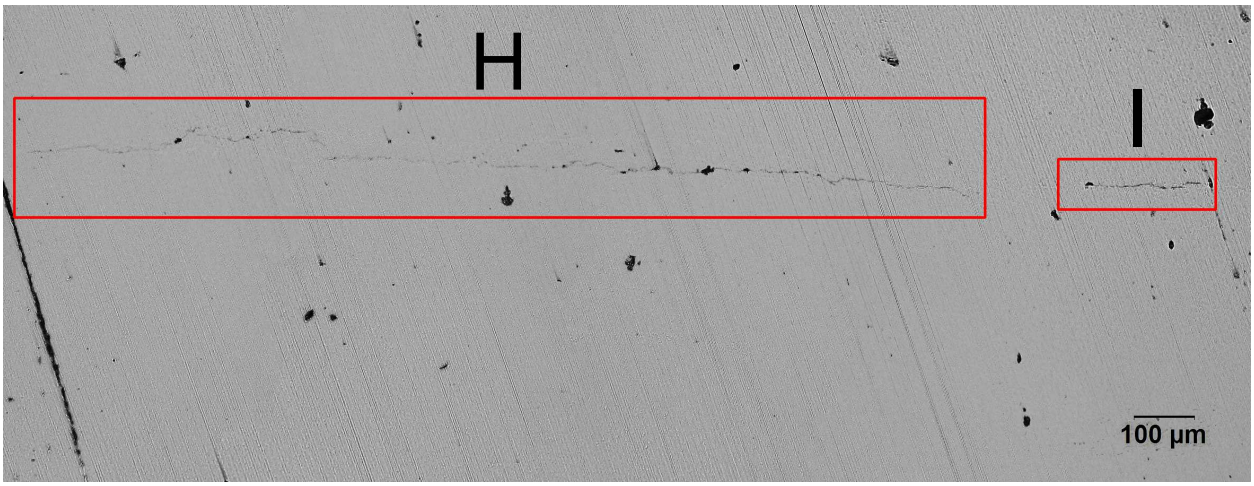

Figure 4.3: Cracks H (large, top) and I (small, bottom) from crack site (e)

A direct comparison between the crack to backwall data (Fig. 4.4) and the microscope images confirms the location and spread of ultrasonic cracks. It can be seen that cracks (b)-(c) are located as partial cracks in two zones. Crack (a) reaches more into the second zone from the bottom (location 34) and is picked up as a full crack. The crack sites (d) and (e) show multiple cracks in single locations.

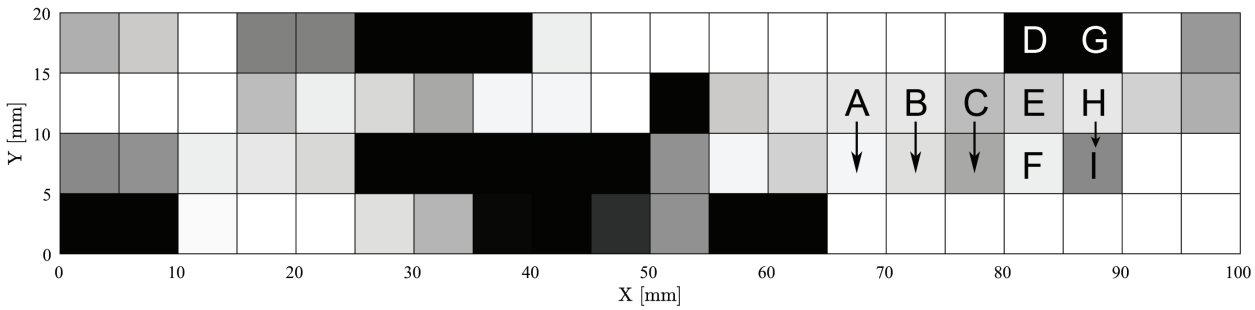

Figure 4.4: Ultrasonic map (CBR) for steel X70-X after 8 days in NACE TM0284-2016 solution C with pH 2.7 at 1 atm H_2S with crack indicators A-I. CBR values are represented in 32 tone grey scale, with white being crack free and black being completely cracked areas.

To further verify and characterize the ultrasonic methodology, a series of theoretical calculations was completed. As a result of these calculations, the maximum angle between probe and sample is defined to be 1.45°. Any positive derivation of this angle can be associated with significant signal loss. However, the ideal offset angle between probe and sample should be closer to 0°. Based on the maximum offset angle of 1.45°, the reliability of ultrasonic peaks can be determined using near and far field relations. Assuming that the signal is perpendicular until the far field is reached, three backwall signal peaks can be considered unaffected by the beam diversion. However, calculations based exclusively on the diversion angle indicate, for a diversion signal attenuation of -6dB, that two backwall signal peaks are unaffected. As such, no inaccuracies caused by a diversion of the ultrasonic beam are expected for the calculation of the CBR and GCBR values. Further information on this can be found in appendix C.

4.2 Ultrasonic Crack Evaluation of Samples

The results obtained by the ultrasonic evaluation of hydrogen-induced cracks is divided into three sections. First, the results from samples submerged into a solution of pH 2.7 are presented. This is followed by the results from pH 5.5 tests.

4.2.1 Severe Sour Service HIC Tests (pH 2.7)

Samples were tested at 0.1 and 1 atm H_2, between 1 and 16 days and at a pH of 2.7. All samples showed cracking along the centerline. In the following subsections, the results, along with the corresponding CBR histograms for 1 and 16 day tests are presented. All CAR and CBR maps can be found in appendix C.

1 atm H_2S

The CBR histogram for steel X70-X, tested for 1 day at a pH of 2.7 and 1 atm H_2S, can be seen in Figure 4.5. Just over half of the testing locations indicated no cracking. Increased peaks can

be seen for local CBR values of 1 and for the range 0.11-0.22. These results suggest fast cracking kinetics, as about 20% of the scanned locations showed strong cracking.

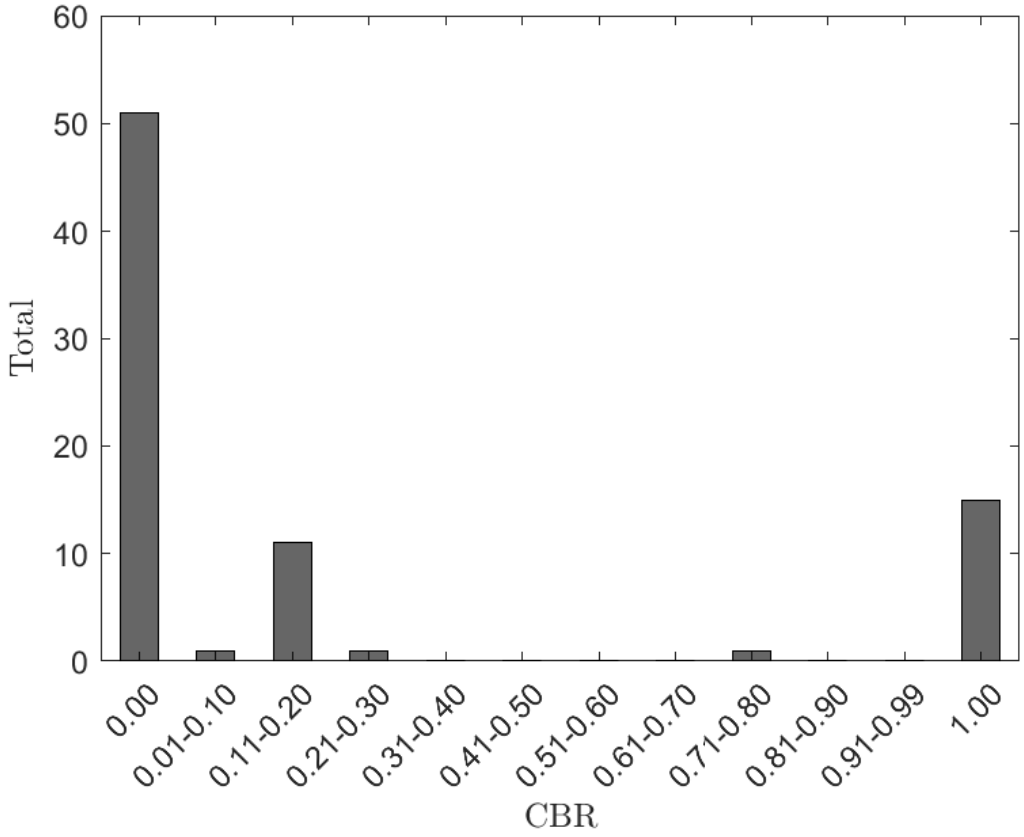

Figure 4.5: Histogram for X70-X, tested for 1 day at a pH of 2.7 and 1 atm H_2S.

By plotting the local CBR values at their corresponding locations (Fig.4.6), it can be seen that cracking started in several locations and propagates in form of smaller cracks.

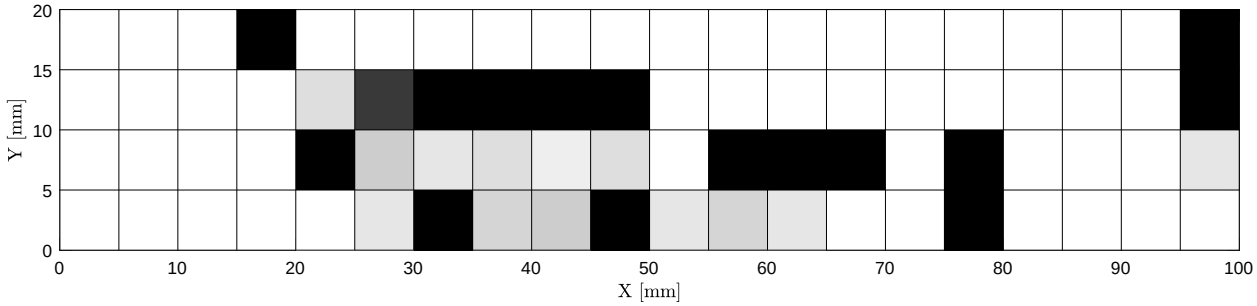

Figure 4.6: CBR map for X70-X, tested for 1 day at a pH of 2.7 and 1 atm H_2S.

After a testing period of 16 days, the CBR histogram (Fig. 4.7) shows an increased concentration

of low CBR cracks. The amount of completely cracked zones remains almost identical to the 1 day test. It can be seen that the majority of the smaller cracks has local CBR values between 0.01 and 0.3. This suggests that cracks grow from an initiation point, rather than the formation of new crack sites.

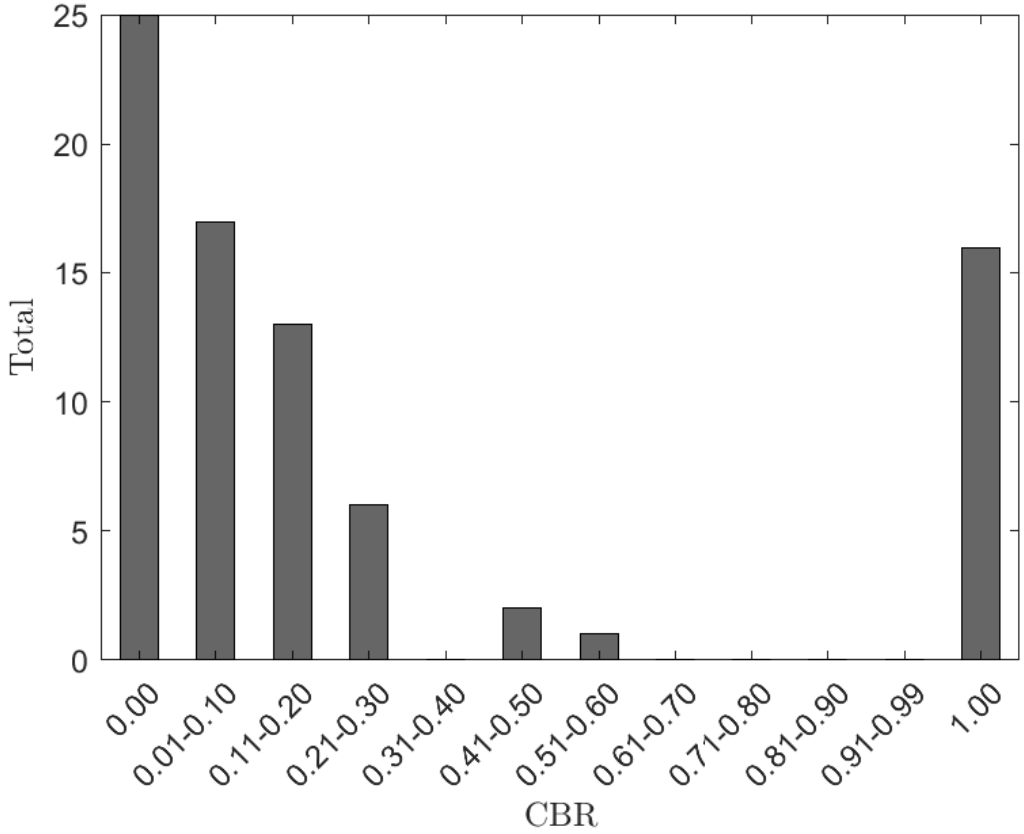

Figure 4.7: Histogram for X70-X, tested for 16 days at a pH of 2.7 and 1 atm H_2S.

The CBR map for the 16 day test (Fig. 4.8) shows a total of six crack initiation sites and several smaller cracks surrounding these.

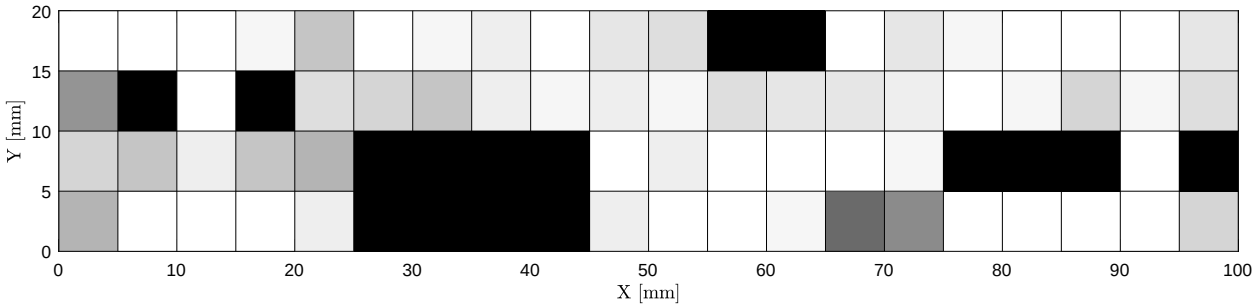

Figure 4.8: CBR map for X70-X, tested for 16 days at a pH of 2.7 and 1 atm H_2S.

The CBR histogram for steel X70-B, tested for 1 day at a pH of 2.7 and 1 atm H_2S shows similar results than those obtained for X70-X. About half the scanning locations did not show any cracking, close to 20% of the locations indicated complete cracking and increased peaks between 0.01 and 0.3.

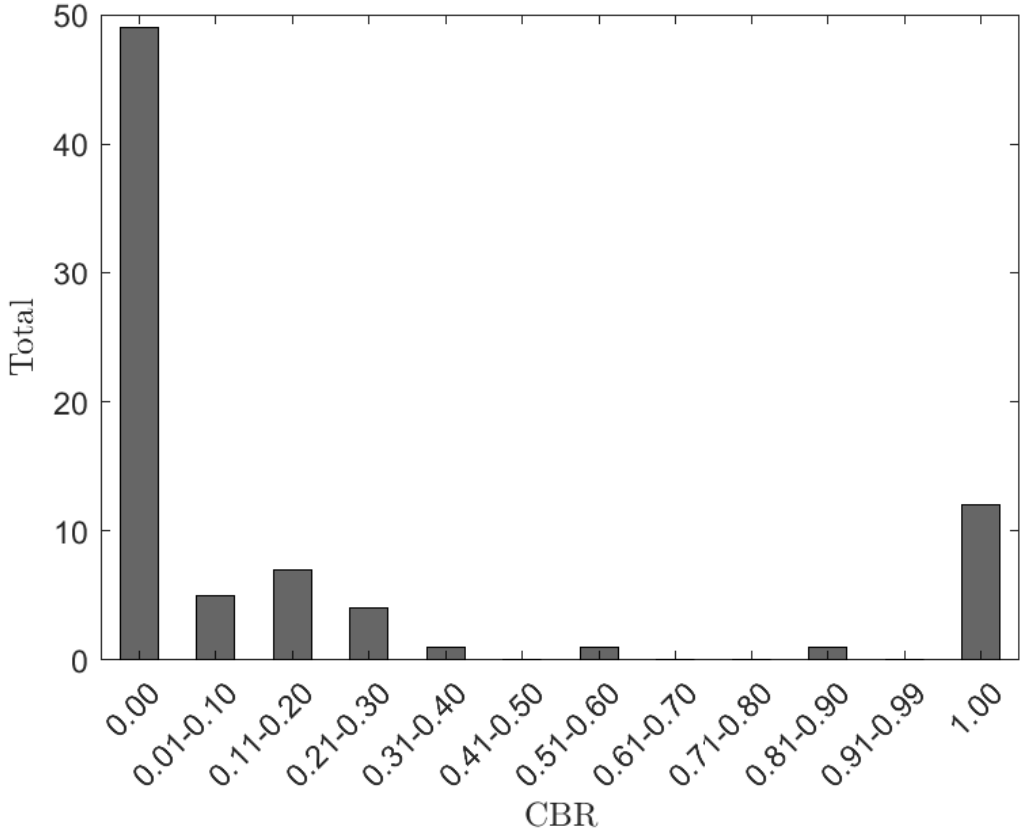

Figure 4.9: Histogram for X70-B, tested for 1 day at a pH of 2.7 and 1 atm H_2S.

The corresponding CBR map shows 5 crack initiation sites. Most of the smaller cracks are located in the immediate vicinity of these cracks and did likely propagate from these complete cracks.

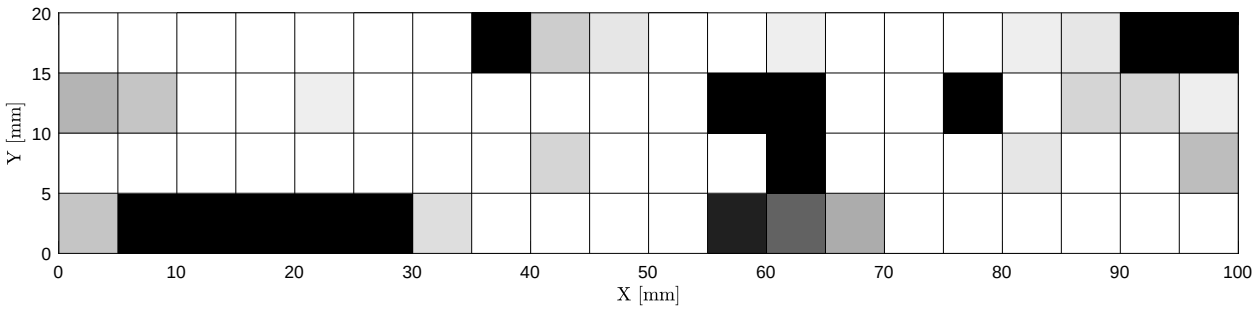

Figure 4.10: CBR map for X70-B, tested for 1 day at a pH of 2.7 and 1 atm H_2S.

Looking at the CBR histogram for the 16 day test for X70-B, it can be seen that a significant amount of cracks show a CBR value of 1, indicating complete cracking. Only about 10% of the zones did not show any cracking and the majority of small cracks lays in the 0.11-0.4 range.

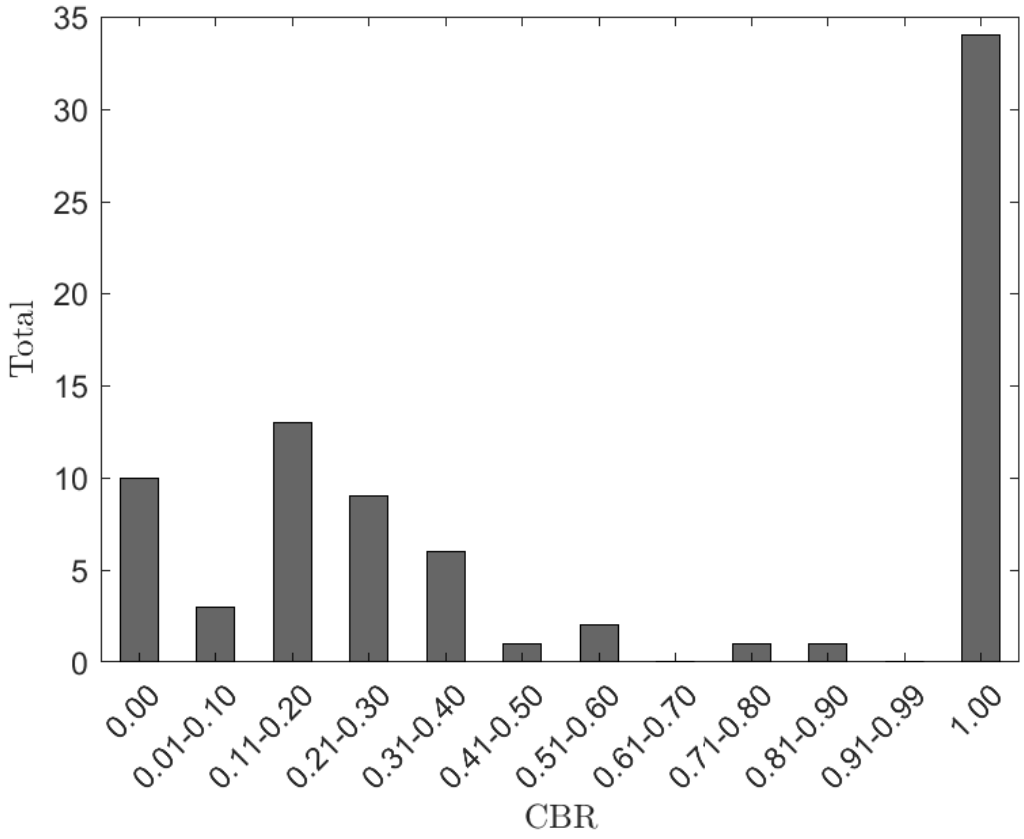

Figure 4.11: Histogram for X70-B, tested for 16 days at a pH of 2.7 and 1 atm H_2S.

The CBR map for the 16 day test indicates 4 crack clusters from which most the smaller cracks seem to propagate from.

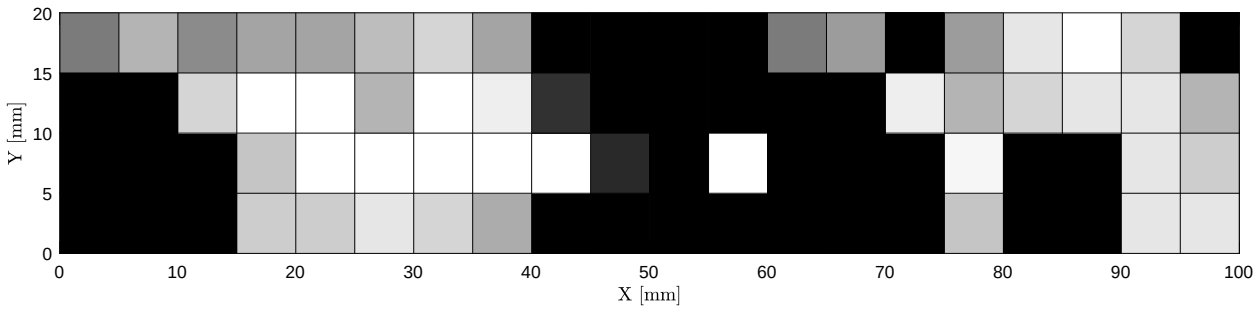

Figure 4.12: CBR map for X70-B, tested for 16 days at a pH of 2.7 and 1 atm H_2S.

Overall, X70-X shows less cracking than X70-B. Both steels showed cracking after 1 day. For a pH of 2.7 and 1 atm H_2S, severe cracking can be observed. This can be seen in Figure 4.13. Both X70-X and X70-B show crack to backwall ratios of about 20% after one day. For steel X70-X, the crack to backwall ratio remains relatively constant between 4 and 16 days and seems to stagnate at about 35% cracking. X70-B shows faster cracking and reaches a somewhat steady state after 2 days. The overall crack to backwall ratio averages to about 45%. It appears that X70-X generally performs slightly better than X70-B with respect to their resistance to corrosion.

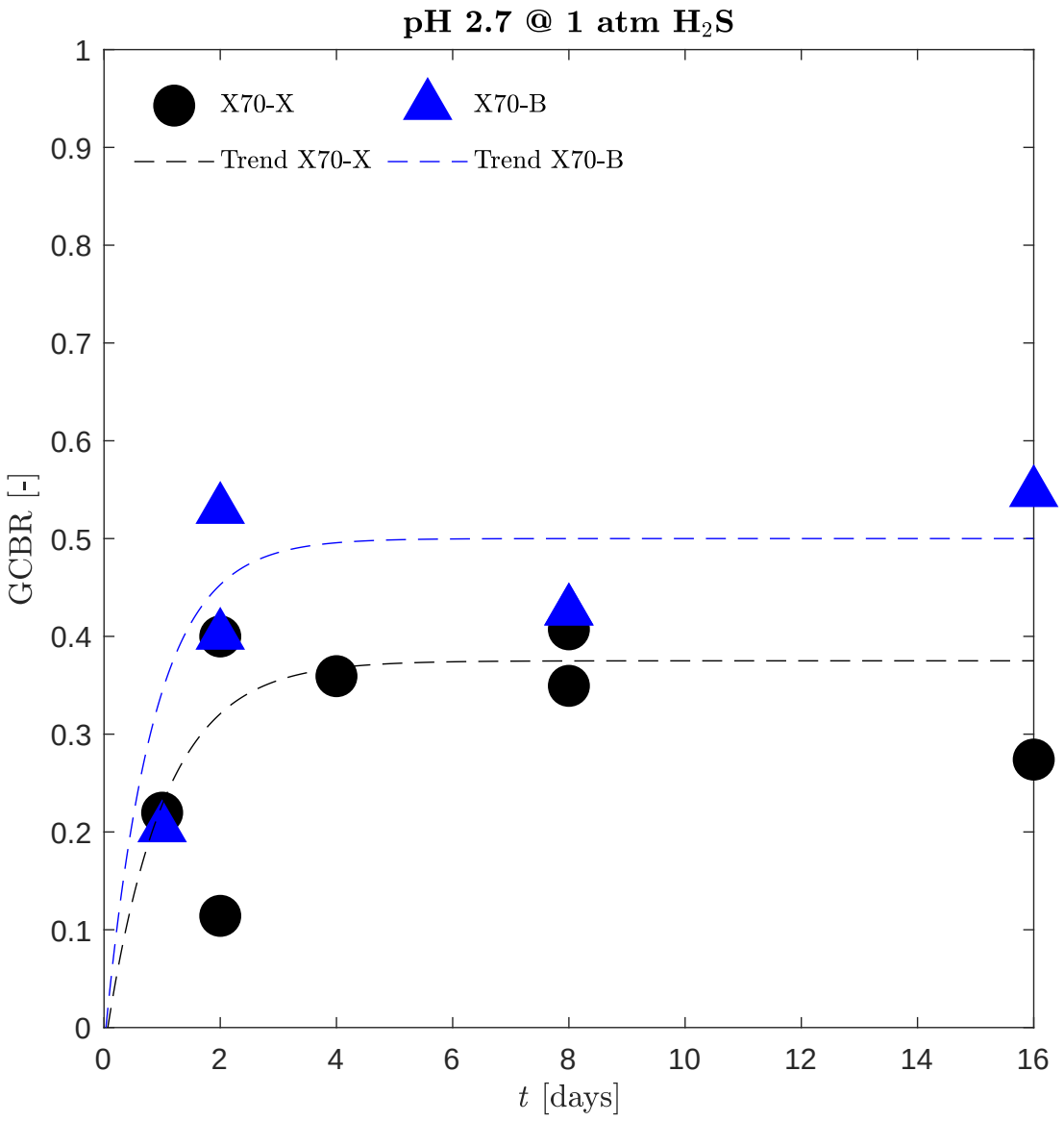

Figure 4.13: Crack to backwall ratios for tests carried out at a pH of 2.7 and 1 atm H_2S.

4.2.2 Intermediate Sour Service HIC Tests (pH 5.5)

The CBR histogram for the 32 day pH 5.5 X70-B test (Fig.4.14) indicates that about 70% of the scanned location are unaffected by cracking. The majority of the small cracks shows CBR ranging from 0.01-0.2. 12 locations were found to have CBR values of 1, i.e. complete cracking. No cracking was observed for a X70-X steel under the same conditions.

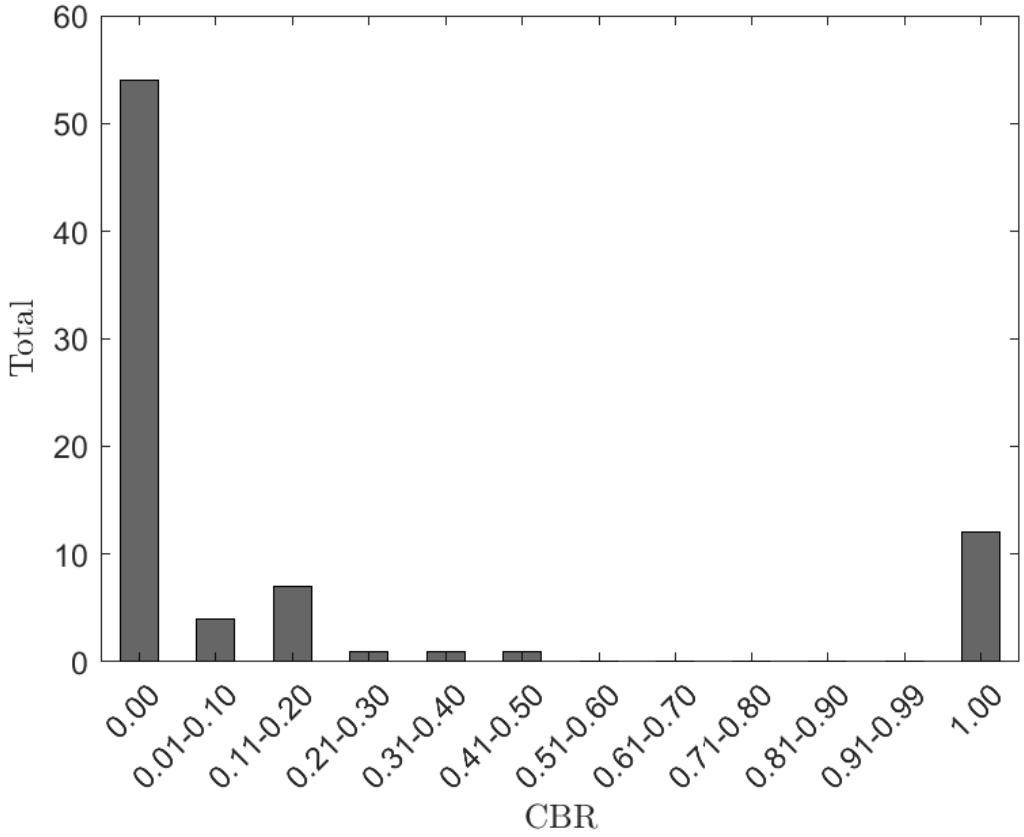

Figure 4.14: Histogram for X70-B, tested for 32 days at a pH of 5.5 and 1 atm H_2S.

The corresponding CBR map (Fig. 4.15) shows 2 crack sites and smaller cracks surrounding these. Only few of these smaller, partial cracks have local CBR values of more than 20%.

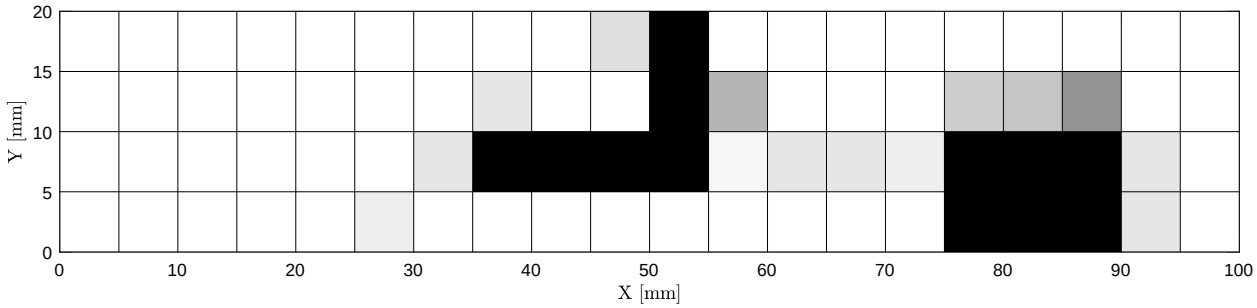

Figure 4.15: CBR map for X70-B, tested for 32 days at a pH of 5.5 and 1 atm H_2S.

Figure 4.16 shows the histogram for a 64 day pH 5.5 test using X70-X. More than half of the scanned locations are unaffected by cracks and about a quarter show severe, complete cracking. The majority of the partial cracks possesses local CBR of 0.11-0.3.

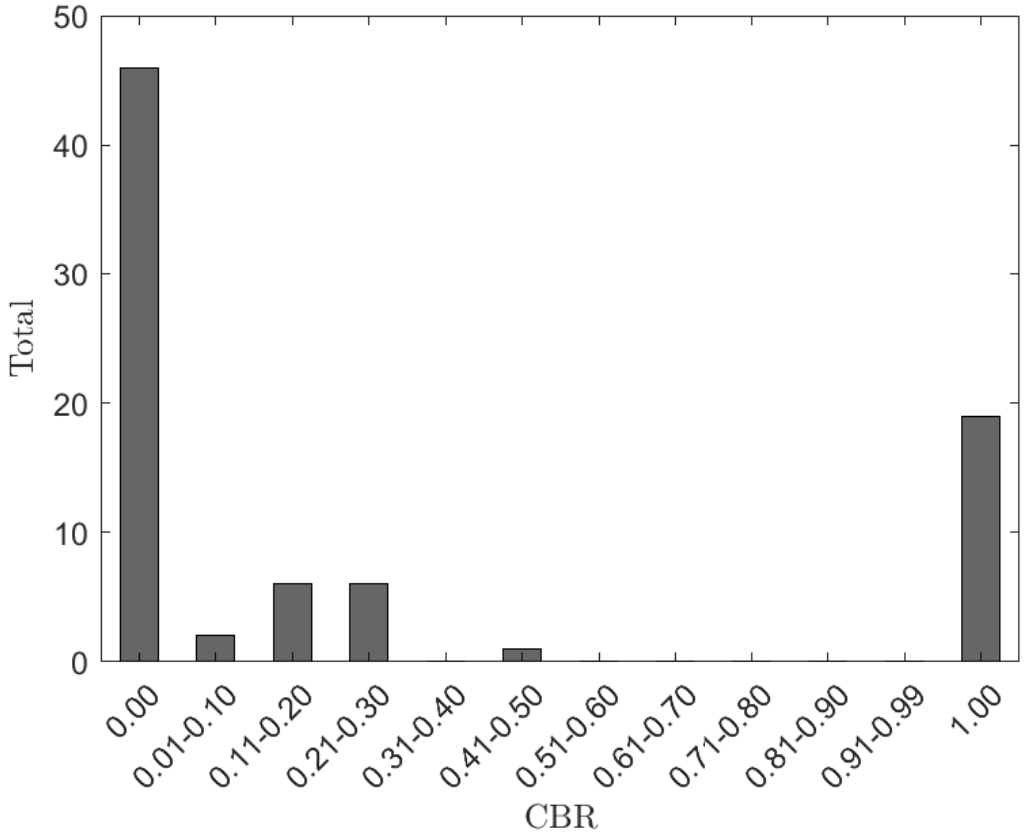

Figure 4.16: Histogram for X70-X, tested for 64 days at a pH of 5.5 and 1 atm H_2S.

As can be seen in the CBR map for X70-X (Fig.4.17), two crack sites formed during the 64 day test period. These cracks seem to be aligned with the rolling direction and measure 30 and 40 mm in length and up to 10 mm in width. All partial cracks are located near full cracks.

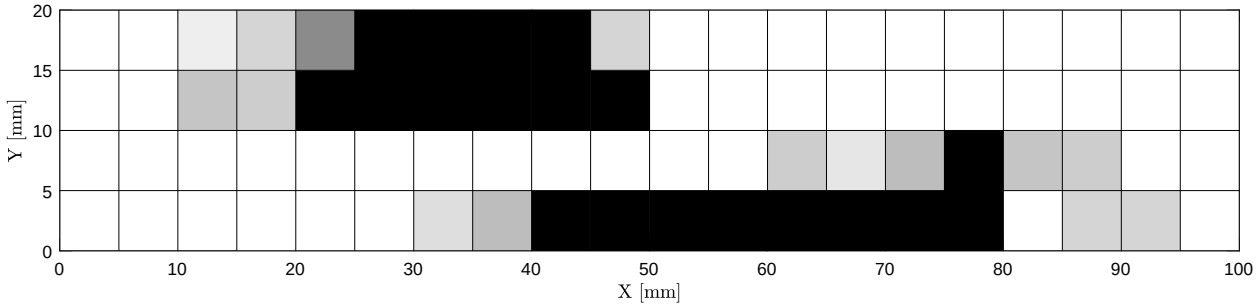

Figure 4.17: CBR map for X70-X, tested for 64 days at a pH of 5.5 and 1 atm H_2S.

The CBR histogram of the 64 day X70-B test (4.18) shows that the majority of scanned locations is unaffected by cracking. 12 locations show severe, complete cracking. All partial cracks are evenly

distributed with local CBR ranging from 0.01-0.4.

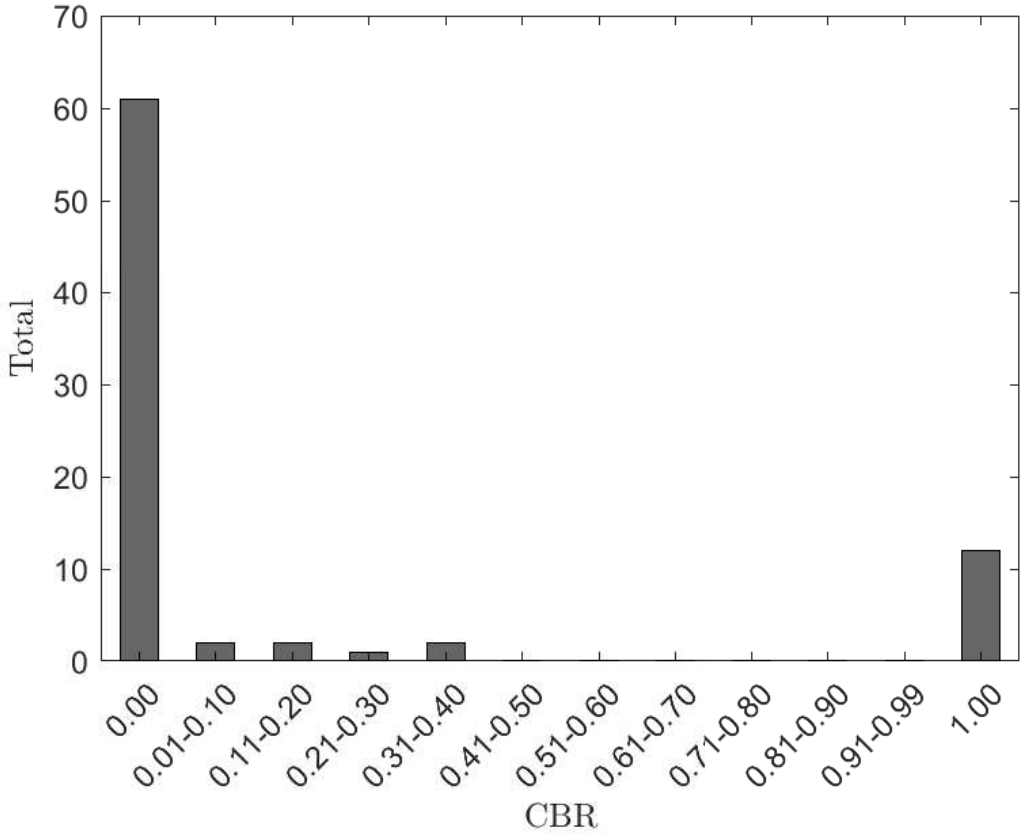

Figure 4.18: Histogram for X70-B, tested for 64 days at a pH of 5.5 and 1 atm H_2S.

Figure 4.19 shows the CBR map for the 64 day X70-B test. A total 4 full cracks, in 12 locations, can be seen. However, the only fully independent crack is located at the bottom of the map, the other cracks seem to be connected by a network of partial cracks. All cracks seem to propagate along the rolling direction.

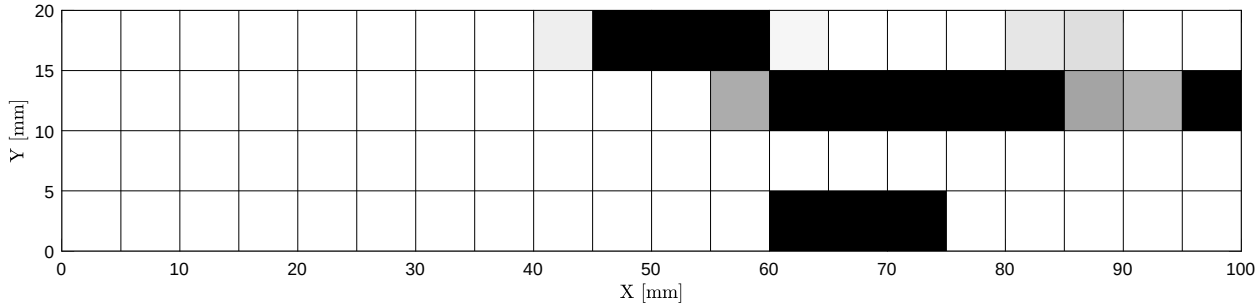

Figure 4.19: CBR map for X70-B, tested for 64 days at a pH of 5.5 and 1 atm H_2S.

HIC testing carried out at a pH of 5.5 and 1 atm H_2S did not result in any cracking for testing times of 16 days and less (Fig. 4.20). After 32 days, no cracking was observed for X70-X while X70-B showed a CBR of about 20%. For a testing time of 64 days, the crack to area ratio of steel X70-B is almost unchanged. X70-X shows a CAR of about 30%. Tests carried out at a pH of 4.5 and 0.1 atm H_2S and pH 6.5 and 1 atm H_2S did not result in cracking for a testing time of 16 days. This is consistent with the pH 5.5 tests.

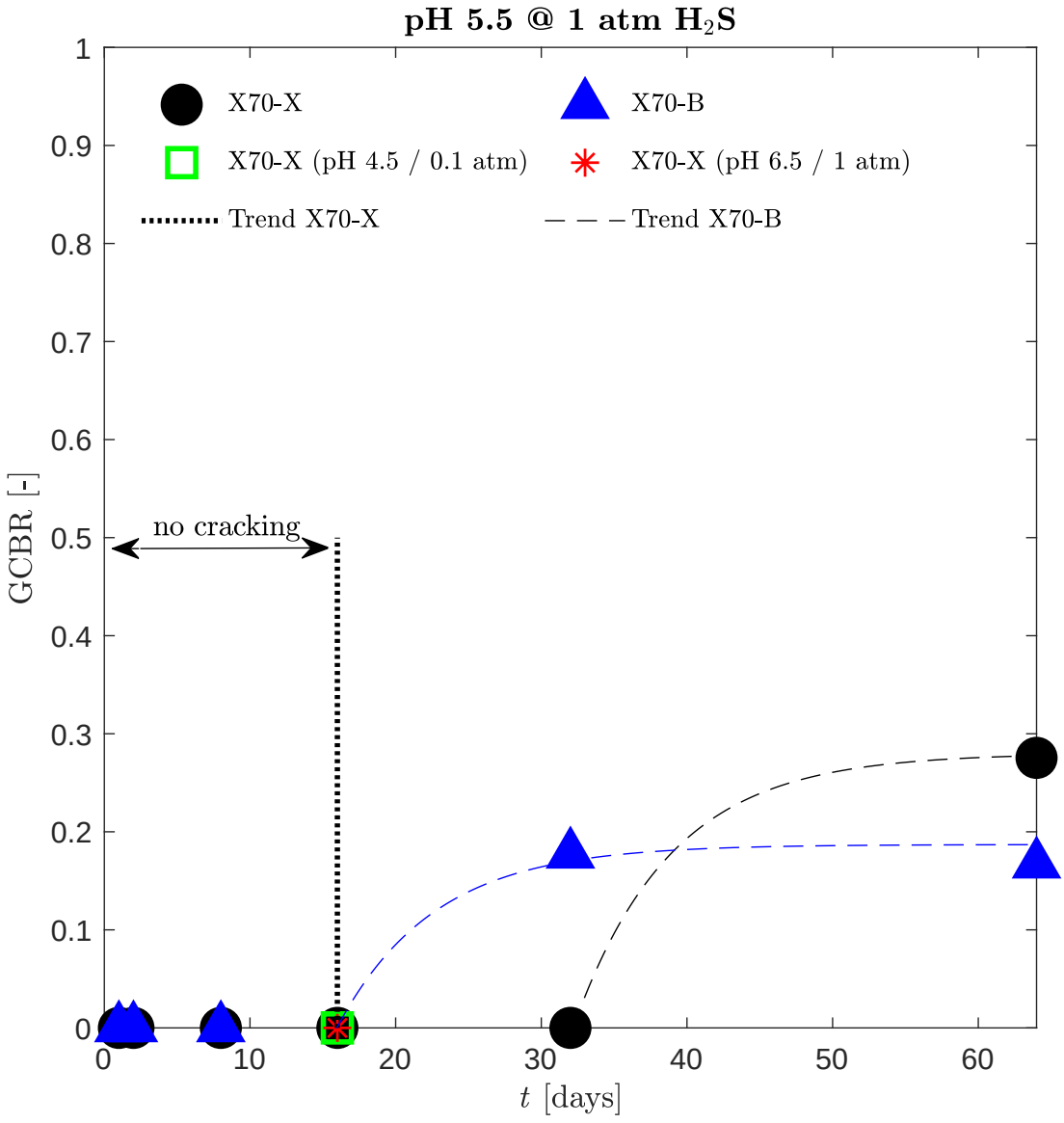

Figure 4.20: Crack to backwall ratios for tests carried out at a pH of 5.5 and 1 atm H_2S.

4.3 Inclusions in Steel Samples

As suggested by many authors, manganese sulfide is one of the main initiation and propagation side for hydrogen induced cracks. To confirm the presence of manganese sulfide in the steel samples used in this work, an already tested and cracked sample (Fig. 4.21) of steel X70-X was pried open. This was achieved by cutting a notch close to both crack ends and levering the sample open using a screwdriver and a hammer. During this process and the resulting deformation, copper from the screwdriver was abraded and adhered to the surface of the sample. However, this did not interfere with the results obtained using EDX. The corresponding SEM images can be found in appendix D.

As can be seen in Figure 4.21, the crack located using the standard NACE TM0284 analysis shows the typical step wise propagation of hydrogen-induced Cracks. The crack length of more than 1 cm made it possible to clearly see the crack without the use of polishing techniques.

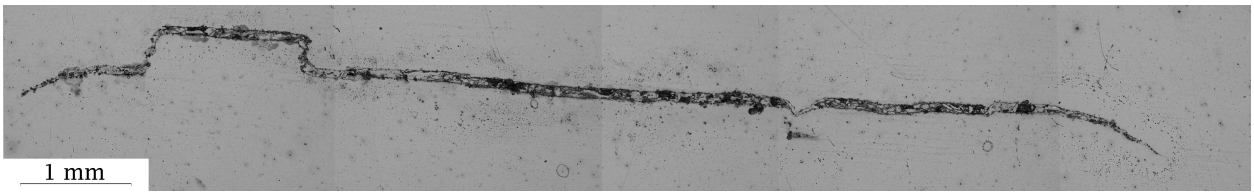

Figure 4.21: Centerline crack on steel X70-X after 8 days at 1 atm H_2S and a pH of 2.7.

Figure 4.22 shows one half of the opened sample. The light grey area in the centre is the crack site. Due to the cutting process, part of the crack surface was removed by the abrasive disc. The orange scratch on the right side of the crack surface is a residual mark left by the screw driver used to open the sample.

Figure 4.22: Crack surface of sample X70-X. The triangular, lighter gray area is the opened crack.

Two locations where scanned. Figure 4.23 shows an SEM image with 600x magnification of the opened crack site. The corresponding SEM parameters can be found in the legend of the image and are the same for all EDX scans of the same location. It can be seen that darker areas spread vertically. These darker areas can be confirmed to be manganese sulfide inclusions running along the rolling direction of the steel.

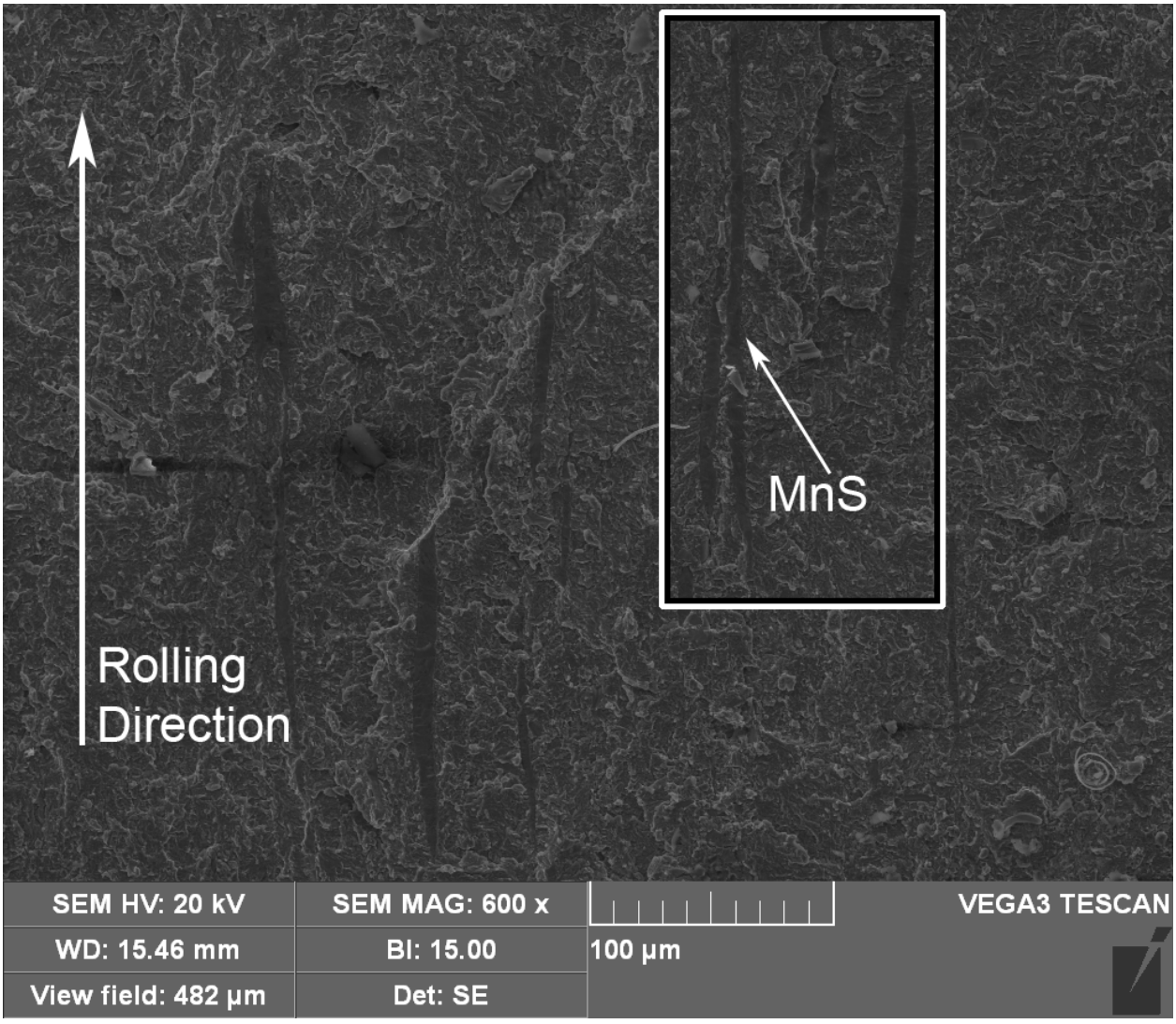

Figure 4.23: Section on sample X70-X showing manganese sulfide inclusions at the opened crack side. The sample was tested at a pH of 2.7, 1 atm H_2S and a testing period of 8 days.

The EDX maps for manganese and sulfur presented in Figures 4.24 and 4.25, respectively, indicate high concentrations of both manganese and sulfur along the darker areas presented in Figure 4.23. This proves the presence of manganese sulfide in steel X70-X. As can be seen, the length of these inclusions ranges from about 50 μm to about 200 μm, with thicknesses of up to 10 μm. Inclusions of this length can be detrimental to the corrosion resistance of steels and pose as

crack initiation sites.

When looking at the element maps for sulfur and manganese, it can be seen that the intensity for sulfur is greater than for manganese. However, no calcium was detected along with sulfur during the EDX scans, suggesting the presence of complex of non-stoichiometric molecules. During the scan, mostly aluminum, niobium, manganese and sulfur were detected. A super-positioned EDX map showing aluminum (orange), carbon (gray), manganese (purple), niobium (blue) and sulfur (red) can be seen in Figure4.26. The individual maps were processed in Adobe Photoshop and noise was removed using the dust and scratches filter with a radius of 1 pixel and 0 levels of threshold. This resulted in the removal of random intensities and left only clusters greater than 1 pixel.

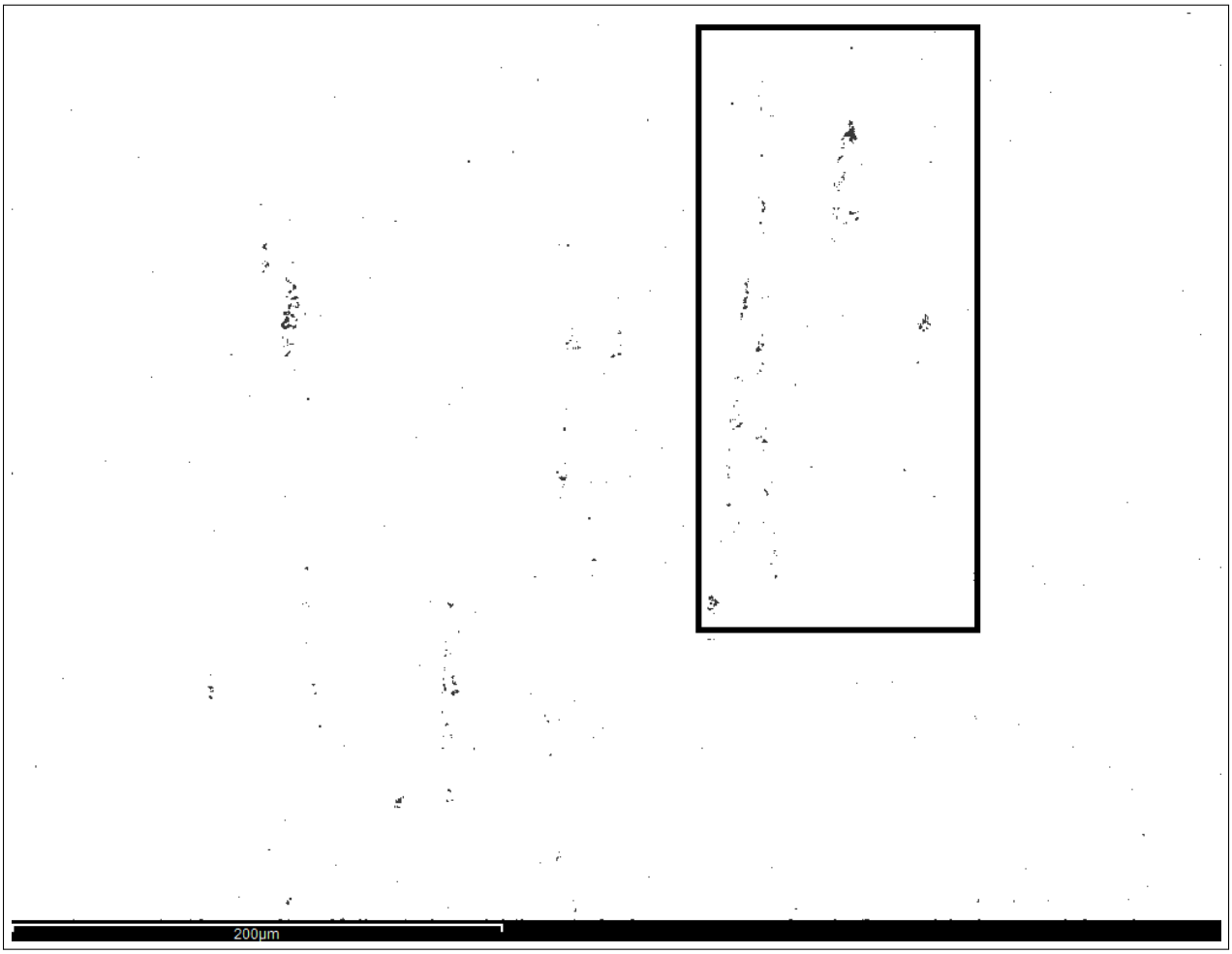

Figure 4.24: EDX map for manganese of section shown in Fig. 4.23.

Only one carbon cluster can seen in the center of the second quarter from the left. This area can be seen as a dark circular area in the SEM image. Although the detection of calcium resulted in mostly randomly distributed noise, signs of clustering can be detected in this area as well.

When looking at the aluminum concentrations (orange), it can be seen that aluminum is not

present at locations rich in manganese or sulfur. The only other element that can be found at the manganese sulfide sites is niobium (blue). This suggests the presence of complex (Mn,Nb)S or niobium sulfide (NbS_2) inclusions. An alternative explanation could be the precipitation of niobium carbides on manganese inclusions.

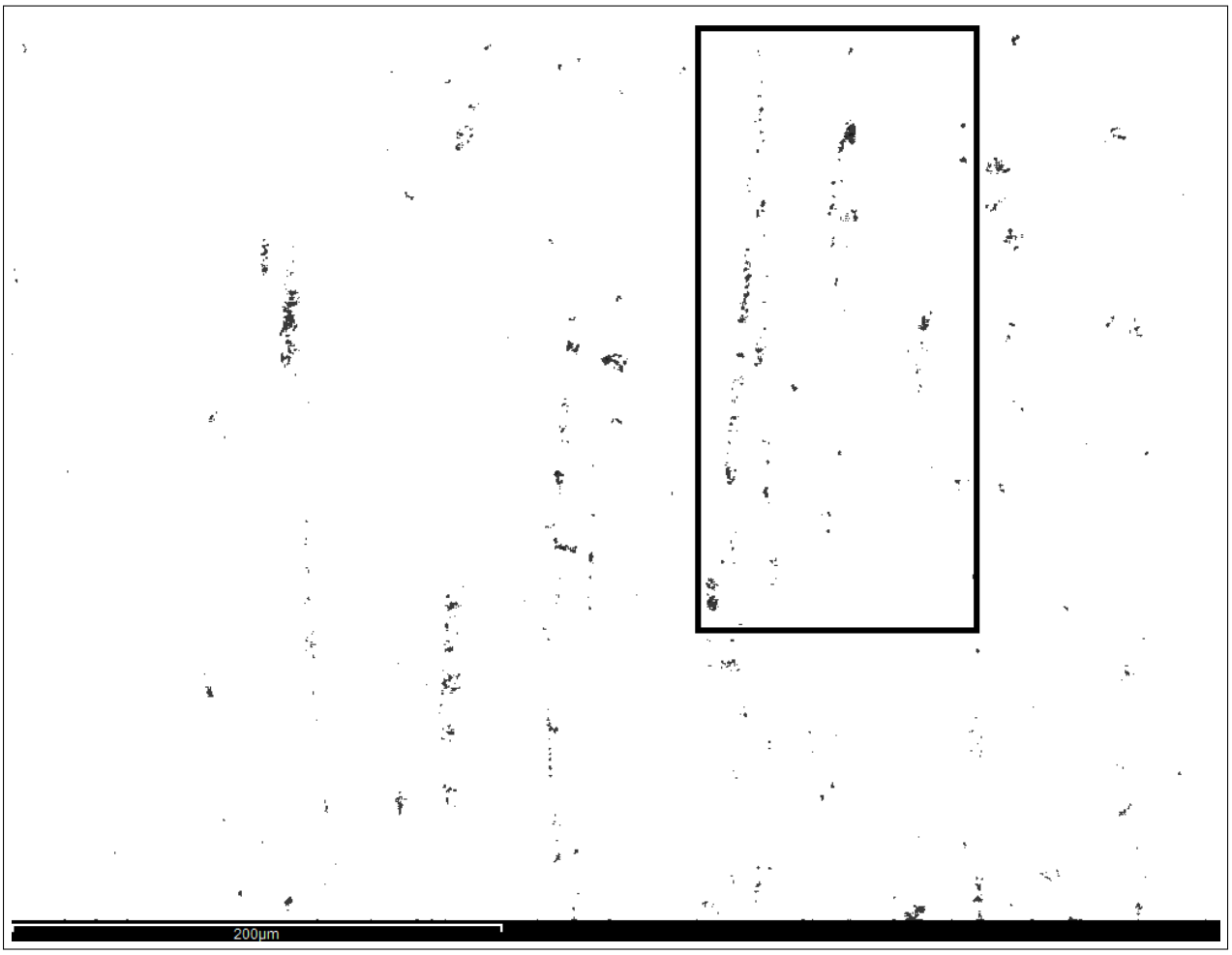

Figure 4.25: EDX map for sulfur of section shown in Fig. 4.23.

Figure 4.26 shows a superposition of the EDX maps for aluminum (orange), carbon (grey), manganese (purple), niobium (blue) and sulfur (red). As pointed out by the arrows A-E, several globular aluminum clusters can be observed. This indicates the presence of globular Al_2O_3 inclusions. Arrow F shows a cluster of globular carbon.

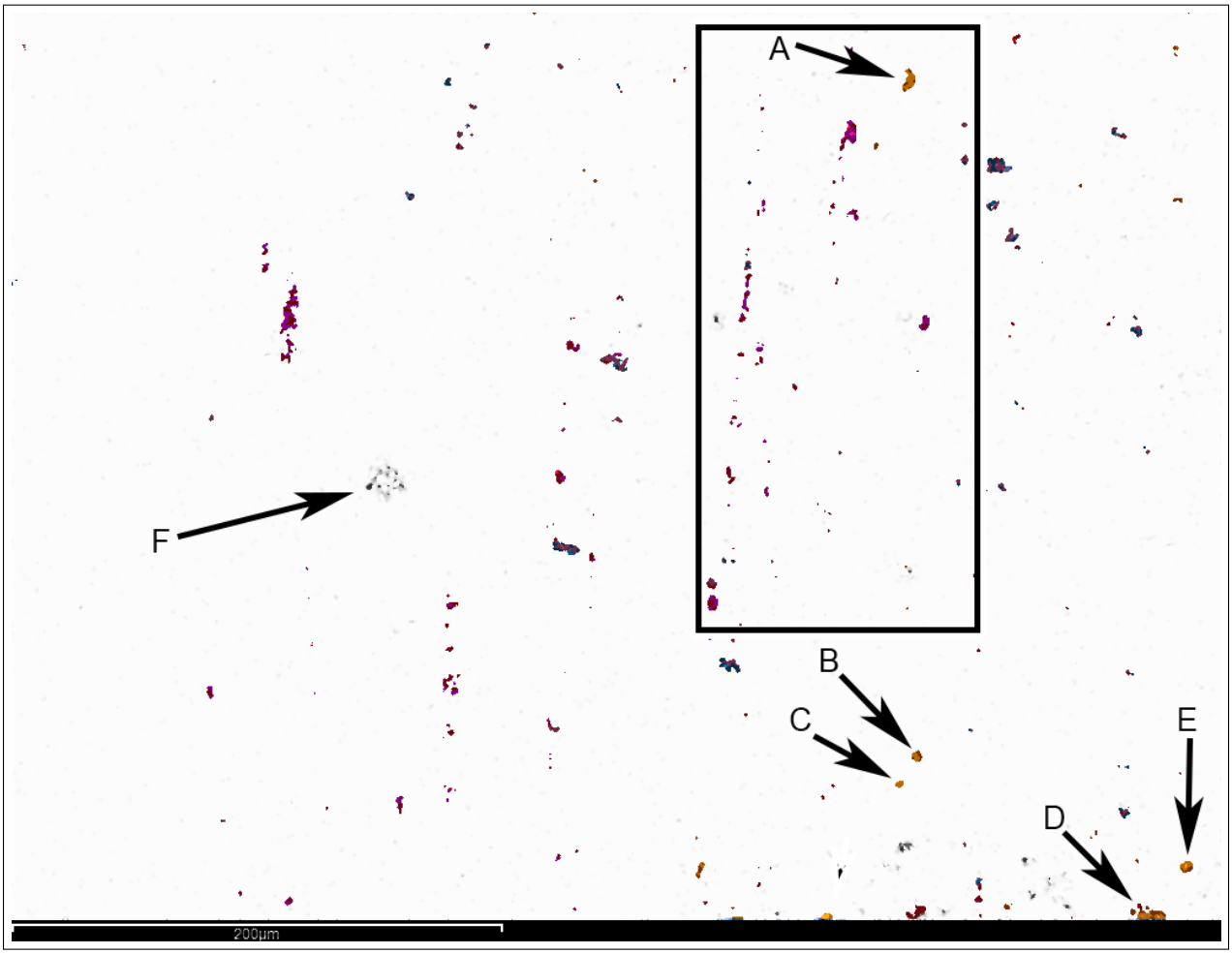

Figure 4.26: Super-positioned EDX map for aluminum (orange), carbon (grey), manganese (purple), niobium (blue) and sulfur (red) of section shown in Fig. 4.23.

Figure 4.27 shows another section of the crack at 600x magnification. The corresponding SEM parameters can be found in the legend of the image and are the same for all EDX scans of the same location. Visible as vertical, elongated inclusions is manganese sulfide. Once again, the presence of manganese sulfide can be confirmed by EDX maps of the area for manganese (Fig. 4.28) and sulfur (Fig. 4.29). Areas of increased concentrations of manganese and sulfur are detected in agreement with the inclusions of interest, visible in Figure 4.27. These manganese sulfide inclusions have a length of about 100-200 μm and a thickness of up to about 10 μm.

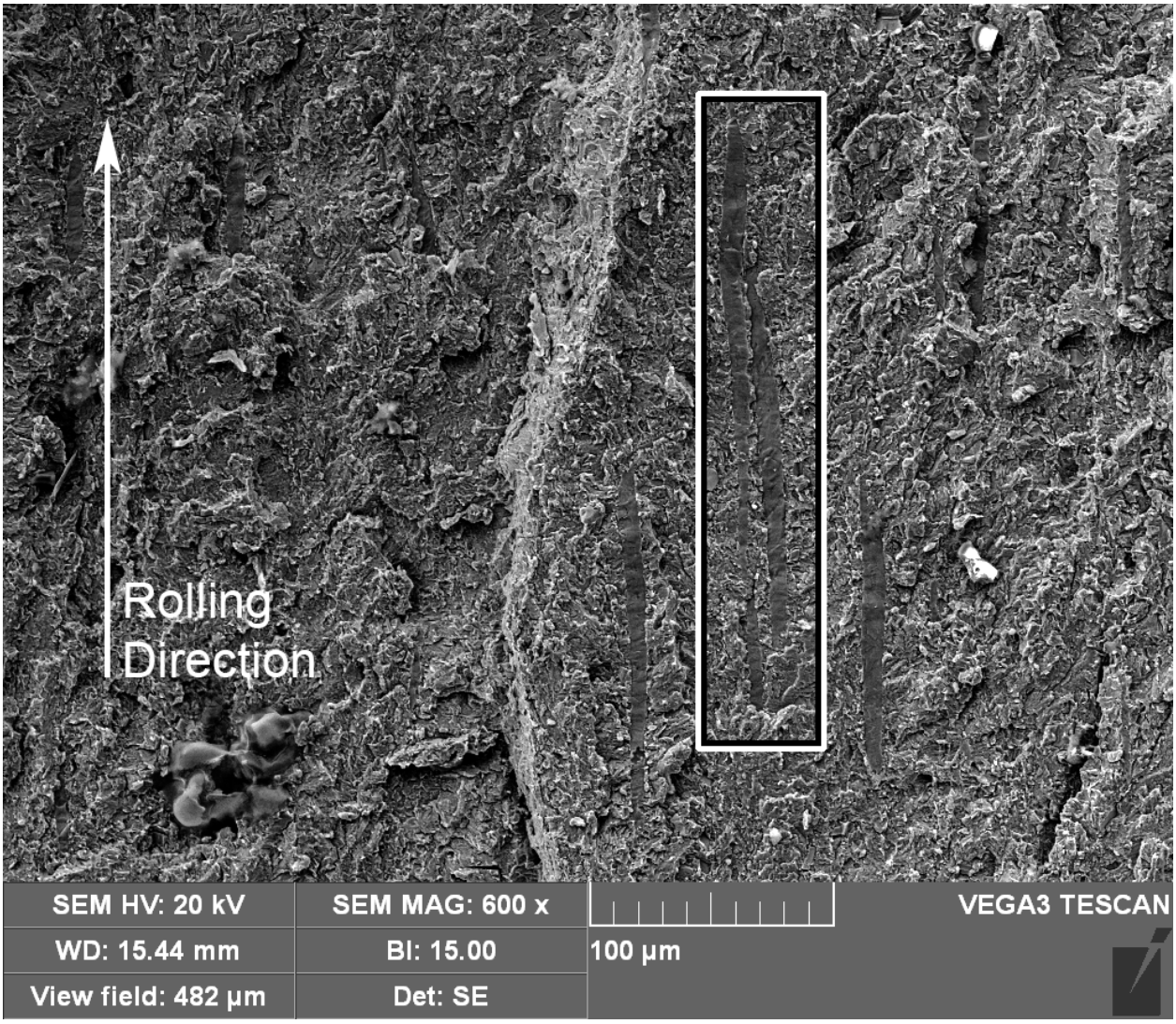

Figure 4.27: Section on sample X70-X showing manganese sulfide inclusions at the opened crack side. The sample was tested at a pH of 2.7, 1 atm H_2S and a testing period of 8 days.

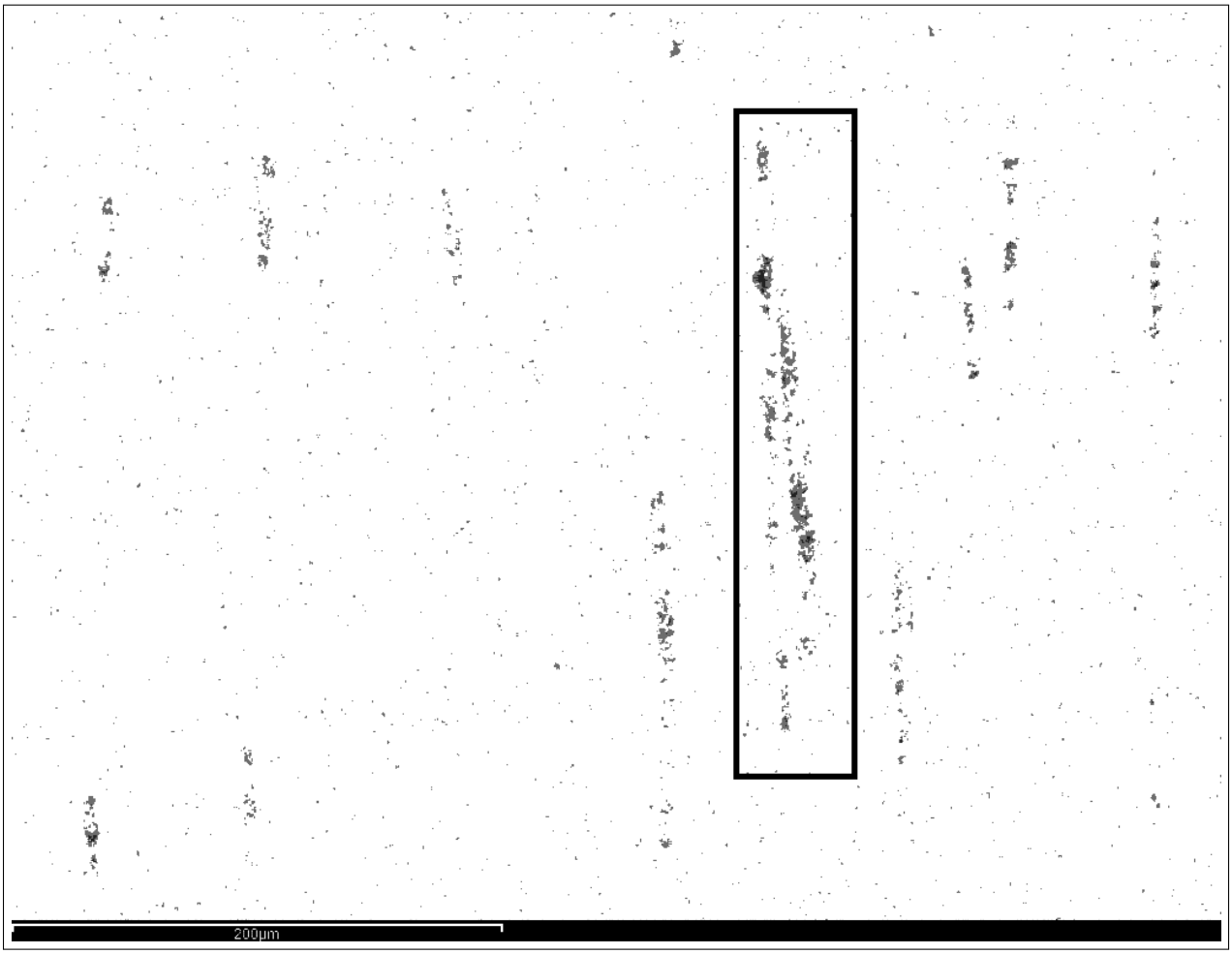

Figure 4.28: EDX map for manganese of section shown in Fig. 4.27.

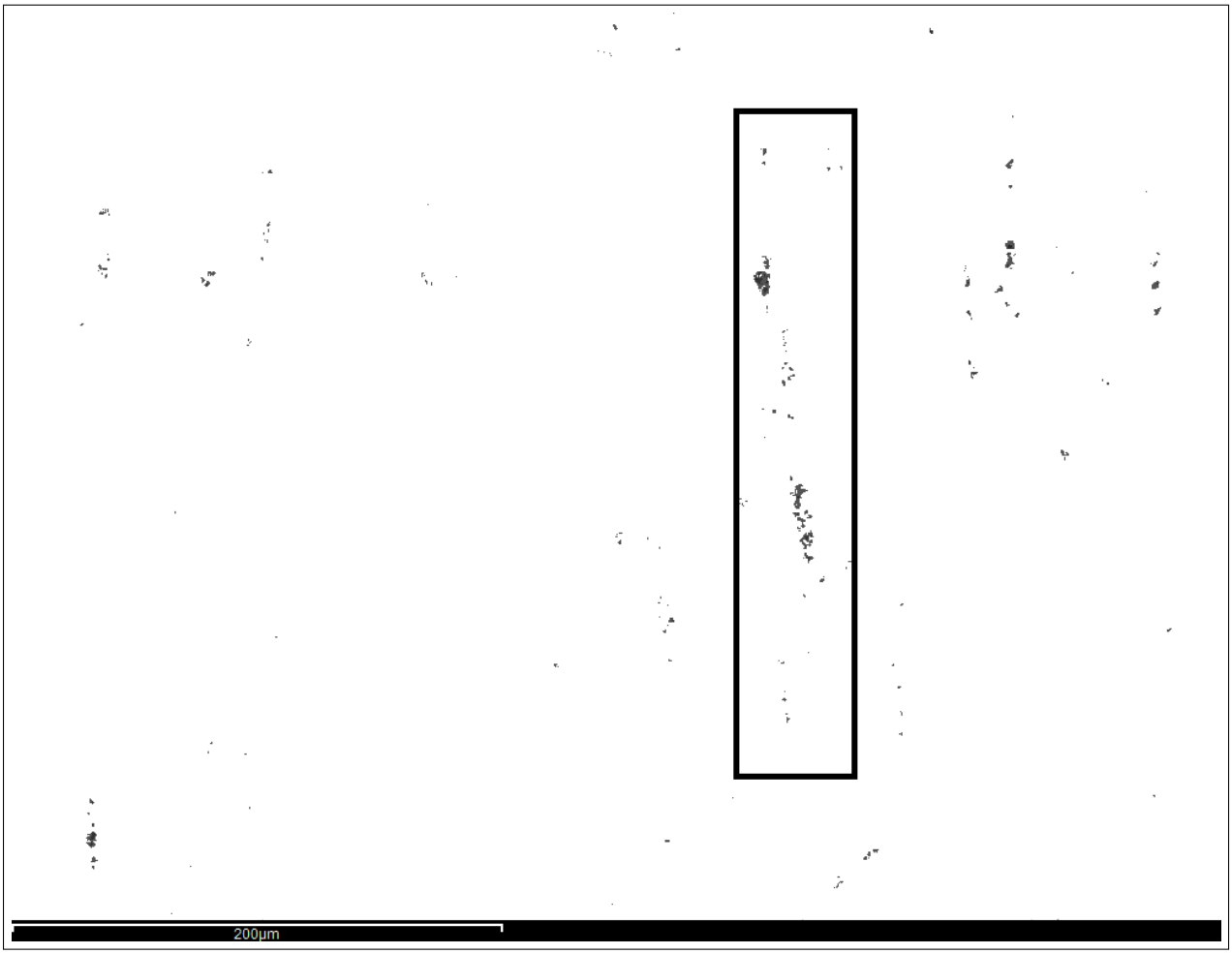

Figure 4.29: EDX map for sulfur of section shown in Fig. 4.27.

The EDX maps of both locations did not show any calcium sulfide inclusions. EDX scans for calcium appear to be mostly random. However, applying digital filters to the EDX map for calcium reveals a small, globular cluster of calcium in the area highlighted in Figure 4.30. This can be seen in Figure 4.31. For the same area, no significant amounts of sulfur are detected. Figure 4.26 shows a carbon cluster in this area (Arrow F). This suggests that the area does not contain calcium sulfide, but rater other calcium inclusions, such as calcium oxide, or calcium carbide slag. However, no EDX scan for oxygen was carried out, due to the likelihood of surface oxidation. Furthermore, the purpose of the EDX maps was to confirm the presence of manganese sulfide in steel X70-X.

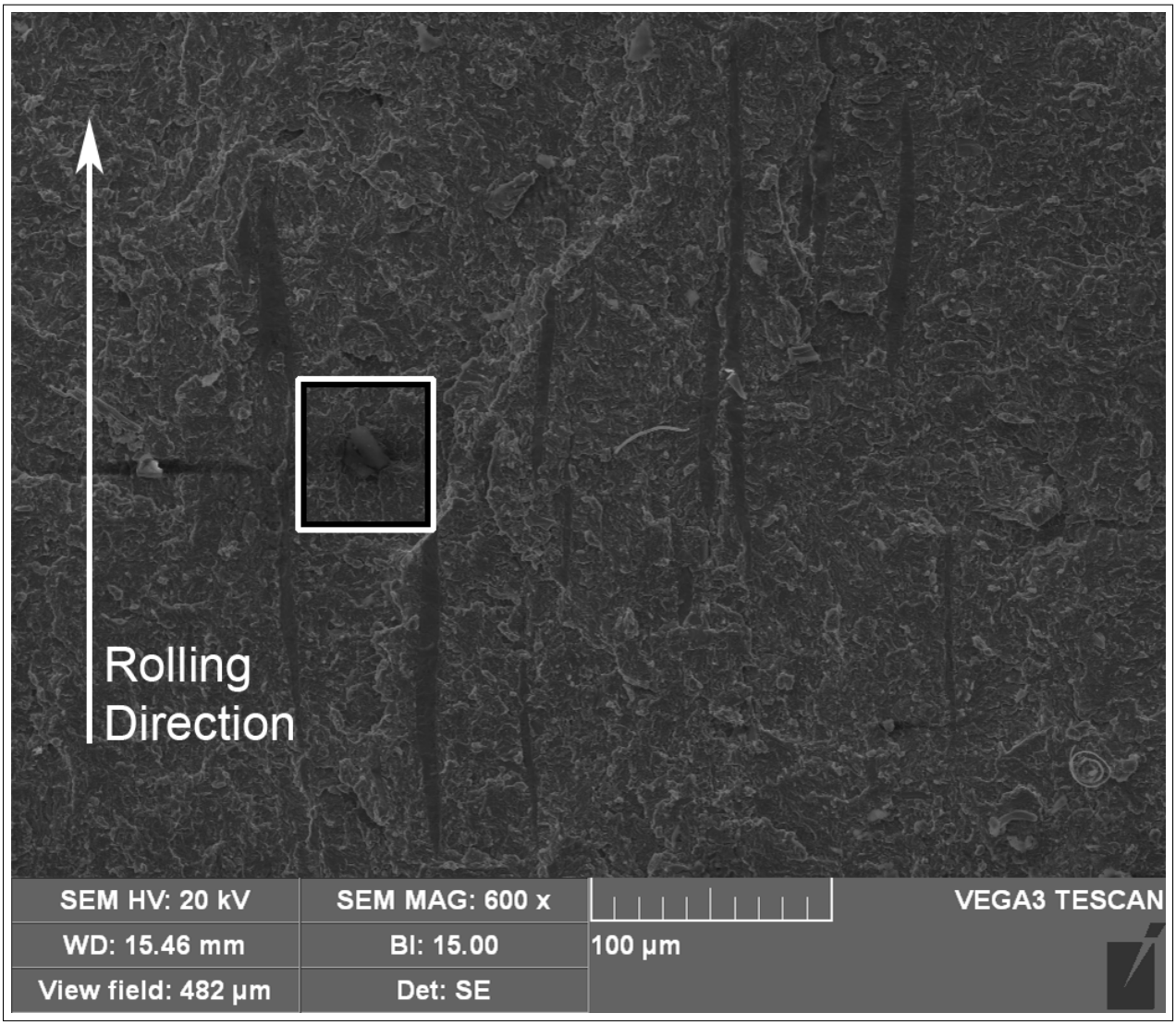

Figure 4.30: Section on sample X70-X showing manganese sulfide inclusions at the opened crack side. The sample was tested at a pH of 2.7, 1 atm H_2S and a testing period of 8 days. The highlighted area indicates a small calcium cluster.

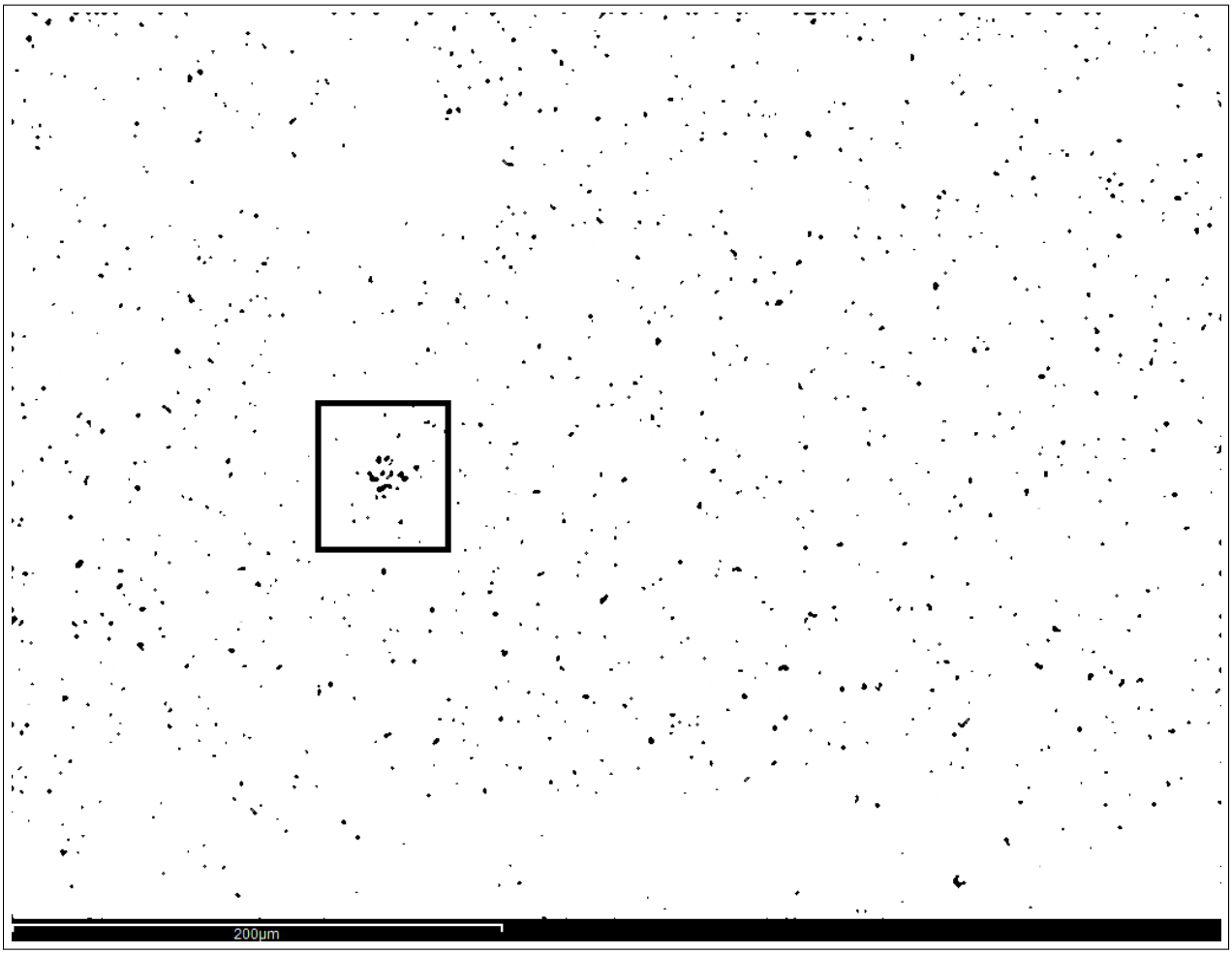

Figure 4.31: Filtered EDX map for calcium of section shown in Fig. 4.30.

Figure 4.32 shows an aluminum silicon oxide inclusion (highlighted area) at the crack side of an X70-B sample tested for 16 days in a pH 2.7 test solution under 1 atm H_2S partial pressure. The inclusion shows a globular shape and is about 10 μm long. The corresponding EDX maps for the elements aluminum, sulfur and oxygen can be found in Figure 4.33.

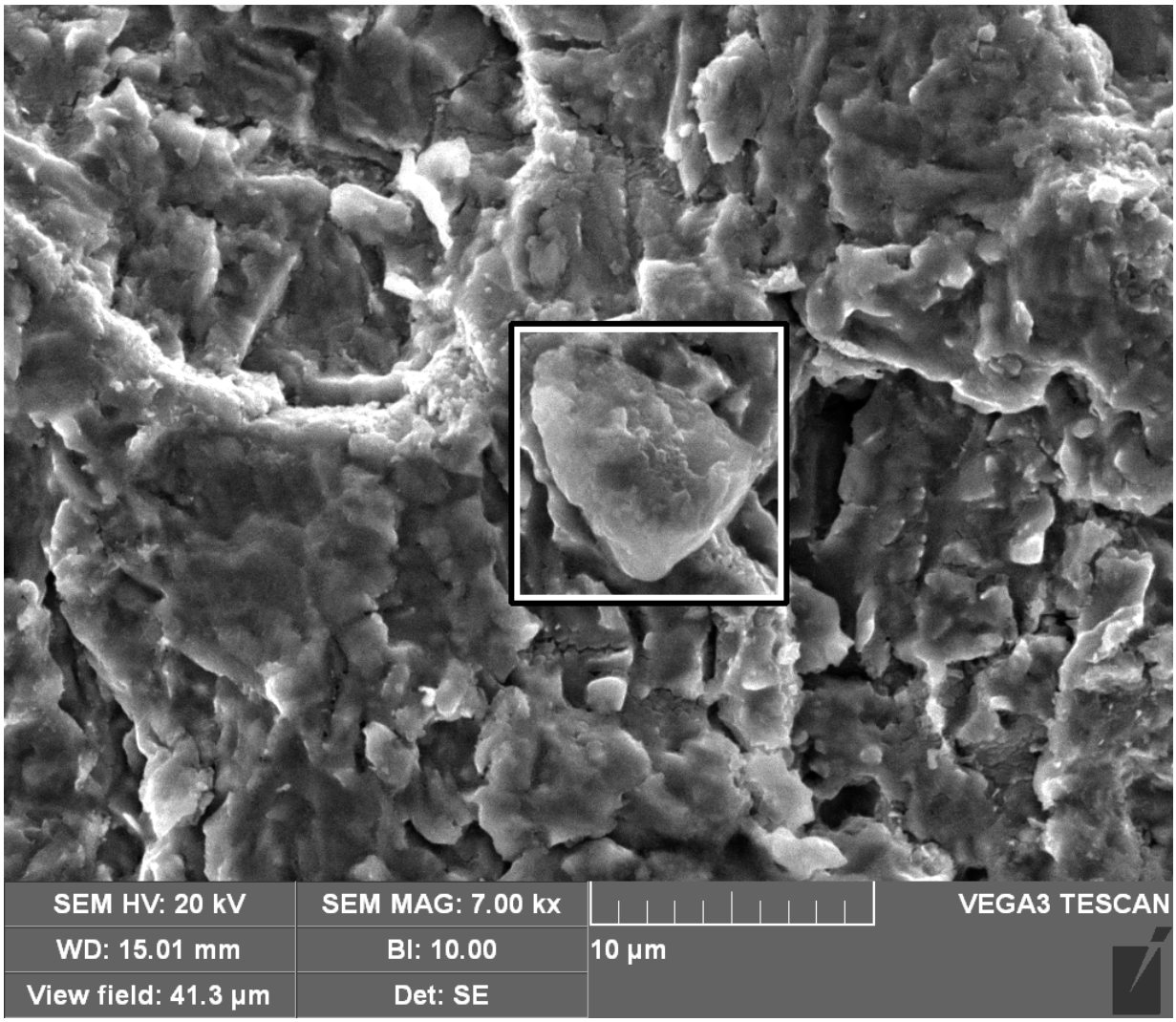

Figure 4.32: Section on sample X70-B showing aluminum silicon oxide inclusions at the opened crack side. The sample was tested at a pH of 2.7, 1 atm H_2S and a testing period of 16 days.

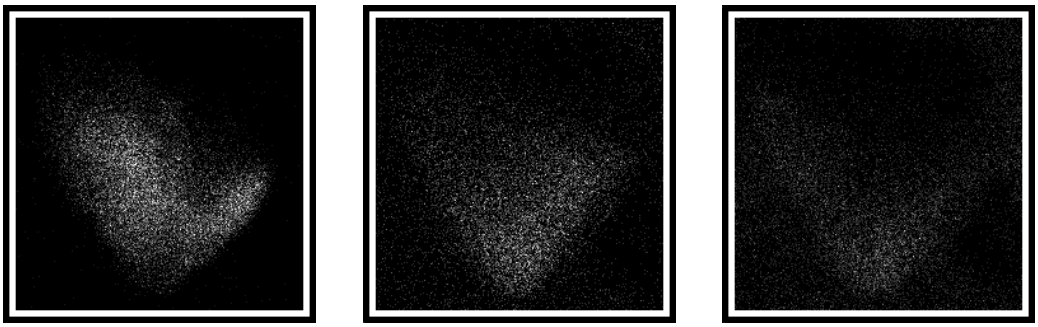

(a) Al (b) Si (c) O

Figure 4.33: EDX scans for aluminum (a), silicon (b) and oxygen (c) of area shown in Fig. 4.32.

During the SEM analysis of X70-B, niobium titanium nitride inclusions were found. A SEM image showing cubic (Nb,Ti)N inclusions with a length of about 5 μm can be found in Figure 4.34. The corresponding EDX maps for the elements niobium, titanium and nitrogen can be found in Figure 4.35. The selection shown in the SEM image indicates three individual (Nb,Ti)N inclusions in close proximity.

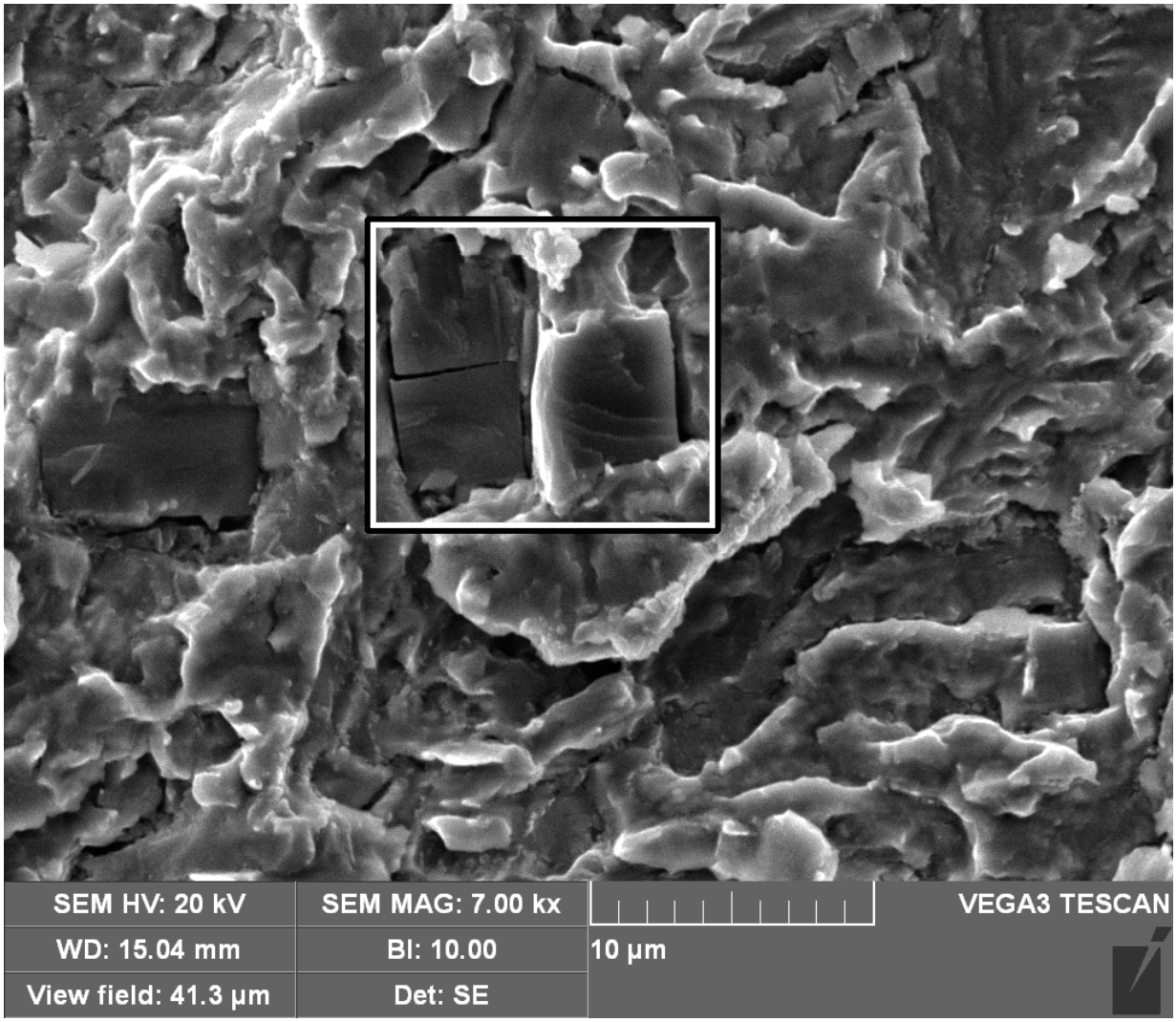

Figure 4.34: Section on sample X70-B showing niobium titanium nitride inclusions at the opened crack side (highlighted). The sample was tested at a pH of 2.7, 1 atm H_2S and a testing period of 16 days.

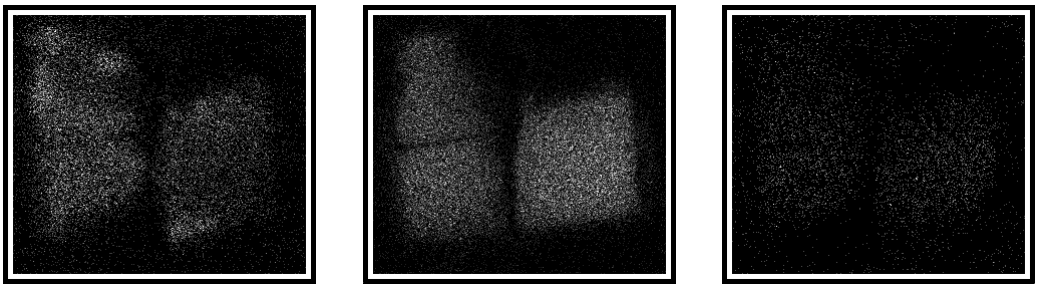

(a) Nb (b) Ti (c) N

Figure 4.35: EDX scans for niobium (a), titanium (b) and nitrogen (c) of area shown in Fig. 4.34.

Figure 4.36 shows a cluster of niobium titanium nitride inclusions embedded in iron. The EDX maps for niobium, titanium, nitrogen and iron (Fig. 4.37) show large quantities of titanium in the selection. Niobium concentrations appear higher at the edges of the inclusions. The EDX map for iron indicates an increased concentration of iron in the elongated section of the inclusion cluster, as well as in the area surrounding the inclusion. Nitrogen is present in the same areas as niobium and titanium.

Close inspection shows a crack on the left side of the inclusion, followed by a potential crack propagation line. This is indicated by the arrows. It is unclear whether the crack initiated or ended at the inclusion.

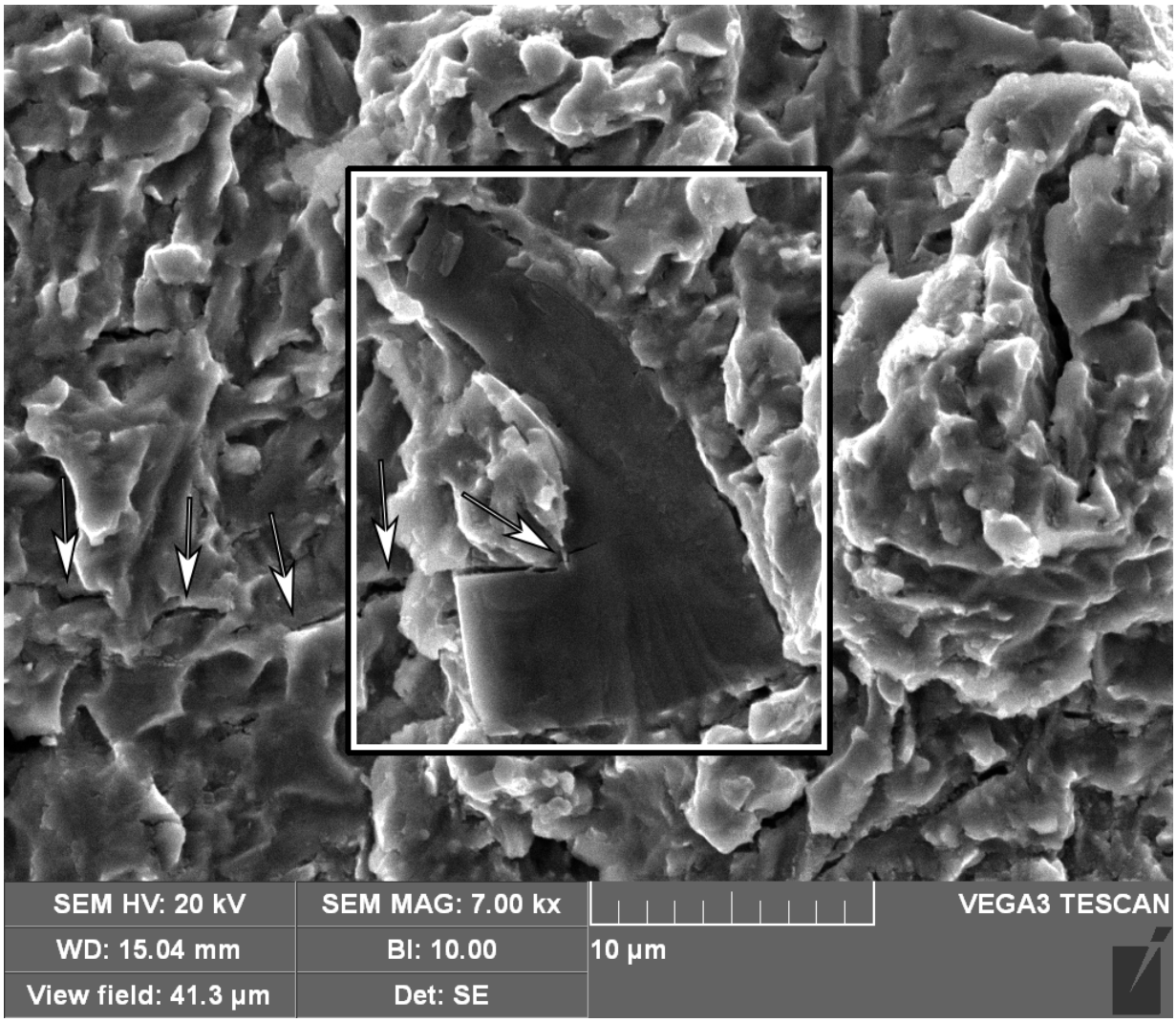

Figure 4.36: Section on sample X70-B showing niobium titanium nitride inclusions at the opened crack side (highlighted). The arrows indicate a potential crack propagation path. The sample was tested at a pH of 2.7, 1 atm H_2S and a testing period of 16 days.

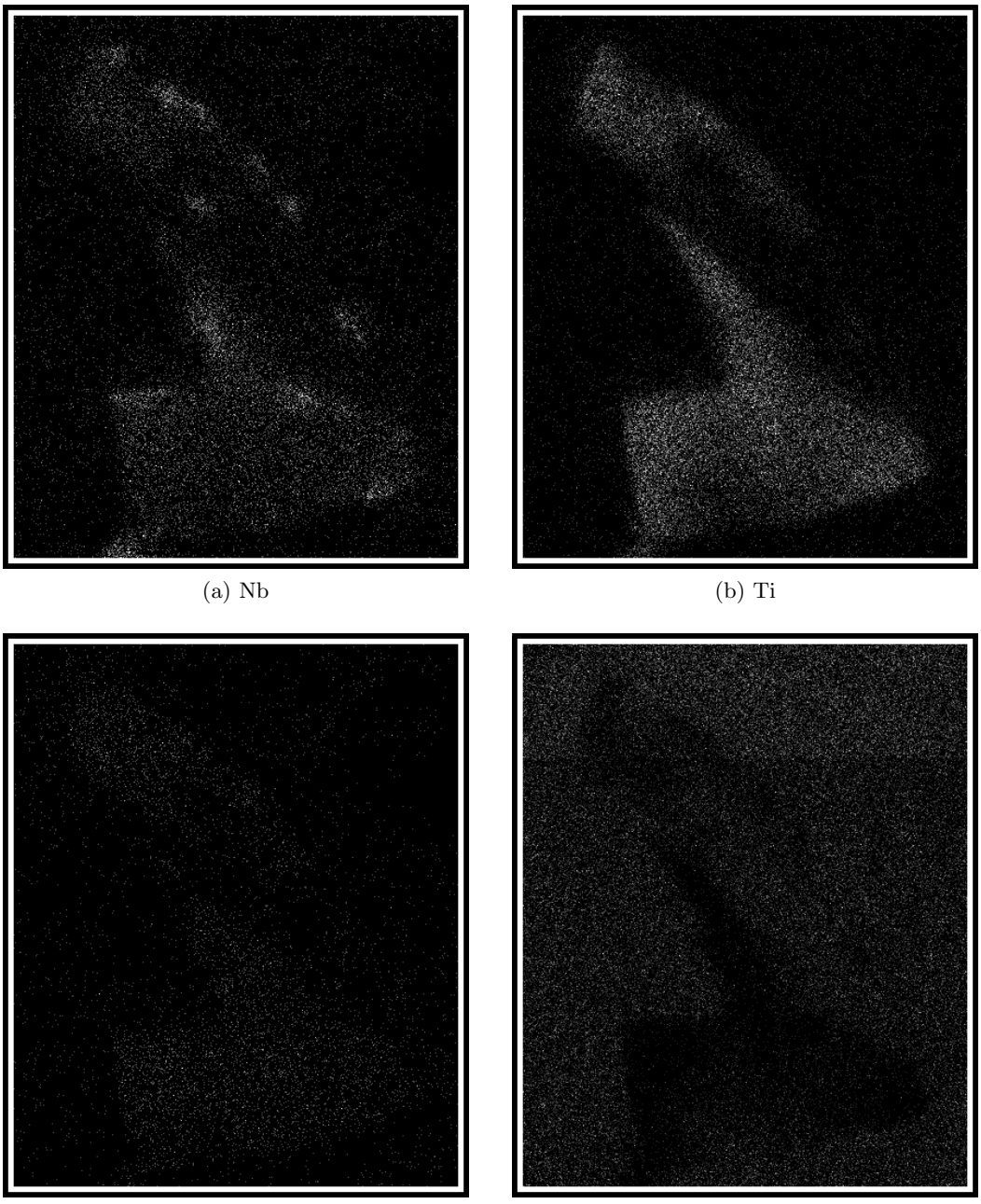

(a) Nb (b) Ti

(c) N (d) Fe

Figure 4.37: EDX scans for niobium (a), titanium (b), nitrogen (c) and iron (d) of area shown in Fig. 4.36.

4.4 Hydrogen Concentration Measurements

Prior to analyzing testing HIC samples in the LECO D603 hydrogen analyzer, a series of untested samples with different weights was measured to determine the base level of hydrogen and the

sensitivity to changes in mass. A plot of the data is shown in Figure 4.38. It can be seen that the average hydrogen concentration of steel X70-X is about 0.87 ppm, whereas the average hydrogen concentration of steel X70-B is about 0.55 ppm. Both samples fluctuate within the 50% error margin of the calibration sample. The effect of sample weight appears to be smaller than the statistical fluctuation of the samples. This can be seen by comparing the hydrogen concentration for light, medium and heavy samples of X70-X. While a 5 g sample of steel X shows a hydrogen concentration of about 1.4 ppm, samples with weights 10 g and 20 g were measured to have about 1 ppm of hydrogen. For steel X70-X, the hydrogen concentration averages to be about 0.87 ppm. Overall, the hydrogen content in steel X70-B is lower than the concentration in steel X70-X.

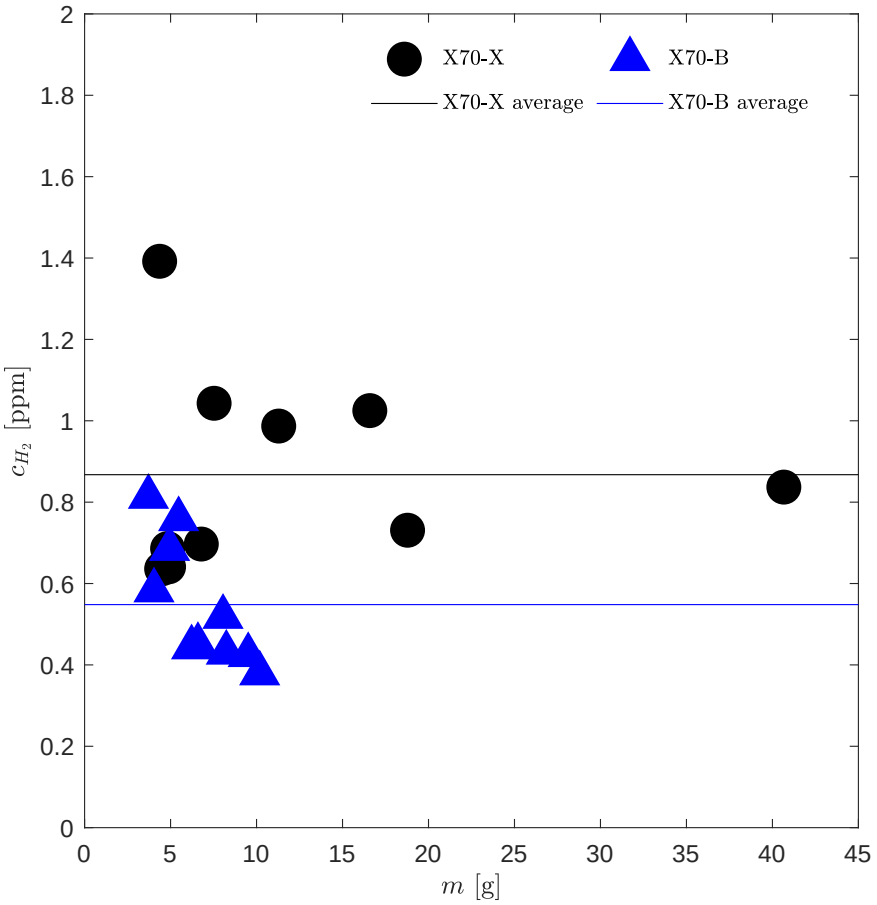

Figure 4.38: Hydrogen content measured using LECO D603 in untested samples for different sample weights

Figures 4.39 and 4.40 show the hydrogen concentrations determined for steels tested under pH 2.7 and 5.5, respectively. It can be seen that both steel X70-X and Steel X70-B show significant fluctuations. As can be seen in the results for a testing time of 1 day, the variation is larger than the

average value of each sample. Furthermore, the concentrations determined after 8 days in NACE solution indicate similar values between steel X70-X and X70-B of the same pH. For a pH of 2.7, a hydrogen concentration of about 2 ppm was determined. The samples tested at pH 5.5 indicate a hydrogen concentration of about 0.5 ppm, which is lower than the base level of steel X70-X.

Overall, the results show significant fluctuations and inconclusive trends and are not reliable. As a result of the data presented in this section, further hydrogen testing was not carried out.

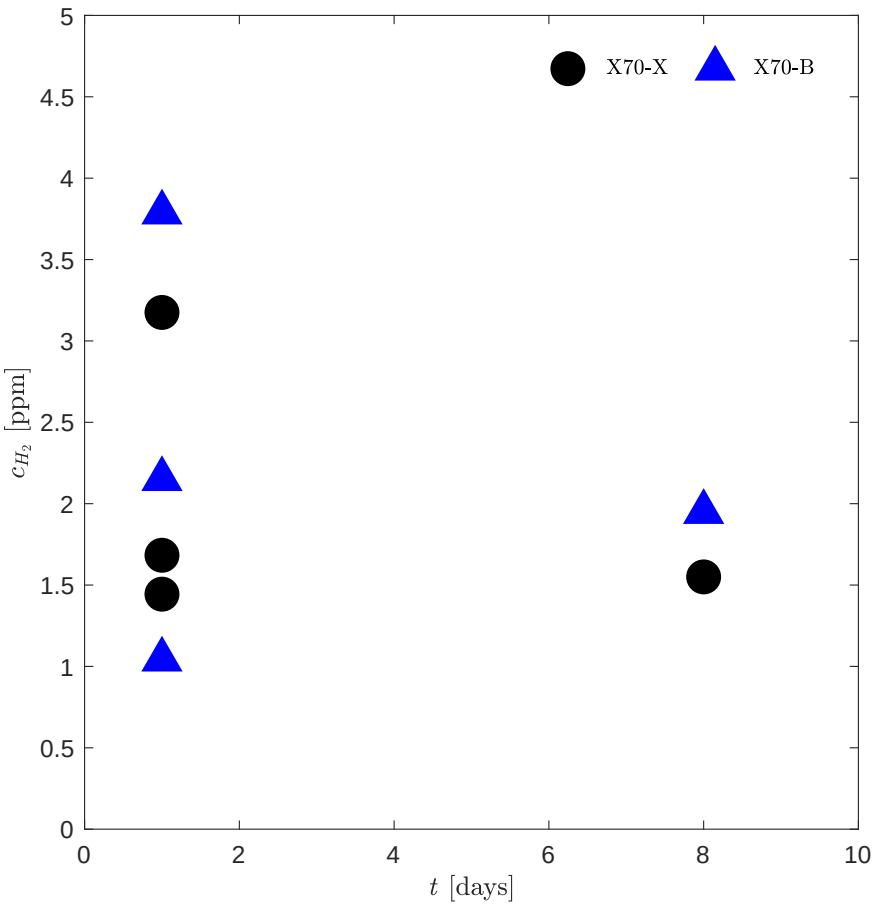

Figure 4.39: Hydrogen content measured using LECO D603 in samples tested at a pH of 2.7.

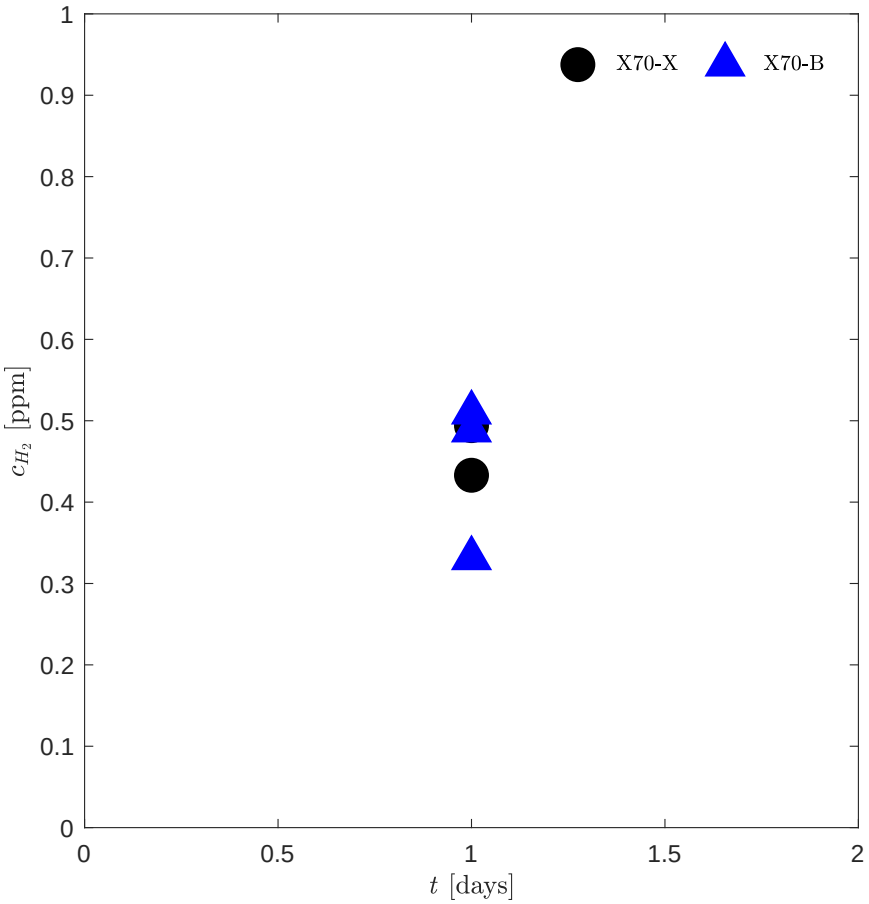

Figure 4.40: Hydrogen content measured using LECO D603 in samples tested at a pH of 5.5.

4.5 Summary

In the following subsections, the most significant results for hydrogen-induced cracking, hydrogen concentration measurements and manganese sulfide inclusions are summed up.

4.5.1 Hydrogen-Induced Cracking

As expected, low pH and high H_2S partial pressure resulted in the most severe cracking. Samples showed crack to backwall ratios of about 20% after one day of testing time. For X70-B, a crack limit appears to be reached after two days. X70-X reached a crack limit after 4 days. Both steels stagnate at a CBR of about 0.4. However, X70-B generally performs slightly worse with respect to the HIC resistance. For a pH of 5.5 and 1 atm H_2S, cracking was observed after 32 days for X70-B and 64 days for X70-X. The 64 day pH 5.5 test is the only test in which X70-B performed better than X70-X. The X70-B remains relatively constant for 32 and 64 days, suggesting a crack limit.

No cracks were observed for testing times of 16 days. This is confirmed by a pH 6.5 and 1 atm H_2S, as well as a pH 4.5 and 0.1 H_2S test.

All samples indicated the initiation of few crack sites and propagation during increased exposure to the test solution. Samples tested at a pH of 5.5 show a crack propagation along the rolling direction. For samples tested at a pH of 2.7, no clear propagation trend can be observed.

Due to the probe diameter of 5mm, a limitation in resolution can be observed. Although general trends of crack propagation are clear, the crack initiation sites can only be determined with an accuracy of 5mm. This also applies to cracks near the surface.

4.5.2 Manganese Sulfide Inclusions

EDX scans of X70-X tested at a pH of 2.7 and 1 atm H_2S confirmed the presence of manganese sulfide inclusions despite the ideal calcium to sulfur ratio of 2.5. Multiple locations showed MnS inclusions with lengths of 100-250 μm. No calcium was detected using this method. This suggests the presence of calcium sulfide inclusions in solution. Some locations enriched in manganese also showed the presence of niobium. This suggests the presence of either niobium sulfide or complex (Mn,Nb)S inclusions, or the precipitation of niobium on manganese inclusions in form of NbC. At higher magnifications, globular (Al,Si)O and cubic (Nb,Ti)N inclusions were found. A crack propagation was observed along a (Nb,Ti)N inclusion.

4.5.3 Hydrogen Concentration Measurements

Measurement of hydrogen content in untested X70-X and X70-B showed baseline hydrogen concentration of about 0.87 ppm for X70-X and about 0.55 ppm for X70-B. Although rated for 5 grams per sample, the LECO D603 showed normal fluctuations for smaller and greater sample sizes. This suggests that the hydrogen analyzer can be used for larger samples by adjusting the heating and measuring cycle. However, measuring of the residual hydrogen content in samples tested at a pH of 2.7 and 1 atm H_2S showed conflicting results. Samples tested for 1 day showed hydrogen concentrations of 1.5-3 ppm (X70-X) and 1-4 ppm (X70-B). After 8 days the concentration for both steels was about 2 ppm, suggesting that the hydrogen content decreases over time. For a pH of 5.5 and 1 atm H_2S, hydrogen concentrations below the baseline level of both steels were detected.

Chapter 5

Discussion

In the following sections, the results of this work are discussed. First, the advantages of the crack to backwall signal ratio with respect to the analysis of hydrogen-induced cracks is examined. This is followed by a discussion of the resistance of X70-X and X70-B to hydrogen-induced cracking with consideration of the effects of pH and time. A brief discussion of the inclusions present in the steels is presented. Lastly, the results obtained from the LECO D603 Hydrogen Analyzer are examined.

5.1 Ultrasonic Testing of Hydrogen-Induced Cracks

The discussion of the ultrasonic methods used in this work is divided into three subsections. First, the ability to detect and locate cracks using a ultrasonic probe is evaluated. This is followed by a examination of the use of crack to area ratios for the quantification of cracking. Lastly, the crack to backwall signal ratio and its capability to measure the extent of crack severity is discussed.

5.1.1 Detection and Location of HIC cracks

The analysis of HIC samples using metallographic techniques can present many challenges. For mild to intermediate cracking (i.e low amount of cracking) or short testing times, the metallographic analysis method can be prone to missing cracks, as the sample is cut every 25 mm (cuts A, B and C) and exclusively analyzed at the cut surfaces. An example of this can be seen in Figure 5.1. In this case, the crack region located between 55 and 70 mm is completely missed by cuts B and C. Depending on the accuracy of the cutting process (cut C), the crack located at 75 mm might be missed as well. As a result of this, only the first cut (A) will result in the detection of cracking. A combination of ultrasonic testing and metallographic analysis would suggest to cut the samples at 10, 40, 60, 80 and 95 mm to obtain information on small and large cracks in the sample. Furthermore, it is likely that the cracks found between 35 and 40 mm, as well as between 75 and 80 mm are crack initiation sites and would pose as good locations for a microstructural analysis.

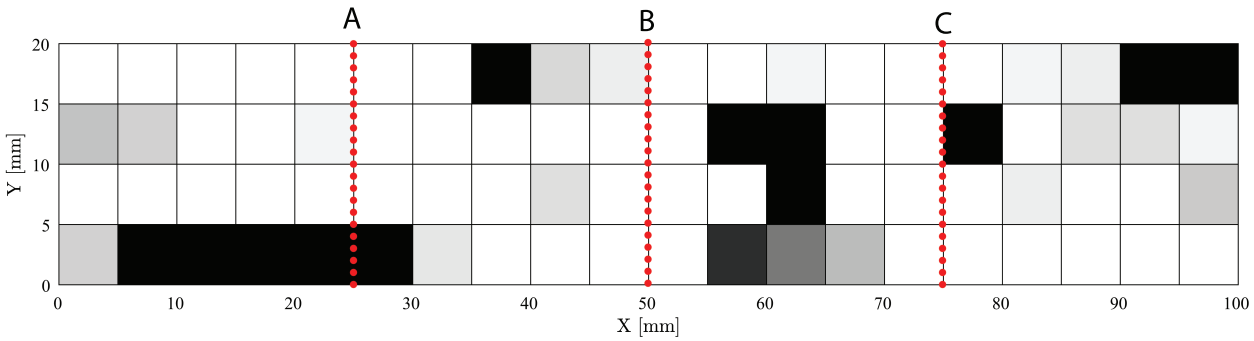

Figure 5.1: CBR map for steel X70-B for pH 2.7, 1 atm H_2S after 1 days with indicated lines for the NACE cutting method (red).

The use of ultrasonic analysis methods resulted in an accurate detection of crack in mild to severe conditions. Most of the cracks observed in this work appear to be in close proximity of the side surfaces of the samples (e.g. Fig. 4.17). For samples tested at a pH of 2.7, a large crack cluster can be observed for a test duration of more than four days. This can be seen in Figure 5.2 between 25 and 60 mm. For this test, a GCBR of about 36% was calculated. Although seemingly propagating along the rolling direction of the steel, no clear trend can be observed due to the severe nature of cracking.

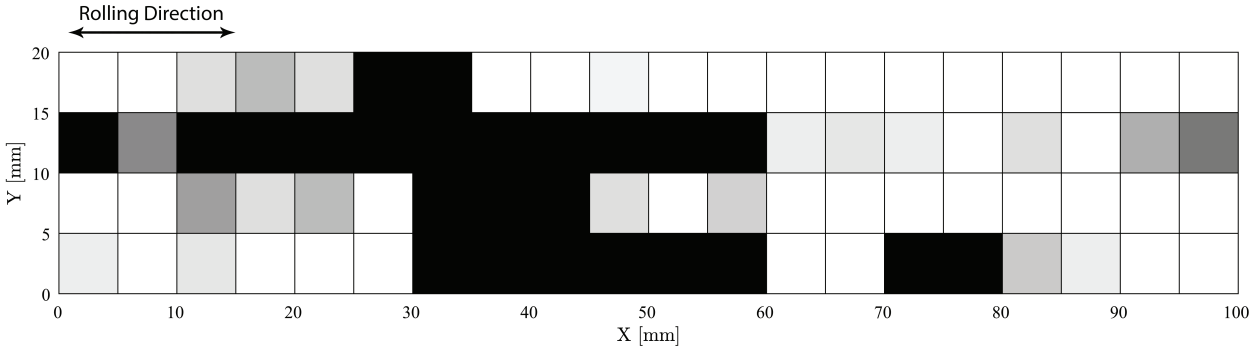

Figure 5.2: CBR map for steel X70-X for pH 2.7 and 1 atm H_2S after 4 days with indicated rolling direction.

Samples tested at a pH of 5.5 indicate a clear crack propagation along the rolling direction. For all cracked samples, multiple crack initiation sites were detected. Both phenomena can be seen in Figure 4.15, 4.19 and 4.17.

Overall, the use of ultrasonic analysis methods is efficient for mild and intermediate conditions, such as high pH levels or low pH levels and short testing times.

5.1.2 Quantification of Cracking using Crack to Area Ratio (CAR)

The calculation of CAR values allows the quantification of cracking on a global scale. Although commonly used in the literature [39], only limited information on the severity, initiation and propagation of cracking can be obtained. As such, CAR values are generally greater than GCBR values, suggesting more severe cracking. Furthermore, the accuracy of CAR methods depends strongly on the resolution, i.e. the sensor size. Smaller sensors would allow a more accurate representation of cracking within the sample.

Due to the binary nature of this method, no separation between crack initiation and propagation is possible. This is especially problematic for severely cracked samples, as the majority of the CAR map cells would be black, indicating severe cracking. As such, the use of CAR is most useful for moderate conditions and minor cracking.

One advantage of the use of crack to area ratios is the determination of regions of high crack severity and, when combined with a metallographic analysis would give more information than the NACE TM0284 analysis method.

5.1.3 Severity, Initiation and Directional Propagation of Cracking using Crack to Backwall Signal Ratio (CBR)

One of the advantages of CBR is the ability to detect the severity of cracking. As a result of this, crack propagation along the rolling direction of the steel can be observed. Additionally, the ability to characterize a crack based on its size allows the determination of potential crack initiation sites. In most cases, severely cracked regions, i.e. regions with a CBR of about one (1), are surrounded by smaller cracks (e.g. fig 4.10), suggesting that cracks propagate from already initiated cracks, rather than the formation of new cracks sites.

The general propagation trend observed in this work appears to be in rolling direction. This can be seen clearly for samples tested at a pH of 5.5 (e.g. fig 4.17). For samples tested at a pH of 2.7 this trend can only be observed for short testing times (e.g. Fig. 4.10). For prolonged testing times, CBR values show an increasing amount of severe cracking, and as such, less information about crack propagation and initiation sites can be obtained for longer testing times.

Overall, for severe sour service conditions, the use of CBR for the quantification of crack initiation and propagation is only meaningful for short test periods. However, the use of GCBR values for the characterization of HIC resistance shows consistent results for one to sixteen days of HIC testing. As GCBR considers the intensity of the crack relative to the scanning area, all values are smaller than their corresponding CAR value. This can be seen in Figure 5.3.

CBR maps seem to indicate that cracks grow exclusively from few initiation sites. Thus, a metallographic analysis could be focused on these initiation sites. In addition, CBR maps indicate that most cracks are located near the surface are likely to penetrate the surface of the sample and release hydrogen back into the test solution, and thus preventing the hydrogen pressure to exceed the critical pressure required to propagate a crack. Using these assumptions and premises, an

evaluation of HIC resistance based on the number and location of crack initiation sites using CBR values could be conducted. This would, for a pH level of 2.7, allow for a reduction in testing time to one day and therefore reduce the cost and use of hydrogen sulfide for the test.

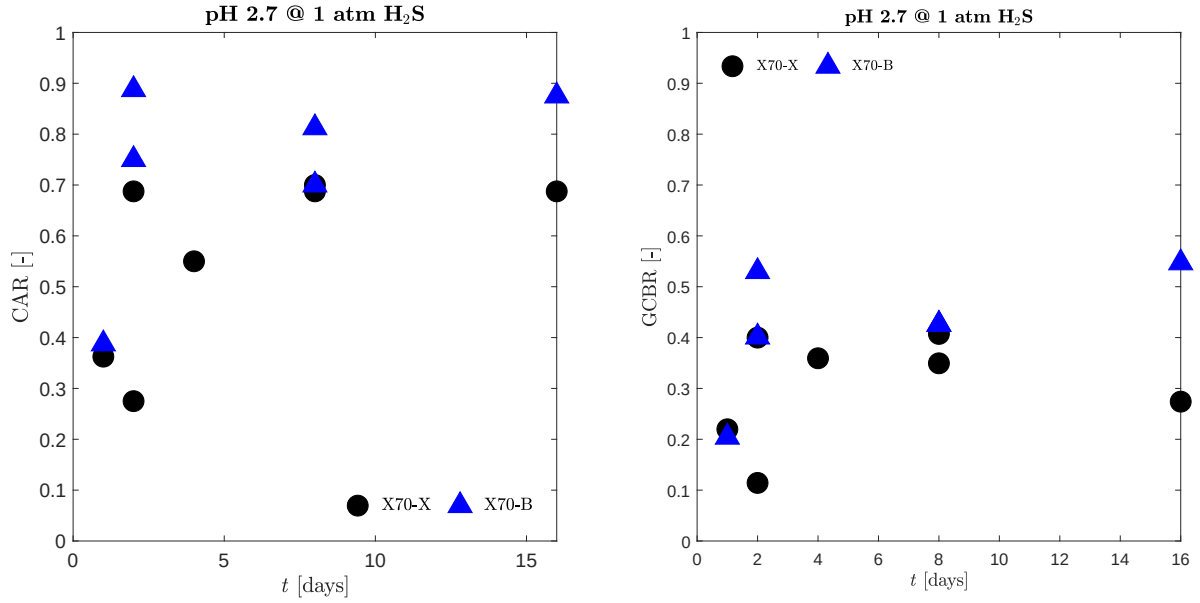

(a) CAR results for samples tested at a pH of 2.7.

(b) GCBR results for samples tested at a pH of 2.7.

Figure 5.3: Results obtained for samples tested at a pH of 2.7, presented in CAR (a) and GCBR(b).

5.2 X70 Resistance to HIC

Two different X70 grade pipeline steels (X70-X and X70-B) have been tested in a NACE TM0284-2016 test solution C. To determine the resistance of these steels to hydrogen-induced cracking a CBR analysis was conducted. The discussion of this analysis is divided into severe and intermediate sour service conditions.

5.2.1 Use of CBR under Severe Sour Service Conditions

Due to the extent of cracking observed under severe sour service conditions, no clear trend with respect to the crack propagation can be observed using CAR. For relatively short testing times, the use of the CBR technique allows insight into the crack propagation and suggests that cracks propagate from few initial crack sites. This can be seen in Figure 5.4. After eight days of testing, three distinct crack sites and a crack cluster containing two to three cracks can be seen. This is consistent with the number of crack sites observed after one day tests (Fig. 4.6 and 4.10).

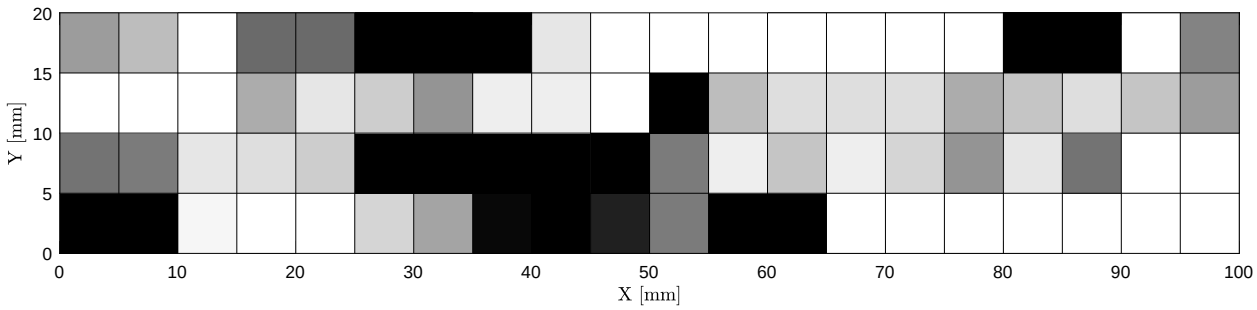

Figure 5.4: CBR map for steel X70-X for pH 2.7 and 1 atm H_2S after 8 days.

Furthermore, the majority of cracks appears to be in close proximity to the side surfaces of the sample (e.g. Fig. 4.8). Using CBR, the crack initiation sites for short testing periods can be identified on the CBR map as locations of localized severe cracking.

Based on the results obtained from the CBR and GCBR values (Fig. 4.13), X70-X possesses a slightly better resistance to hydrogen-induced cracking as the overall GCBR is lower at the suggested crack limit. The corresponding GCBR value for X70-X and X70-B are about 0.4 and about 0.5, respectively.

5.2.2 Use of CBR under Intermediate Sour Service Conditions

Testing carried out at mild and intermediate sour service conditions (i.e. pH levels of 4.5-6.5) showed no cracking for testing times up to and including 16 days. Using CBR, a GCBR of about 20% was calculated for steel X70-B after 32 days. X70-X did not show any cracking under identical conditions. After 64 days, the GCBR values for X70-X and X70-B were calculated to be about 30% and about 20%, respectively. The use of CBR resulted in the detection of two distinct cracks in each steel (e.g. Fig. 4.17). All cracks observed appear to be propagating in rolling direction.

Due to the low severity of the intermediate sour service tests, the results obtained using CBR are meaningful. The low crack intensities allow for a clear distinction between individual cracks and their propagation.

5.2.3 Effect of Steel Chemistry

Overall, X70-X exhibits a better resistance to hydrogen-induced cracking (i.e. a lower GCBR) than X70-B. It is expected that the majority of the sulfur in X70-X should react with the calcium and only little sulfur is available for the formation of manganese sulfide. A greater number of smaller inclusions can be beneficial for the resistance to hydrogen-induced cracking. This can overall delay the formation of cracks as the pressure exerted by the hydrogen on the steel matrix is lower at the individual inclusions. For X70-B, an undesirable calcium to sulfur ratio of less than 0.5 can be observed. This suggests two things. First, more manganese sulfide can be formed due to the lack of calcium. This could result in larger manganese sulfide inclusions, which are more detrimental than smaller ones. Secondly, literature suggests that calcium to sulfur ratios of less than 2 result

in incompletely spherical calcium sulfide inclusions. These inclusions are less stable than those formed at a calcium to sulfide ratio of 2.0 and can break apart during the rolling process. This would create further crack initiation sites.

5.3 Variation of Test Parameters

Testing was carried out for one to 64 days and for pH levels between 2.7 and 5.5. In the following two subsection, the effect of both pH and testing time on hydrogen-induced cracking is discussed.

5.3.1 Effect of pH Level on HIC

Samples tested at a pH of 2.7 showed more severe cracking than those tested at pH levels of 4.5, 5.5 and 6.5. Furthermore, crack initiation occurred earlier at lower pH levels. For a pH of 2.7, cracks were found after one day. Samples tested at a pH of 5.5 did not show any cracking for testing times of 16 days or less. This can also be observed in samples tested at a pH of 4.5 and 6.5.

One of the most significant factors for the creation of hydrogen ions, and therefor the extent of corrosion, is the pH level of the electrolyte. Solving equation for the calculation of the pH level (eq. A.1) with respect to the concentration of hydrogen ions leads to the following equation:

$$\left[\mathrm{H}^+\right] = 10^{-\mathrm{pH}} \tag{5.1}$$

As can be seen in Table 5.1, the hydrogen concentration in the electrolyte changes rapidly. A decrease from a pH of 5.5 to a pH of 4.5 results in an increase of hydrogen concentration by a factor of 10. At a pH of 2.7, the hydrogen concentration in the electrolyte is more than 600 times higher than compared to at a pH of 5.5. Assuming a linear decrease in hydrogen build-up in the HIC sample with respect to pH and testing time, this change in hydrogen concentration would indicate a huge increase in testing time to achieve the same level of cracking in a sample. However, hydrogen-induced cracking depends on more than just the pH level. While the pH level effectively influences the build-up of hydrogen inside the steel on the amount of hydrogen itself, the partial pressure of hydrogen sulfide, and thus the level of hydrogen sulfide poisoning, affects the formation of molecular hydrogen. A decrease in partial pressure of hydrogen sulfide results in a reduced hydrogen sulfide saturation in the electrolyte, which effectively reduced the amount of hydrogen sulfide poisoning and allows the formation of molecular hydrogen in solution to some extent.

Table 5.1: Comparison between the hydrogen concentrations at pH 2.7, 4.5, 5.5 and 6.5

pH	2.7	4.5	5.5	6.5
$\left[\mathbf{H}^+\right]$ **[mole]**	1.995×10^{-3}	3.162×10^{-5}	3.162×10^{-6}	3.162×10^{-7}
Multiple of pH 6.5	6309	100	10	1

Another important aspect for the formation of cracks is the electrochemical stability of iron. Looking at the Pourbaix diagram for the Fe-H_2O-H_2S system (Fig. 2.5 and 5.5), iron in its Fe state is not stable in water at any time. For a pH of up to about 4.5, Fe^{2+} is the desired state of iron in a solution containing a low concentration of oxygen. If the pH level of a solution is greater than 4.5, Fe^{2+} is no longer stable and variants of iron sulfide are formed. During the formation of Fe^{2+}, free electrons are generated. These free electrons are necessary for the hydrogen evolution reaction. A lack in formation of Fe^{2+} would therefore correlate to a limitation in discharge and desorption. Combining this effect with the decreased overall concentration of hydrogen, it becomes clear that pH levels of 4.5 or greater effectively inhibit the formation of molecular hydrogen sulfide.

For a pH of 5.5, cracking was observed after 32 days for X70-B and after 64 days for X70-X. For the 64 day test, X70-X shows a greater crack to backwall ratio than X70-B. This could be explained by the limited amount of test samples, however, another explanation could be the increased copper content in steel X70-B from Heat B2. With a copper content of 0.36 and a pH of 5.5, this steel is capable of forming a copper protective film, as described by Jones [98] and Yamada [97]. This would explain the difference in crack to area ratio between the two steels, as the protective film only forms at pH levels greater than 4.5.

The delayed crack initiation for samples tested in a pH of 5.5 was also observed in the work of Kittel et al. [39]. Their numerical hydrogen concentration profiles for a partial pressure of 100 mbar H_2S indicate a significantly slower slower hydrogen concentration build-up at the centerline for samples tested at a pH of 5.5, compared to samples tested at pH levels of 3.5 and 4.5. On average, more than 40 days in a pH 5.5 solution were necessary to achieve a critical pressure in their steel. For pH levels of 3.5 and 4.5, 7 days or less were sufficient to reach this pressure.

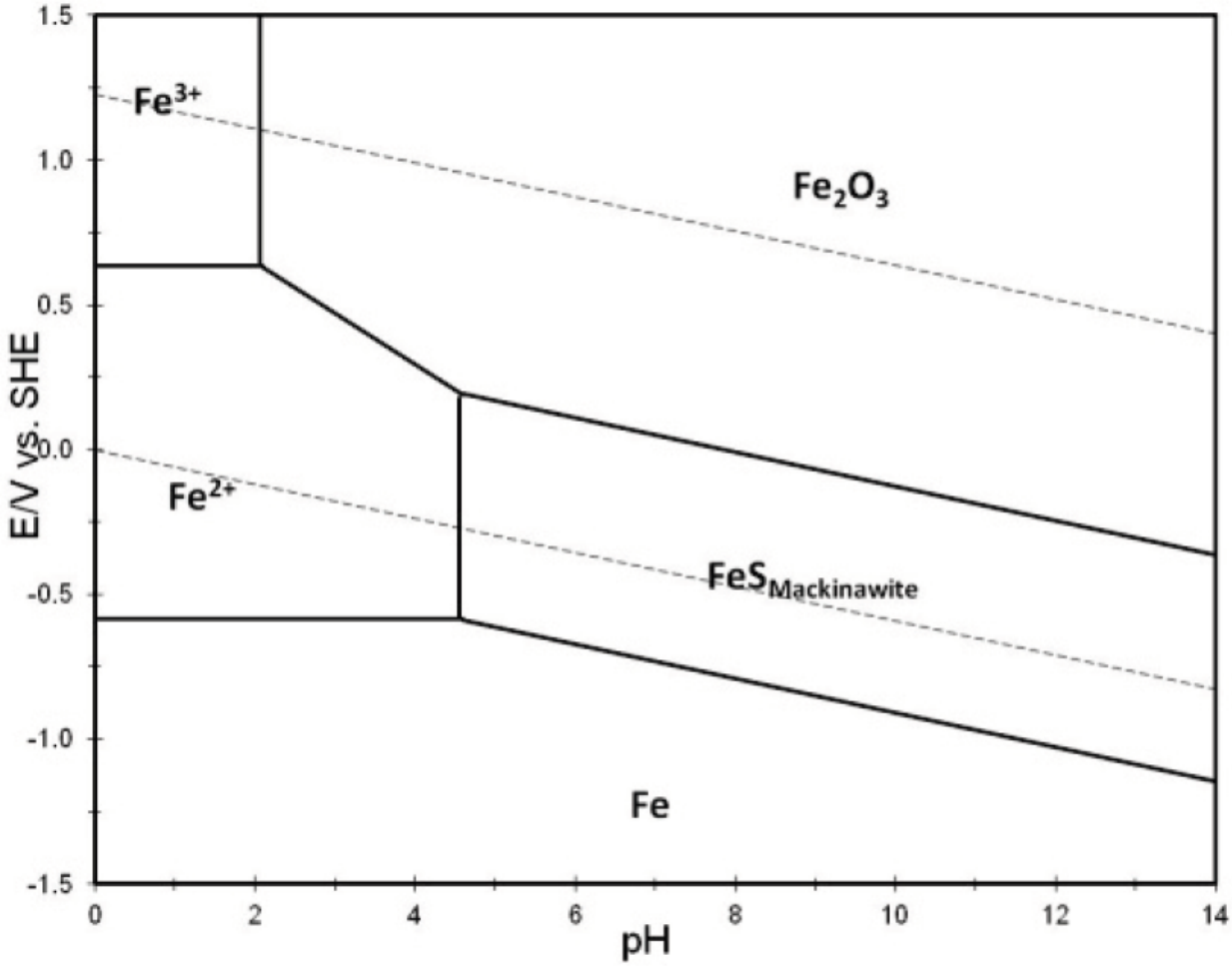

Figure 5.5: Pourbaix diagram for Fe-H_2O-H_2S (mackinawite) system at 25 °C [43]

5.3.2 Effect of Testing Time on HIC

The effect of testing time depends on the pH level. For samples tested at a pH of 2.7, cracking was observed after one day for both X70-X and X70-B. For X70-B, a upper limit in cracking was observed after two days. A similar crack equilibrium was detected after four days for X70-X. This behaviour can be explained by the severity of the test solution. Atomic hydrogen is forced into the steel matrix and form molecular hydrogen at inclusions, grain boundaries or other desirable locations. This localized clustering of hydrogen molecules results in an local increase of pressure, exerted by the hydrogen onto the steel matrix increases locally. As the pressure reaches a critical value, cracking is initiated. The initiation and propagation of these cracks results in the formation of gaps within the steel. As more atomic hydrogen enters the steel, these gaps can act as a reservoir for hydrogen. Due to the larger size of these gaps, compared to inclusions and the ground boundary interfaces, a significantly greater amount of hydrogen is needed for the propagation of the cracks through the gap. Furthermore, it is likely for the cracks to have, to some extent, penetrated the

steel surface. As such, hydrogen can escape through the surface before a critical pressure within the steel is reached. The ultrasonic data obtained from the pH 5.5 samples indicated the initiation of only few crack sites. In order to achieve more cracking, at least one of the following conditions must be fulfilled:

- Greater hydrogen build-up than escape rate.
- Initiation of additional crack sites.
- No formation of surface cracks.
- Availability of a large number of desirable trapping locations.

Overall, greater pH levels require longer testing times for the initiation of cracks. After reaching a crack limit, no visible change in cracking is observed for longer testing periods.

5.4 Inclusions in Steel Samples

During the SEM analysis of fracture surfaces, a variety of inclusions was detected. The most prominent type of inclusions detected were elongated manganese sulfide inclusions with a total length of about 250 μm. This type of inclusion is well known in literature and is commonly linked to the crack initiation and propagation of hydrogen-induced cracks. The relatively large quantities observed in this work indicate an increased likelihood of crack initiation from these inclusions.

At higher magnifications, globular (Al,Si)O inclusions with a length of about 10 μm were detected. Although globular inclusions are generally believed to be less detrimental to the corrosion resistance of steels, it has been found that silicon enriched aluminum oxide inclusions can be linked to crack initiation due to their hardness, brittleness and incoherence with the metal matrix.

Clusters of cubic (Nb,Ti)N inclusions were found. Although research generally associates hydrogen-induced cracking with with the presence of elongated MnS or globular oxide inclusions, such as (Al,Si)O, cracking was observed along (Nb,Ti)N inclusions. However, it is unclear whether the crack initiated or ended at the inclusions.

5.5 Hydrogen Concentration Measurements

The results obtained from the LECO D603 Hydrogen Analyzer showed conflicting information. The base level hydrogen concentration of untested X70-X and X70-B were determined to be 0.87 ppm and 0.55 ppm, respectively. An sensitivity analysis of the effect of the sample weight on the hydrogen content showed mostly statistical fluctuation within the error of the calibration sample. However, results obtained from a one day pH 5.5 test showed hydrogen concentrations below the respective base levels of X70-X and X70-B. Samples tested at a pH of 2.7 show a spread from about 1.5 to 3 ppm for X70-X and about 1 to 4 ppm for X70-B. Although these values are above the

base level of the respective steel, the relatively wide spread of the data points indicates a strong statistical influence.

When comparing the data points obtained from samples tested at pH 2.7 and 5.5, it can be seen that data obtained from pH 5.5 tests show significantly smaller statistical fluctuations. Samples tested at a pH of 5.5 did not show any cracks after one day, and as such are unlikely to have formed surface cracks through which hydrogen could escape. For a pH of 2.7, cracking was observed in all samples. Furthermore, CBR maps indicate the formation of cracks at or near the long sides (X-Z plane) of the samples. All cracks detected by the ultrasonic probe were found in the centerline region. This suggests a strong presence of hydrogen molecules in this region. As cracks are initiated by a critical pressure exerted by hydrogen onto the steel matrix, it is possible for hydrogen to escape through these surface cracks. As a result, local peaks in hydrogen concentration can be expected. When cutting the sample, as part of the analysis process, three general scenarios are possible. In a first scenario, the hydrogen peaks fall into the selected part of the sample and the overall hydrogen concentration would be relatively high. In the second scenario, hydrogen peak concentrations are not present in the selected part of the sample. This would result in a lower overall hydrogen concentration. In the third scenario, a hydrogen reservoir is cut, allowing all mobile hydrogen in this area to escape. Similar to scenario two, the result of the analysis would be a lower hydrogen concentration.

Overall, the LECO D603 Hydrogen Analyzer seems unsuitable for the detection of hydrogen build-up as the analyzer requires the samples to be cut in order to be properly analyzed. Two alternative methods for the measurement of hydrogen build-up are mercury or glycerin displacement and modified hydrogen permeation tests. However, both methods have disadvantages. Mercury is an inherently dangerous and toxic material, and to fully detect all hydrogen, measurements should be done at elevated temperatures. Glycerin is known to absorb hydrogen and other gases and therefore produces a measurement error. Furthermore, large lab to lab variations have been recorded. For hydrogen permeation, specialized samples need to be prepared. The thickness of these samples needs to be significantly thinner than its other dimensions in order to assume one dimensional diffusion. However, the biggest advantage of this method is the ability to measure hydrogen permeation in-situ. More information about these methods can be found in appendix E.

Chapter 6

Conclusions

Conclusions are drawn from the results obtained in this work. In a first section, concluding remarks are presented about the crack to backwall signal ratio developed in this work. This is followed by a summary of the analysis of the HIC tests carried out at different conditions. In a last section, a conclusion of the methodology for the measurement of hydrogen is presented.

6.1 Ultrasonic Quantification of Cracking

Local crack to backwall signal ratios show great potential for the detection of crack initiation points and the propagation of these cracks. An average of all CBR values results in the GCBR. This value can be used to compare different test more accurately. Advantages of this method over the existing crack to area ratio are:

- More information about cracks based on their intensities. This allows the visualization of crack initiation and propagation.
- Cracks are no longer detected in a binary matter. Smaller cracks have less impact on the characterization as opposed to larger cracks.
- Negative effects of low resolution ultrasonic scanning, such as the resulting discretization of crack outlines, can be compensated.

Besides the advantages over the CAR, the GCBR also has several advantages over the standard NACE TM0284 method:

- Greatly improved analysis time. For the GCBR, no cutting, mounting, polishing or etching of the sample is necessary. For the purposes of this work, the analysis time of a single HIC bar, including the cleaning of the sample, the application of the measuring grid, the ultrasonic scanning and the Matlab analysis is about 40 minutes. For the standard NACE TM0248 method, including cutting, cleaning, mounting, polishing and etching the sample, as well as the analysis of the sample using the microscope, can take more than one day, depending on the epoxy used to mount the sample.

- The use of ultrasonic waves allows re-testing of individual samples or test locations.
- Increased amount of analysis locations. Using the GCBR method, a total of 80 locations over the entire length and width of the sample is analyzed. The NACE method relies on three locations, 25 mm apart from another. This increases the statistical significance of GCBR tested samples.
- Areas of interest can be determined prior to cutting the sample. By knowing the locations and intensities of the cracks, an analysis of selected areas is possible.

The use of both CAR and CBR have proven valuable for the detection of cracks in intermediate sour service conditions. As cracking is less extensive compared to severe sour service conditions, crack propagation and, using CBR, initiation can be observed for prolonged test durations. Under severe sour service regions, the use of CAR is not recommended, as the extent of cracking increases rapidly. Crack to backwall signal ratios are useful for relatively short testing times of four to eight days.

6.2 HIC Testing of X70 Steels

The results obtained in this work are as expected and can be summed up as follows:

- Steel X70-X generally shows better resistance to hydrogen-induced cracking than X70-B.
- Test solutions with a pH of 2.7 cause greater cracking after shorter periods of time compared to solutions with a pH of 5.5. For a pH of 2.7, a crack limit seems to be reached after two to four days. Samples tested at a pH of 5.5 did not show any cracking for testing times of 16 days or less. This is confirmed by samples tested at a pH of 6.5, 1 atm H_2S and 16 days, as well as at a pH of 4.5, 0.1 atm H_2S and 16 days.
- Cracking seems to be initiated in few location and propagates from these crack sites. For a pH of 5.5, crack propagation along the rolling direction can be observed in the CBR maps.

Overall, greater pH levels result in greater cracking after shorter periods of time. With increasing testing time, the GCBR ratio increases until a limit in cracking is reached. For X70-X and a pH of 2.7, this limit is reached after four days and stagnates at a value of about 0.35. For X70-B and identical conditions, the equilibrium GCBR is reached after 2 days and is fluctuating around 0.45.

6.3 Hydrogen Concentration Measurements

Based on the results obtained from the LECO D603 Hydrogen Analyzer, the methodology used in this work did not show useful and significant results. Potential reasons for this are as follows:

- Loss of hydrogen from reservoirs due to cutting process.

- Loss of hydrogen through surface cracks.
- Lack of significant amount of hydrogen due to insignificant sample size and distribution of hydrogen within the sample.
- Loss of diffusible hydrogen between end of HIC test and submersion in liquid nitrogen.

A different methodology is required to measure statistical meaningful amounts of hydrogen.

Chapter 7

Future Work

In this section, the potential future work is presented. First, potential improvements to GCBR method are presented. This is followed by possible, additional HIC tests to further study the crack limitations observed in this work. Lastly, suggestions for the measurement of the hydrogen build-up in steel are presented.

7.1 Ultrasonic Quantification of Cracking

The GCBR method developed in this work shows great potential. However, the method can be improved and potentially adapted to in situ HIC testing analysis as follows:

- Improve the crack to backwall signal ratio by considering attenuation correlations for more accurate CBR.
- Modify test set-up for in situ measurement of crack growth in test solution.

7.2 HIC Testing

The results obtained in this work indicate a crack limitation after a certain testing time. Building on these crack limitations, the following research could be carried out.

- Testing of additional samples at moderate conditions.
- Testing of samples with different chemistries (e.g. different Ca/S) and different types of material (e.g. ML80, X100 etc.).
- Test samples at pH intervals of 0.5 to determine crack correlations.
- Conduct research on the cracking equilibrium observed in this work by increasing the test duration of severe sour service tests.
- Explore the cracking behaviour samples re-submerged into the test solution after initial standard HIC test.

- Development HIC severity region diagram, similar to NACE MR0175.

Naturally occurring hydrogen-induced cracking is often influenced by different environmental effects. To fully understand the effects of pH and testing time, as well as the steel chemistry, the following aspects need to be considered as well:

- Effect of temperature.
- Effect of pH gradient.
- Effect of biofilms.
- Mono-directional diffusion through the steel.
- Effect of non-quiescent electrolyte.
- Corrosion resistance under abrasive and erosive conditions.

7.3 Hydrogen Measurements

For a more accurate measurement of the hydrogen build-up in steel, alternative methods are needed. Potential methods for this endeavour are:

- Modified hydrogen permeation tests in NACE TM0284 test solution.
- Mercury displacement method.
- Glycerin displacement method.
- Induction melting.

However, all of the methods listed above have distinctive disadvantages. Ideally, a method for the measurement of hydrogen should fulfill the following criteria:

- Low measuring error.
- Full-sized sample testing.
- Complete detection of both diffusible and non-diffusible hydrogen.
- Low health and environmental risks.
- Low cost in operation.
- Reproducibility of the results.

Bibliography

[1] H. Ritchie and M. Roser, "Global fossil fuel consumption over the long-term," 2017, last opened: 02/14/2018. [Online]. Available: https://ourworldindata.org/fossil-fuels

[2] F. Paredes and W. Mize, "Unusual pipeline failure traced to hydrogen blisters," *Oil and Gas Journal*, vol. 53, no. 33, pp. 99–101, 1954.

[3] M. Elboujdaini, "Hydrogen-induced cracking and sulfide stress cracking," *Uhlig's Corrosion Handbook*, vol. 3, pp. 183–194, 2011.

[4] E. Moore and J. Warga, "Factors influencing the hydrogen cracking sensitivity of pipeline steels," *Mater. Performance; (United States)*, vol. 15, no. 17, 6 1976.

[5] NACE, "NACE TM0284-2003 - evaluation of pipeline and pressure vessel steels for resistance to hydrogen-induced cracking."

[6] ——, "NACE TM0284-2016 - evaluation of pipeline and pressure vessel steels for resistance to hydrogen-induced cracking."

[7] R. Merrick, "Refinery experiences with cracking in wet H_2S environments," *Mater. Performance; (United States)*, vol. 27, no. 1, 1988.

[8] NACE, "MR0175-1999 - standard material requirements, sulfide stress cracking resistant metallic materials for oilfield equipment, nace international," ISBN 1-57590-021-1, Tech. Rep., 1999.

[9] R. Merrick, "Prevention of cracking in wet H_2S environments," *Corrosion*, vol. 269, 1989.

[10] T. McLaury, "API survey - extent of equipment cracking in wet hydrogen sulfide environments," *American Petroleum Institute mid-year refining meeting (Chicago, Il)*, April 1989.

[11] W. Bruckhoff, O. Geier, K. Hofbauer, O. Schmitt, and D. Steinmetz, "Rupture of a sour line pipe due to SOHIC: Failure analysis, experimental results and corrosion prevention," *Corrosion*, no. 389, 1985.

[12] Corrosionpedia, "Tensile stress," 2019, opened: 09/09/2019. [Online]. Available: https://www.corrosionpedia.com/definition/1073/tensile-stress

[13] H. I. McHenry, H. I. McHenry, T. R. Shives, D. T. Read, J. D. McCloskey, C. H. Brady, and P. T. Purtscher, *Examination of a pressure vessel that ruptured at the Chicago Refinery of the Union Oil Company on July 23, 1984*, 1986.

[14] A. Saleh, D. Hejazi, A. Gazder, D. Dunne, and E. Pereloma, "Investigation of the effect of electrolytic hydrogen charging of X70 steel: II. microstructural and crystallographic analyses of the formation of hydrogen induced cracks and blisters," *International Journal of Hydrogen Energy*, vol. 41, no. 28, pp. 12 424 – 12 435, 2016.

[15] Welding Answers, "Factors influencing hydrogen induced cracking," 2018, opened: 07/12/2018. [Online]. Available: http://weldinganswers.com/wp-content/uploads/2016/10/HIC-3-Factors.jpg

[16] R. Marriott, P. Pirzadeh, J. Marrugo-Hernandez, and S. Raval, "Hydrogen sulfide formation in oil and gas," *Canadian Journal of Chemistry*, vol. 94, no. 4, pp. 406–413, 2016.

[17] W. Orr and J. Sinnighe Damste, "Geochemistry of sulfur in fossil fuels," *ACS Symposium Series*, vol. 429, pp. 2–29, 1990.

[18] T. Hyodo, M. Iino, A. Ikeda, M. Kimura, and M. Shimizu, "The hydrogen permeation and hydrogen-induced cracking behaviour of linepipe in dynamic full scale tests," *Corrosion Science*, vol. 27, no. 10, pp. 1077 – 1098, 1987.

[19] M. Mohtadi-Bonab and M. Eskandari, "A focus on different factors affecting hydrogen induced cracking in oil and natural gas pipeline steel," *Engineering Failure Analysis*, vol. 79, pp. 351 – 360, 2017.

[20] M. Y. Matrosov, O. N. Sychev, A. M. Korchagin, and O. P. Talanov, "Corrosion resistant plates for pipes operated in sour environments," in *Production and Further Processing of Flat Products*, ser. Materials Science Forum, vol. 854. Trans Tech Publications, 6 2016, pp. 106–111.

[21] M. Mohtadi-Bonab, J. Szpunar, and S. Razavi-Tousi, "A comparative study of hydrogen induced cracking behavior in API 5L X60 and X70 pipeline steels," *Engineering Failure Analysis*, vol. 33, pp. 163 – 175, 2013.

[22] M. Mohtadi-Bonab, J. Szpunar, L. Collins, and R. Stankievech, "Evaluation of hydrogen induced cracking behavior of API X70 pipeline steel at different heat treatments," *International Journal of Hydrogen Energy*, vol. 39, no. 11, pp. 6076 – 6088, 2014.

[23] F. Huang, X. G. Li, J. Liu, Y. M. Qu, J. Jia, and C. W. Du, "Hydrogen-induced cracking susceptibility and hydrogen trapping efficiency of different microstructure X80 pipeline steel," *Journal of Materials Science*, vol. 46, no. 3, pp. 715–722, Feb 2011.

[24] H.-Y. Liou, R.-I. Shieh, F.-I. Wei, and S.-C. Wang, "Roles of microalloying elements in hydrogen induced cracking resistant property of hsla steels," *Corrosion*, vol. 49, no. 5, pp. 389–398, 1993.

[25] H. Xue and Y. Cheng, "Characterization of inclusions of X80 pipeline steel and its correlation with hydrogen-induced cracking," *Corrosion Science*, vol. 53, no. 4, pp. 1201 – 1208, 2011.

[26] K. O. Findley, M. K. O'Brien, and H. Nako, "Critical assessment 17: Mechanisms of hydrogen induced cracking in pipeline steels," *Materials Science and Technology*, vol. 31, no. 14, pp. 1673–1680, 2015.

[27] S. U. Koh, K. Y. Kim, and B. Y. Boo, "The efect of chromium and molybdenum on the susceptibility to sulfide stress cracking of API X70 grade linepipe steels," *Corrosion*, pp. 262–274, 2004.

[28] G. Herbsleb, R. K. Poepperling, and W. Schwenk, "Occurrence and prevention of hydrogen induced stepwise cracking and stress corrosion cracking of low alloy pipeline steels," *Corrosion*, vol. 37, no. 5, pp. 247–256, 1981.

[29] X. Du, W. Cao, C. Wang, S. Li, J. Zhao, and Y. Sun, "Effect of microstructures and inclusions on hydrogen-induced cracking and blistering of A537 steel," *Materials Science and Engineering: A*, vol. 642, pp. 181–186, 2015.

[30] W. K. Kim, S. U. Koh, B. Y. Yang, and K. Y. Kim, "Effect of environmental and metallurgical factors on hydrogen induced cracking of HSLA steels," *Corrosion Science*, vol. 50, no. 12, pp. 3336 – 3342, 2008.

[31] M. A. Al-Anezi, G. S. Frankel, and A. K. Agrawal, "Susceptibility of conventional pressure vessel steel to hydrogen-induced cracking and stress-oriented hydrogen-induced cracking in hydrogen sulfide-containing diglycolamine solutions," *Corrosion*, vol. 55, no. 11, pp. 1101–1109, 1999.

[32] Y. I. Matrosov, A. A. Kholodnyi, M. Y. Matrosov, E. S. Popov, G. N. Konovalov, and S. V. Sosin, "Effect of accelerated cooling parameters on microstructure and hydrogen cracking resistance of low-alloy pipe steels," *Metallurgist*, vol. 59, no. 1, pp. 60–68, May 2015.

[33] T. Jin, Z. Liu, and Y. Cheng, "Effect of non-metallic inclusions on hydrogen-induced cracking of API 5L X100 steel," *International Journal of Hydrogen Energy*, vol. 35, no. 15, pp. 8014 – 8021, 2010.

[34] K. H. Lynch, A. H. Abdu, M. Schobert, and J. J. Dennis, "Genomic characterization of JG068, a novel virulent podovirus active against burkholderia cenocepacia," *BMC Genomics*, vol. 14, no. 1, p. 574, Aug 2013.

[35] A. J. Haq, K. Muzaka, D. Dunne, A. Calka, and E. Pereloma, "Effect of microstructure and composition on hydrogen permeation in X70 pipeline steels," *International Journal of Hydrogen Energy*, vol. 38, no. 5, pp. 2544 – 2556, 2013.

[36] R. K. Dayal and H. J. Grabke, "Hydrogen induced stress corrosion cracking in low and high strength ferritic steels of different phosphorus content in acid media," *Materials and Corrosion*, vol. 38, no. 8, pp. 409–416, 1987.

[37] X. Shi, W. Yan, W. Wang, Y. Shan, and K. Yang, "Novel Cu-bearing high-strength pipeline steels with excellent resistance to hydrogen-induced cracking," *Materials and Design*, vol. 92, pp. 300 – 305, 2016.

[38] K. Baba, D. Mizuno, K. Yasuda, H. Nakamichi, and N. Ishikawa, "Effect of Cu addition in pipeline steels on prevention of hydrogen permeation in mildly sour environments," *Corrosion*, vol. 72, no. 9, pp. 1107–1115, 2016.

[39] J. Kittel, V. Smanio, M. Fregonese, L. Garnier, and X. Lefebvre, "Hydrogen induced cracking (HIC) testing of low alloy steel in sour environment: Impact of time of exposure on the extent of damage," *Corrosion Science*, vol. 52, no. 4, pp. 1386 – 1392, 2010.

[40] J. Kittel, J. W. Martin, and T. Cassagne, "Hydrogen induced cracking (HIC) - laboratory testing assessment of low alloy steel linepipe," *Corrosion NACE-08110*, 2008.

[41] P. Taylor, "Stereochemistry of iron sulfides: a structural rationale for the crystallization of some metastable phases from aqueous solution," *Am. Mineral.;(United States)*, vol. 65, no. 9, 1980.

[42] J. Smith and J. Miller, "Nature of sulphides and their corrosive effect on ferrous metals: a review," *British Corrosion Journal*, vol. 10, no. 3, pp. 136–143, 1975.

[43] J. Ning, Y. Zheng, D. Young, B. Brown, and S. Nešić, "Thermodynamic study of hydrogen sulfide corrosion of mild steel," *Corrosion*, vol. 70, no. 4, pp. 375–389, 2013.

[44] S. N. Smith, B. N. Brown, and W. N. Sun, "Corrosion at higher H_2S concentrations and moderate temperatures," *Corrosion*, 2011.

[45] W. Sun, "Kinetics of iron carbonate and iron sulfide scale formation in carbon dioxide/hydrogen sulfide corrosion," Ph.D. dissertation, Ohio University, Athens, OH, 2006.

[46] K. Lee, "A mechanistic modeling of CO_2 corrosion of mild steel in the presence of H_2S," Ph.D. dissertation, Ohio University, Athens, OH, 2004.

[47] M. Singer, A. Camacho, B. Brown, and S. Nešić, "Sour top-of-the-line corrosion in the presence of acetic acid," *Corrosion*, vol. 67, no. 8, pp. 085 003–1, 2011.

[48] M. Singer, S. Nesic, J. N. Al-Khamis *et al.*, "Corrosion assessment in karan gas field development," in *Corrosion*. NACE International, 2012.

[49] Chemistry LibreTexts, "Pourbaix diagrams," 2019, opened: 02/05/2019. [Online]. Available: https://chem.libretexts.org/Bookshelves/Inorganic_Chemistry/Book%3A_Inorganic_Chemistry_(Wikibook)/Chapter_04%3A_Redox_Stability_and_Redox_Reactions/4.5%3A_Pourbaix_diagrams

[50] S. Gao, B. Brown, D. Young, and M. Singer, "Formation of iron oxide and iron sulfide at high temperature and their effects on corrosion," *Corrosion Science*, vol. 135, pp. 167–176, 2018.

[51] Y. Zhao, J. Xie, G. Zeng, T. Zhang, D. Xu, and F. Wang, "Pourbaix diagram for HP-13Cr stainless steel in the aggressive oilfield environment characterized by high temperature, high CO_2 partial pressure and high salinity," *Electrochimica Acta*, vol. 293, pp. 116–127, 2019.

[52] K. A. Zarasvand and V. R. Rai, "Microorganisms: induction and inhibition of corrosion in metals," *International Biodeterioration & Biodegradation*, vol. 87, pp. 66–74, 2014.

[53] N. S. I. Geweely, "Evaluation of ozone for preventing fungal influenced corrosion of reinforced concrete bridges over the river nile, egypt," *Biodegradation*, vol. 22, no. 2, pp. 243–252, Apr 2011.

[54] R. Javaherdashti, H. Nikraz, M. Borowitzka, N. Moheimani, and M. Olivia, "On the impact of algae on accelerating the biodeterioration/biocorrosion of reinforced concrete: A mechanistic review," *European Journal of Scientific Research*, vol. 36, no. 3, pp. 394–406, 2009.

[55] R. Thauer, K. Jungermann, and K. Decker, "Energy conservation in chemotrophic anaerobic bacteria," *Bacteriol.*, vol. 41, pp. 100–180, 1977.

[56] J. Szliard and R. Haynes, "Ultrasonic detection of hydrogen embrittlement in steel," in *1978 Ultrasonics Symposium.* IEEE, 1978, pp. 316–319.

[57] Iowa State University - Center for Nondestructive Evaluation, "A-scans and c-scans," 2019, opened: 05/29/2019. [Online]. Available: https://www.cnde.iastate.edu/research/ultrasonic/a-scans-and-c-scans/

[58] R. Revie, V. Sastri, G. Hoey, R. Ramsingh, D. Mak, and M. Shehata, "Hydrogen-induced cracking of linepipe steels part 1—threshold hydrogen concentration and pH," *Corrosion*, vol. 49, no. 1, pp. 17–23, 1993.

[59] S. Krüger, J. Rebello, and P. De Camargo, "Hydrogen damage detection by ultrasonic spectral analysis," *Ndt & E International*, vol. 32, no. 5, pp. 275–281, 1999.

[60] R. M. Nardo, D. Cerniglia, P. Lombardo, S. Pecoraro, and A. Infantino, "Detection, characterization and sizing of hydrogen induced cracking in pressure vessels using phased array ultrasonic data processing," *Procedia Structural Integrity*, vol. 2, pp. 581–588, 2016.

[61] Y.-I. Hwang, H.-J. Kim, S.-J. Song, Z. S. Lim, and S.-W. Yoo, "Improving the ultrasonic imaging of hydrogen-induced cracking using focused ultrasound," *Journal of Mechanical Science and Technology*, vol. 31, no. 8, pp. 3803–3809, 2017.

[62] F. Chemat, "Eco-extraction du végétal," *Procédés Innovants et Solvants Alternatifs*, 2011.

[63] Olympus, "Ultrasonic flaw detection tutorial - 2.3 wave propagation," 2019, opened: 03/19/2019. [Online]. Available: https://www.olympus-ims.com/en/ndt-tutorials/flaw-detection/wave-propagation/

[64] ——, "Ultrasonic flaw detection tutorial - 2.5 wave front dynamics," 2019, opened: 03/19/2019. [Online]. Available: https://www.olympus-ims.com/en/ndt-tutorials/flaw-detection/wave-front/

[65] D. C. Giancoli, *Physik Lehr- und Übungsbuch*, 3rd ed. Slovakia: Pearson, 2010, ch. 35: Die Wellennatur des Lichts; Interferenz, pp. 1160–1184.

[66] Lumen Learning, "Diffraction - huygens' principle," 2019, opened: 04/02/2019. [Online]. Available: https://courses.lumenlearning.com/boundless-physics/chapter/diffraction/

[67] NDT Training Online, "Calculating bream spread," 2019, opened: 03/28/2019. [Online]. Available: http://www.courses.ndttrainingonline.com/wp-content/uploads/2013/06/MT_Math_Practice_Module/story_content/external_files/003_CALCULATING%20BEAM%20SPREAD.pdf

[68] D. C. Giancoli, *Physik Lehr- und Übungsbuch*, 3rd ed. Slovakia: Pearson, 2010, ch. 36: Beugung und Polarisation, pp. 1187–1219.

[69] TWI-Global, "Faq: What factors influence the beam spread of an ultrasonic probe in the far zone?" 2019, opened: 03/28/2019. [Online]. Available: https://www.twi-global.com/technical-knowledge/faqs/faq-what-factors-influence-the-beam-spread-of-an-ultrasonic-probe-in-the-far-zone

[70] K. T. Selvan and R. Janaswamy, "Fraunhofer and fresnel distances : Unified derivation for aperture antennas," *IEEE - Antennas and Propagation Magazine*, vol. 59, no. 4, pp. 12–15, 2017.

[71] J. B. Wiskel and J. Kennedy, K. Vasudev, D. G. Ivey and H. Henein, "Measurement and modelling of through thickness ultrasonic velocity in X70 pipeline steel," in *19th World Conference on Non-Destructive Testing*, 2016, pp. 1–11.

[72] K. J. Buschow, R. W. Cahn, M. C. Flemings, B. Ilschner, E. J. Kramer, and S. Mahajan, *Encyclopedia of materials.* Amsterdam, New York: Elsevier, 2001, vol. 1.

[73] Olympus, "Ultrasonic flaw detection tutorial - 2.2 generating ultrasound (transducers)," 2019, opened: 03/20/2019. [Online]. Available: https://www.olympus-ims.com/en/ndt-tutorials/flaw-detection/generating-ultrasound/

[74] D. C. Giancoli, *Physik Lehr- und Übungsbuch*, 3rd ed. Slovakia: Pearson, 2010, ch. 26: Gleichstromkreise, p. 904.

[75] D. Zhu and T. Oda, "Trap effect of vacancy on hydrogen diffusivity in bcc-Fe," *Journal of Nuclear Materials*, vol. 469, pp. 237–243, 2016.

[76] J. Charles and S. Chan, "Effect of carbon content on hydrogen occlusivity and embrittlement of ferrite–pearlite steels," *Materials Science and Technology*, vol. 2, no. 9, pp. 956–962, 1986.

[77] X.-B. Shi, W. Yan, W. Wang, L.-Y. Zhao, Y.-Y. Shan, and K. Yang, "HIC and SSC behavior of high-strength pipeline steels," *Acta Metallurgica Sinica (English Letters)*, vol. 28, no. 7, pp. 799–808, 2015.

[78] F. Huang, J. Liu, Z. Deng, J. Cheng, Z. Lu, and X. Li, "Effect of microstructure and inclusions on hydrogen induced cracking suceptibility and hydrogen trapping efficiency of X120 pipeline steel," *Material Science and Engineering: A*, vol. 527, pp. 6997–7001, 2010.

[79] S. Ouhiba, "Hydrogen induced cracking and sulfide stress cracking," Master's thesis, University of Alberta, Edmonton, AB, 2017.

[80] L. Gan, F. Huang, X. Zhao, J. Liu and F. Cheng, "Hydrogen trapping and hydrogen induced cracking of welded X100 pipeline steel in H_2S environments," *International Journal of Hydrogen Energy*, vol. 43, pp. 2293–2206, 2018.

[81] C. Dong, X. Li, Z. Liu, and Y. Zhang, "Hydrogen-induced cracking and healing behaviour of x70 steel," *Journal of Alloys and Compounds*, vol. 484, no. 1, pp. 966 – 972, 2009.

[82] J. Li, X. Gao, L. Du and Z. Liu, "Relationship between microstructure and hydrogen induced cracking behaviour in a low alloy pipeline steel," *Journal of Materials Science & Technology*, no. 33, pp. 1504–1512, 2017.

[83] A.V. Latifi, R. Miresmaeili and A. Abdollah-Zadeh, "The mutual effects of hydrogen and microstructure on hardness and impact energy of SMA welds in X65 steel," *Materials Science and Engineering: A*, vol. 679, pp. 87–94, 2017.

[84] B. Beidokhti, A. Dolati and A.H. Koukabi, "Effects of alloying elements and microstructure on the susceptibility of the welded hsla steel to hydrogen-induced cracking and sulfide stress cracking," *Materials Science and Engineering: A*, vol. 507, pp. 167–173, 2009.

[85] G.T. Park, S.U. Koh, H.G. Jung and K.Y. Kim, "Effect of microstructure on the hydrogen trapping efficiency and hydrogen induced cracking of linepipe steel," *Corrosion Science*, vol. 50, no. 7, pp. 1865–1871, 2008.

[86] R.A. Carneiro, R.C. Ratnapuli and V.d.F.C. Lins, "The influence of chemical composition and microstructure of api linepipe steels on hydrogen induced cracking and sulfide stress corrosion cracking," *Materials Science and Engineering: A*, vol. 357, pp. 104–110, 2003.

[87] H. Kerst, "Method for deoxygenation of water," Jul. 14 1981, US Patent 4,278,635.

[88] I. I. Vasilenko, O. Y. Shul'te, and O. I. Radkevich, "Effects of steel composition and production technology on hydrogen-induced cracking sensitivity and hydrogen sulfide corrosion cracking: Survey of foreign research," *Soviet materials science : a transl. of Fiziko-khimicheskaya mekhanika materialov / Academy of Sciences of the Ukrainian SSR*, vol. 26, no. 4, pp. 383–394, Jul 1991.

[89] L. Luyckx, J. R. Bell, A. McLean, and M. Korchynsky, "Sulfide shape control in high strength low alloy steels," *Metallurgical Transactions*, vol. 1, pp. 3341–3350, 1970.

[90] K. Ushijima, Y. Sugitani, S. Yamaguchi, S. Shiode, M. Hashio, and H. Tomono, "The technology of continuous casting for the application of HSLA steels," in *Int. Conf. on HSLA Steels, Technology and Application (Materials Park, OH: ASM International, 1984)*, pp. 403–409.

[91] A. Wilson, "Characterizing inclusion shape control in low-sulfur C-Mn-Nb steels," *HSLA Steels, Technology and Applications*, pp. 419–427, 1983.

[92] R. Hammer and R. W. Simon, "Metallurgical requirements in the production of HSLA steels," *HSLA Steels, Technology and Applications*, pp. 359–376, 1983.

[93] G. Pressouyre, R. Blondeau, and L. Cadiou, "HSLA steels with improved hydrogen sulfide cracking resistance," *Journal of materials for energy systems*, vol. 6, no. 1, pp. 59–65, 1984.

[94] P. Kaushik, A. Brown, B. Guyer, and C. Muller, "Improving sulfide shape control in high-quality heavy plate steel grades at arcelormittal coatesville," *Iron & Steel Technology*, vol. 16, no. 7, pp. 46–62, 2019.

[95] E. T. Turkdogan *et al.*, *Fundamentals of steelmaking.* London, UK: Institute of Materials London, 1996, ch. 9, pp. 285–295.

[96] H. Suito and R. Inoue, "Thermodynamics on control of inclusions composition in ultraclean steels," *ISIJ international*, vol. 36, no. 5, pp. 528–536, 1996.

[97] K. Yamada, Y. Satoh, N. Tanaka, H. Murayama, Z. Chano, and K. Itoh, "Influence of metallurgical factors on HIC of high strength ERW line pipe for sour gas service," in *International Conference on Technology and Applications of HSLA Steels, Philadelphia, Pensylvania*, 1983, pp. 835–842.

[98] C. Jones, P. Rodgerson, and A. Brown, *Mechanism of hydrogen induced cracking in pipeline steels.* British Gas Corporation, Engineering Research Station, 1983.

[99] H. Ohtani, T. Hashimoto, Y. Komizo, J. Murayama, T. Sawamura, K. Bessyo, and T. Kyogoku, "Development of low P cm high grade line pipe for arctic service and sour environment," in *Proceedings of the International Conference on Technology and Applications of HSLA Steels*, 1983, pp. 843–854.

[100] T. Taira, "Development of super tough acicular ferrite steel for line pipe," in *ASM International Conference 3-6 Oct. 1983*, 1983.

[101] B. E. Popov, *Corrosion Engineering - Principles and Solved Problems*, 1st ed. Amsterdam, Oxford, Waltham: Elsevier, 2015, ch. 8: Hydrogen Permeation and Hydrogen-Induced Cracking, pp. 327–364.

[102] D. A. MacInnes and L. Adler, "Hydrogen overvoltage," *Proceedings of the National Academy of Sciences of the United States of America*, vol. 5, no. 5, pp. 160–163, 1919.

[103] J. O. M. Bockris and A. K. N. Reddy, *Modern Electrochemistry.* New York: Plenum Press, 1970.

[104] J. O. M. Bockris and P. K. Subramanyan, "The equivalent pressure of molecular hydrogen in cavities within metals in terms of the overpotential developed during the evolution of hydrogen," *Electrochimica Acta*, vol. 16, no. 12, pp. 2169–2179, 1971.

[105] L. I. Antropov and A. Beknazarov, *Theoretical Electrochemistry.* Moscow: Mir Publishers, 1972.

[106] G. Zheng, B. N. Popov, and R. E. White, "Surface treatment for mitigation of hydrogen absorption and penetration into AISI 4340 steel," *Journal of the Electrochemical Society*, vol. 140, no. 11, pp. 3153–3158, 1993.

[107] A. Kawashima, K. Hashimoto, and S. Shimodaira, "Hydrogen electrode reaction and hydrogen embrittlement of mild steel in hydrogen sulfide solutions," *Corrosion*, vol. 32, no. 8, pp. 321–331, 1976.

[108] C. Carter and M. Hyatt, "Review of stress corrosion cracking in the low-alloy and lowstrength steels," in *International Conference on Stress Corrosion Cracking and Hydrogen Embrittlement of Iron Base Alloys, Preprint-Nr. E-1*, 1973.

[109] L. Shreir, *Corrosion: corrosion control.* George Newnes Limited, 1963.

[110] G. Okamoto, M. Nagayama, and N. Sato, "International committee of electrochemical thermodynamics and kinetics," in *8th Meeting, Madrid*, 1956, p. 445.

[111] D. L. Olson, J. L. Davidson, and B. F. Dixon, "Hydrogen and preheat management in welded high strength steel for defense application. (TTCP workshop and joint seminar). volume II: Joint seminar papers." Colorado School of Mines, Golden, Tech. Rep., 1997.

[112] O. D. Gonzalez, "The measurement of hydrogen permeation in alpha iron - an analysis of the experiments," *Trans Met Soc AIME*, vol. 245, no. 4, pp. 607–612, 1969.

[113] W. Choo and J. Y. Lee, "Thermal analysis of trapped hydrogen in pure iron," *Metallurgical Transactions A*, vol. 13, no. 1, pp. 135–140, 1982.

[114] W. M. Robertson and A. W. Thompson, "Permeation measurements of hydrogen trapping in 1045 steel," *Metallurgical Transactions A*, vol. 11, no. 4, pp. 553–557, 1980.

[115] G. M. Pressouyre and I. M. Bernstein, "A quantitative analysis of hydrogen trapping," *Metallurgical transactions A*, vol. 9, no. 11, pp. 1571–1580, 1978.

[116] G. Pressouyre and I. Bernstein, "A kinetic trapping model for hydrogen-induced cracking," *Acta Metallurgica*, vol. 27, no. 1, pp. 89–100, 1979.

[117] I. M. Bernstein, "The effect of hydrogen on the deformation of iron." Carnegie-Mellon University of Pittsburgh, Pa Metalls Research Lab, Tech. Rep., 1974.

[118] J. L. Lee and J. Y. Lee, "Hydrogen trapping in AISI 4340 steel," *Metal Science*, vol. 17, no. 9, pp. 426–432, 1983.

[119] K. Lee, J.-Y. Lee, and D. Kim, "A study of hydrogen-trapping phenomena in AISI 5160 spring steel," *Materials Science and Engineering*, vol. 67, no. 2, pp. 213–220, 1984.

[120] R. Gibala, "Internal friction in hydrogen-charged iron," *Transactions of the Metallurgical Society of AIME*, vol. 239, pp. 1574–1585, 1967.

[121] I. Welding, "ISO 3690:2012: welding and allied processes—determination of hydrogen content in arc weld metal," *ISO*, 2012.

[122] I. AS/NZS, "AS/NZS 3752:2006: welding and allied processes—determination of hydrogen content in arc weld metal," *AS/NZS*, 2006.

[123] A. W. Society, "AWS A4.3-93 R2016: Standard methods for determination of the diffusible hydrogen content of martensitic, bainitic, and ferritic steel weld metal produced by arc welding," *American Welding Society*, 2006.

[124] J. I. Standards, "JIS 3118: 2007: Method for measurement of amount of hydrogen evolved from steel welds," *Japanese Industrial Standards*, 2007.

[125] D. Nolan and M. Pitrun, "Diffusible hydrogen testing in australia," *Welding in the World*, vol. 48, no. 1-2, pp. 14–20, 2004.

[126] N. Jenkins, P. Hart, and D. Parker, "An evaluation of rapid methods for diffusible weld hydrogen," *Welding Journal-Including Welding Research Supplement*, vol. 76, no. 1, pp. 1s–10s, 1997.

[127] R. D. Smith, G. P. Landis, I. Maroef, D. L. Olson, and T. R. Wildeman, "The determination of hydrogen distribution in high-strength steel weldments part 1: Laser ablation methods," *Welding Journal*, vol. 80, no. 5, pp. 115s–121s, 2001.

[128] R. D. Smith, D. K. Benson, I. Maroef, D. L. Olson, and T. R. Wildeman, "The determination of hydrogen distribution in high-strength steel weldments part 2: opto-electronic diffusible hydrogen sensor," *Welding Journal*, vol. 80, no. 5, pp. 122s–125s, 2001.

[129] S. K. Alber, "A new method to measure the diffusible hydrogen content in steel weldments using a polymer electrolyte-based hydrogen sensor," *Welding Journal-Including Welding Research Supplement*, vol. 76, no. 7, pp. 251s – 255s, 1997.

[130] G. R. Angus, "Hydrogen induced damage in pipeline steels," Master's thesis, Colorado School of Mines, Golden, CO, 2014.

[131] J.-L. Lee and J.-Y. Lee, "The interaction of hydrogen with the interface of Al_2O_3 particles in iron," *Metallurgical Transactions A*, vol. 17, no. 12, pp. 2183–2186, 1986.

[132] C. E. Mortimer and U. Müller, *Chemie*, 10th ed. Würzburg: Thieme, 2010, ch. 19: Säure-Base-Gleichgewichte, pp. 303–329.

[133] L. J. Henderson, "The theory of neutrality regulation in the animal organism," *Am J Physiol*, vol. 21, pp. 427–448, 1908.

[134] K. A. Hasselbalch, "Die Berechnung der Wasserstoffzahl des Blutes auf der freien und gebundenen Kohlensäure desselben, und die Sauerstoffbindung des Blutes als Funktion der Wasserstoffzahl," *Biochem Z*, vol. 78, pp. 112–144, 1916.

[135] C. E. Mortimer and U. Müller, *Chemie*, 10th ed. Würzburg: Thieme, 2010, ch. 4: Stöchiometrie Teil II: Chemische Reaktionsgleichungen, pp. 40–41.

[136] ——, *Chemie*, 10th ed. Würzburg: Thieme, 2010, ch. 15: Reaktionen in wässriger Lösung, pp. 239, 248–249.

[137] ——, *Chemie*, 10th ed. Würzburg: Thieme, 2010, ch. 18: Säuren und Basen, pp. 291–302.

[138] ——, *Chemie*, 10th ed. Würzburg: Thieme, 2010, ch. 32: Organische Chemie Teil II: Funktionelle Gruppen, pp. 564–576.

[139] ——, *Chemie*, 10th ed. Würzburg: Thieme, 2010, ch. 28: Kohlenstoff, Silicium und Bor, pp. 465–466.

[140] ——, *Chemie*, 10th ed. Würzburg: Thieme, 2010, ch. Anhang B: Gleichgewichtskonstanten bei 25°C, p. 689.

[141] P. M. May and D. Batka and G. Hefter and E. Königsberger and D. Rowland, "Goodbye to S2- in aqueous solution," *Chem. Commun.*, vol. 54, pp. 1980–1983, 2018.

[142] C. E. Mortimer and U. Müller, *Chemie*, 10th ed. Würzburg: Thieme, 2010, ch. 3: Stöchiometrie Teil I: Chemische Formeln, p. 27.

[143] ——, *Chemie*, 10th ed. Würzburg: Thieme, 2010, ch. 7: Eigenschaften der Atome und die Ionenbindung, p. 97.

[144] ——, *Chemie*, 10th ed. Würzburg: Thieme, 2010, ch. 22: Elektrochemie, p. 359.

[145] ——, *Chemie*, 10th ed. Würzburg: Thieme, 2010, ch. 29: Metalle, p. 481.

[146] ——, *Chemie*, 10th ed. Würzburg: Thieme, 2010, ch. 23: Wasserstoff, p. 389.

[147] ——, *Chemie*, 10th ed. Würzburg: Thieme, 2010, ch. 24: Halogene, pp. 396–397.

[148] Jean D' Ans and Ellen Lax, *Taschenbuch für Chemiker und Physiker: Band 3: Elemente, anorganische Verbindungen und Materialien, Minerale.* Berlin, Heidelberg, New York: Springer Verlag, 1998.

[149] M. K. Wilkinson, J. W. Cable, E. O. Wollan, and W. C. Koehler, "Neutron diffraction investigations of the magnetic ordering in $FeBr_2$, $CoBr_2$, $FeCl_2$, and $CoCl_2$," *Phys. Rev.*, vol. 113, pp. 497–507, Jan 1959.

[150] B. R. Tarr, H. S. Booth, and A. Dolance, *Anhydrous Iron(III) Chloride (Ferric Chloride).* Wiley-Blackwell, 2007, pp. 191–194.

[151] William M. Haynes, *CRC Handbook of Chemistry and Physics*, 92nd ed. Boca Raton, Fl: CRC Press.

[152] Wikipedia, "Iron(iii) oxide-hydroxide," 2018, opened: 11/30/2018. [Online]. Available: https://en.wikipedia.org/wiki/Iron(III)_oxide-hydroxide

[153] Zanichelli Scienze, "Esperienza - formazione di idrossidi insolubili: idrossidi di ferro," 2011, opened: 11/30/2018. [Online]. Available: http://online.scuola.zanichelli.it/chimicafacile/files/2011/03/Formazione-idrossidi.pdf

[154] O. Muraza and A. Galadima, "Aquathermolysis of heavy oil: A review and perspective on catalyst development," *Fuel*, vol. 157, pp. 219–231, 2015.

[155] L. Dilworth, C. Riley, and D. Stennett, "Chapter 5 - plant constituents: Carbohydrates, oils, resins, balsams, and plant hormones," in *Pharmacognosy*, S. Badal and R. Delgoda, Eds. Boston: Academic Press, 2017, pp. 61 – 80.

[156] D. C. Podgorski, Y. E. Corilo, L. Nyadong, V. V. Lobodin, B. J. Bythell, W. K. Robbins, A. M. McKenna, A. G. Marshall, and R. P. Rodgers, "Heavy petroleum composition. 5. compositional and structural continuum of petroleum revealed," *Energy & Fuels*, vol. 27, no. 3, pp. 1268–1276, 2013.

[157] S. K. Maity, J. Ancheyta, and G. Marroquín, "Catalytic aquathermolysis used for viscosity reduction of heavy crude oils: A review," *Energy & Fuels*, vol. 24, no. 5, pp. 2809–2816, 2010.

[158] *The second international conference on heavy crude and tar sands*, Caracas, Venezuela, 1982.

[159] L. L. Barton and G. D. Fauque, "Chapter 2 biochemistry, physiology and biotechnology of sulfate-reducing bacteria," ser. Advances in Applied Microbiology. Academic Press, 2009, vol. 68, pp. 41 – 98.

[160] E.-D. Schulze and H. A. Mooney, *Functional Groups of Microorganisms*. Berlin, Heidelberg, New York: Springer-Verlag, 1994, ch. 4, pp. 88–90.

[161] G. Muyzer and A. J. M. Stams, "The ecology and biotechnology of sulphate-reducing bacteria," *Nature Reviews Microbiology*, vol. 6, pp. 441–454, 2008.

[162] Y. Shen and R. Buick, "The antiquity of microbial sulfate reduction," *Earth-Science Reviews*, vol. 64, no. 3, pp. 243 – 272, 2004.

[163] A. Amrani, "Organosulfur compounds: Molecular and isotopic evolution from biota to oil and gas," *Annual Review of Earth and Planetary Sciences*, vol. 42, no. 1, pp. 733–768, 2014.

[164] Wikipedia, "Sulfate ion," 2018, opened: 07/11/2018. [Online]. Available: https://en.wikipedia.org/wiki/Sulfate#/media/File:Sulfate-ion-2D-dimensions.png

[165] ——, "Adenosine 5'phosphosulfate," 2018, opened: 07/11/2018. [Online]. Available: https://upload.wikimedia.org/wikipedia/commons/thumb/e/e4/Adenosine_phosphosulfate.svg/1280px-Adenosine_phosphosulfate.svg.png

[166] ——, "Sulfite ion," 2018, opened: 07/11/2018. [Online]. Available: https://en.wikipedia.org/wiki/Sulfite#/media/File:Sulfite-ion-2D-dimensions.png

[167] ——, "Hydrogen sulfide molecule," 2018, opened: 07/11/2018. [Online]. Available: https://upload.wikimedia.org/wikipedia/commons/thumb/c/c6/Hydrogen-sulfide-2D-dimensions.svg/2000px-Hydrogen-sulfide-2D-dimensions.svg.png

[168] R. Worden, P. Smalley, and M. Cross, "The influence of rock fabric and mineralogy on thermochemical sulfate reduction: Khuff formation, abu dhabi," *Journal of Sedimentary Research*, vol. 70, no. 5, p. 1210, 2000.

[169] *Estimation of Sulfur Deposition During the Production of Lean Sour Gas*, Abu Dhabi, UAE, 2007.

[170] H. Lu, P. Greenwood, T. Chen, J. Liu, and P. Peng, "The separate production of H_2S from the thermal reaction of hydrocarbons with magnesium sulfate and sulfur: Implications for thermal sulfate reduction," *Applied Geochemistry*, vol. 27, no. 1, pp. 96 – 105, 2012.

[171] T. P. Goldstein and Z. Aizenshtat, "Thermochemical sulfate reduction a review," *Journal of Thermal Analysis*, vol. 42, no. 1, pp. 241–290, Jul 1994.

[172] T. Zhang, G. S. Ellis, Q. Ma, A. Amrani, and Y. Tang, "Kinetics of uncatalyzed thermochemical sulfate reduction by sulfur-free paraffin," *Geochimica et Cosmochimica Acta*, vol. 96, pp. 1 – 17, 2012.

[173] Y. Kiyosu, "Chemical reduction and sulfur-isotope effects of sulfate by organic matter under hydrothermal conditions," *Chemical Geology*, vol. 30, no. 1, pp. 47 – 56, 1980.

[174] P. Pirzadeh, S. Raval, and R. A. Marriott, "On the fate of hydraulic fracturing fluid additives: Thermochemical sulfate reduction reaction of sodium dodecyl sulfate," *Organic Geochemistry*, vol. 83-84, pp. 94 – 100, 2015.

[175] J. Gary and G. Handwerk, *Petroleoum Refining Technology and Economics (2nd Ed.)*. New York: Marcel Dekker, Inc, 1984.

[176] R. Abedini, M. Koolivand Salooki, and S. Ghasemian, "Modeling and simulation of condensed sulfur in catalytic beds of claus process: rapid estimation," *Chemical Engineering Research Bulletin*, vol. 14, pp. 110–114, 2010.

[177] H. K. Rae, *Selecting Heavy Water Processes*. Washington, DC: American Chemical Society, 1978, vol. 68, ch. 1, pp. 1–26.

[178] B. M. Andreev , "Separation of hydrogen isotops in H_2O-H_2S system," *Separation Science and Technology*, vol. 36, no. 8-9, pp. 1949–1989, 2001.

[179] The Engineering Toolbox, "Speed of sound in common liquids," 2019, opened: 09/09/2019. [Online]. Available: https://www.engineeringtoolbox.com/sound-speed-liquids-d_715.html

[180] Olympus, "Material sound velocities," 2019, opened: 09/09/2019. [Online]. Available: https://www.olympus-ims.com/en/ndt-tutorials/thickness-gage/appendices-velocities/

[181] International Organization for Standardization, "ISO 80000-3:2006 - quantities and units - part 3: Space and time," 2006.

[182] Z. Wang, M. Liu, M. Lu, L. Zhang, J. Sun, Z. Zhang, and X. Tang, "The effect of temperature on the hydrogen permeation of pipeline steel in wet hydrogen sulfide environments," *International Journal of Electrochemical Science*, vol. 13, pp. 915–924, 2018.

Appendix A

Additional Literature Review

A.1 Acid and Base Reactions in NACE TM0284-2016 Solution

One of the most fundamental parameters in the field of electrochemistry is the pH. The pH scale is a logarithmic scale, ranging from 0 to 14, to quantify the acidity or basicity of an aqueous solution, where a pH level of 0 refers to a strong acid, 14 to a strong base and 7 to a neutral solution. Generally, the pH level is a function of the concentration of hydrogen ions in solution [132]:

$$\mathrm{pH} = -\log_{10}\left(\left[\mathrm{H}^+\right]\right) \tag{A.1}$$

where $\left[\mathrm{H}^+\right]$ is the concentration of hydrogen ions. As the hydrogen atom in its protium configuration does not have any neutrons, the H^+ ion is a proton. Protons in aqueous solution, having a very high reactivity, attach themselves to water molecules to form hydronium ions. Therefore, the pH level can be expressed as a function of the hydronium concentration in solution:

$$\mathrm{pH} = -\log_{10}\left(\left[\mathrm{H_3O}^+\right]\right) \tag{A.2}$$

where $\left[\mathrm{H_3O}^+\right]$ refers to the concentration of hydronium ions in solution. Analogously, the pOH can be described as a function of the concentration of hydroxide ions in solution [132]:

$$\mathrm{pOH} = -\log_{10}\left(\left[\mathrm{OH}^-\right]\right) \tag{A.3}$$

where $\left[\mathrm{OH}^-\right]$ is the concentration of hydroxide ions. The pH and pOH of a solution follow the following relation [132]

$$\mathrm{pH} + \mathrm{pOH} = 14\ . \tag{A.4}$$

For weak acids, the Henderson-Hasselbalch equation is commonly used to calculate the pH level [133, 134]:

$$\mathrm{pH} = \mathrm{p}K_a + \log_{10}\left(\frac{\left[\mathrm{A}^-\right]}{\left[\mathrm{HA}\right]}\right) \tag{A.5}$$

where $\left[\mathrm{A}^{-}\right]$ is the molar concentration of the acids conjugate base and [AH] is the molar concentration of the undissociated acid. $\mathrm{p}K_a$ is calculated as follows:

$$\mathrm{p}K_a = -\log_{10}\left([K_a]\right) = -\log_{10}\left(\frac{\left[\mathrm{H}^{+}\right]\left[\mathrm{A}^{-}\right]}{[\mathrm{HA}]}\right) \tag{A.6}$$

where K_a is the acid dissociation coefficient, $\left[\mathrm{H}^{+}\right]$ the hydrogen ion concentration in mole, $\left[\mathrm{A}^{-}\right]$ the concentration of the acids conjugate base in mole and [AH] the molar concentration of the undissociated acid.

The substances involved in the NACE TM0284-2016 solution C have a neutral pH (deionized water) and both acidic and basic pH levels. In the following sections, the dissociation of the individual chemical substances will be shown below.

A.1.1 Acetic Acid

Acetic acid is a monoprotic carboxylic acid and dissociates as follows: [135–138]

$$\mathrm{CH_3COOH}\,(\,aq) \longrightarrow \mathrm{CH_3COO^{-}}\,(\,aq) + \mathrm{H^{+}}\,(\,aq) \tag{A.7}$$

A.1.2 Carbon Dioxide

Carbon dioxide in its gas state is not an acid. However, when in aqueous solution, carbon dioxide and water will form carbonic acid [136, 137, 139]:

$$\mathrm{CO_2}\,(\,aq) + \mathrm{H_2O}\,(\,l) \rightleftharpoons \mathrm{H_2CO_3}\,(\,aq) \tag{A.8}$$

Carbonic acid is a weak, diprotic acid and dissociates according to the following two reactions:

$$\mathrm{H_2CO_3}\,(\,aq) + \mathrm{H_2O}\,(\,l) \rightleftharpoons \mathrm{HCO_3^{-}}\,(\,aq) + \mathrm{H_3O^{+}}\,(\,aq) \tag{A.9}$$

$$\mathrm{HCO_3^{-}}\,(\,aq) + \mathrm{H_2O}\,(\,l) \rightleftharpoons \mathrm{CO_3^{2-}}\,(\,aq) + \mathrm{H_3O^{+}}\,(\,aq) \tag{A.10}$$

A.1.3 Deionized Water

Water is neither a base, nor an acid, but will reach an equilibrium state in which there is an equal number of hydroxide and hydrogen ions [132]:

$$\mathrm{H_2O}\,(\,l) \rightleftharpoons \mathrm{H^{+}}\,(\,aq) + \mathrm{OH^{-}}\,(\,aq) \tag{A.11}$$

A.1.4 Hydrochloric Acid

Hydrochloric acid is a strong, monoprotic acid and dissociates according to the following reaction [135–137]:

$$\mathrm{HCl}\,(\,aq) \longrightarrow \mathrm{H^{+}}\,(\,aq) + \mathrm{Cl^{-}}\,(\,aq) \tag{A.12}$$

A.1.5 Hydrogen Sulfide

In aqueous solution, hydrogen sulfide forms a weak, diprotic acid. The two dissociation reactions are as follows [132, 136, 140]:

$$\mathrm{H_2S}\,(\,aq) \rightleftharpoons \mathrm{HS^-}\,(\,aq) + \mathrm{H^+}\,(\,aq)\mathrm{HS^-}\,(\,aq) \rightleftharpoons \mathrm{S^{2-}}\,(\,aq) + \mathrm{H^-}\,(\,aq) \tag{A.13}$$

According to May et al. [141], the sulfide ion cannot exist in aqueous solution. In a binary solution with water, sulfide will act as a base and revert back to $\mathrm{HS^-}$ and hydroxide:

$$\mathrm{S^{2-}}\,(\,aq) + \mathrm{H_2O}\,(\,l) \rightleftharpoons \mathrm{HS^-}\,(\,aq) + \mathrm{OH^-}\,(\,aq) \tag{A.14}$$

A.1.6 Sodium Acetate

Sodium acetate is a weak basic salt. In aqueous solution, it will form acetic acid and sodium hydroxide [132]:

$$\mathrm{CH_3COONa}\,(\,aq) + \mathrm{H_2O}\,(\,l) \longrightarrow \mathrm{CH_3COOH}\,(\,aq) + \mathrm{NaOH}\,(\,aq) \tag{A.15}$$

A.1.7 Sodium Chloride

Sodium Chloride is the salt created by the reaction of hydrochloric acid and sodium hydroxide. In aqueous solution, it dissociates into sodium and chlorine ions [136, 142–145]:

$$\mathrm{NaCl}\,(\,aq) \rightleftharpoons \mathrm{Na^+}\,(\,aq) + \mathrm{Cl^-}\,(\,aq) \tag{A.16}$$

A.1.8 Sodium Hydroxide

Sodium hydroxide is a strong, monoprotic base. The dissociation is as follows [132, 135, 146, 147]:

$$\mathrm{NaOH}\,(\,aq) \longrightarrow \mathrm{OH^-}\,(\,aq) + \mathrm{Na^+}\,(\,aq) \tag{A.17}$$

A.1.9 Dissociation Coefficients

Table A.1 shows the dissociation coefficients for the acids and bases involved in test solution C, as well as the dissociation coefficient for water (K_w). Both hydrochloric acid and sodium hydroxide are considered to be strong acids and bases, therefore the amount of dissociated $\mathrm{H^+}$ and $\mathrm{OH^-}$ ions, respectively, can be considered to be of the same concentration as the initial substance itself [132]. Sodium acetate forms sodium hydroxide and acetic acid when in aqueous solution. The K_a value is calculated using the following equation:

$$K_a \cdot K_b = K_w \tag{A.18}$$

where K_a is the dissociation coefficient of the acid, K_b the dissociation coefficient of the base and K_w the dissociation coefficient of water. It should be noted, that even though Mortimer [140] indicates the dissociation coefficient of HS^- to be 1×10^{-14}, literature [141] suggests that the resulting S^{2-} ion does not exist in water.

Table A.1: Dissociation Coefficients for Acids and Bases in NACE TM0284-2016 Test Solution C [140]

Substance	K_a [-]	K_b [-]	K_w [-]
CH_3COOH	1.8×10^{-5}	-	-
H_2CO_3	4.2×10^{-7}	-	-
HCO_3^-	4.8×10^{-11}	-	-
H_2O	-	-	1×10^{-14} [132]
HCl	Strong	-	-
H_2S	1.1×10^{-7}	-	-
HS^-	1×10^{-14}	-	-
CH_3COONa	5.56×10^{-10}	1.8×10^{-5}	-
NaOH	-	Strong	-

A.2 pH Level Calculation of NACE TM0284-2016 Solution

As shown in Equation A.1, the pH value is a function of the concentration of hydrogen ions. Assuming that every hydrogen ion will initially be attached to a water molecule, forming hydronium (H_3O^+), Equation A.6 can be modified to relate the dissociation coefficient to product/reactant concentration ratio of each component:

$$K_a = \frac{\left[H^+\right]\left[A^-\right]}{[HA]} \tag{A.19}$$

where H^+ is the hydrogen ion concentration, A^- is the conjugate base concentration and HA is the initial concentration of the acid or base. It is to be expected that the concentration of H^+ and A^- is identical at all times. The summation of the final concentration of the reactant and the concentration of the product, must be equal to the initial acid concentration. Therefore, Equation A.19 can be modified using the variables x and y for the concentrations:

$$K_a = \frac{[x]\,[x]}{[y-x]} \tag{A.20}$$

where x is the product concentration and y is the initial concentration. Equation A.20 can then be brought into quadratic form:

$$x^2 + x \times K_a - y \times K_a = 0 \tag{A.21}$$

Solving and considering logical solutions will yield the following equation:

$$x = \sqrt{K_a \left(y - \frac{K_a}{4} \right)} - \frac{K_a}{2} \tag{A.22}$$

Replacing the variable x with $\left[\mathrm{H}^+\right]_i$ and y with c_i as well as K_a with $K_{a,i}$ leads to the final equation:

$$\left[\mathrm{H}^+\right]_i = \sqrt{K_{a,i} \left(c_i - \frac{K_{a,i}}{4} \right)} - \frac{K_{a,i}}{2} \tag{A.23}$$

which can be used to calculate the hydrogen ion concentration for each substance. For diprotic acids, the final product concentration of the first dissociation can be used to describe the initial reactant concentration of the second dissociation. Therefore, two calculations are needed to describe the pH level.

The calculation of the total hydrogen ion concentration in the solution can then be used to calculate the pH level:

$$\mathrm{pH} = -\log_{10} \left(\sum_{i=1}^{N} \left[\mathrm{H}^+\right]_i \right) \tag{A.24}$$

where i indicates the contributing species.

A.3 Surface Reactions

As an effect of the submersion of a steel sample in an electrolytic solution, such as the NACE TM0284-2016 solution C, reactions between the electrolyte and the metallic surface will occur. Given that the steels used in this work are considered low alloyed steels, only iron (Fe) is considered for these reactions. Furthermore, only simple reactions are assumed. The most critical reaction is the creation of Ferrous Sulfide. Given that the electrolyte contains sodium chloride, as well as hydrochloric acid, the formation of ferric chloride is likely to occur. Depending on the pH level, iron will dissociate into electrons and its Fe^{2+} state:

$$\mathrm{Fe} \longrightarrow \mathrm{Fe}^{2+} + 2\,\mathrm{e}^- \tag{A.25}$$

The reasons for this behaviour will be described in section 2.2.2.

A.3.1 Formation of Ferrous Sulfide from Hydrogen Sulfide

Ferrous Sulfide (FeS) is a black, insoluble solid created during the reaction of iron and hydrogen sulfide:

$$\mathrm{H_2S\,(\,}aq\mathrm{)} + \mathrm{Fe\,(\,}s\mathrm{)} \longrightarrow \mathrm{FeS\,(\,}s\mathrm{)} + \mathrm{H_2\,(\,}g\mathrm{)} \tag{A.26}$$

In the presence of hydrochloric acid, iron sulfide will react to ferric chloride, allowing the reformation of hydrogen sulfide into the electrolyte [148]:

$$\mathrm{FeS\,(\,}s\mathrm{)} + 2\,\mathrm{HCl\,(\,}aq\mathrm{)} \longrightarrow \mathrm{FeCl_2\,(\,}s\mathrm{)} + \mathrm{H_2S\,(\,}aq\mathrm{)}$$

A.3.2 Formation of Ferrous Chloride from Hydrochloric Acid

The presence of hydrochloric acid in the electrolyte can result in the formation of iron (II) chloride. Iron (II) chloride in its anhydrous form is a white, or off-white, soluble and hygroscopic solid. When dissolved in water, the solution will turn pale green. Continuous oxidation will change the colour to a rust brown [149]. The chemical reaction is as follows:

$$\mathrm{Fe\,(\,}s\mathrm{)} + 2\,\mathrm{HCl\,(\,}aq\mathrm{)} \longrightarrow \mathrm{FeCl_2\,(\,}s\mathrm{)} + \mathrm{H_2\,(\,}g\mathrm{)} \tag{A.27}$$

Iron (II) chloride is commonly used for the synthesis of iron (III) chloride [150].

A.3.3 Formation of Ferric Chloride from Hydrochloric Acid

Ferric chloride, or iron(III) chloride is a highly soluble [151], green-black solid that can be formed from iron under the presence of hydrochloric acid. Other than ferrous chloride, ferric chloride is a molecule involving iron in its +3 oxidation state. The reaction, according to the stoichiometric balance, is as follows:

$$2\,\mathrm{Fe\,(\,}s\mathrm{)} + 6\,\mathrm{HCl\,(\,}aq\mathrm{)} \longrightarrow 2\,\mathrm{FeCl_3\,(\,}s\mathrm{)} + 3\,\mathrm{H_2\,(\,}g\mathrm{)} \tag{A.28}$$

A.3.4 Formation of Ferric Hydroxide from Ferric Chloride and Sodium Hydroxide

Ferric hydroxide, or iron(III) oxide-hydroxide, is a dark orange solid formed by the reaction of ferric chloride and sodium hydroxide. It is polymorphic and can occur as α, β, γ or δ iron(III) oxide-hydroxide and is insoluble in water at neutral pH levels [152]. The chemical reaction is as follows [152, 153]:

$$\mathrm{FeCl_3\,(\,}s\mathrm{)} + 3\,\mathrm{NaOH\,(\,}aq\mathrm{)} \longrightarrow \mathrm{Fe(OH)_3\,(\,}s\mathrm{)} + 3\,\mathrm{NaCl\,(\,}aq\mathrm{)} \tag{A.29}$$

A.4 Aquathermolysis

According to Muraza [154], the main components in heavy oils are resins, asphaltenes and their associated derivatives. Resins are usually classified into phenolic and terpenoid resins and are based on carbohydrate structures [155]. Asphaltenes are carbohydrates composed of carbon, hydrogen, nitrogen, sulfur and oxygen [156].

When exposed to temperatures above 300°C, these molecules can decompose [157]. In the presence of hot water and steam, decomposition can take place according to the following reaction [157, 158]:

$$RCH_2CH_2SCH_3 + 2\,H_2O \rightleftharpoons RCH_3 + CO_2 + H_2 + H_2S + CH_4 \tag{A.30}$$

It can be seen that during the decomposition reaction, carbon dioxide, hydrogen sulfide, molecular hydrogen, methane, as well as residual carbohydrates are created. It should be noted, that the decomposition of resins and asphaltenes is not restricted to the presence of water. It has been shown that hydrocarbon components in heavy oils can decompose if the temperature is above 300°C [157]. Hydrogen sulfide will be produced, however, due to the absence of water, the reaction will not be the same and different hydrocarbons will form.

A.5 Microbial Sulfate Reduction

Sulfate-reducing microorganisms are considered to be the oldest type of microbes [159]. These microorganisms are believed to have formed 3.5 billion years ago and have, soon after life began on earth, contributed to the sulfur cycle. In contrast to other microorganisms, sulfate-reducing bacteria, such as *Desulfovibrio vulgaris*, depend on sulfates and elemental sulfur for the anaerobic oxidization of organic substrates [160]. The anaerobic respiration of these microbes uses sulfates (SO_4^{2-}) as the terminal electron acceptor [161]. The reaction can be described as follows:

1. **Activation of sulfate:** Using the protein complex sulfate adenylytransferase (Sat), the sulfate ion (Fig.A.1 (a)) is converted to Adenosine 5'Phosphosulfate (APS) (Fig.A.1 (b)). This first step is essential for the electron acceptance.

2. **Reduction of APS:** The second step of the reaction uses the protein complex Adenosyl phosphosulfate reductase (Apr) to reduce the Adenosine 5'Phosphosulfate (Fig.A.1 (b)) to a sulfite ion (Fig.A.1 (c)). During this step, 2 electrons are accepted.

3. **Reduction of Sulfite:** The third, and final step is the reduction of sulfite (Fig.A.1 (c)) to hydrogen sulfide (Fig.A.1 (d)). This is initiated by the protein complex dissimilatory sulfite reductase. 6 electrons are transferred.

According to Shen [162] and Amrani [163], this reaction usually occurs in shallow or uplifted deep reservoirs. A commonly accepted temperature range for this reaction is $T < 80°C$.

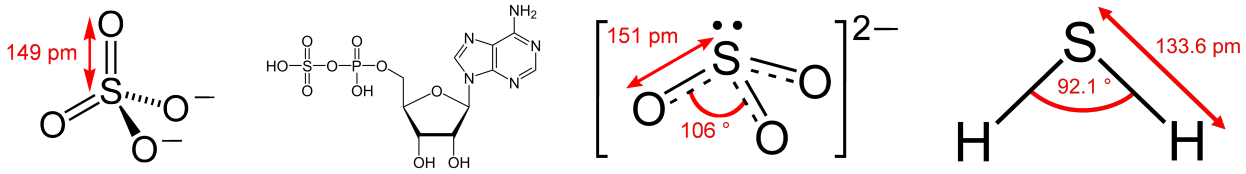

(a) Molecular structure of a sulfate ion (SO_4^{2-}) [164]

(b) Molecular structure of Adenosine 5'Phosphosulfate (APS) [165]

(c) Molecular structure of a sulfite ion (SO_3^{2-}) [166]

(d) Molecular structure of hydrogen sulfide (H_2S) [167]

Figure A.1: Molecules involved in dissimilatory sulfate reduction

A.6 Thermochemical Sulfate Reduction

According to Worden et al. [168], an increase in depth and temperature leads to favourable conditions for thermochemical sulfate reduction. Pivotal for this process is the presence of naturally occurring sulfates, such as $CaSO_4$, initial concentration of hydrogen sulfide and aliphatic hydrocarbon ($C_{x+1}H_{2x+4}$). In a sour reservoir, a simplified overall reaction can occur in the following manner [169]:

$$^3/_4x\,CaSO_4\,(s) + C_{x+1}H_{2x+4} \longrightarrow {}^3/_4x\,H_2S + {}^1/_4x\,CO_2 + {}^1/_4x\,H_2O + {}^3/_4x\,CaCO_3\,(s) + CH_4 \quad \text{(A.31)}$$

According to Lu et al., a very important factor is the temperature [170]. The reaction is thermodynamically favourable at temperatures as low as 20°C. However, the reaction kinetics at this temperature are extremely slow [171]. To study these phenomena, laboratory scale experiments are conducted at temperatures of up to 600°C to compensate for the limiting reaction kinetics [170]. Furthermore, it has been shown that a decrease in pH level can lower the activation energy of the reaction and therefore increase the kinetics [170, 172–174].

A.7 Applications of Hydrogen Sulfide

Hydrogen sulfide is essential for many industrial areas. Examples are in agriculture, in form of fertilizer and pesticides, chemical industries, in form of sulfuric acid, as well as the nuclear industry, where hydrogen sulfide can be used to enrich heavy water. During the production processes, the reaction vessels are exposed to hydrogen sulfide, usually at temperatures above room temperature. In the following section, the Claus process and the Girdler sulfide process are presented to demonstrate the importance of corrosion resistance due to hydrogen sulfide. Followed by this is a description of mechanisms that lead to the natural formation of hydrogen sulfide.

Claus Process

According to Marriott et al. [16], the oil and gas industry started reducing SO_2 emissions as early as the 1940s. By using the Claus process [175,176], SO_2 can be converted to elemental sulfur through H_2S separation using the following reactions:

$$2\ H_2S + 3\ O_2 \xrightarrow{980-1540^{\circ}C} SO_2 + 2\ H_2O \tag{A.32}$$

$$4\ H_2S + 2\ SO_2 \xrightarrow{200-315^{\circ}C} 3\ S_2 + 4\ H_2O \tag{A.33}$$

The production of elemental sulfur is of great significance for the production of sulfuric acid, which is necessary for the production of large quantities of fertilizer [16].

Girdler Sulfide Process

The Girdler sulfide process is a chemical exchange process in which the hydrogen isotope deuterium is concentrated. According to Rae [177], the process is based on two distillation columns operating at different temperatures. One chamber, referred to as the cold tower, is maintained at 30°C, the other chamber, referred to as the hot tower, is maintained at 130°C. Using a difference in equilibrium constants between the two temperatures, the following reaction takes place:

$$H_2O + HDS \rightleftharpoons HDO + H_2S \tag{A.34}$$

where D refers to the deuterium. In the low temperature column, deuterium enriched hydrogen sulfide, from the high temperature column, and freshwater are inserted. Due to a lower equilibrium constant, the deuterium is concentrated as heavy water. The high temperature column operates in a reverted manner. Hydrogen sulfide is enriched in deuterium by exploiting the difference in equilibrium constant.

Using this process, water can be enriched to contain 15%-20% heavy water (D_2O) [178]. Higher concentrations of D_2O can be reached by different processes, such as distillation.

Appendix B

HIC Test Parameters

B.1 Sample Indicators

Tables B.1 and B.2 list all tests done as part of this thesis. The indicator is composed of H_2S composition, pH level and the testing time. Samples of type X70-B show a higher composition of sulfur, compared to sample X70-X. Furthermore, the Ca/S ratio of sample X70-X has a more desirable value than that of sample X70-B. All samples analyzed using ultrasonic methods are standard 100 mm samples.

Table B.1: Experimental plan for experiments (100% H_2S)

Indicator	**Samples**	**pH**	**Time [days]**
100% H_2S			
2.7_BX_1_100	X70-B + X70-X	2.7	1
2.7_BX_2_100#1	X70-B + X70-X	2.7	2
2.7_BX_2_100#2	X70-B + X70-X	2.7	2
2.7_X_4_100	X70-X	2.7	4
2.7_BX_8_100#1	X70-B + X70-X	2.7	8
2.7_BX_8_100#2	X70-B + X70-X	2.7	8
2.7_BX_16_100	X70-B + X70-X	2.7	16
5.5_BX_1_100	X70-B + X70-X	5.5	1
5.5_BX_2_100	X70-B + X70-X	5.5	2
5.5_BX_8_100	X70-B + X70-X	5.5	8
5.5_BX_16_100	X70-B + X70-X	5.5	16
5.5_BX_32_100	X70-B + X70-X	5.5	32
5.5_BX_64_100	X70-B + X70-X	5.5	64
6.5_X_16_100	X70-X	6.5	16

Table B.2: Experimental plan for experiments (10% H_2S)

Indicator	Samples	pH	Time [days]
10% H_2S			
2.7_BX_1_10_N_2	X70-B + X70-X	2.7	1
2.7_BX_8_10_CO_2	X70-B + X70-X	2.7	8
2.7_BX_8_10_N_2	X70-B + X70-X	2.7	8
2.7_BX_16_10_N_2	X70-B + X70-X	2.7	16
4.5_X_16_10	X70-X	4.5	16

B.2 pH and Concentration Data

Tables B.3 and B.4 show the pre, H_2S and final pH levels of the test solution, as well as the initial and final saturation concentration of H_2S in solution. The pre pH was measured before deaeration, the H_2S pH was determined after purging with H_2S for 1h and the final pH was measured after the test was done. For the initial saturation concentration of H_2S in solution, liquid was extracted from the test vessel after 1h of purging H_2S into solution. The liquid was analyzed using iodometric titration. Analogously, the final saturation concentration of H_2S was measured after the test was done.

Table B.3: Saturation Concentrations of hydrogen sulfide in solution (100% H_2S)

Indicator	pre pH	H_2S pH	final pH	initial cH_2S [ppm]	final cH_2S [ppm]
100% H_2S					
2.7_BX_1_100	2.71	2.75	3.64	2829	2658
2.7_BX_2_100#1	2.72	2.90	3.58	2590	2420
2.7_BX_2_100#2	2.71	2.87	3.68	2400	2350
2.7_X_4_100	2.72	2.87	3.65	2500	2469
2.7_BX_8_100#1	2.63	2.70	3.91	2760	2420
2.7_BX_8_100#2	2.72	2.88	3.69	2450	2400
2.7_BX_16_100	2.73	2.89	3.70	2400	2350
5.5_BX_1_100	5.52	5.17	5.28	2761	2692
5.5_BX_4_100	5.47	5.17	5.23	2560	2352
5.5_BX_8_100	5.52	5.18	5.19	2556	2488
5.5_BX_16_100	5.50	5.17	5.85	2560	2345
5.5_BX_32_100	5.50	5.18	5.34	2539	2450
5.5_BX_64_100	5.52	5.23	5.35	2440	2450
6.5_X_16_100	6.52	6.22	5.31	2430	2350

Table B.4: Saturation Concentrations of hydrogen sulfide in solution (10% H_2S)

Indicator	pre pH	H_2S pH	final pH	initial cH_2S [ppm]	final cH_2S [ppm]
10% H_2S					
2.7_BX_1_10_N_2	2.72	2.54	3.53	250	240
2.7_BX_8_10_CO_2	2.70	2.79	3.69	240	235
2.7_BX_8_10_N_2	2.75	2.58	3.67	250	230
2.7_BX_16_10_N_2	2.73	2.56	3.68	250	230
4.5_X_16_10	4.51	4.45	5.08	240	230

B.3 Iodometric Titration

Iodometric titration is a method used to determine the H_2S concentration in the test solution [6]. In a first step, the necessary testing equipment and reagents will be presented. Afterwards, the testing procedure will be explained.

B.3.1 Test Equipment and Reagents

For the iodometric titration volumetric pipettes, volumetric flasks, Erlenmeyer flasks, beakers, burettes and syringes are needed. The following sizes are used [6]:

- 10 mL and 25 mL volumetric pipettes
- 50 mL and 100 mL volumetric flasks
- 250 mL conical (Erlenmeyer) flask
- 100 mL beaker
- 25 mL burette
- 50 mL syringe (graduated to 60 mL)

The chemicals needed for the iodometric titration are iodine solution, sodium thiosulfate, hydrochloric acid and starch solution. All chemicals are certified and of analytical grade. The following list shows the concentrations of the required solutions [6]:

- Standard 0.1 N iodine solution (0.0995 - 0.1005 N, Certified, Analytical Grade)
- Standard 0.1 N sodium thiosulfate solution (0.0995 - 0.1005 N, Certified, Analytical Grade)
- Standard 0.01 N iodine solution (0.0095 - 0.0105 N, Certified, Analytical Grade)
- Standard 0.01 N sodium thiosulfate solution (0.0095 - 0.0105 N, Certified, Analytical Grade)
- Concentrated HCl (approx. 37 wt.% HCl, Analytical Grade)
- Starch solution (approx. 1 wt.%, Analytical Grade)

B.3.2 Procedure

For the iodometric titration, the volumes and molar ratios of iodine to sodium thiosulfate must correspond to the values specified in Table B.5. In a first step, 25 mL of either 0.1 N or 0.01 N iodine solution are transferred into conical cylinder using a pipette. The solution is then acidified using a few drops of hydrochloric acid. If the syringe is chosen for testing, the conical cylinder must be weighted and the result recorded.

Testing procedure using volumetric pipette: Initially, 25-50 mL of test solution is transferred into a clean beaker. The beaker is then rinsed with the test solution and discarded, to avoid contamination. The volumetric flask is then used to transfer a sufficient amount of testing solution (Tbl. B.5) into the beaker. The test solution is then transferred into the the acidified iodine solution. The volume of test solution must be recorded.

Testing procedure using volumetric flask: Analogously to using the volumetric pipette, the flask is initially filled with 25-50 mL of test solution, rinsed and emptied to avoid contamination. Afterwards a sufficient amount of test solution (Tbl. B.5) is transferred into the flask and poured into the acidified iodine solution. The volume added to the acidified iodine solution must be recorded.

Testing procedure using volumetric syringe: The syringe is initially filled with 25-50 mL of test solution and then rinsed to avoid contamination. Afterwards, a sufficient amount of test solution (Tbl. B.5) is taken from the test vessel using the syringe and immediately transferred into the acidified iodine solution. The conical flask is the re-weighted and the result recorded. It is important to determine the exact volume of test solution transferred into the acidified iodine solution.

Either 0.1 N or 0.01 N sodium thiosulfate solution is titrated into test solution until colour changes from dark yellow or tan to pale yellow. After the desired colour of the test solution has been achieved, a few drops of starch solution are added to the test solution. It is crucial for the test method to add the starch to the solution when the colour starts to fade, i.e. when the iodine has mostly been removed from the test solution. This is important as the starch solution will otherwise form insoluble, blue iodine complexes which will prevent the iodine from reacting.

After the starch solution has been added to the test solution, sodium thiosulfate is slowly titrated into the test solution until the solution changes its colour from dark blue to milky yellow. The milky yellow colour comes from colloidal sulfur which created during the titration. It is crucial to record the total volume of sodium thiosulfate used during titration. The amount of hydrogen sulfide in the initial solution can then be calculated using the following equation:

$$c_{\mathrm{H_2S}} = \frac{(\mathrm{A} - \mathrm{B})}{\mathrm{C}} \times 17,040 \tag{B.1}$$

where A is the normality of the iodine solution, B the normality of the sodium thiosulfate solution and C the volume of the test solution. The factor of 17040 originates from the following relation:

$$17040 = \frac{34.08 \text{ g/mole } \mathrm{H_2S} \times 1000 \text{ mg/g}}{2 \text{ equivalents/mole } \mathrm{H_2S}} \tag{B.2}$$

Table B.5: Parameters for the iodometric titration to determine the H_2S concentration in the NACE TM0284-2016 Test Solution [6]

pH_2S [bar]	**xH_2S** [mole-%]	**cH_2S** [mg/L]	**Sample Vol.** [mL]	**$I/Na_2S_2O_3$ Conc.** [N]
$0.40 - 1.00$	$40 - 100$	$920 - 2300$	10	0.1
$0.16 - 0.40$	$16 - 40$	$370 - 920$	25	0.1
$0.08 - 0.20$	$8.0 - 20$	$185 - 460$	50	0.1
$0.04 - 0.10$	$4.0 - 10$	$92 - 230$	100	0.1
$0.016 - 0.04$	$1.6 - 4.0$	$37 - 92$	25	0.01
$0.008 - 0.02$	$0.8 - 2.0$	$18 - 46$	50	0.01
< 0.01	< 1.0	< 23	100	0.01

Appendix C

Ultrasonic Evaluation of Cracks

C.1 CAR Maps

C.1.1 pH 2.7 and 1 atm H_2S

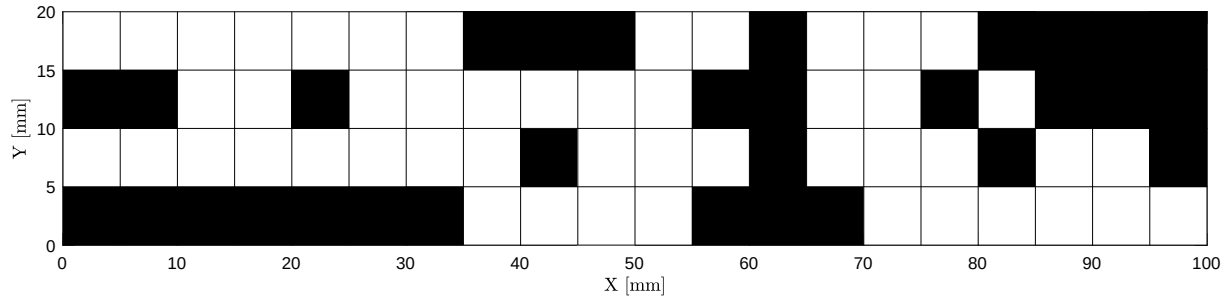

Figure C.1: CAR map for steel X70-B for pH 2.7 and 1 atm H_2S after 1 day.

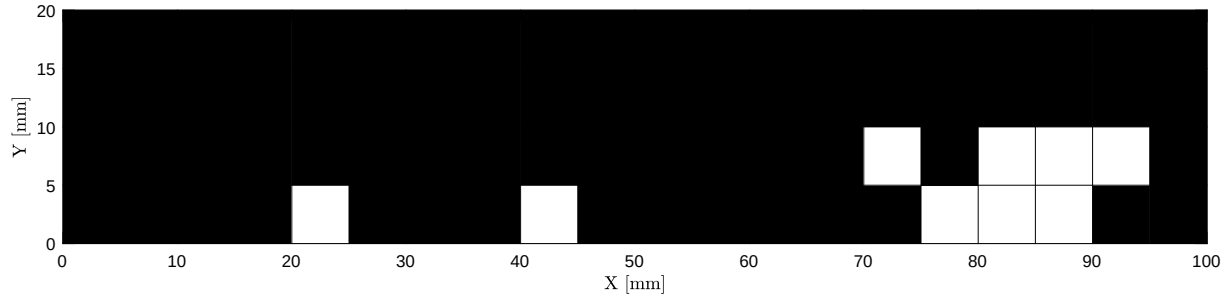

Figure C.2: CAR map for steel X70-B for pH 2.7 and 1 atm H_2S after 2 days.

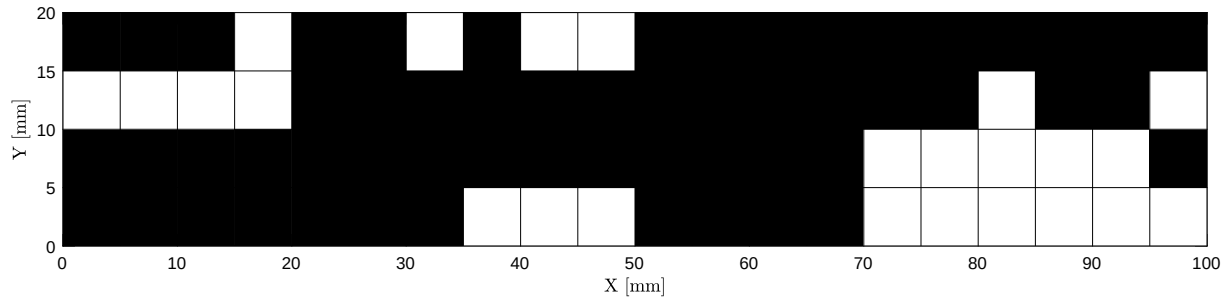

Figure C.3: CAR map for steel X70-B for pH 2.7 and 1 atm H_2S after 8 days.

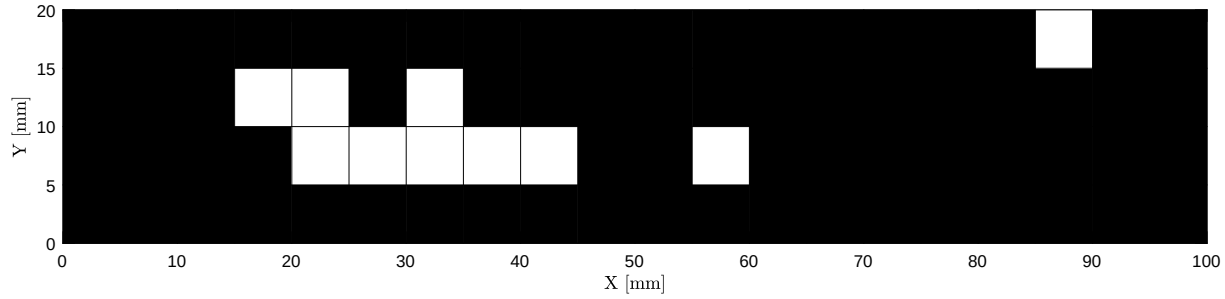

Figure C.4: CAR map for steel X70-B for pH 2.7 and 1 atm H_2S after 16 days.

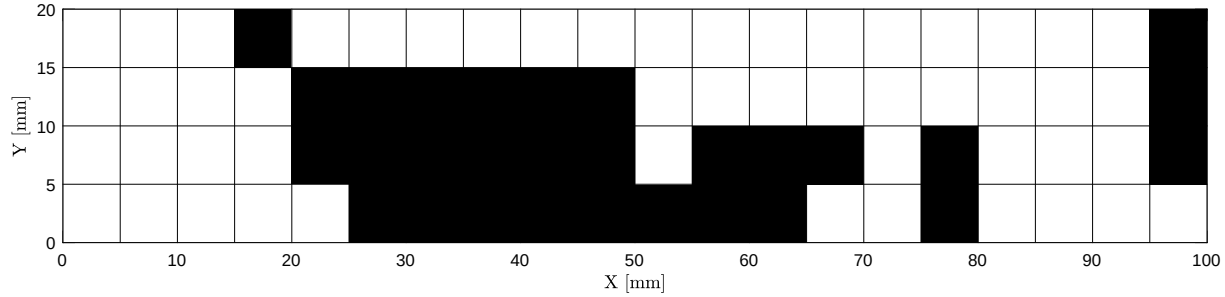

Figure C.5: CAR map for steel X70-X for pH 2.7 and 1 atm H_2S after 1 day.

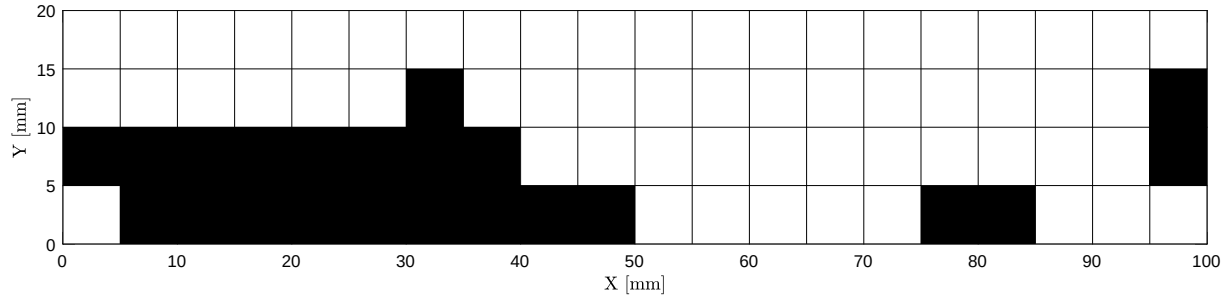

Figure C.6: CAR map for steel X70-X for pH 2.7 and 1 atm H_2S after 2 days.

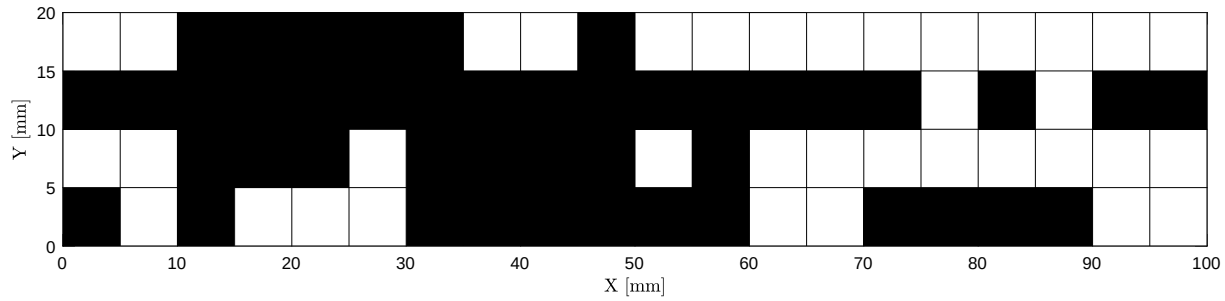

Figure C.7: CAR map for steel X70-X for pH 2.7 and 1 atm H_2S after 4 days.

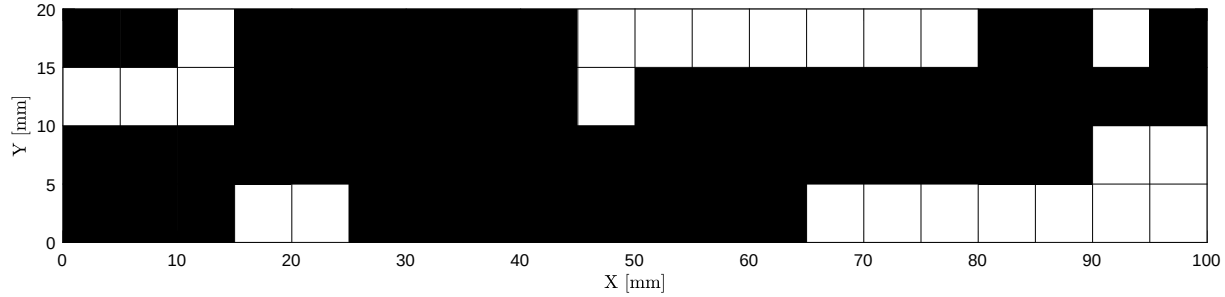

Figure C.8: CAR map for steel X70-X for pH 2.7 and 1 atm H_2S after 8 days.

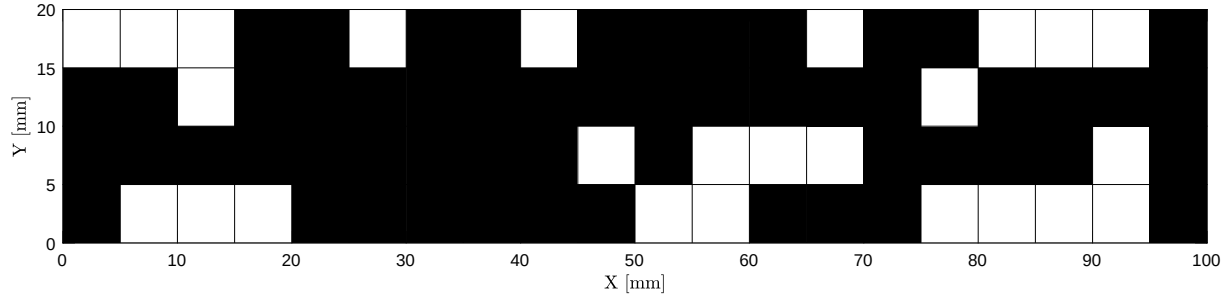

Figure C.9: CAR map for steel X70-X for pH 2.7 and 1 atm H_2S after 16 days.

C.1.2 pH 2.7 and 0.1 atm H_2S

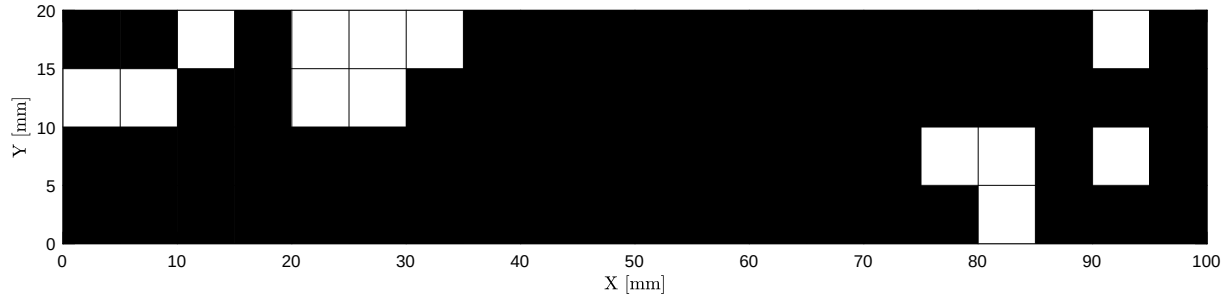

Figure C.10: CAR map for steel X70-B for pH 2.7, 1 atm H_2S and 0.9 atm N_2 after 8 days.

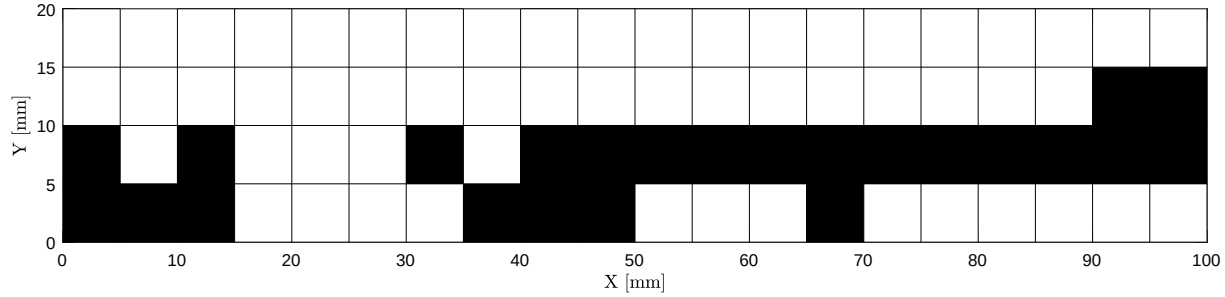

Figure C.11: CAR map for steel X70-B for pH 2.7, 1 atm H_2S and 0.9 atm CO_2 after 8 days.

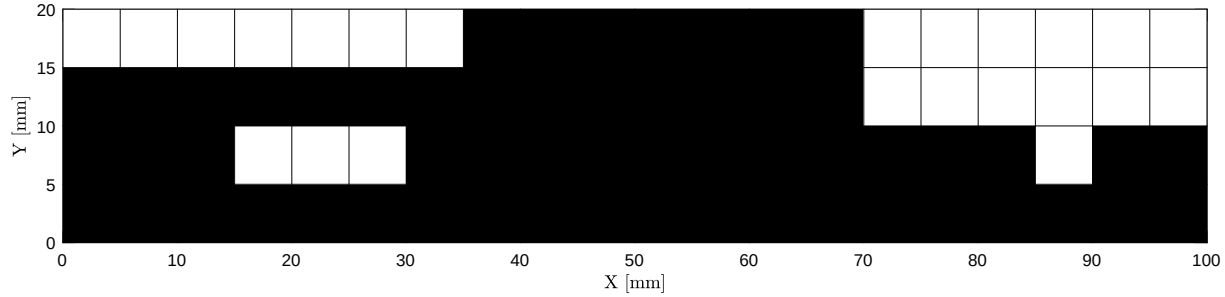

Figure C.12: CAR map for steel X70-B for pH 2.7, 1 atm H_2S and 0.9 atm N_2 after 8 days.

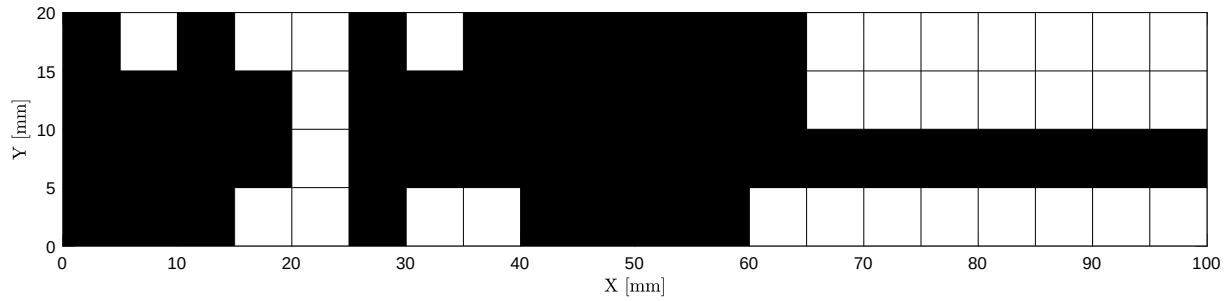

Figure C.13: CAR map for steel X70-B for pH 2.7, 1 atm H_2S and 0.9 atm N_2 after 16 days.

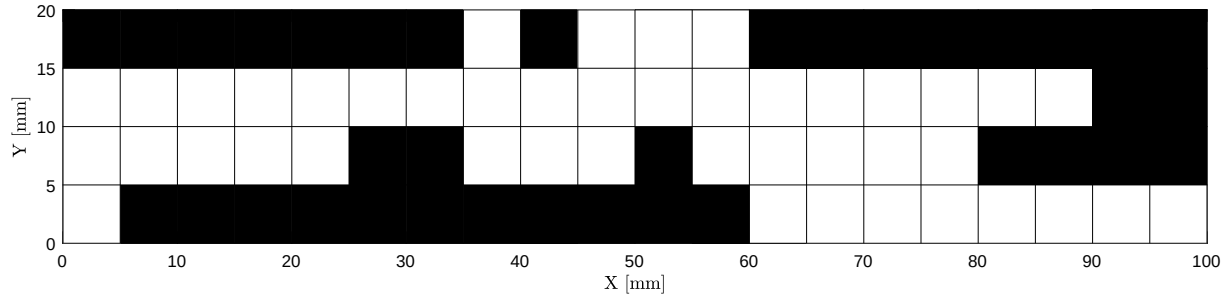

Figure C.14: CAR map for steel X70-X for pH 2.7, 1 atm H_2S and 0.9 atm N_2 after 8 days.

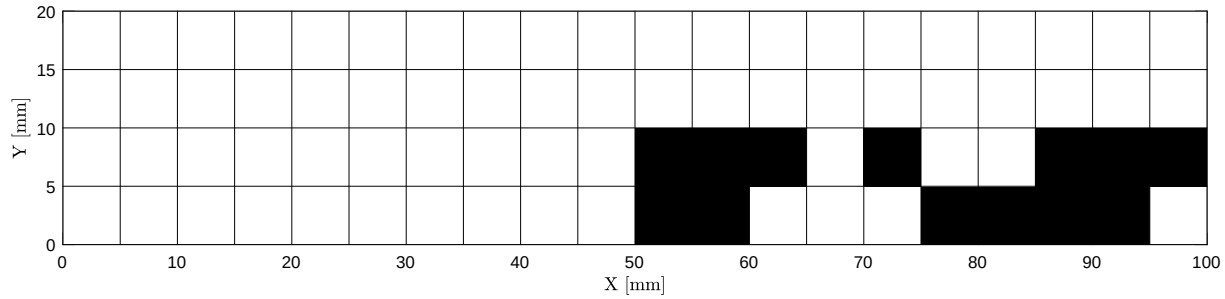

Figure C.15: CAR map for steel X70-X for pH 2.7, 1 atm H_2S and 0.9 atm CO_2 after 8 days.

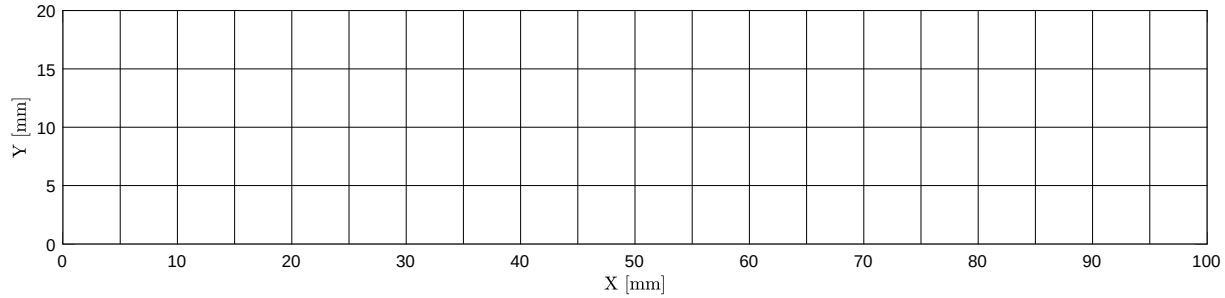

Figure C.16: CAR map for steel X70-X for pH 2.7, 1 atm H_2S and 0.9 atm N_2 after 8 days.

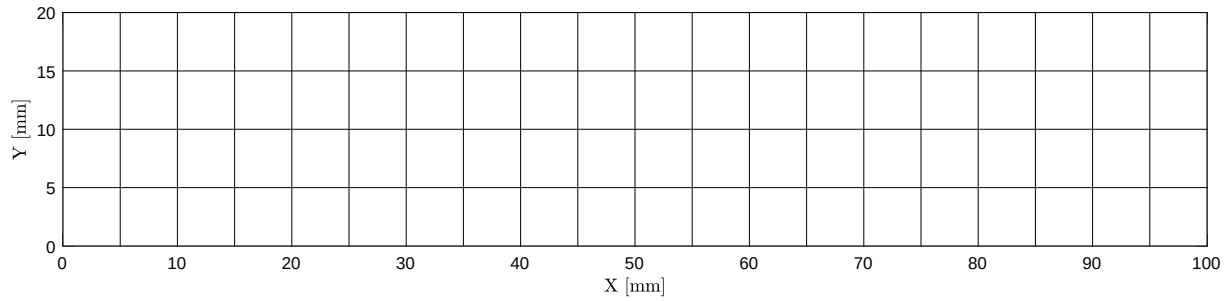

Figure C.17: CAR map for steel X70-X for pH 2.7, 1 atm H_2S and 0.9 atm N_2 after 16 days.

C.1.3 pH 4.5 and 0.1 atm H_2S

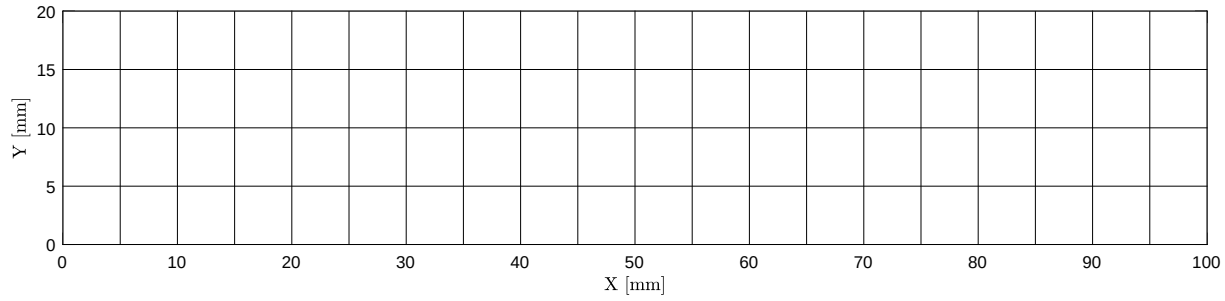

Figure C.18: CAR map for steel X70-X for pH 4.5, 0.1 atm H_2S and 0.9 atm CO_2 after 16 days.

C.1.4 pH 5.5 and 1 atm H_2S

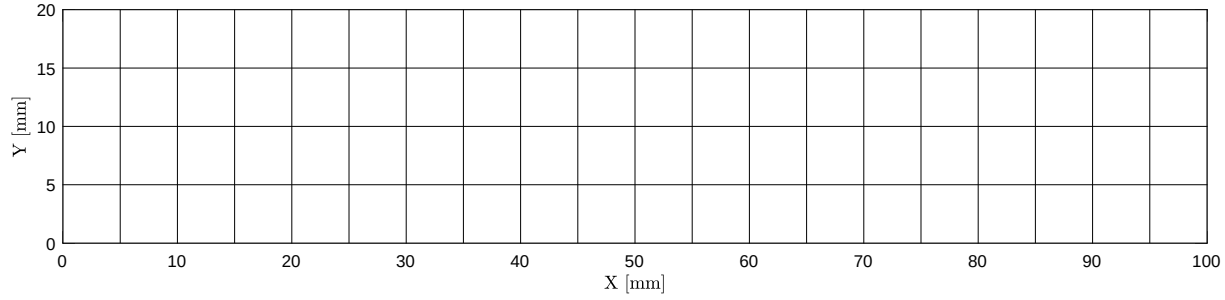

Figure C.19: CAR map for steel X70-B for pH 5.5 and 1 atm H_2S after 1 day.

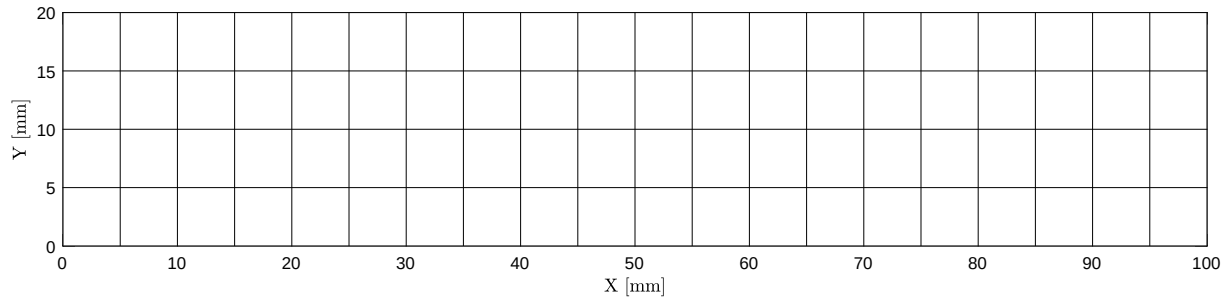

Figure C.20: CAR map for steel X70-B for pH 5.5 and 1 atm H_2S after 2 days.

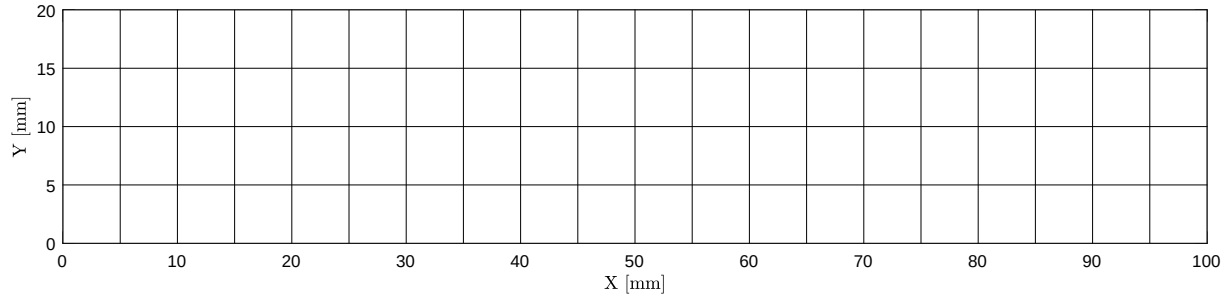

Figure C.21: CAR map for steel X70-B for pH 5.5 and 1 atm H_2S after 8 days.

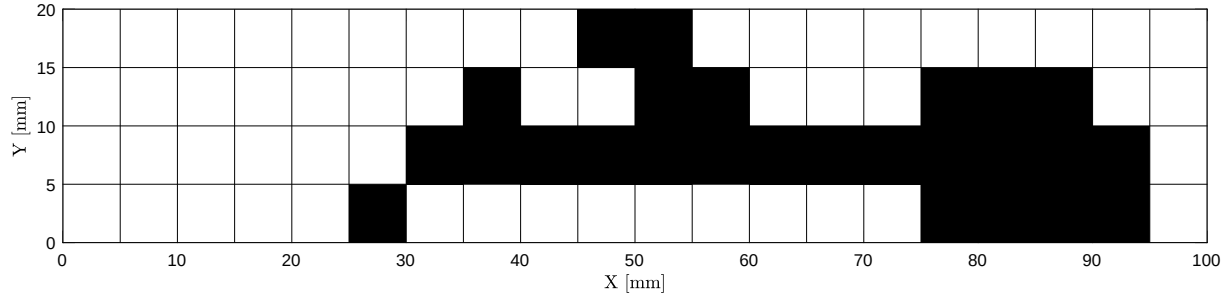

Figure C.22: CAR map for steel X70-B for pH 5.5 and 1 atm H_2S after 32 days.

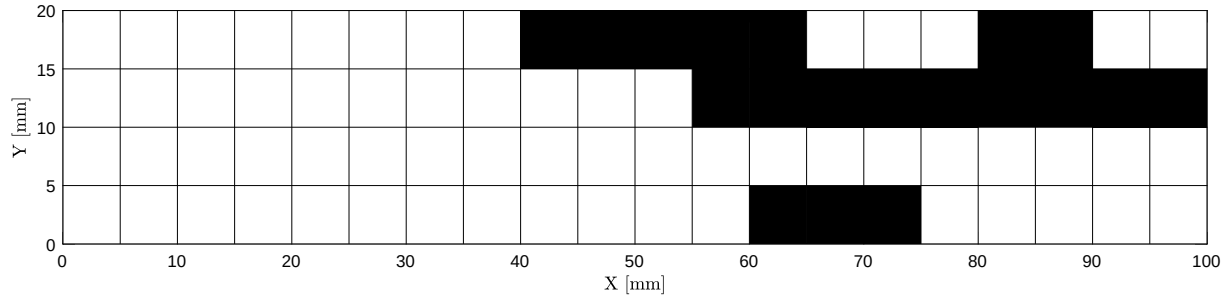

Figure C.23: CAR map for steel X70-B for pH 5.5 and 1 atm H_2S after 64 days.

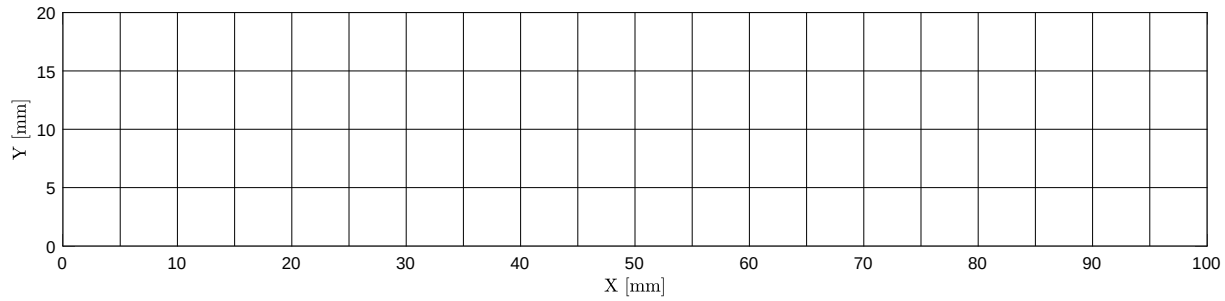

Figure C.24: CAR map for steel X70-X for pH 5.5 and 1 atm H_2S after 1 day.

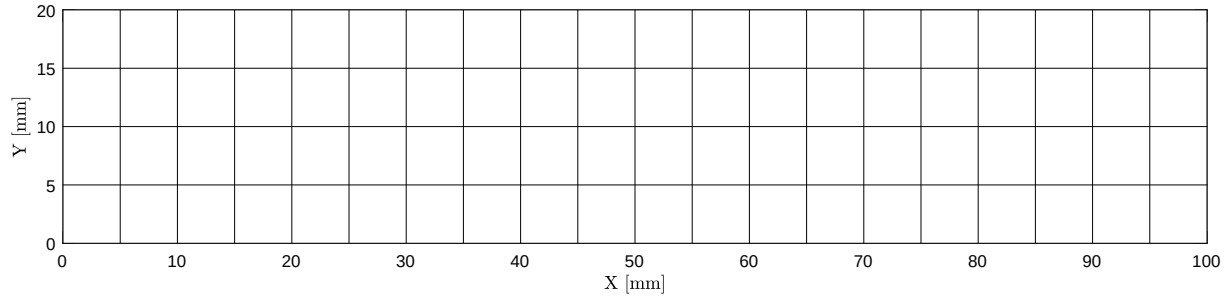

Figure C.25: CAR map for steel X70-X for pH 5.5 and 1 atm H_2S after 2 days.

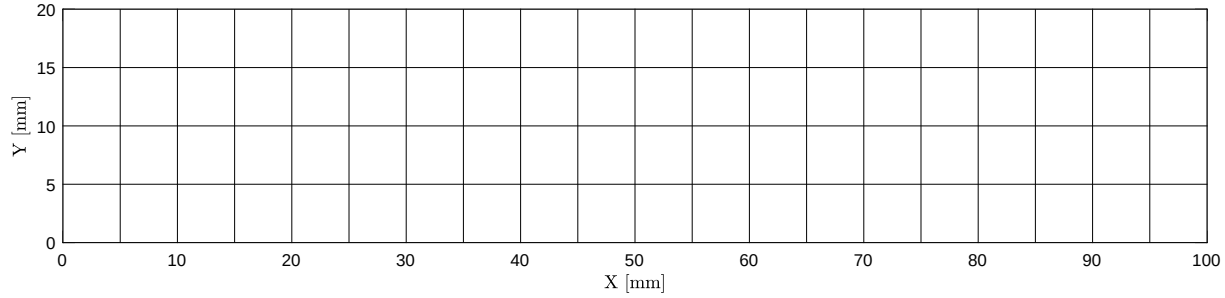

Figure C.26: CAR map for steel X70-X for pH 5.5 and 1 atm H_2S after 8 days.

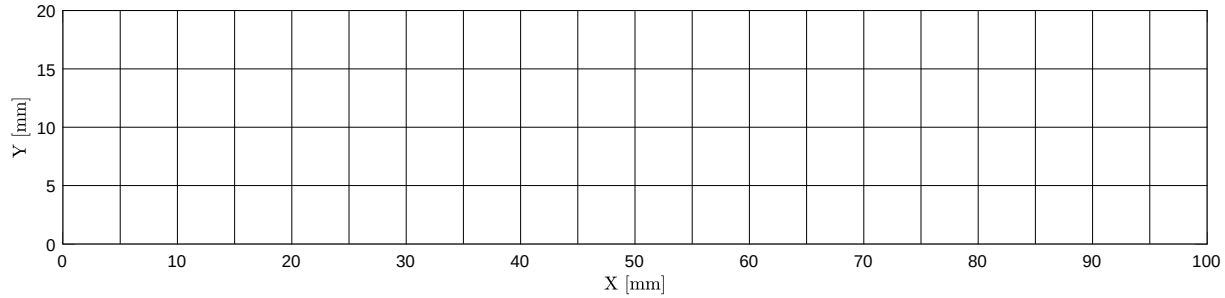

Figure C.27: CAR map for steel X70-X for pH 5.5 and 1 atm H_2S after 16 days.

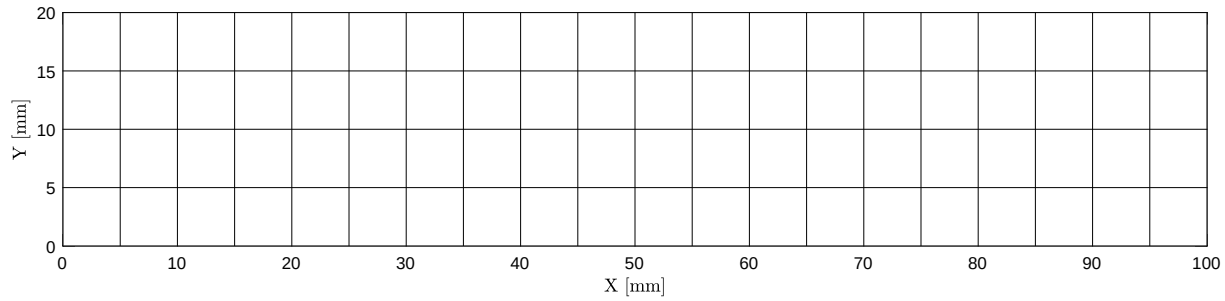

Figure C.28: CAR map for steel X70-X for pH 5.5 and 1 atm H_2S after 32 days.

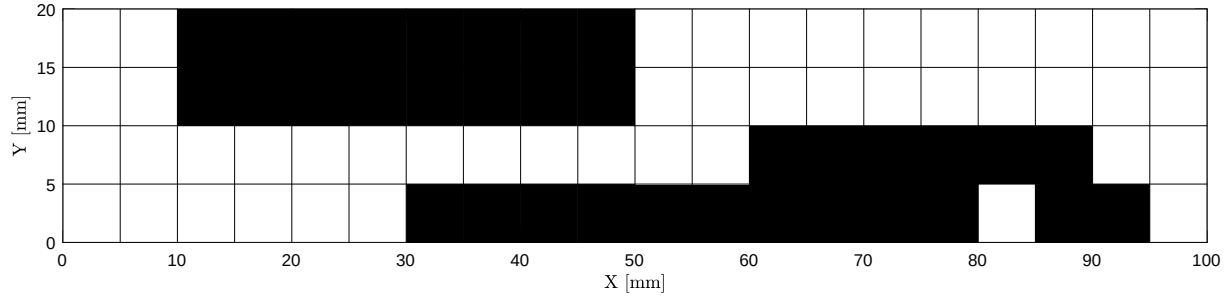

Figure C.29: CAR map for steel X70-X for pH 5.5 and 1 atm H_2S after 64 days.

C.1.5 pH 6.5 and 1 atm H_2S

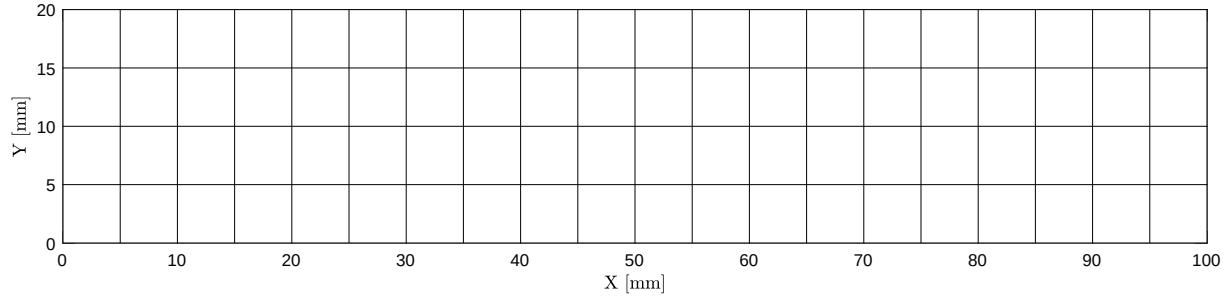

Figure C.30: CAR map for steel X70-X for pH 6.5 and 1 atm H_2S after 16 days.

C.2 CBR Maps

C.2.1 pH 2.7 and 1 atm H_2S

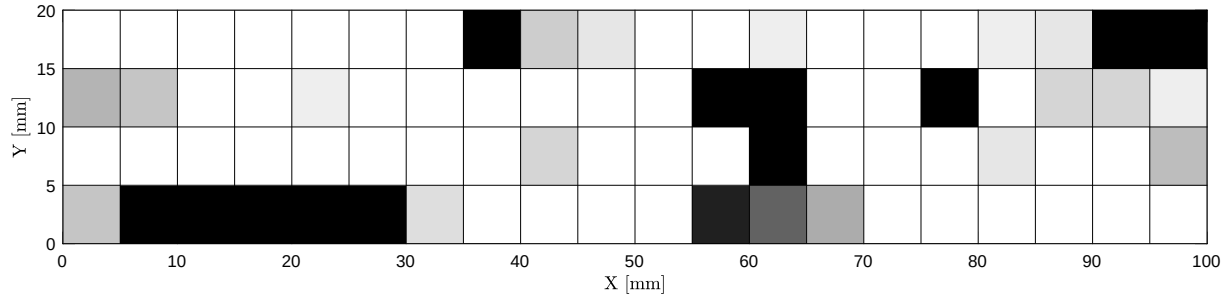

Figure C.31: CBR map for steel X70-B for pH 2.7 and 1 atm H_2S after 1 day.

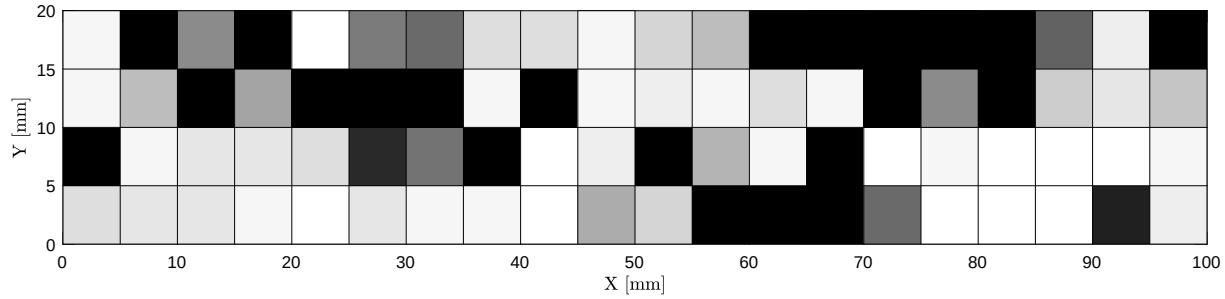

Figure C.32: CBR map for steel X70-B for pH 2.7 and 1 atm H_2S after 2 days.

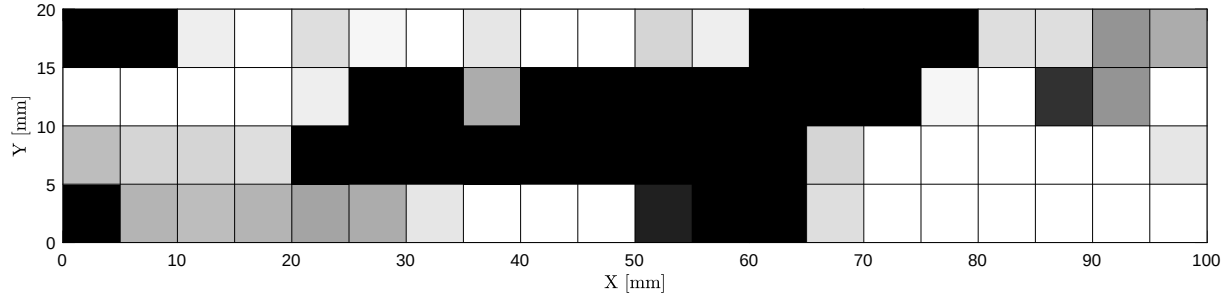

Figure C.33: CBR map for steel X70-B for pH 2.7 and 1 atm H_2S after 8 days.

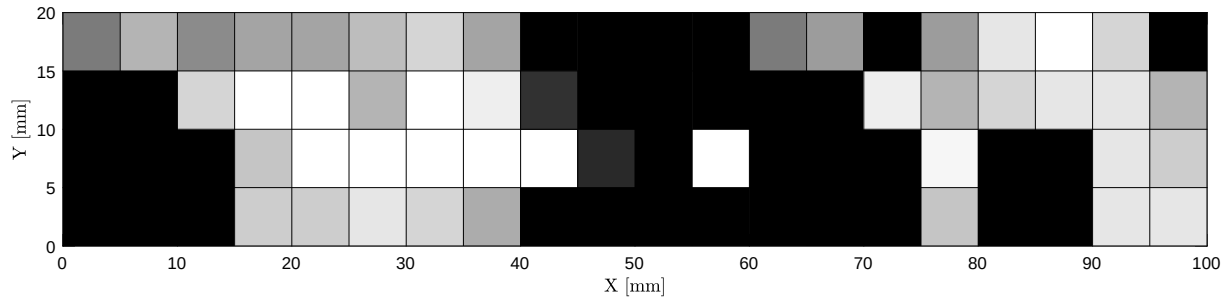

Figure C.34: CBR map for steel X70-B for pH 2.7 and 1 atm H_2S after 16 days.

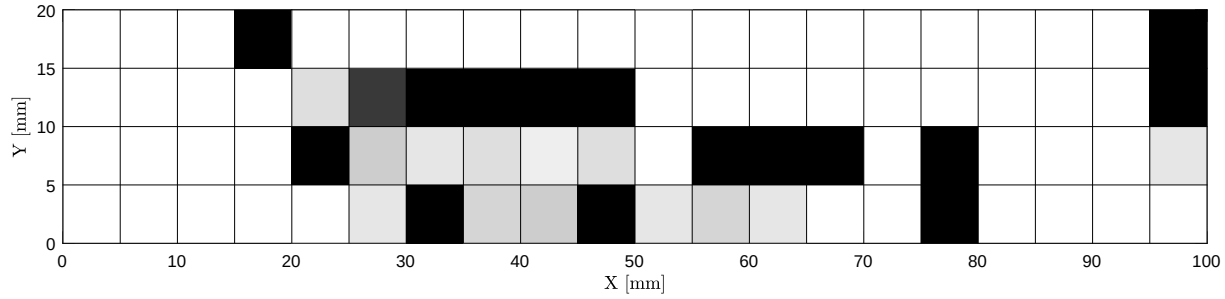

Figure C.35: CBR map for steel X70-X for pH 2.7 and 1 atm H_2S after 1 day.

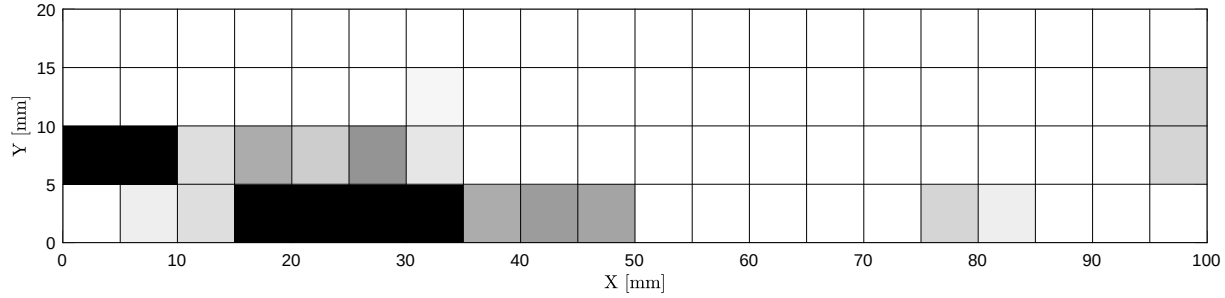

Figure C.36: CBR map for steel X70-X for pH 2.7 and 1 atm H_2S after 2 days.

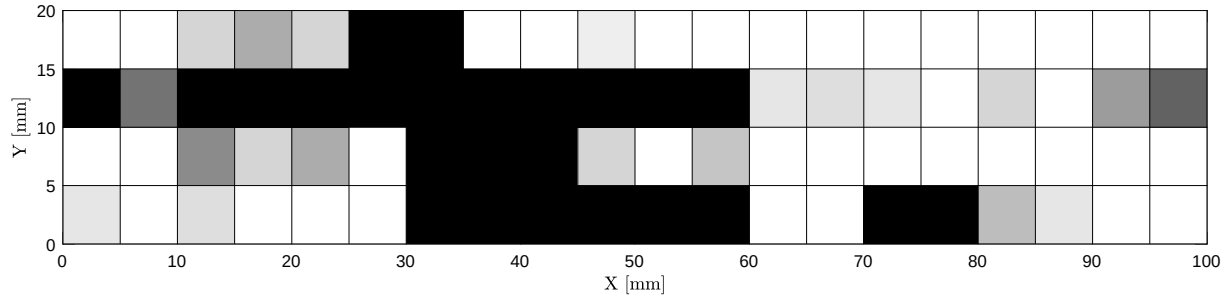

Figure C.37: CBR map for steel X70-X for pH 2.7 and 1 atm H_2S after 4 days.

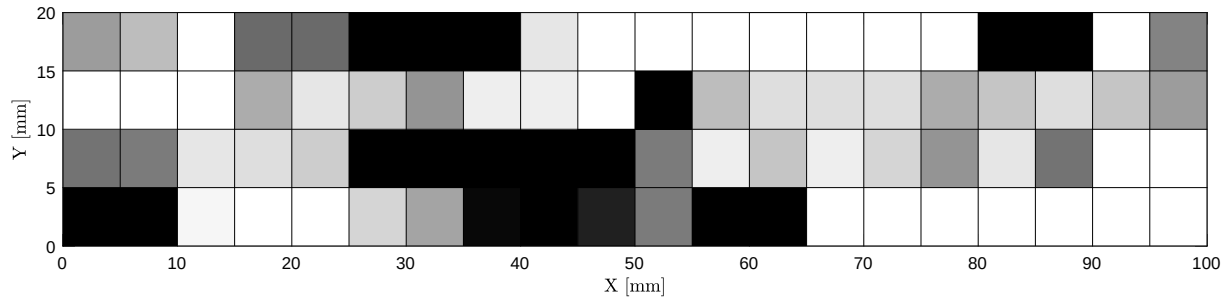

Figure C.38: CBR map for steel X70-X for pH 2.7 and 1 atm H_2S after 8 days.

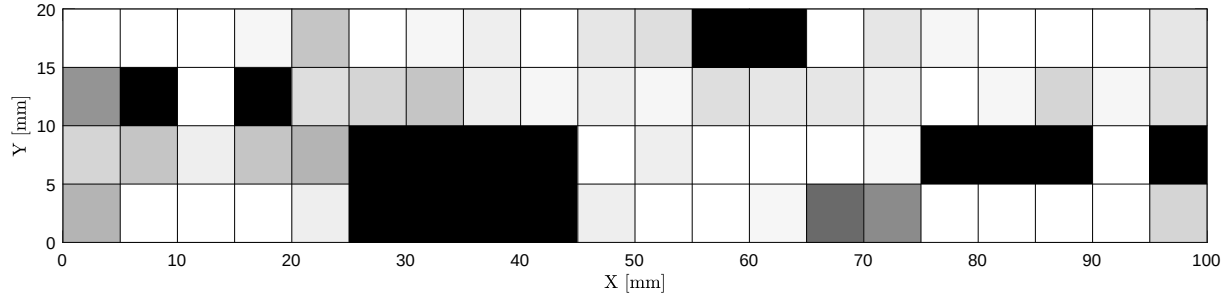

Figure C.39: CBR map for steel X70-X for pH 2.7 and 1 atm H_2S after 16 days.

C.2.2 pH 2.7 and 0.1 atm H_2S

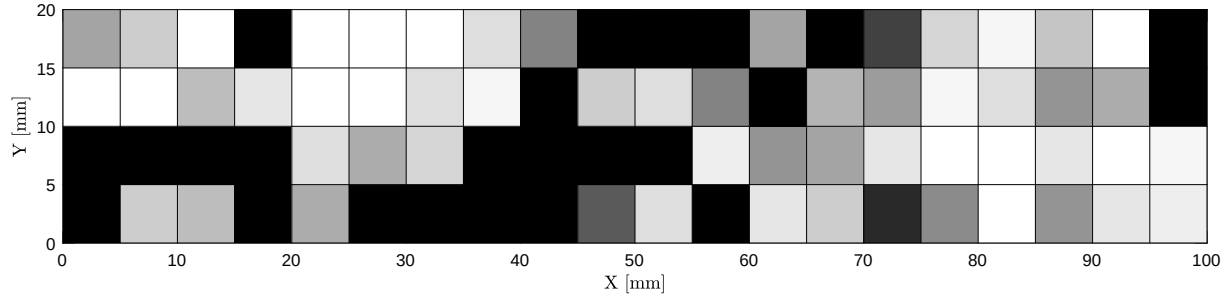

Figure C.40: CBR map for steel X70-B for pH 2.7, 1 atm H_2S and 0.9 atm N_2 after 8 days.

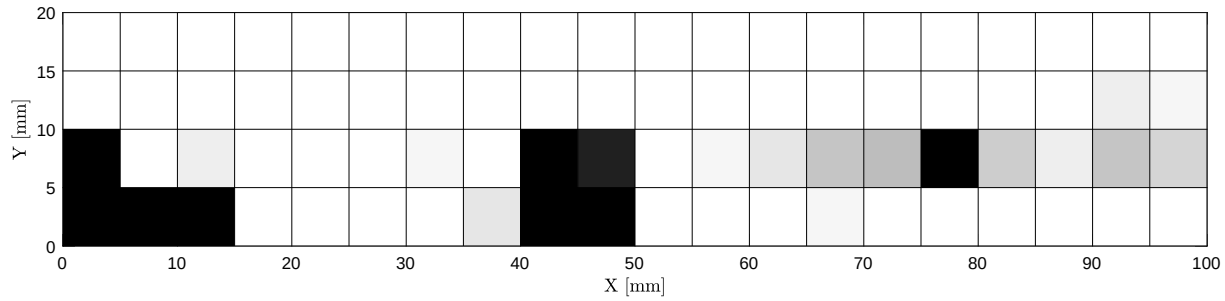

Figure C.41: CBR map for steel X70-B for pH 2.7, 1 atm H_2S and 0.9 atm CO_2 after 8 days.

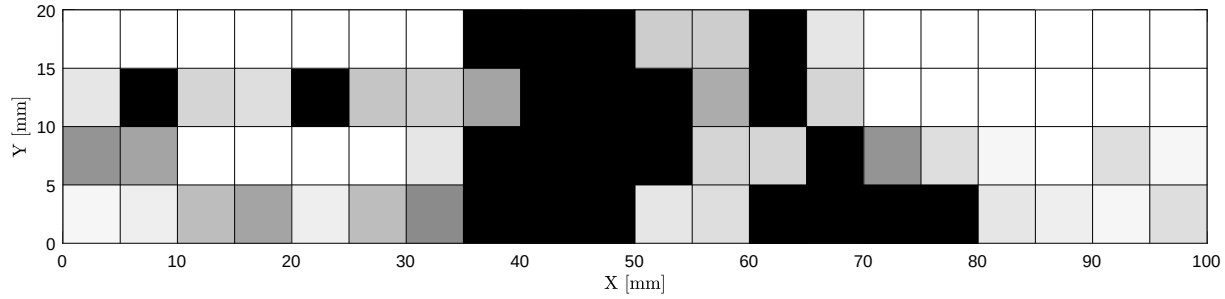

Figure C.42: CBR map for steel X70-B for pH 2.7, 1 atm H_2S and 0.9 atm N_2 after 8 days.

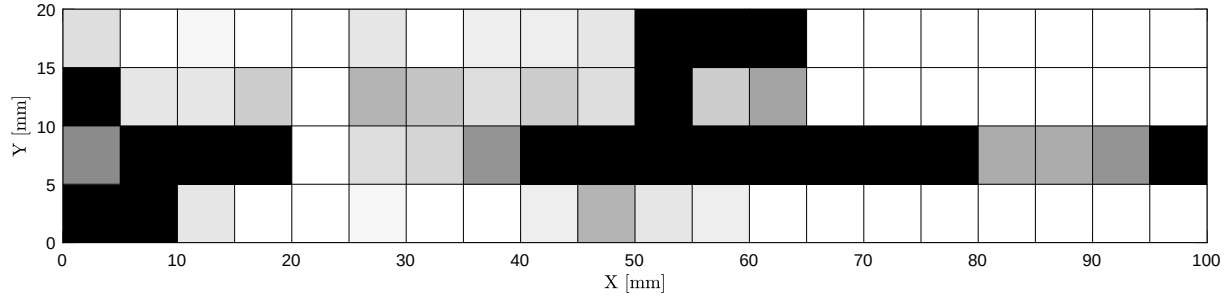

Figure C.43: CBR map for steel X70-B for pH 2.7, 1 atm H_2S and 0.9 atm N_2 after 16 days.

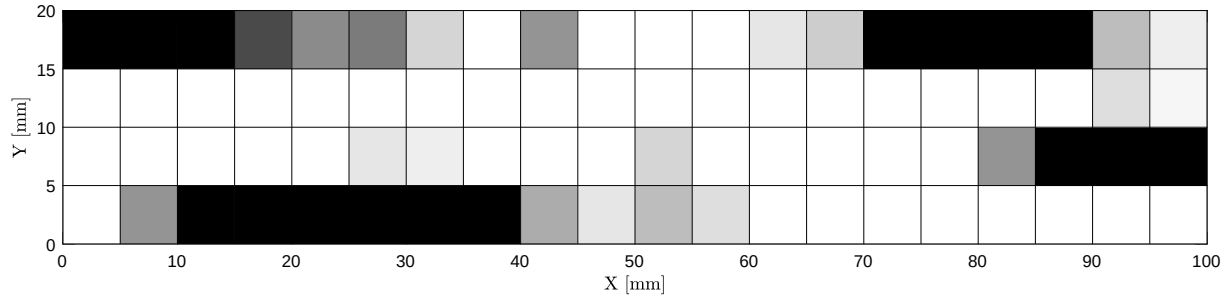

Figure C.44: CBR map for steel X70-X for pH 2.7, 1 atm H_2S and 0.9 atm N_2 after 8 days.

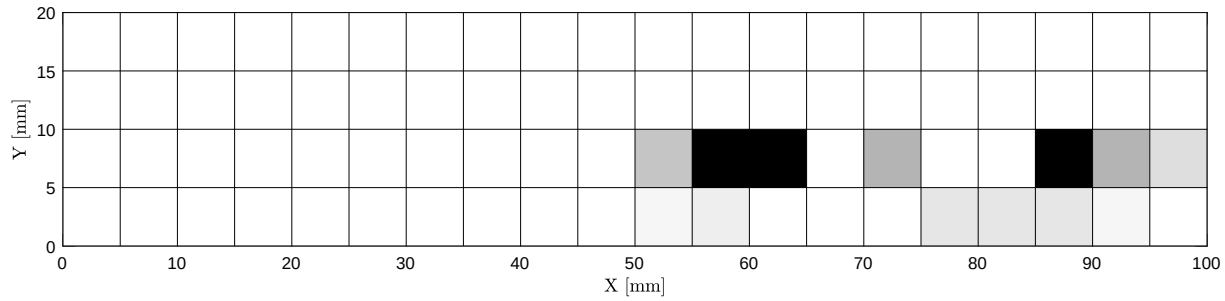

Figure C.45: CBR map for steel X70-X for pH 2.7, 1 atm H_2S and 0.9 atm CO_2 after 8 days.

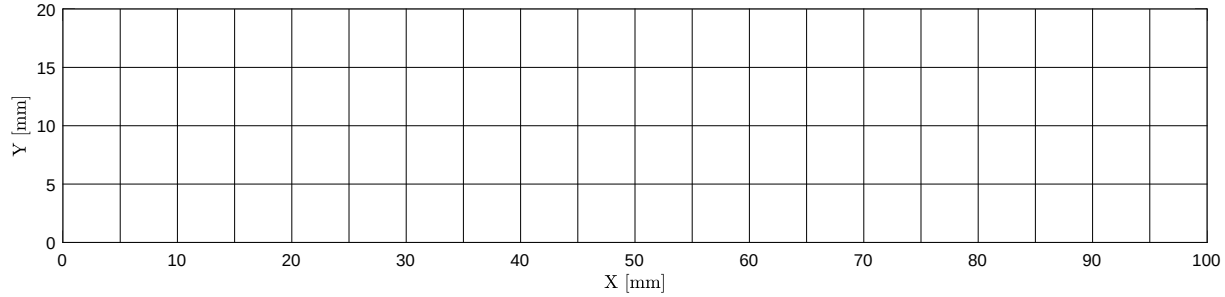

Figure C.46: CBR map for steel X70-X for pH 2.7, 1 atm H_2S and 0.9 atm N_2 after 8 days.

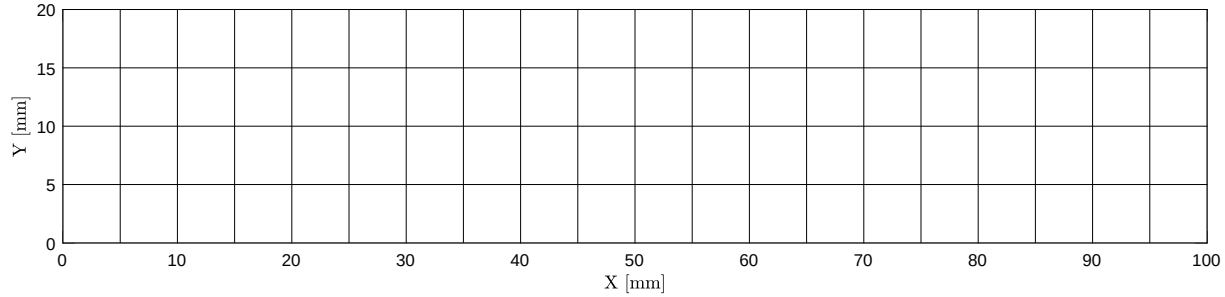

Figure C.47: CBR map for steel X70-X for pH 2.7, 1 atm H_2S and 0.9 atm N_2 after 16 days.

C.2.3 pH 4.5 and 0.1 atm H_2S

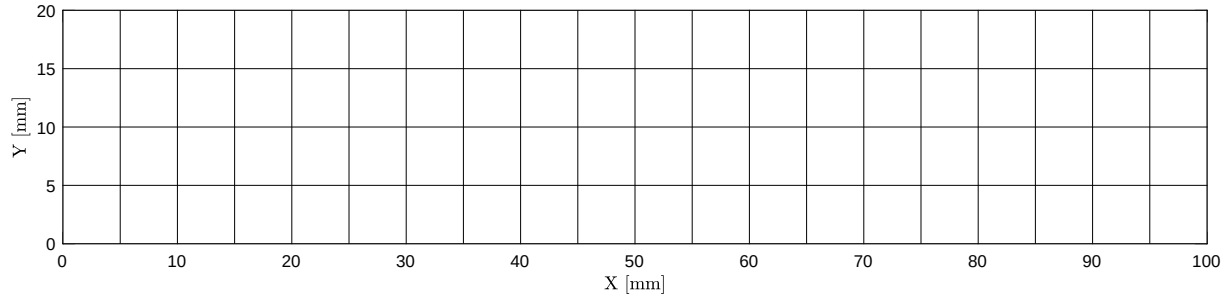

Figure C.48: CBR map for steel X70-X for pH 4.5, 0.1 atm H_2S and 0.9 atm CO_2 after 16 days.

C.2.4 pH 5.5 and 1 atm H_2S

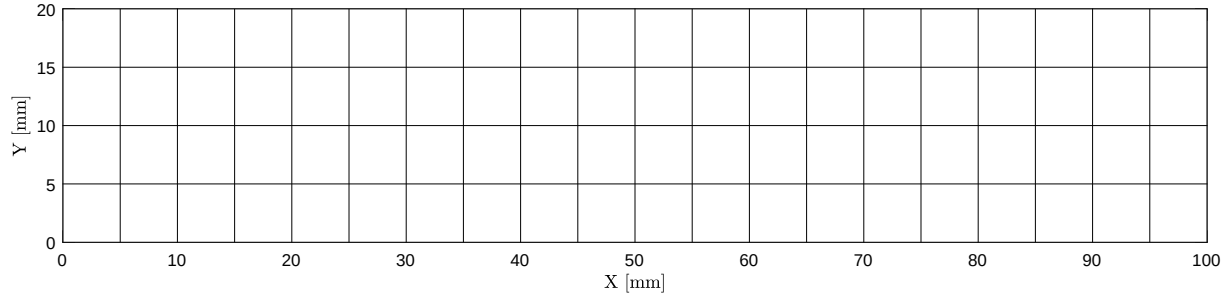

Figure C.49: CBR map for steel X70-B for pH 5.5 and 1 atm H_2S after 1 day.

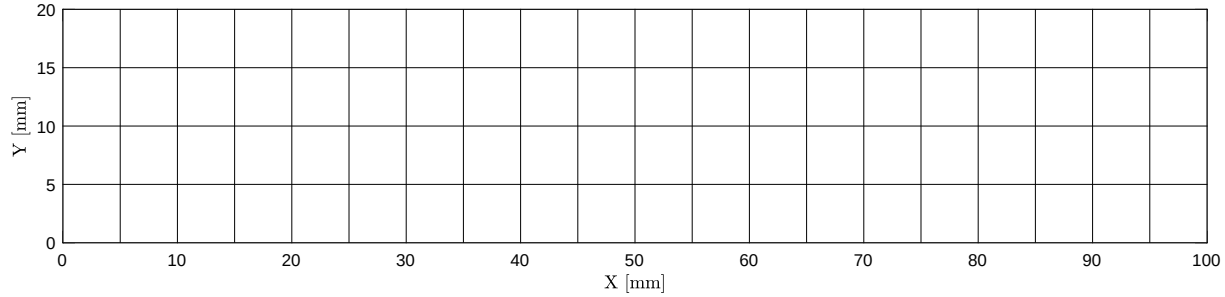

Figure C.50: CBR map for steel X70-B for pH 5.5 and 1 atm H_2S after 2 days.

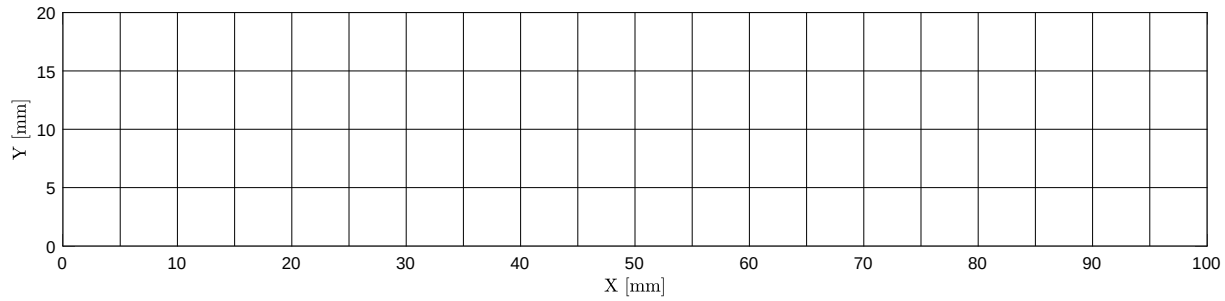

Figure C.51: CBR map for steel X70-B for pH 5.5 and 1 atm H_2S after 8 days.

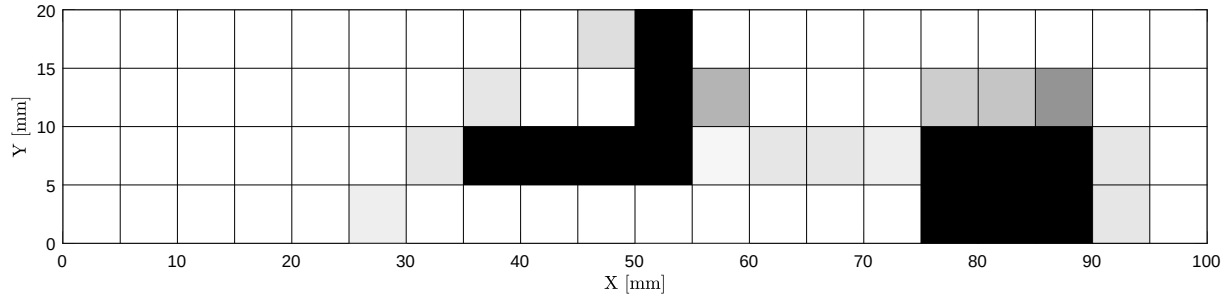

Figure C.52: CAR map for steel X70-B for pH 5.5 and 1 atm H_2S after 32 days.

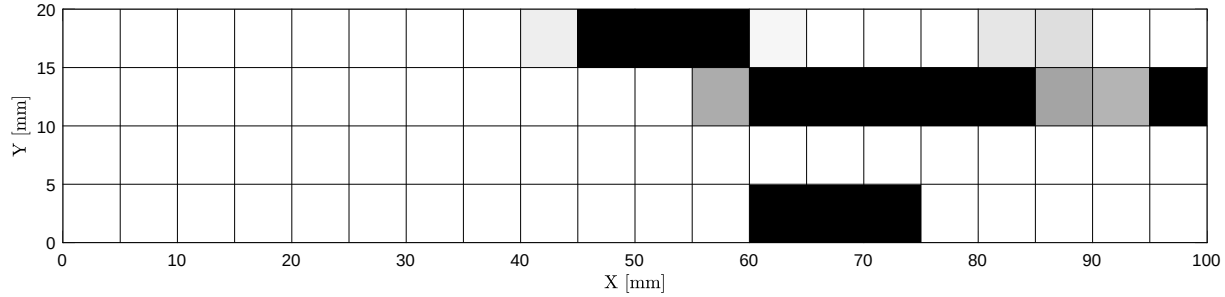

Figure C.53: CBR map for steel X70-B for pH 5.5 and 1 atm H_2S after 64 days.

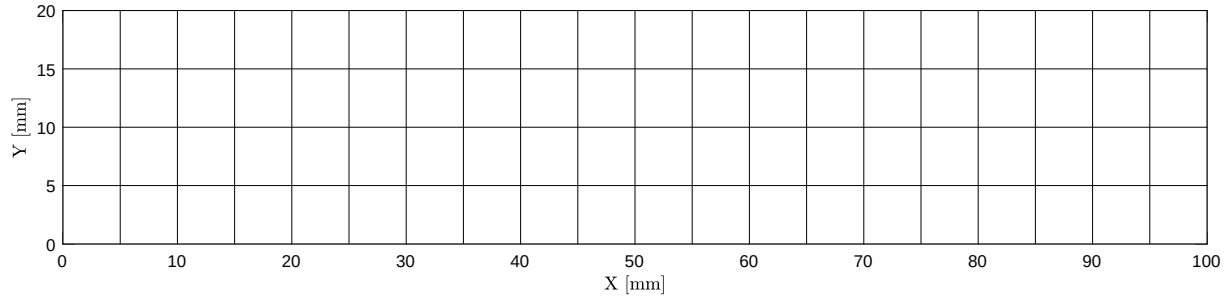

Figure C.54: CBR map for steel X70-X for pH 5.5 and 1 atm H_2S after 1 day.

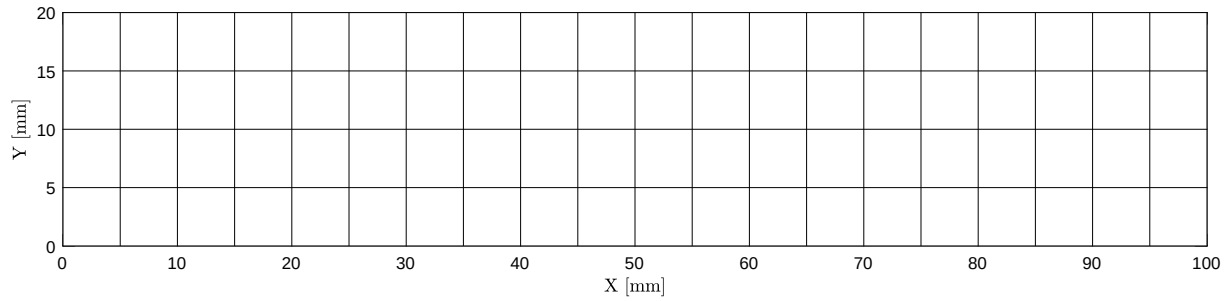

Figure C.55: CBR map for steel X70-X for pH 5.5 and 1 atm H_2S after 2 days.

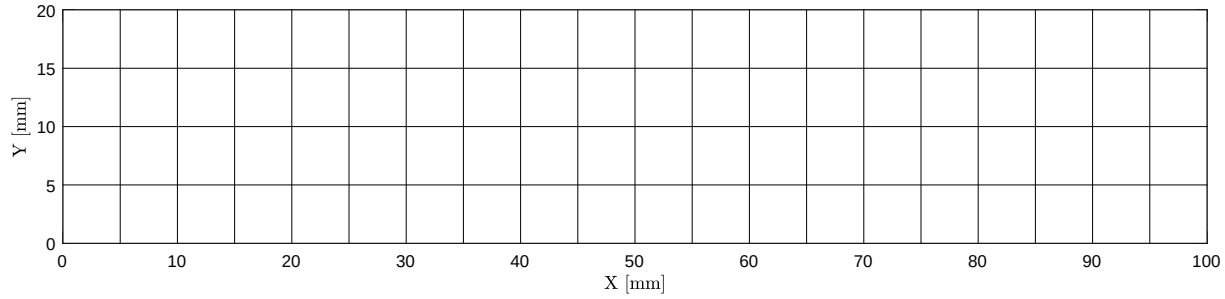

Figure C.56: CBR map for steel X70-X for pH 5.5 and 1 atm H_2S after 8 days.

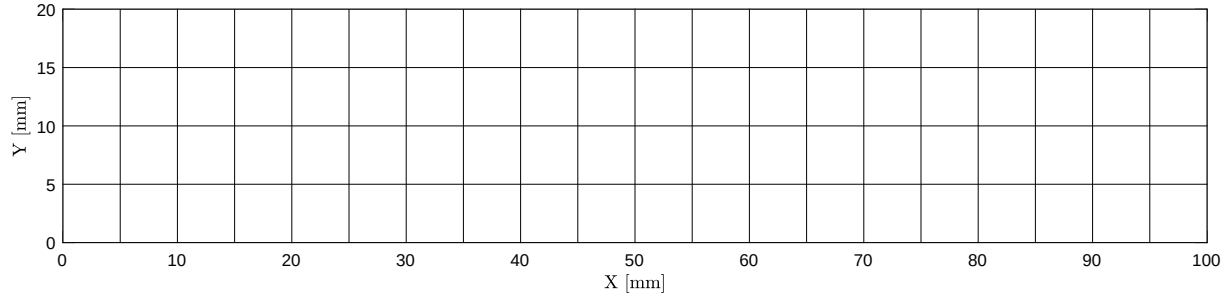

Figure C.57: CBR map for steel X70-X for pH 5.5 and 1 atm H_2S after 16 days.

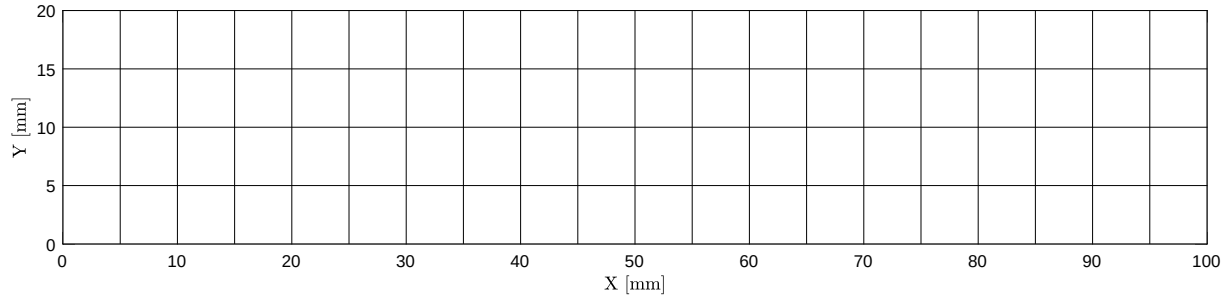

Figure C.58: CBR map for steel X70-X for pH 5.5 and 1 atm H_2S after 32 days.

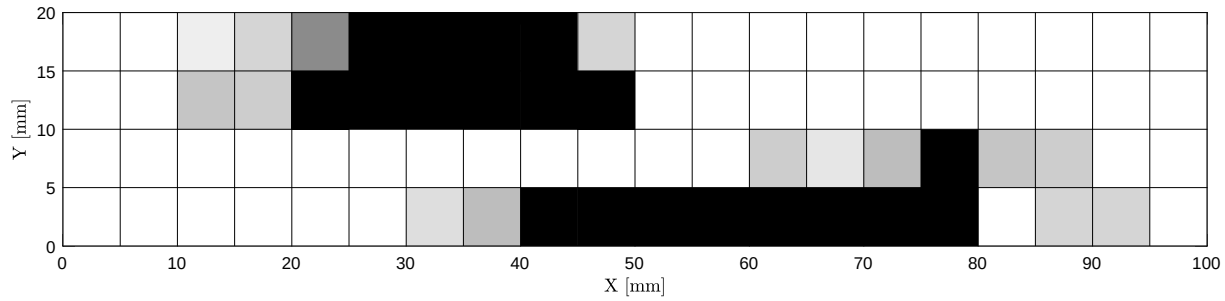

Figure C.59: CBR map for steel X70-X for pH 5.5 and 1 atm H_2S after 64 days.

C.2.5 pH 6.5 and 1 atm H_2S

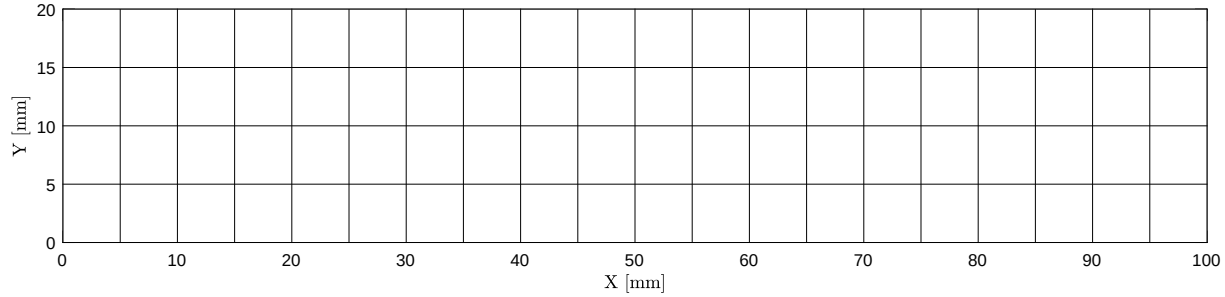

Figure C.60: CBR map for steel X70-X for pH 6.5 and 1 atm H_2S after 16 days.

C.3 Histograms

C.3.1 pH 2.7 and 1 atm H_2S

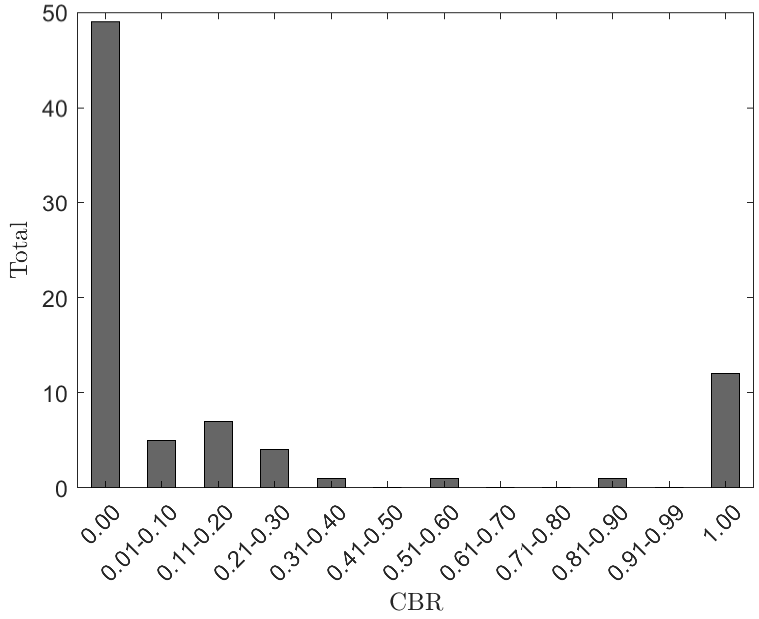

Figure C.61: Histogram for X70-B, tested for 1 days at a pH of 2.7 and 1 atm H_2S.

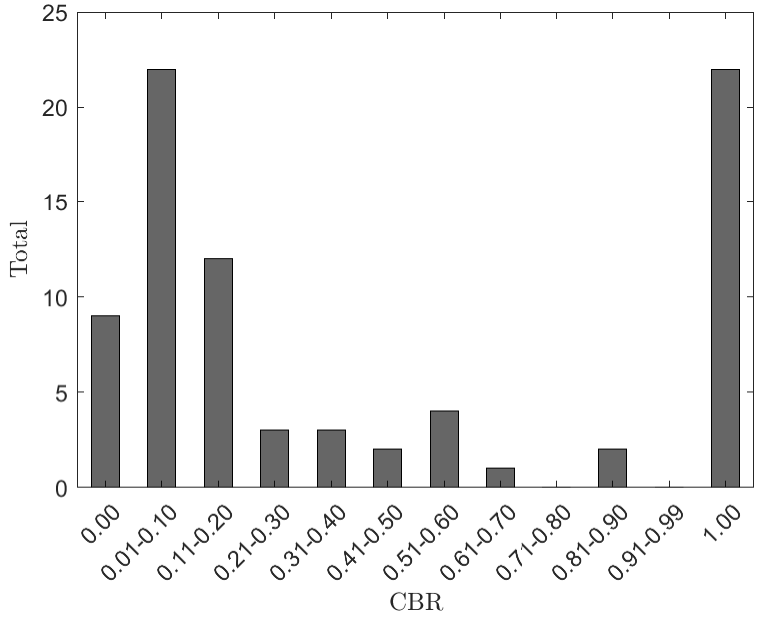

Figure C.62: Histogram for X70-B, tested for 2 days at a pH of 2.7 and 1 atm H_2S.

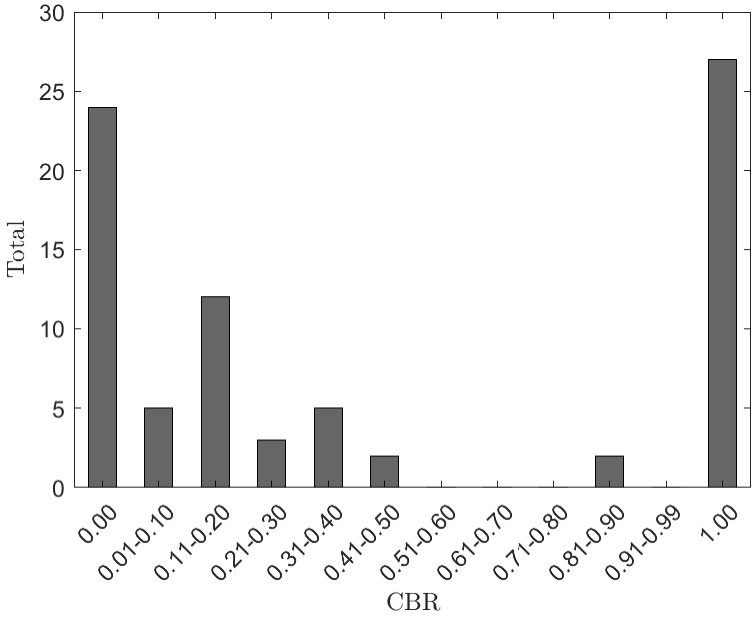

Figure C.63: Histogram for X70-B, tested for 8 days at a pH of 2.7 and 1 atm H_2S.

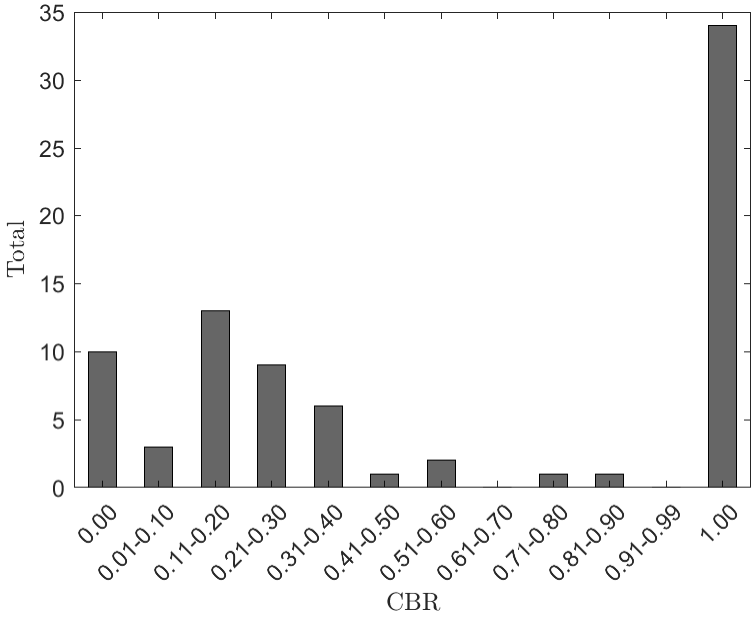

Figure C.64: Histogram for X70-B, tested for 16 days at a pH of 2.7 and 1 atm H_2S.

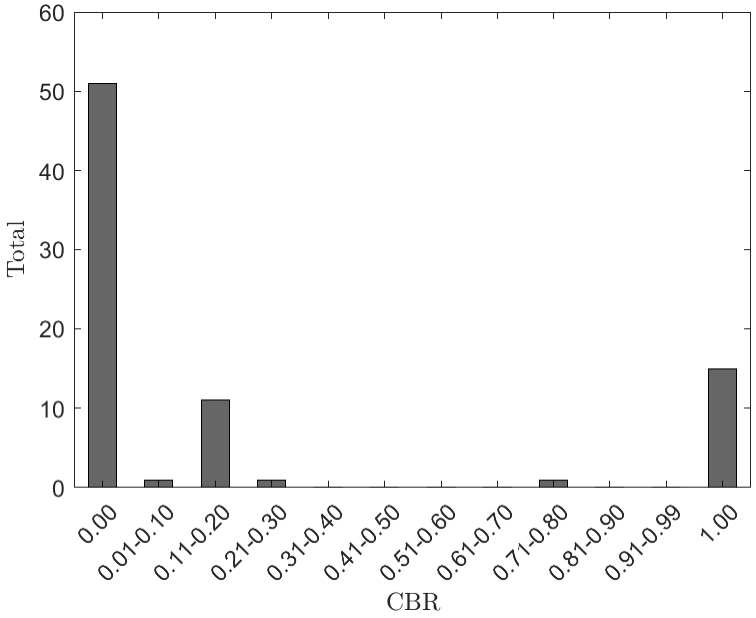

Figure C.65: Histogram for X70-X, tested for 1 days at a pH of 2.7 and 1 atm H_2S.

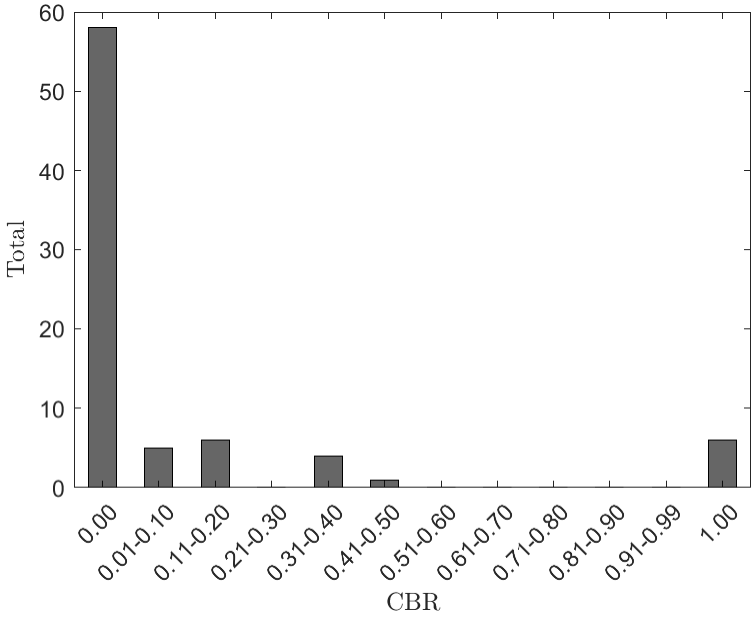

Figure C.66: Histogram for X70-X, tested for 2 days at a pH of 2.7 and 1 atm H_2S.

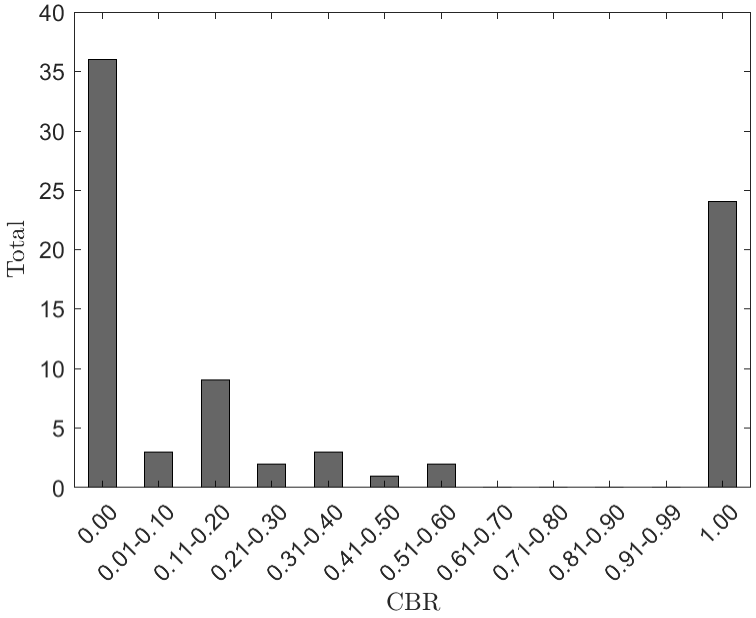

Figure C.67: Histogram for X70-X, tested for 4 days at a pH of 2.7 and 1 atm H_2S.

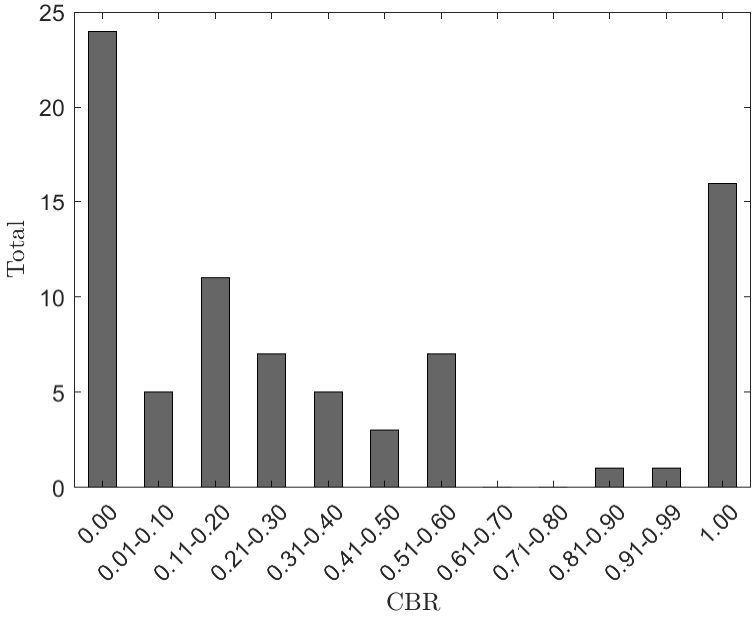

Figure C.68: Histogram for X70-X, tested for 8 days at a pH of 2.7 and 1 atm H_2S.

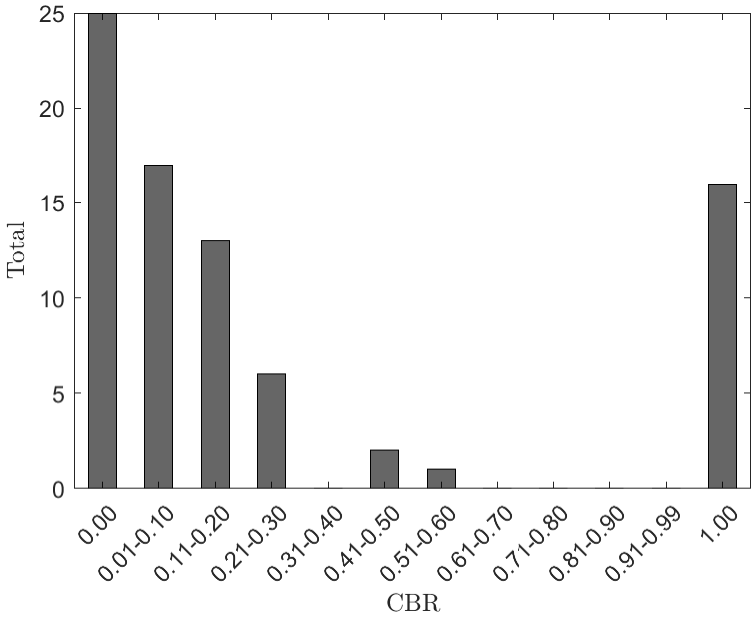

Figure C.69: Histogram for X70-X, tested for 16 days at a pH of 2.7 and 1 atm H_2S.

C.3.2 pH 2.7 and 0.1 atm H_2S

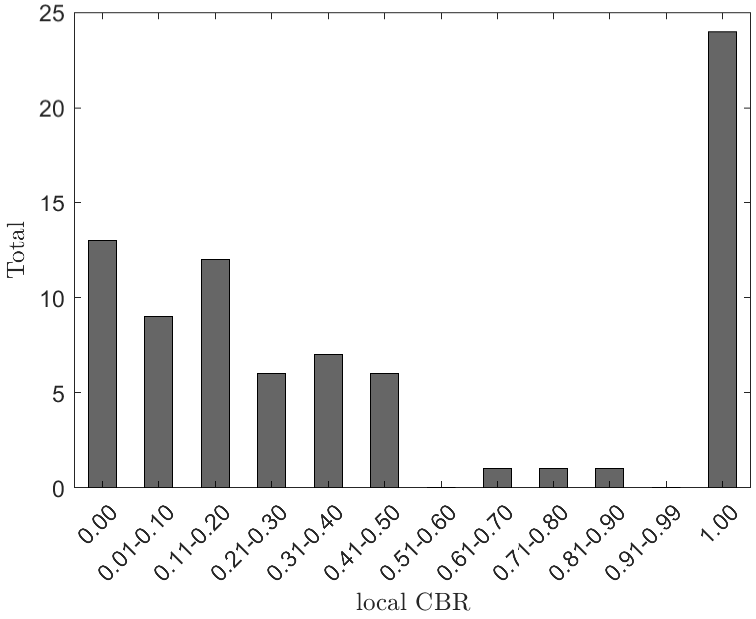

Figure C.70: Histogram for X70-B, tested for 1 days at a pH of 2.7 and 0.1 atm H_2S and 0.9 N_2.

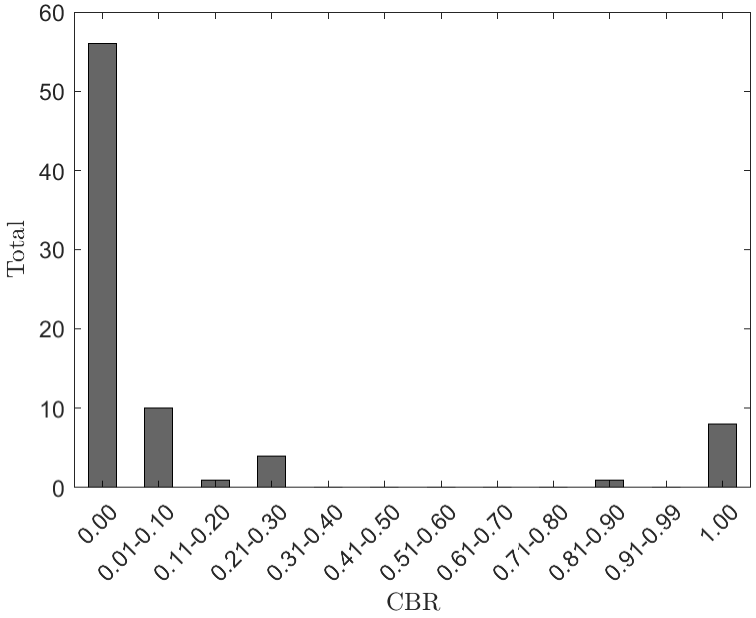

Figure C.71: Histogram for X70-B, tested for 8 days at a pH of 2.7 and 0.1 atm H_2S and 0.9 CO_2.

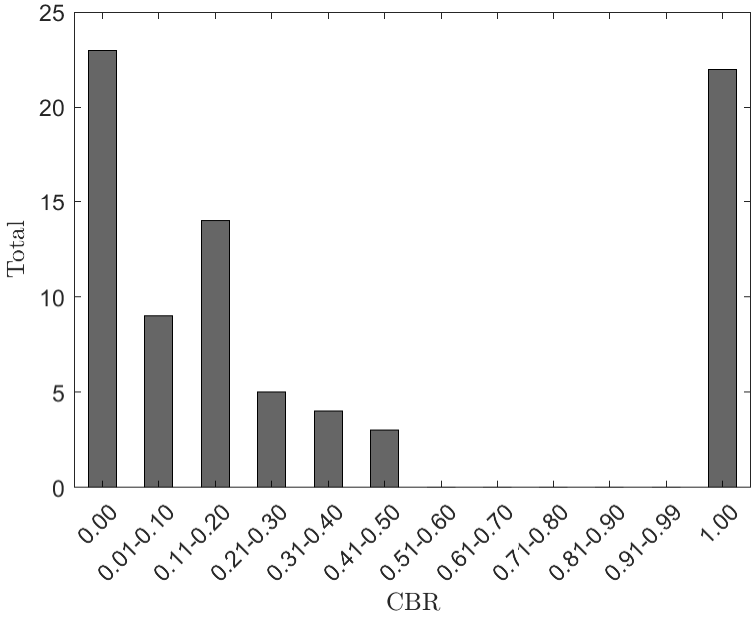

Figure C.72: Histogram for X70-B, tested for 8 days at a pH of 2.7 and 0.1 atm H_2S and 0.9 atm N_2.

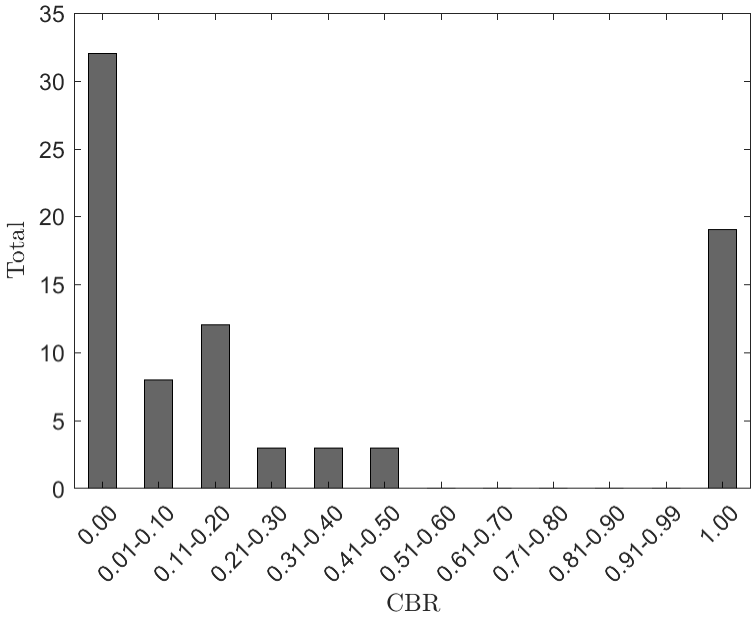

Figure C.73: Histogram for X70-B, tested for 16 days at a pH of 2.7 and 0.1 atm H_2S and 0.9 atm CO_2.

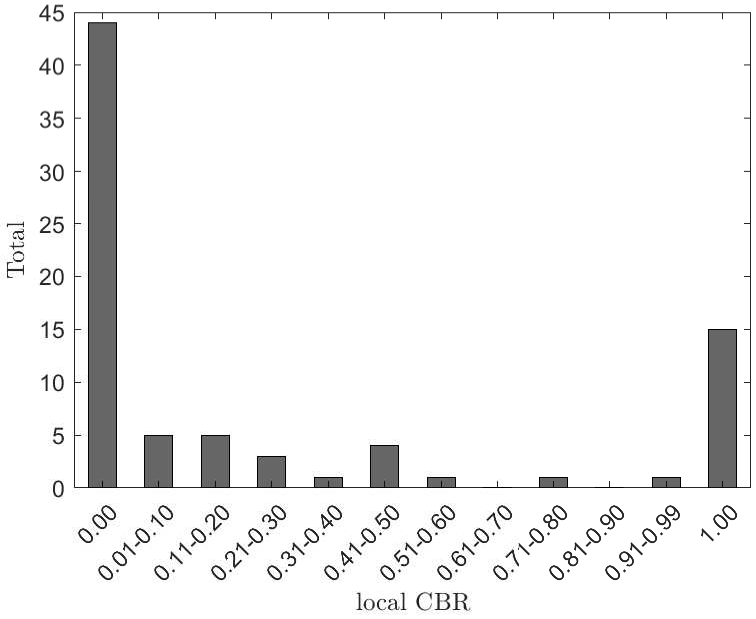

Figure C.74: Histogram for X70-X, tested for 8 days at a pH of 2.7 and 0.1 atm H_2S and 0.9 N_2.

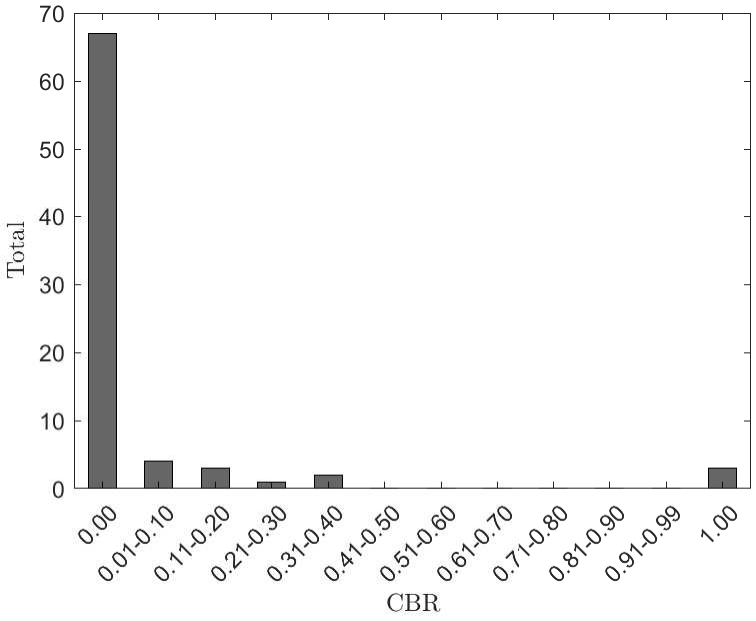

Figure C.75: Histogram for X70-X, tested for 8 days at a pH of 2.7 and 0.1 atm H_2S and 0.9 CO_2.

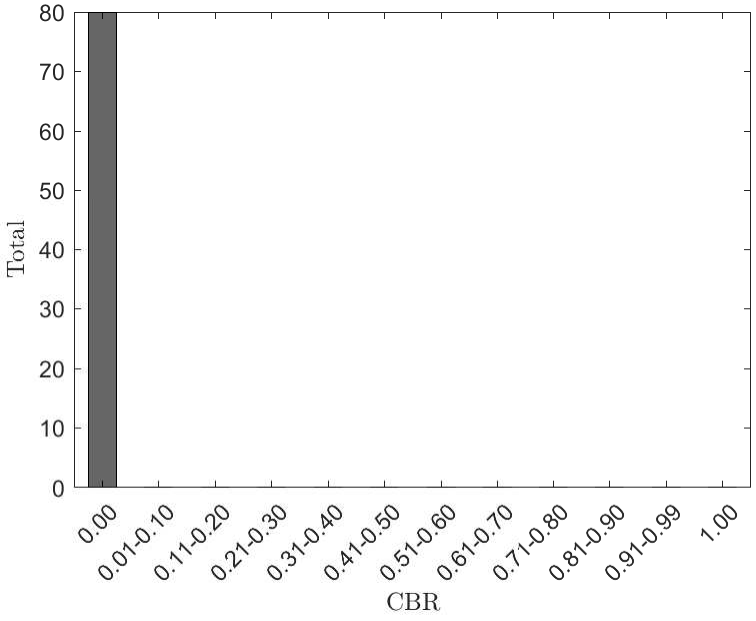

Figure C.76: Histogram for X70-X, tested for 8 days at a pH of 2.7 and 0.1 atm H_2S and 0.9 atm N_2.

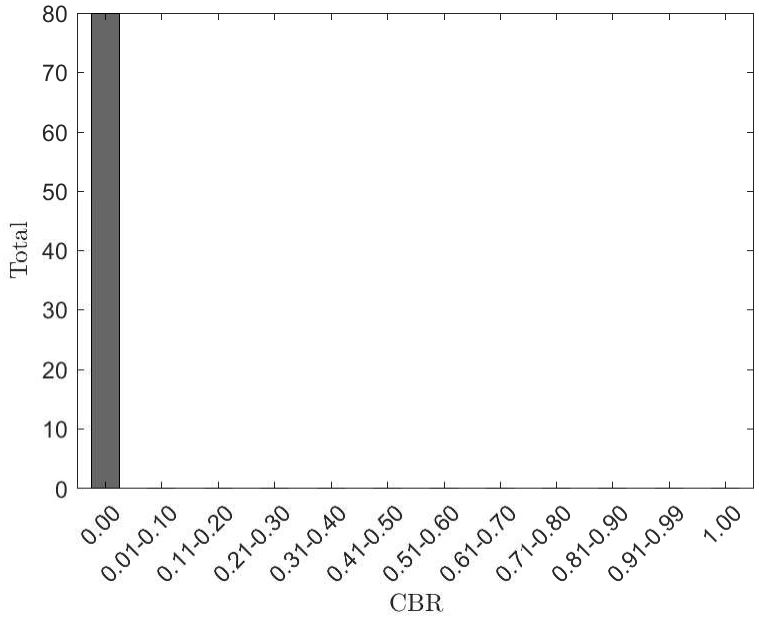

Figure C.77: Histogram for X70-X, tested for 16 days at a pH of 2.7 and 0.1 atm H_2S and 0.9 atm CO_2.

C.3.3 pH 4.5 and 0.1 atm H_2S

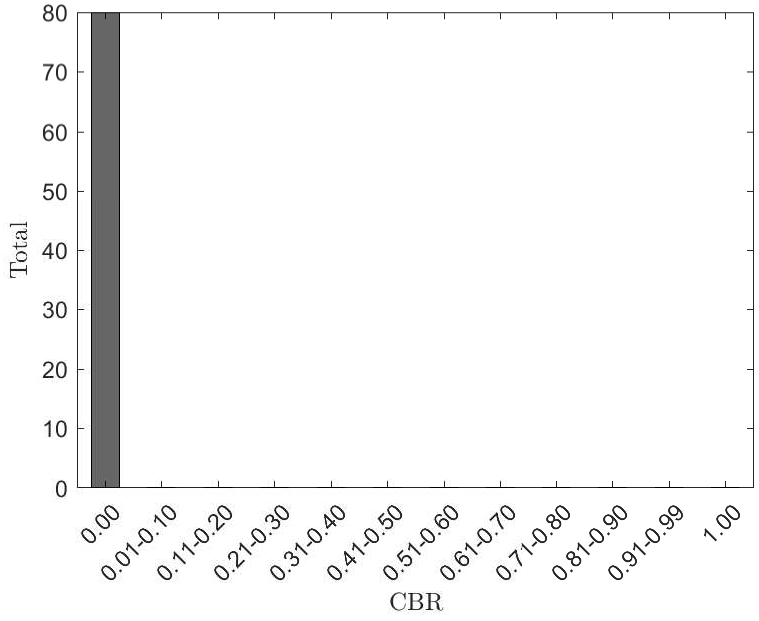

Figure C.78: Histogram for X70-X, tested for 16 days at a pH of 4.5 and 0.1 atm H_2S and 0.9 atm CO_2.

C.3.4 pH 5.5 and 1 atm H_2S

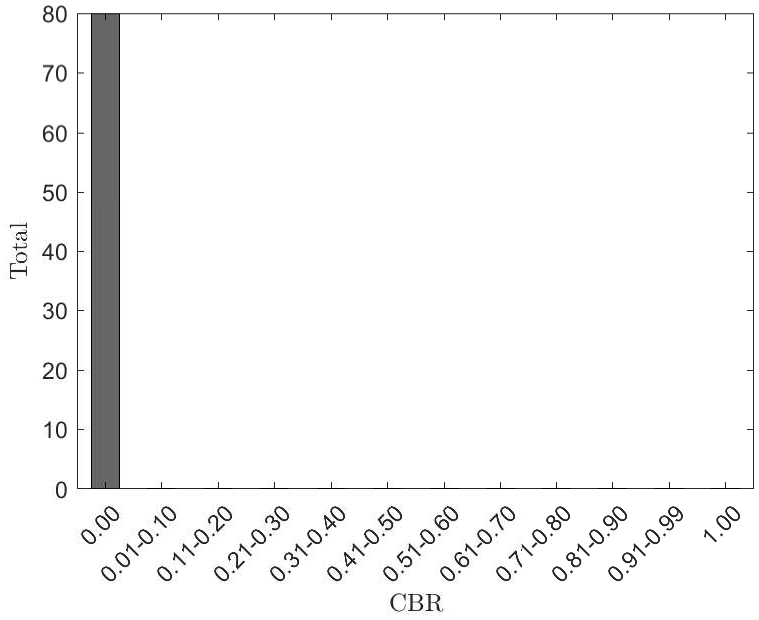

Figure C.79: Histogram for X70-B, tested for 1 days at a pH of 5.5 and 1 atm H_2S.

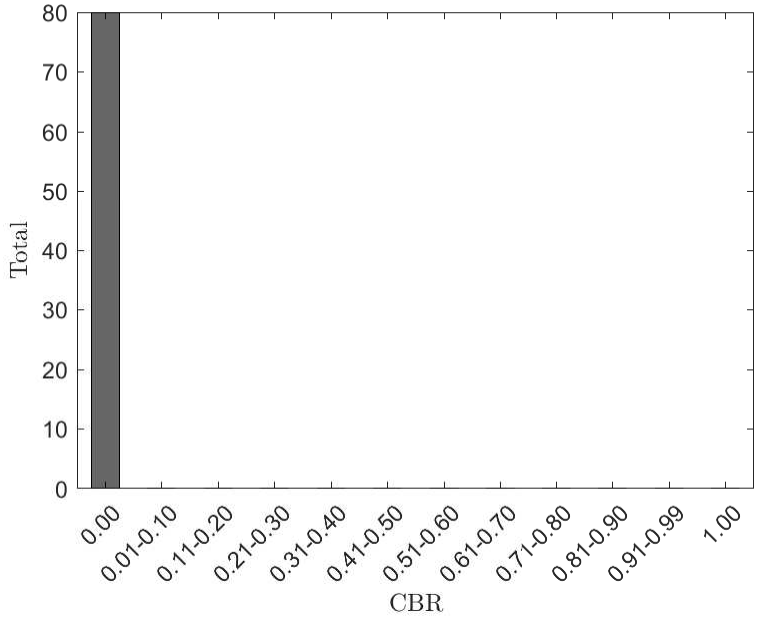

Figure C.80: Histogram for X70-B, tested for 2 days at a pH of 5.5 and 1 atm H_2S.

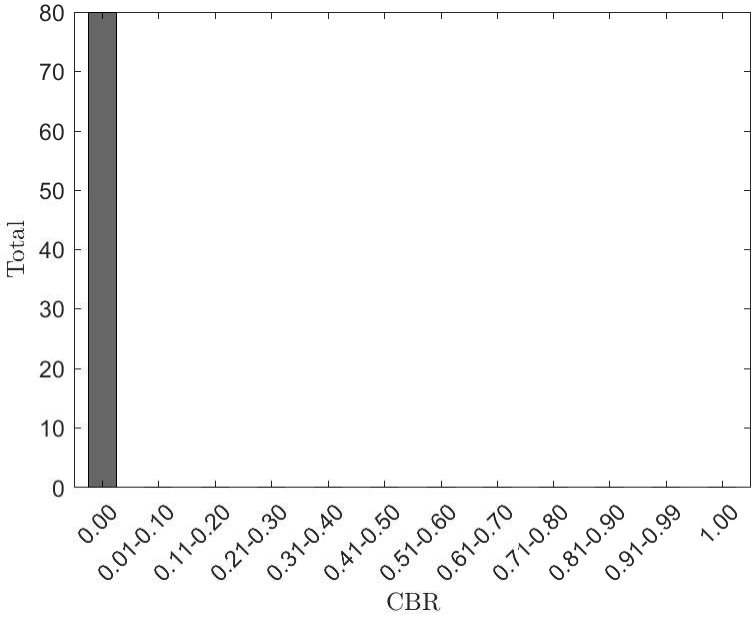

Figure C.81: Histogram for X70-B, tested for 8 days at a pH of 5.5 and 1 atm H_2S.

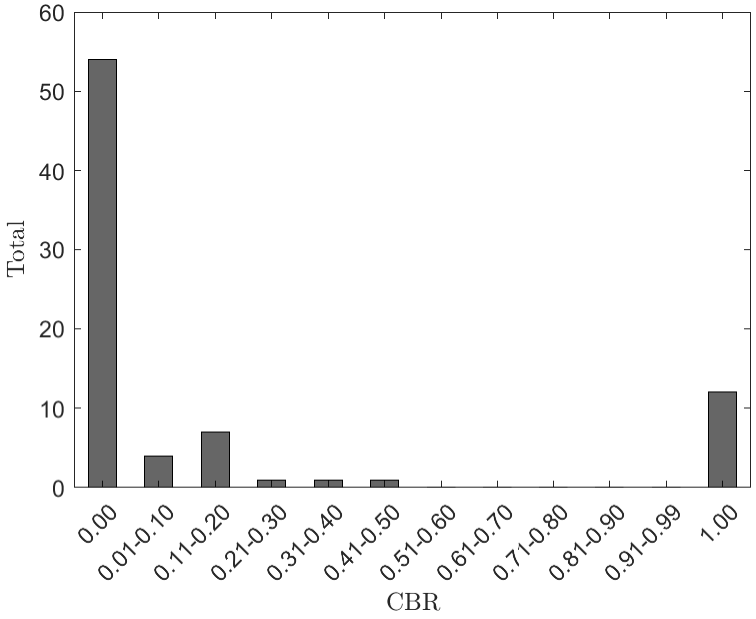

Figure C.82: Histogram for X70-B, tested for 32 days at a pH of 5.5 and 1 atm H_2S.

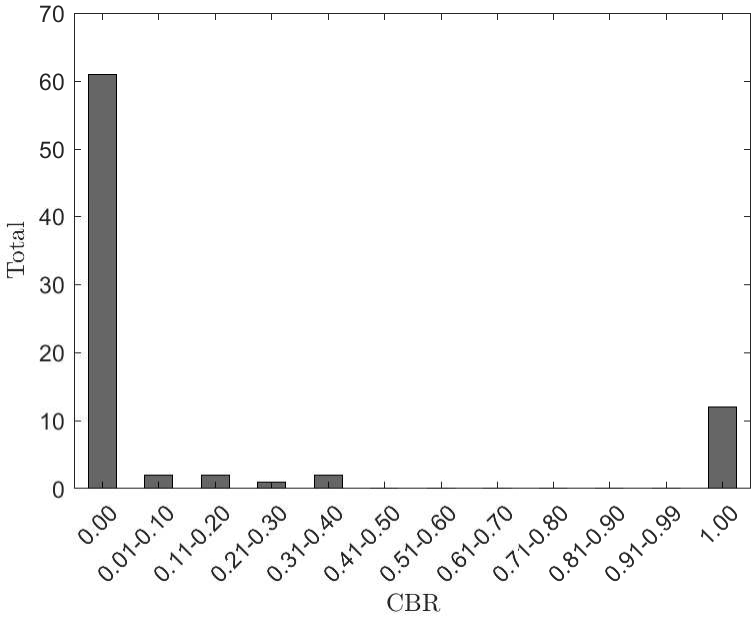

Figure C.83: Histogram for X70-B, tested for 64 days at a pH of 5.5 and 1 atm H_2S.

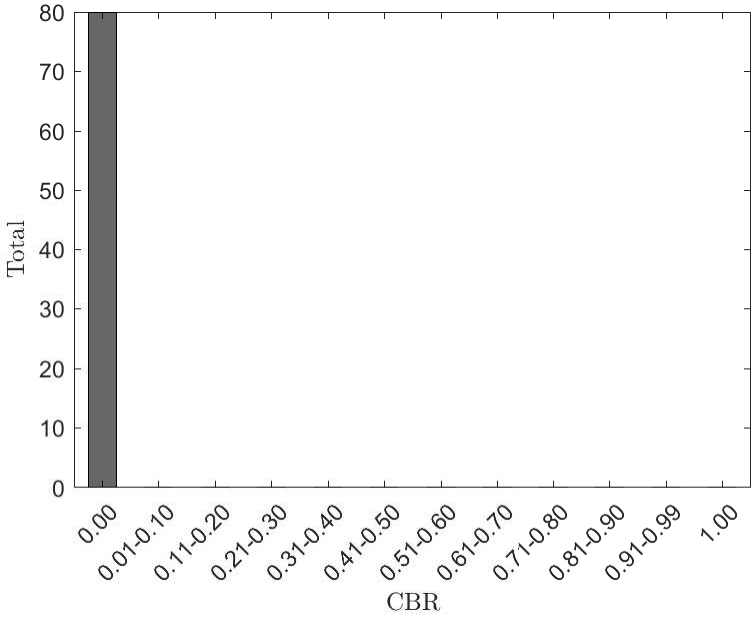

Figure C.84: Histogram for X70-X, tested for 1 days at a pH of 5.5 and 1 atm H_2S.

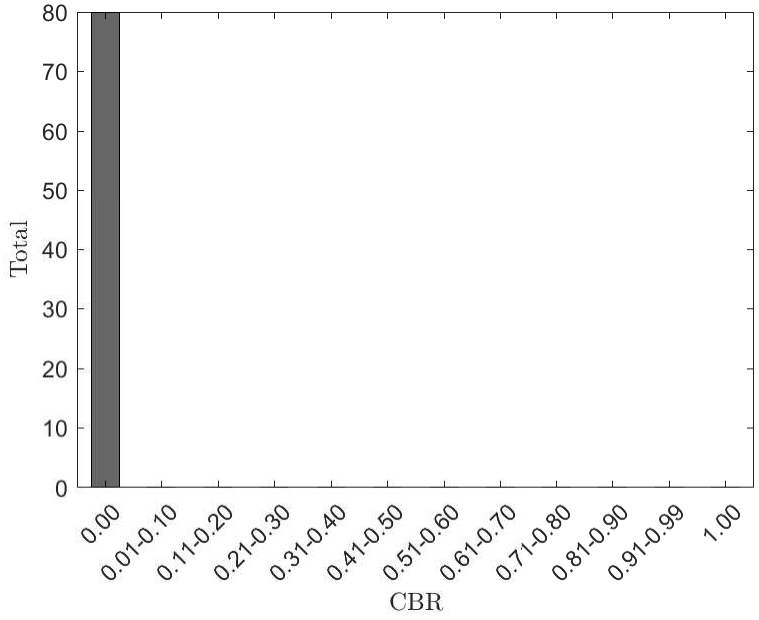

Figure C.85: Histogram for X70-X, tested for 2 days at a pH of 5.5 and 1 atm H_2S.

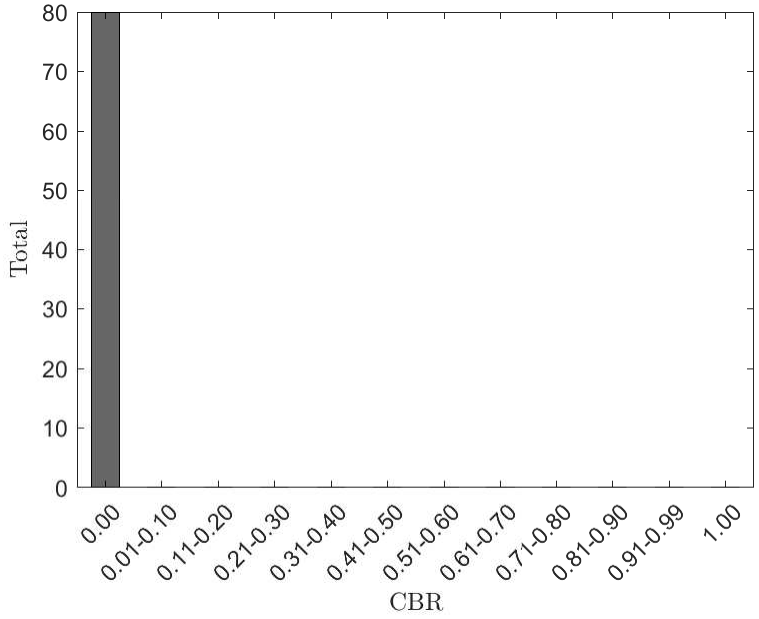

Figure C.86: Histogram for X70-X, tested for 8 days at a pH of 5.5 and 1 atm H_2S.

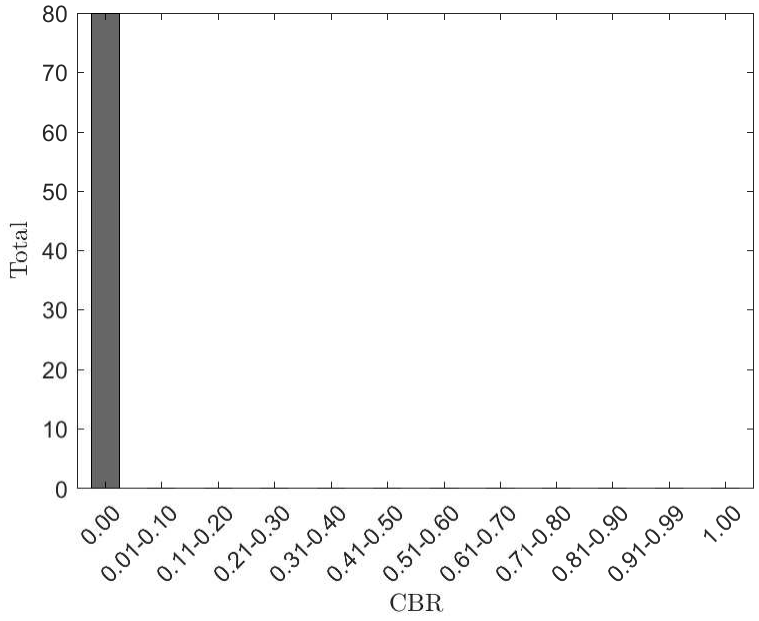

Figure C.87: Histogram for X70-X, tested for 16 days at a pH of 5.5 and 1 atm H_2S.

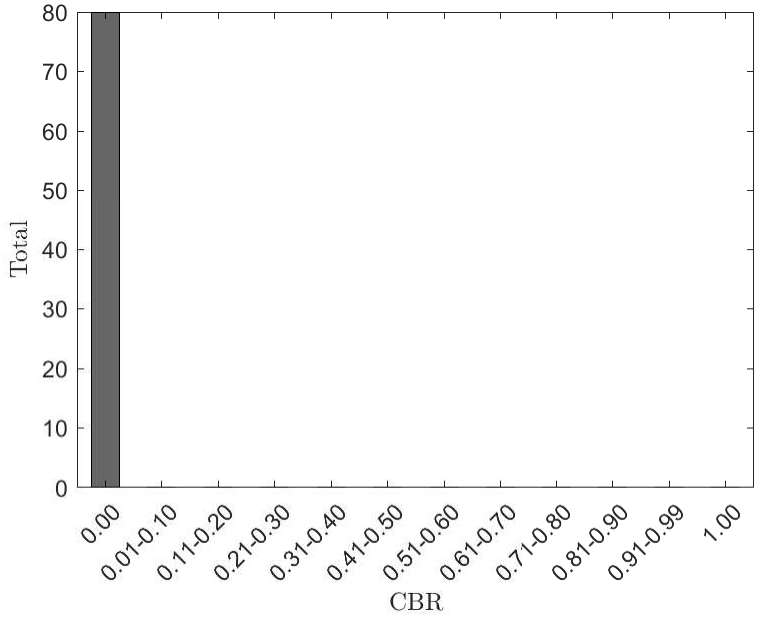

Figure C.88: Histogram for X70-X, tested for 32 days at a pH of 5.5 and 1 atm H_2S.

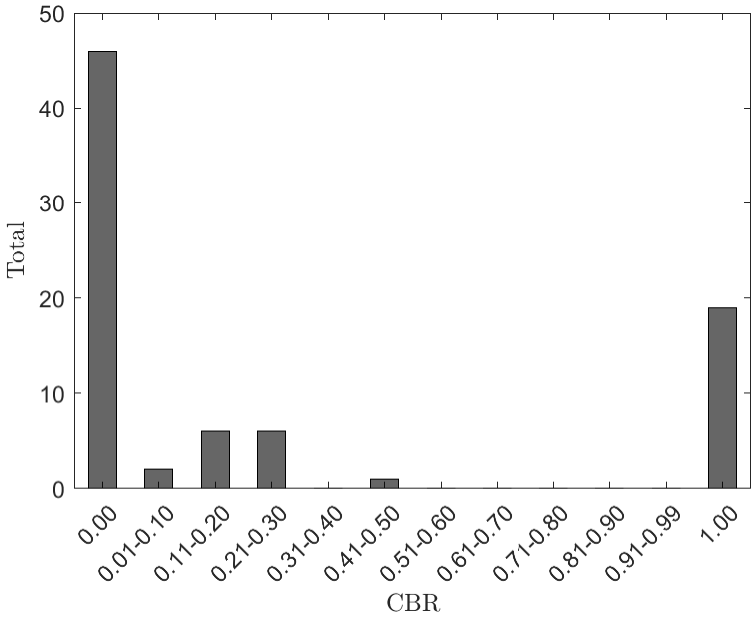

Figure C.89: Histogram for X70-X, tested for 64 days at a pH of 5.5 and 1 atm H_2S.

C.3.5 pH 6.5 and 1 atm H_2S

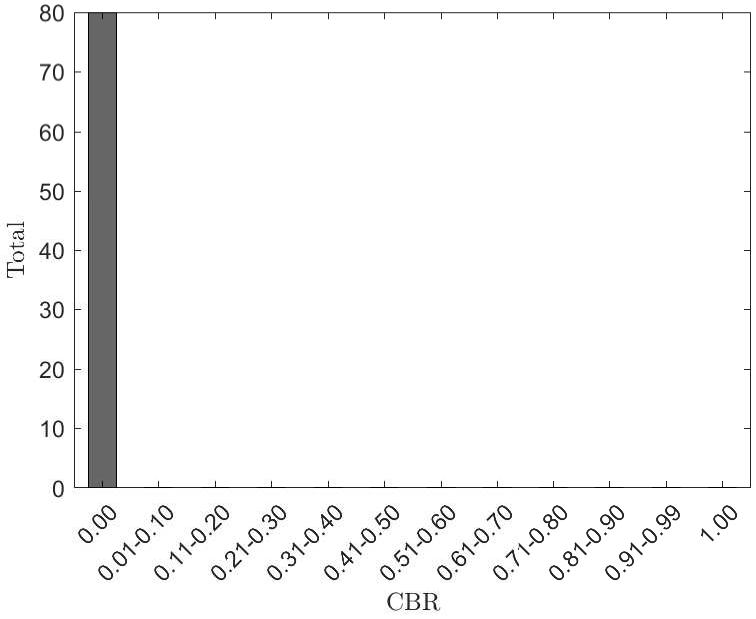

Figure C.90: Histogram for X70-X, tested for 16 days at a pH of 6.5 and 1 atm H_2S.

C.4 Test Results 0.1 atm H_2S

Figure C.91 shows the GCBR values obtained from the 0.1 atm H_2S tests. No conclusions can be drawn, due to unexpected and conflicting results. Originally, additional testing for two (2) and sixteen (16) days was scheduled, however, the samples got lost during the shipping process. It is possible that the one (1) and sixteen (16) day tests were mixed up. However, due to the limited number of available results, the 0.1 atm H_2S tests are not considered to be part of the analysis of this work.

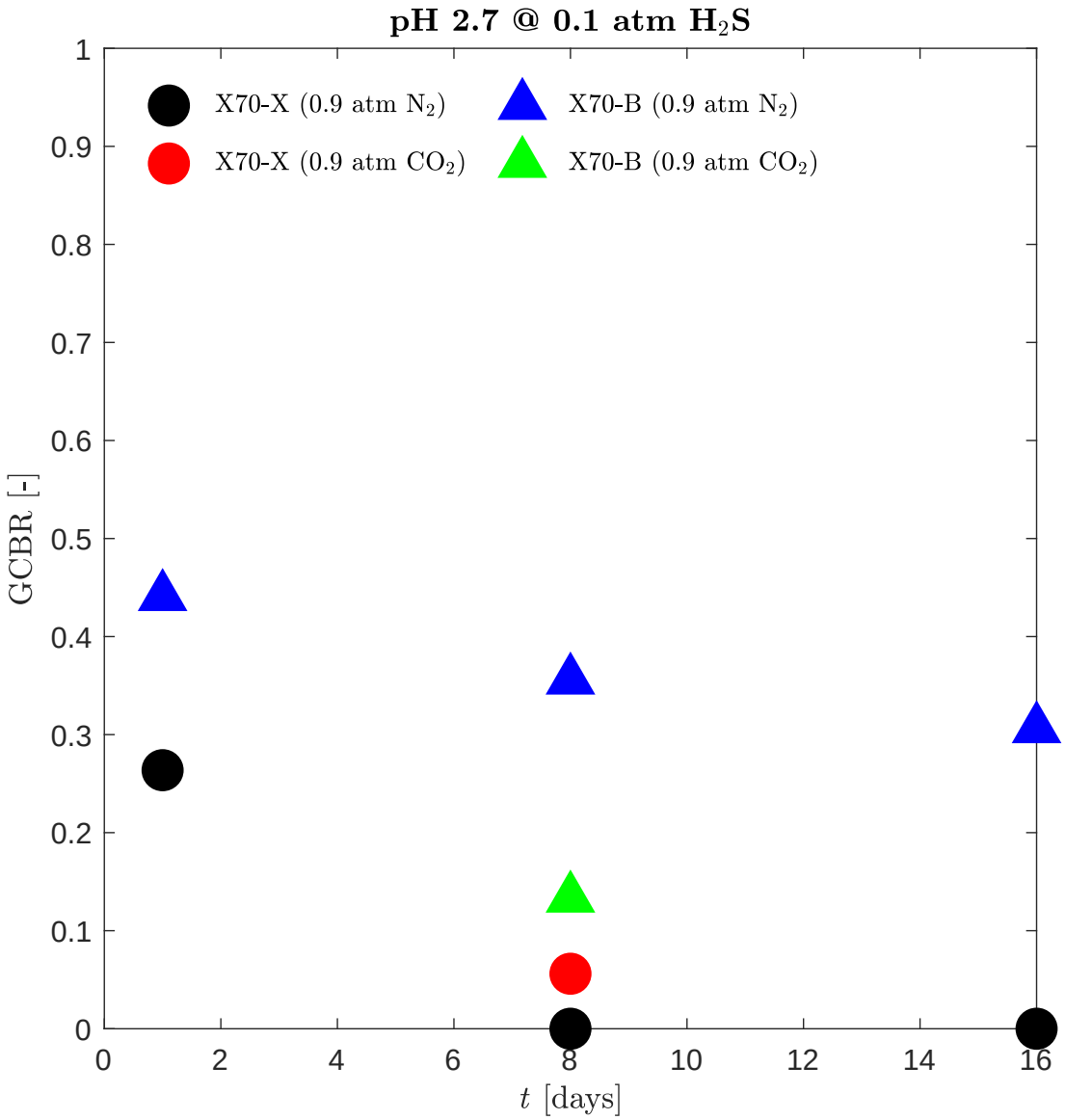

Figure C.91: Crack to area ratios for tests carried out at a pH of 2.7 and 0.1 atm H_2S.

C.5 Matlab Code

```
clc; clear; close all;
%% Manual Adjustment Section
sample = '27x8_100';     % name of folder containing rawultrasonic data
threshold = 0.015;       % lowest value for peak detection in y direction
cutOffLimit = 3.2;       % threshold for detection of crack
MinPeakDistance = 1.2;   % minimum distance between two peaks
% This section is allows for the manual correction of detected cracks. The
% value assigned to the location on the grid should be either 0 or 1.
%Example for location x: manualN(x) = 0;
%% Definition of global variables and functions
% Creation of matrices used to separate crack and backwall data.
noCrackPeaks = double.empty;
noCrackLocs = double.empty;
CrackPeaks = double.empty;
CrackLocs = double.empty;
locsTotal = zeros(80,100,2);
peaksTotal = zeros(80,100,2);
indexTotal = zeros(80,1,2);
% Creation of matrices for the storage of fitting parameters
coeffA = double.empty;
coeffACrack1 = zeros(1,80);
coeffB = double.empty;
coeffBCrack1 = zeros(1,80);
% Definition of the fitting function and start parameters.
fitEqn1 = fittype('a*exp(-b*x)');
startA = 1;
startB = 0.1;
%% Parameters for analysis
nXA = 20;                % number of zones in x direction
nYA = 4;                 % number of zones in y direction
ZA=zeros(nYA+1,nXA+1);   % matrix for UT map
valueCount  = 0;         % valueCount is used to count the number of cracks
                         % detected. If no crack is detected, the colour
                         % space of the UT map is inverted
%% Process UT data
n = 80;                  % limit for loops. 80 equals the total number of UT
                         % files.
% pre, pathname and names are used to read the ultrasonic data and store
% all data in the matrix "data".
pre = '';
pathname = strcat('C:\UltrasonicTesting\',sample);
names = {};
%% Read data for face A
% This loop reads all ultrasonic files to the temporary variable "temp" and
% saves them in the matrix "data".
for ka = 1:n
```

```
47      names = [names;strcat([pre,num2str(ka,'%02d'),'.txt'])];
        fullFileName = char(fullfile(pathname,names(ka)));
49      temp = dlmread(fullFileName,'\t',7,0);
        data(:,ka) = temp(:,1);
51  end
    % Every time the main loop is run, the temporary variables "temp", "names"
53  % and "fullFileName" are cleared.
    clear temp names fullFileName
55
    [lengthTA, widthTA] = size(data);       % lengthTA and widthTA represent
57                                          % the dimensions of the data matrix.
    range = linspace(0,100,lengthTA);       % The range matrix is used to plot
59                                          % the ultrasonic data.
    %% Clearing Section
61  clear names pathname pre                % Temporary variables are cleared.
    %% Peak detection Face A
63  % Main loop for peak detection. Peaks and location are stored in pksA and
    % locsA.
65  for k = 1:n
        TempLocs = double.empty;
67      TempPKS = double.empty;
        TempIndex = double.empty;
69      TempIndexFull = double.empty;

71      [pksA, locsA] = findpeaks(data(:,k),range,'MinPeakHeight',threshold,...
            'MinPeakDistance',MinPeakDistance);
73      lengthP = length(locsA);

75      count = 1;
        % This loop limits the peaks to a range between 5 and 30 milliseconds
77      % to elimitinate peaks generated by the interface between the probe and
        % the coupling oil and to reduce the amount of noise gained at greater
79      % signal times.
        for i = 1:lengthP
81          if ((locsA(i) > 5) && (locsA(i) < 30)) && (locsA(i)-locsA(1) > 1.5)
                location(count) = locsA(i);
83              peaks(count) = pksA(i);
                count = count + 1;
85          end
        end
87      lengthL = length(location); % lengthL stores the number of peaks.
        % This loop creates a new set of relevant peaks based on the previous
89      % filter loop and the amount of peak locations.
        count = 1;
91      for j = 2:lengthL
            peakDist(count) = location(j)-location(j-1);
93          count = count + 1;
        end
```

```
95      averageDist = mean(peakDist);   % Calculation of the average distance
                                        % between two peaks.
97      % This if loop is used to relate the peaks to the cracking behaviour.
        % If the average peak distance is smaller than the treshold, the
99      % corresponding set of ultrasonic data is marked as a crack. If the
        % crack intensity is lower than the backwall intensity, a crack to
101     % backwall ratio (CBR) is calculated.
        if manualN(k) == -1
103         if averageDist<cutOffLimit
                value(k) = 1;
105             valueCount = valueCount + 1;
                for j = 2:length(peakDist)
107                 CrackPeaks = [CrackPeaks, peaks(j)];
                    CrackLocs = [CrackLocs, location(j)];
109             end
                for i = 1:(length(location)-1)
111                 if peaks(i)<peaks(i+1)
                        TempIndex = [TempIndex, i];
113                     TempLocs = [TempLocs, location(i)];
                        TempPKS = [TempPKS, peaks(i)];
115                 end
                    locsTotal(k,1:length(TempLocs),2) = TempLocs;
117                 peaksTotal(k,1:length(TempPKS),2) = TempPKS;
                    TempIndexFull = [TempIndexFull, i];
119             end
                locsTotal(k,1:length(setdiff(TempIndexFull,TempIndex)),1) = location(
    setdiff(TempIndexFull,TempIndex));
121             peaksTotal(k,1:length(setdiff(TempIndexFull,TempIndex)),1) = peaks(
    setdiff(TempIndexFull,TempIndex));
                indexTotal(k,1) = length(setdiff(TempIndexFull,TempIndex));
123             indexTotal(k,2) = length(TempIndexFull);
                if length(peaksTotal(k,1:indexTotal(k,:,1),1))>1
125                 funcTemp1 = fit(locsTotal(k,1:indexTotal(k,:,1),1)',peaksTotal(k,1:
    indexTotal(k,:,1),1)',fitEqn1,'startpoint',[startA startB]);
                    if funcTemp1.a > 0
127                     coeffACrack1(k) = funcTemp1.a;
                        coeffBCrack1(k) = funcTemp1.b;
129                 end
                    if peaksTotal(k,2,2)>0 && peaksTotal(k,2,2)<=(coeffACrack1(k)*exp(-
    coeffBCrack1(k)*locsTotal(k,2,2)))
131                     value(k) = peaksTotal(k,2,2)/(coeffACrack1(k)*exp(-coeffBCrack1(
    k)*locsTotal(k,2,2)));
                    else
133                     value(k) = 1;
                    end
135             else
                    value(k) = 1;
137             end
```

```
        else
            value(k) = 0;
            funcTemp = fit(location',peaks',fitEqn1,'startpoint',[startA startB]);
            if funcTemp.a > 0
                coeffA = [coeffA, funcTemp.a];
                coeffB = [coeffB, funcTemp.b];
            end
            for j = 2:length(peakDist)
                noCrackPeaks = [noCrackPeaks, peaks(j)];
                noCrackLocs = [noCrackLocs, location(j)];
            end
        end
    else
        value(k) = manualN(k);
        if manualN(k) == 1
            valueCount = valueCount + 1;
        end
    end
    % This section generates the ultrasonic map, row by row.
    if (k<=20)
        ZA(1,k) = value(k);
    elseif (k>20 && k<=40)
        ZA(2,k-20) = value(k);
    elseif (k>40 && k<=60)
        ZA(3,k-40) = value(k);
    elseif (k>40 && k<=80)
        ZA(4,k-60) = value(k);
    end
%     % This section plots the ultrasonic data for each location to allow for
%     % validate the results. Using the section, the ultrasonic crack
%     % detection can be calibrated.
    figure(k)
        hold on
            plot(range,data(:,k))
            plot(location,peaks,'o','MarkerFaceColor','r',...
                'MarkerEdgeColor','r','MarkerSize',8)
        hold off
        xlabel('\textit{t} [$\mu$s]','Interpreter','Latex')
        ylabel('\textit{U} [V]','Interpreter','Latex')
        axis([0 30 -1 1])
        set(gca, 'fontsize', 11)
        box on
%     % All variables that are not used any further are cleared to free up
%     % memory.
    clear flaw flawLocationRawA flawLocationA pksA locsA ...
          noisePeakA noiseLocationA trashPeakA trashLocationA lengthP ...
          peakMatrix noisePeakIndexA noiseFinalPeaks location ...
          peaks lengthL peakDist averageDist savepath filename TempLocs ...
```

```
            TempPKS TempIndex TempIndexFull
187 end
    %% Plot Data for CAR
189 % This section defines the colour space of the ultrasonic maps. map1
    % represents the crack to area ratio (CAR) and map2 represents the crack to
191 % backwall ratio (CBR)
    if valueCount > 0
193     map1 = [ 1 1 1
                 0 0 0];
195     map2 = 1-gray(32);
    elseif valueCount == 0
197     map1 = [ 0 0 0
                 1 1 1];
199     map2 = map1;
    end
201 % The final ultrasonic map is plotted.
    figure('Position',[200 200 1100 230])
203     xA=linspace(0,100,nXA+1);
        yA=linspace(0,20,nYA+1);
205     [XA,YA] = meshgrid(xA,yA);
        sA = pcolor(XA,YA,ZA);
207     xlabel('X [mm]','Interpreter','Latex');
        ylabel('Y [mm]','Interpreter','Latex');
209     zlabel('Z [mm]','Interpreter','Latex');
        sA.CData = ceil(ZA);
211     colormap(map1)
        axis([0 100 0 20])
213 % This section saves the ultrasonic map as both .eps and .jpg file. The
    % folder "files" may need to be created manually.
215 savepath = strcat('C:\UltrasonicTesting\',sample,'\files\');
    filenameEPS = strcat(savepath,'CARmap_',sample,'.eps');
217 filenameJPG = strcat(savepath,'CARmap_',sample,'.jpg');
    saveas(gcf,filenameEPS)
219 saveas(gcf,filenameJPG)
    %% Plot Data for CBR
221 % The Crack to Backwall Ratio map is plotted
    figure('Position',[200 200 1100 230])
223     xA=linspace(0,100,nXA+1);
        yA=linspace(0,20,nYA+1);
225     [XA,YA] = meshgrid(xA,yA);
        sA = pcolor(XA,YA,ZA);
227     xlabel('X [mm]','Interpreter','Latex');
        ylabel('Y [mm]','Interpreter','Latex');
229     zlabel('Z [mm]','Interpreter','Latex');
        sA.CData = ZA;
231     colormap(map2)
        axis([0 100 0 20])
233 %% Save final map
```

```
% This section saves the ultrasonic map as both .eps and .jpg file. The
% folder "files" may need to be created manually.
savepath = strcat('C:\UltrasonicTesting\',sample,'\files\');
filenameEPS = strcat(savepath,'CBRmap_',sample,'.eps');
filenameJPG = strcat(savepath,'CBRmap_',sample,'.jpg');
saveas(gcf,filenameEPS)
saveas(gcf,filenameJPG)
% The crack to area ratio (CAR) is displayed.
CAR = sum(sum(ceil(ZA)))/80
% A corrected crack to area ratio is calculated and displayed.
CARcorr = sum(value)/n
CBR = value;
edges = linspace(0,1,21);
x = linspace(0,30,1000);
% for j = 1:80
%     figure(100+j)
%     hold on
%     if indexTotal(j,1,1)~=0
%         plot(locsTotal(j,1:indexTotal(j,1,1),1),peaksTotal(j,1:indexTotal(j,1,1)
    ,1),'kx','MarkerSize',8)
%         if peaksTotal(j,2,2)>0
%             plot(locsTotal(j,2,2),peaksTotal(j,2,2),'ro','MarkerSize',8)
%         end
%         plot(x,coeffACrack1(j)*exp(-coeffBCrack1(j)*x),'k:','MarkerSize',8)
%     end
% hold off
% xlabel('\textit{t} [$\mu$s]','Interpreter','Latex')
% ylabel('\textit{U} [V]','Interpreter','Latex')
% axis([0 30 0 1])
% set(gca, 'fontsize', 11)
% box on
% end
%% Plot of crack to backwall ratio histrogram
CBR_bins = discretize(CBR,[0 0.01 0.1 0.2 0.3 0.4 0.5 0.6 0.7 0.8 0.9 0.99 1],...
    'categorical',{'0.00','0.01-0.10','0.11-0.20','0.21-0.30','0.31-0.40',...
    '0.41-0.50','0.51-0.60','0.61-0.70','0.71-0.80','0.81-0.90','0.91-0.99','1.00'})
    ;
% minCBR = min(CBR);
% maxCBR = max(CBR);
% meanCBR = mean(CBR);
% sigmaCBR = std(CBR);
% dim1 = [0.33 0.6 0.3 0.3];
% if min(CBR)==0
%     str_min = '0.00';
% else
%     str_min = num2str(minCBR,2);
% end
% if max(CBR)==1
```

```
%     str_max = '1.00';
% elseif max(CBR)==0
%     str_max = '0.00';
% else
%     str_max = num2str(maxCBR,2);
% end
% if mean(CBR)==1
%     str_mean = '1.00';
% elseif mean(CBR)==0
%     str_mean = '0.00';
% else
%     str_mean = num2str(meanCBR,2);
% end
% if std(CBR)==1
%     str_std = '1.00';
% elseif mean(CBR)==0
%     str_std = '0.00';
% else
%     str_std = num2str(sigmaCBR,2);
% end
% str1 = {'\textbf{Statistics}'};
% str2 = {strcat('min$:~$',str_min,'~~~~~','max$:~$',str_max)};
% str3 = {strcat('mean$:~$',str_mean,'~~~','$\sigma$',':~',str_std)};
% str = char(char(str1),char(str2),char(str3));
figure(9999)
hold on
histogram(CBR_bins,'FaceColor',[0 0 0],'EdgeColor',[0 0 0],'BarWidth',0.5)
% annotation('textbox',dim1,'String',str,'FitBoxToText','on','fontsize',12,'
    interpreter','latex');
hold off
xlabel('CBR','interpreter','latex')
ylabel('Total','interpreter','latex')
box on
set(gca,'FontSize',11)
```

C.6 Error Quantification in Ultrasonic Crack Evaluation

Based on the principles presented in the literature review, it is possible to quantify the theoretical error of the ultrasonic method. As the ultrasonic probe requires sufficiently small angles to maintain the longitudinal wave and to establish contact with the sample, the probe is always aligned as vertical as possible with the aim of maintaining a 0° angle. In the following sections, the maximum offset angle between sample and probe and the resulting errors in horizontal and vertical direction, as well as the reliability of the ultrasonic peaks is determined.

C.6.1 Maximum Offset Angle

For the calculation of the maximum offset angle the following assumtions were made:

1. Any angle change between the ultrasonic probe and the coupling fluid are neglected as a contact angle of 0° can be assumed.
2. The resulting refraction angle is chosen relative to 90° to the sample surface.
3. The back of the sample acts as a perfect reflector.
4. Refraction does not sum up over time. It is assumed that the reflected signal exits the probe at the same angle as it originally did.

The values used for the calculations and their symbols can be found in Table C.1. Based on the assumptions, one can see that any horizontal derivation of greater than half the diameter of the probe will reflect off the back wall and miss the sensor and thus causes a lack of signal. The derivation of the location of the horizontal intersection with the back wall depends on both the initial offset angle and the resulting offset angle. Reforming Equation 2.2 to θ_2 leads to:

$$\theta_s = \arcsin\left(\frac{v_s}{v_c}\sin\left(\theta_c\right)\right) \tag{C.1}$$

where θ_c is the angle between probe and sample, θ_s the refracted angle of the ultrasonic wave within the sample, v_c is the speed of sound in the coupling fluid and v_s is the speed of sound in the sample. The resulting angle, θ_r, would therefore be

$$\theta_r = \theta_c + \arcsin\left(\frac{v_s}{v_c}\sin\left(\theta_c\right)\right) \tag{C.2}$$

Using trigonometric relations, the derivation in horizontal direction, Δx can be determined as followed:

$$\tan\left(\theta_r\right) = \frac{d_t}{\Delta x} \tag{C.3}$$

Realignment of this equations leads to:

$$\Delta x = \frac{d_t}{\tan\left(\theta_r\right)} \tag{C.4}$$

Considering that a wave with derivation greater than $0.5d_p$ would not be detected on its way back to the probe, the following condition must be fulfilled for the maximum combined offset angle:

$$\theta_r \leq \arctan\left(\frac{d_p}{2d_t}\right) \leq 14.04° \tag{C.5}$$

To determine the angle for θ_c, a graphical solution is chosen as θ_r depends on both θ_c and its arcsin, and is therefore non-linear. Rearranging Equation C.2 leads to:

$$\theta_r - \theta_c = \arcsin\left(\frac{v_s}{v_c}\sin\left(\theta_c\right)\right) \tag{C.6}$$

The angle θ_c can now be determined by plotting both the right hand side and the left hand side of Equation C.6. The intersection of these two functions represents the angle θ_c. Figure C.92 shows the plots of the two function. It can be seen that the intersection is at an angle of about 2.83°. Using Equation C.1, the angle for θ_s can now be calculated to 11.20°. Combining θ_c and θ_s leads to a resulting angle θ_r of 14.03°.

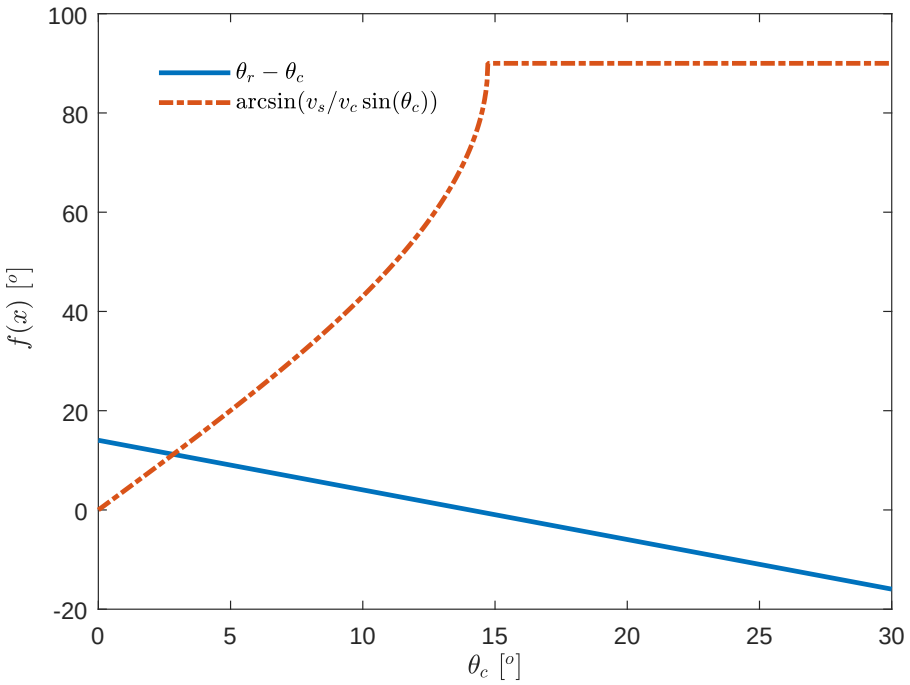

Figure C.92: Intersection of functions from Equation C.6

Table C.1: Parameters for error calculation

Indicator	**Description**	**Value**	**Unit**	**Ref.**
d_p	Diameter of the ultrasonic probe	5×10^{-3}	m	-
d_t	Thickness of the sample	10×10^{-3}	m	-
f	Operating frequency of the ultrasonic probe	10^7	s^{-1}	-
v_c	Speed of sound in the coupling fluid	~ 1500	m s^{-1}	[179]
v_s	Speed of sound in the sample	~ 5900	m s^{-1}	[71, 180]

C.6.2 Derivation in Horizontal Direction

The derivation in horizontal direction can be calculated from simple trigonometric relations. This is shown in Equation C.4. It can be assumed that the detection zone has the same geometric dimensions as the probe itself. Therefore, the effective used sensor ratio can be expressed as a function of the derivation Δx and the probe diameter d_p:

$$\xi_p = 1 - \frac{2\Delta x}{d_p} \tag{C.7}$$

Considering a maximum resulting offset angle θ_r of 14.00°, Δx can be calculated to 2.49 mm. The marginal reduction in maximum offset angle was chosen to allow a minimal detection of the signal at the surface of the probe. Using this value for Δx, the effective used area of the probe can be calculated as follows:

$$A_p = \pi \left(\frac{\xi_p d_p}{2} \right)^2 \tag{C.8}$$

where A_p is the used area of the probe. While the full area of the probe is about 19.6 mm^2, the effective area for an offset of 14.00° is only 3.14×10^{-4} mm^2. Assuming that no prior attenuation of the signal has occurred, and under the assumption that the change in sensor area can be correlated to the overall signal strength, the ratio of power can be expressed as follows [181]:

$$N_p = 10 \times \log_{10} \frac{P}{P_0} \text{ dB} \tag{C.9}$$

In this equation, N_p is the power ratio, P is the actual power and P_0 is the initial power. By relating the actual and initial area of the probe using this equation, the resulting attenuation of the signal can be calculated to about -48 dB. An attenuation of -48 dB is by no means a useful signal, as the intensity would be below the noise level. Considering that a normal signal is bound to attenuation due to energy conversion into heat within the material, a more useful approach for the definition of the offset angle is by defining the energy ratio to be -6 dB for the first two peaks, as this equates to ratio of 0.251, or about 1/4 of the intial power. Using this approach, the new resulting area can be calculated to 4.927 mm^2. This results in a sensor ratio ξ of 0.5 and a Δx of 1.25 mm. The angles θ_c and θ_s can be calculated to 1.45° and 5.70°, respectively. Therefore, the overall offset angle is 7.15°. Considering that the thickness of sample can vary, the following equation can be used to quantify the error in x direction:

$$\Delta x = \pm d_t \tan(7.15°) \tag{C.10}$$

It is assumed that the resulting angle remains constant and that d_t is constant for the entire sample. However, in case of cracking, d_t represents the distance to the crack rather than the total thickness of the sample. As can be seen in this equation, the error get smaller by reducing the thickness of

the sample.

C.6.3 Derivation in Vertical Direction

Similar to the derivation in horizontal direction, the derivation in vertical direction is affected by the offset angle. From trigonometric relations, the following correlation can be obtained:

$$\cos\left(\theta_r\right) = \frac{d_t}{\bar{d_t}} \tag{C.11}$$

In this equation, θ_r is the offset angle, d_t is the thickness of the sample or the distance to the crack, and $\bar{d_t}$ is the distance to the interface at an angle. Using the known correlation for the resulting offset angle (C.2), it is possible to calculate the difference in length, Δy, using the following equation:

$$\Delta y = d_t \left[\frac{1}{\cos\left(\theta_c + \arcsin\left(\frac{v_s}{v_c}\sin\left(\theta_c\right)\right)\right)} - 1 \right] \tag{C.12}$$

This difference can then be used to calculate the ratio between the thickness of the sample and the distance to the interface at the angle θ_r, ξ_t, using the following equation:

$$\xi_t = 1 + \frac{\Delta y}{d_t} \tag{C.13}$$

For the maximum offset angle of 7.15°, the difference in length is 2.43 mm, which is equivalent to a ratio of 1.243 or and increase of 24.3% in length.

C.6.4 Reliability of Ultrasonic Peaks

To determine the reliability of the detected peaks, the Fraunhofer distance to the far field needs to be calculated. This can be done using Equation 2.6:

$$d_f = \frac{2d_p^2 f}{v}$$

where d_f is the Fraunhofer distance, d_p is the diameter of the ultrasonic probe, f the frequency and v the speed of sound in the medium. Using the values from Table C.1, the distance can be calculated to about 84.75 mm. It is assumed that wave will enter the far zone after the sum of distance passed is equal or greater than the Fraunhofer distance. As each peak is a result of a movement of the distance of $2\bar{d_p}$, the number of reliable peaks can be calculated by division of the Fraunhofer distance and the amount of distance between two peaks. The following equation was established for this purpose:

$$n = \lfloor \frac{d_p^2 f \cos\left(\theta_c + \arcsin\left(\frac{v_s}{v_c}\sin\left(\theta_c\right)\right)\right)}{\xi_t v_s d_t} \rfloor \tag{C.14}$$

In this equation, n is the number of reliable peaks, d_p is the probe diameter, f the frequency, ξ_t the ratio of lengths, θ_c the initial offset angle, v_s the speed of sound in the sample, v_c the speed of sound in the coupling and d_t the distance to the interface. As indicated by the rounding brackets, the final result is rounded down to include only full cycles. Assuming d_t is equivalent to the thickness of the sample, 3 peaks are unaffected by bending due to the influence of the far zone for a -6 dB range. All peaks after the first three peaks may be affected by an angle α at the -6 dB boundary. The angle alpha can be calculated using Equation 2.3:

$$\alpha = \sin^{-1}\left(\frac{0.514 v_s}{d_p f}\right) \tag{C.15}$$

where α is the bending angle, 0.514 a constant for the -6 dB boundary, v_s the speed of sound in the sample, d_p the diameter of the ultrasonic probe and f the frequency. Using the values from Table C.1, the angle can be calculated to about 3.48°. This angle is applied in a conical shape from the center of the beam. Therefore, the diameter of the beam is increased and as a consequence, the energy density decreases.

C.6.5 Beam Diversion

Using a generalized Fraunhofer equation, the angle α can be calculated for different attenutation ranges:

$$\alpha = \sin^{-1}\left(K\frac{v}{Df}\right) \tag{C.16}$$

In this equation, α is the half-angle of the beam diversion, K is a constant representing the beam spread range based on the attenuation, v is the speed of sound in steel (5900 m/s), D is the diameter of the probe (5 mm) and f is the operating frequency of the probe (10 MHz). By applying $K = 1.220$ for the absolute diversion, and $K = 0.514$ for a -6dB diversion, the distance at which the beam diversion reached the same width as half the diameter of the probe can be calculated. The results can be seen in Table C.2. When assuming the full diversion of the probe the beam spread surpasses the width of the probe after about 17 mm. However, for practical reasons, a -6dB is generally assumed. Using this assumption, the beam needs to travel over a distance of 41 mm until its spread is wider than the diameter of the probe. As the average sample thickness is about 10 mm, the first 2 backwall peaks detected by the probe are not affected by the beam diversion. As the CBR is calculated by relating a crack peak between the first two backwall data peaks using an exponential fitting function, the beam diversion has no effect on the results.

Table C.2: Calculation of diversion angles and distances

K [-]	α_{rad} [-]	α_{deg} [°]	**Diversion y [mm]**
1.220	0.144	8.277	17.185
0.514	0.060	3.477	41.142

Appendix D

Metallographical Analysis

D.1 Copper Scratch Mark

The scratch mark can be seen in figure D.1. Figure D.2 shows EDX maps for the element copper for the selection shown in Figure D.1. As can be seen, copper is detected at the scratch location and no where else. These scans were conducted to explain any unusual concentration of copper at the crack sides.

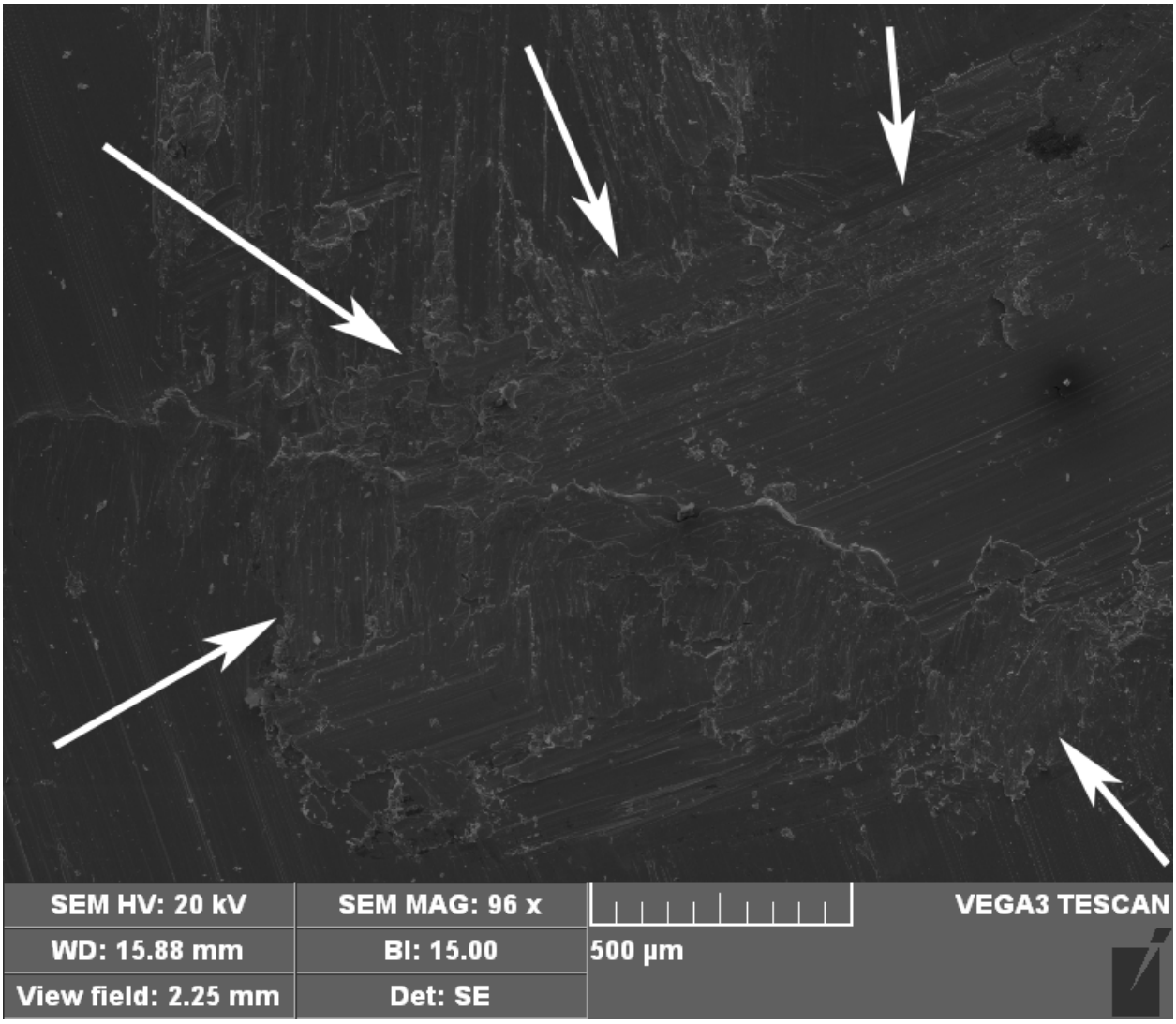

Figure D.1: Section on sample X70-X showing scratch marks from screwdriver as a result of breaking the sample open along the crack. The sample was tested at a pH of 2.7, 1 atm H_2S and a testing period of 8 days.

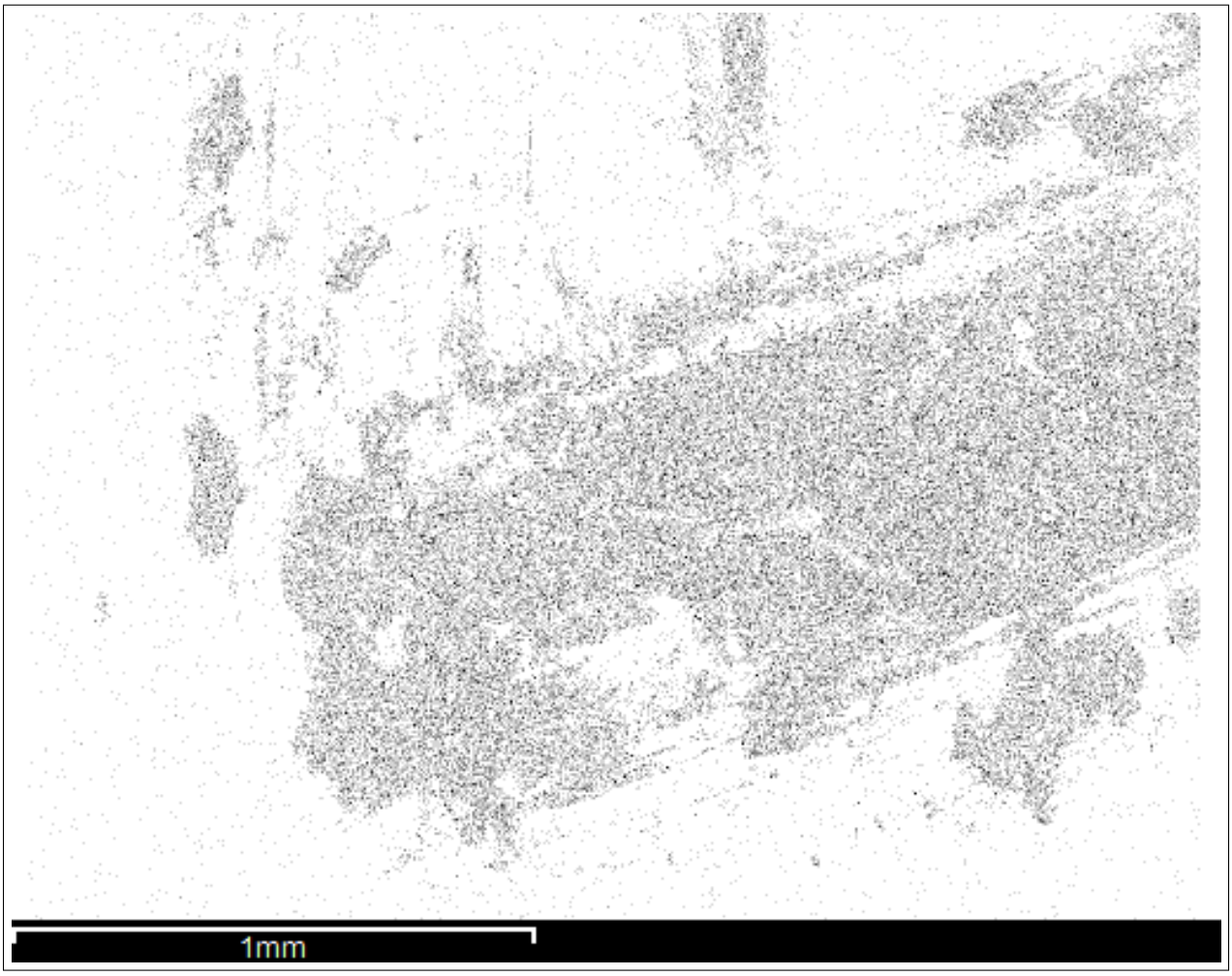

Figure D.2: EDX map for copper showing the mark left by the screwdriver.

Appendix E

Hydrogen Concentration Measurements

E.1 Hydrogen Build-up in Steel

Results obtained using the LECO D603 analyzer indicate a low reliability. The data obtained is characterized by a wide fluctuation and a large error is obtained during the calibration process. Another obstacle is the selection of a relevant sample size. The manual of the analyzer indicates a sample weight of about 5 grams, while a full HIC sample weighs in at around 150 grams. Although, the analysis of weight dependency of the analyzer has shown almost no derivation with respect to the amount of hydrogen measured, the size of a full HIC sample is problematic for the hot extraction, as the temperature gradient within the steel sample is much more present than in a 5 gram sample. Therefore obtaining the hydrogen content as a function of temperature would be prone to measuring error. A direct comparison between the results obtained in this work and the results obtained in the work of Angus [130], show an overall lower concentration of detected hydrogen.

Cutting the HIC bar in individual slices might result in the release of hydrogen during the cutting process. Heat induced during the cutting process, as well as the possibility of hitting a hydrogen reservoir drastically reduces the accuracy of results obtained from HIC slices.

In order to analyze the hydrogen content in HIC samples, alternative methods are needed. A selection of potential methods and its advantages and disadvantages are described in the following sections. In a first section, both the glycerin and mercury displacement methods are presented. Followed by this is a description of the hot extraction method coupled with an analysis using gas chromatography. Lastly, a modified hydrogen permeation test is described that allows for the continuous measurement of hydrogen during the HIC test.

E.1.1 Hydrogen Concentration Measurement using Mercury or Glycerin Displacement Method

The mercury displacement method is based on the submersion of steel sample in mercury in an isolated environment. Commonly, this test is carried out in an evaporated Y-tube. Over time diffusible hydrogen is released from the steel and collected on top of the mercury surface. As the Y-tube was previously evaporated, the addition of hydrogen will change the pressure balance and displace the mercury. The difference in mercury level can then be correlated to the amount of hydrogen released. The volume of hydrogen can be calculated using the following equation:

$$V = \frac{273 \times (p - h)\, \pi r^2 C}{760 \times (273 + T) \times 1000} \tag{E.1}$$

In this equation, p represents the atmospheric pressure, expressed in mmHg, h is the difference in height of mercury in mm, r is the radius of the capillary tubes of the Y-tube in mm, C is the length of the gas column above the mercury in mm and T is the ambient temperature in Celsius. The number 760 refers to the atmospheric pressure, 101.325 Pa, expressed in mmHg, 760 mmHg. More information can be found in ISO 3690:2012 [121].

By increasing the temperature of the mercury, the extraction of non-diffusible hydrogen is possible and the testing time is reduced. However, one very obvious disadvantage of this method is the use of mercury. The danger of mercury poisoning has resulted in abandoning the use of mercury wherever possible. The absorption of mercury commonly happens in its gas phase and will be increased at high temperatures. Therefore, this method has to be treated very carefully and should only be used as a last resort.

A much safer alternative is the Japanese glycerin displacement method. While the experimental setup and theory behind this method are virtually identical, the main difference is the use of glycerin instead of mercury. Results obtained using this method can be converted for compatibility using the following equation [124]:

$$V_{Gl} = 0.79 \times V_{Hg} - 1.73 \tag{E.2}$$

In this equation, V_{Gl} represents the hydrogen volume obtained using the glycerin method and V_{Hg} represents the hydrogen volume calculated from the mercury method. Disadvantages of the method are the absorption of hydrogen and other gases by the glycerin, as well as temperature limitations. Although this method is inherently safer, it also produces a systematic error and has been shown to show lab to lab variations [121].

E.1.2 Hydrogen Concentration Measurement using Hot Extraction and Gas Chromatography

Table 2.3 in Section 2.5.2 has shown that the release of hydrogen is dependent on its location within the steel matrix. While hydrogen located at interstitial lattice sites is released virtually immediately at room temperature, hydrogen trapped at irreversible trapping sites is only released

at significantly higher temperatures. By using the method of hot extraction, a complete extraction of hydrogen from a steel sample is possible in a timely manner. Usually, hot extraction is done using inert or unreactive carrier gases, such as helium or nitrogen. As a result of this, the different gases need to be separated in order to measure the concentration. The separation and analysis of composition can be done using gas chromatography. In this method, different gases are separated in a column using their different physical and chemical properties. This separation occurs due to different particle velocities of the individual gases. The analysis of composition is done using either thermal conductivity or flame ionization detectors. While thermal conductivity detectors are universally applicable, flame ionization detectors are unable to detect water and are more effective for the use of hydrocarbons.

A comparison between this method and the operating principle of the LECO D603 shows almost no differences. However, in order for this method to work successfully, the analysis chamber needs to be optimized for full-sized HIC samples. For the analysis of HIC samples, it would be of interest to generate temperature dependent hydrogen concentration curves. This can be achieved by applying a controlled temperature profile to the steel sample and analyzing the overall amount of hydrogen released in each temperature zone. This information would be valuable for the characterization of trap sites. Lastly, the hydrogen analyzer used in this work showed a fluctuation in results. In order to increase the reliability of this method, the detector needs to be properly maintained and calibrated.

E.1.3 In-situ Hydrogen Concentration Measurement using Modified Hydrogen Permeation Test

In order to determine the kinetics of a sour service HIC test, it would be of interest to measure the hydrogen build-up within the steel over time. One potential test method for this is hydrogen permeation. Rather than measuring the concentration of hydrogen, this test measures the permeation of hydrogen through the steel sample.

In their work, Lu et al. [182], used a modified Devanathan-Stachurski (DS) double cell to measure the permeation of hydrogen through X52 pipeline steel under wet H_2S conditions. A general DS cell consists of two compartments, one hydrogen generation cell and one hydrogen oxidizing cell. A thin steel sample is located in between the two cells and acts as a membrane. At the detection cell, the steel is passivated using sodium hydroxide. The hydrogen oxidizing or generation cell is filled with deionized and deaerated water. Hydrogen is generated by applying an electric potential from the steel membrane to the detection electrode. The resulting current density is measured and recorded. In case of in-situ hydrogen concentration measurement under sour service conditions, Lu et al. continuously bubbled H_2S into the distilled water.

By modifying the method for a standard NACE test, it would be possible to measure the hydrogen flow through the steel as a function of time. This can be achieved by measuring the electric potential generated by the reaction between the acids and the steel. Assuming the effective diffusion of hydrogen through the steel sample remains the same, it would be possible to draw

conclusions about the hydrogen build-up over time from these measurements.

One disadvantage of this method is the sample thickness. In order to assume one dimensional diffusion, the thickness of the sample needs to be significantly thinner than its other dimensions. By applying a safety factor of 10, the dimensions for a 1 cm thick steel plate would need to be 10×10 cm^2.

Appendix F

Steel Compositions

Table F.1: Steel chemistries and heat indicators for steels X70-X and X70-B, provided by EVRAZ NA Regina

Component	**X70-X**	**X70-B**	
[wt.%]	**Heat X**	**Heat B1**	**Heat B2**
C	0.061	0.05	0.04
S	0.001	0.0057	0.0057
Ca/S	2.5	0.386	0.439
N	0.0066	0.0068	0.0062
Mn	1.59	1.62	1.59
Si	0.22	0.23	0.27
Cu	0.28	0.27	0.36
Ni+Cr+V	0.404	0.344	0.354
Cb	0.091	0.089	0.088
Mo	0.055	0.054	0.055
Sn	0.012	0.01	0.011
Al	0.034	0.028	0.036
SAl	0.033	0.027	0.036
Ca	0.0025	0.0022	0.0025
Ti	0.015	0.015	0.018
Ce	0.001	0.0021	0.0016
Sb	0.002	0.003	0.004